

MODEL-BASED HYBRID VARIATIONAL
LEVEL SET METHOD APPLIED TO OBJECT
DETECTION IN GREY SCALE IMAGES



اونيفورسيتي مليسيا قهغ السلطان عبدالله
UNIVERSITI MALAYSIA PAHANG
AL-SULTAN ABDULLAH

DOCTOR OF PHILOSOPHY

UNIVERSITI MALAYSIA PAHANG
AL-SULTAN ABDULLAH

UNIVERSITI MALAYSIA PAHANG AL-SULTAN ABDULLAH

DECLARATION OF THESIS AND COPYRIGHT

Author's Full Name : WANG JING
Date of Birth : 19-04-1984
Title : MODEL-BASED HYBRID VARIATIONAL LEVEL SET
METHOD APPLIED TO OBJECT DETECTION IN
GREY SCALE IMAGES
Academic Session : SEMESTER II 2023/2024

I declare that this thesis is classified as:

- CONFIDENTIAL (Contains confidential information under the Official Secret Act 1997)*
- RESTRICTED (Contains restricted information as specified by the organization where research was done)*
- OPEN ACCESS I agree that my thesis to be published as online open access (Full Text)

I acknowledge that Universiti Malaysia Pahang Al-Sultan Abdullah reserves the following rights:

1. The Thesis is the Property of Universiti Malaysia Pahang Al-Sultan Abdullah
2. The Library of Universiti Malaysia Pahang Al-Sultan Abdullah has the right to make copies of the thesis for the purpose of research only.
3. The Library has the right to make copies of the thesis for academic exchange.

Certified by:

Wang Jing

(Student's Signature)

New IC/Passport Number
Date: 17/06/2024

Liew Siau Chuin

(Supervisor's Signature)

TS. DR LIEW SIAU CHUIN

Name of Supervisor
Date: 17/06/2024

NOTE : * If the thesis is CONFIDENTIAL or RESTRICTED, please attach a thesis declaration letter.

MAKLUMAT PANEL PEMERIKSA PEPERIKSAAN LISAN

(for Faculty of Computing student only)

Tesis ini telah diperiksa dan diakui oleh
This thesis has been checked and verified by

Nama dan Alamat Pemeriksa Dalam : Profesor Madya Ts. Dr. Ferda
Name and Address Internal Examiner Ernawan
Faculty of Computing,
Universiti Malaysia Pahang

Nama dan Alamat Pemeriksa Luar : Prof. Dr. Rahmita Wirza Binti O. K.
Name and Address External Examiner Rahmat
Department of Multimedia
Fakulti Sains Komputer dan Teknologi
Maklumat
Universiti Putra Malaysia

Nama dan Alamat Pemeriksa Luar : Prof. Ts. Dr. Salman Bin Yussof
Name and Address External Examiner  : *Institute of Informatics and*
Computing in Energy
Universiti Tenaga Nasional

اونيورسيتي مليسيا قهغ السلطان عبدالله
UNIVERSITI MALAYSIA PAHANG
AL-SULTAN ABDULLAH

Disahkan oleh Penolong Pendaftar IPS
Verified by Assistant Registrar IPS

Tandatangan:
Signature

Tarikh:
Date

Nama:
Name



اونيورسيتي مليسيا فهغ السلطان عبد الله
UNIVERSITI MALAYSIA PAHANG
AL-SULTAN ABDULLAH

SUPERVISOR'S DECLARATION

I hereby declare that I have checked this thesis and in my opinion, this thesis is adequate in terms of scope and quality for the award of the degree of Doctor of Philosophy.

(Supervisor's Signature)

Full Name : TS.DR.LIEW SIAU CHUIN

Position : SENIOR LECTURER

Date : 17/06/2024



(Co-supervisor's Signature)

Full Name : TS DR DANAKORN NINCAREAN A/L EH PHON

Position : SENIOR LECTURER

Date : 17/06/2024

اونيورسيتي مليسيا فهغ السلطان عبد الله
UNIVERSITI MALAYSIA PAHANG
AL-SULTAN ABDULLAH



اونيورسيتي مليسيا فهغ السلطان عبدالله
UNIVERSITI MALAYSIA PAHANG
AL-SULTAN ABDULLAH

STUDENT'S DECLARATION

I hereby declare that the work in this thesis is based on my original work except for quotations and citations which have been duly acknowledged. I also declare that it has not been previously or concurrently submitted for any other degree at Universiti Malaysia Pahang Al-Sultan Abdullah or any other institutions.

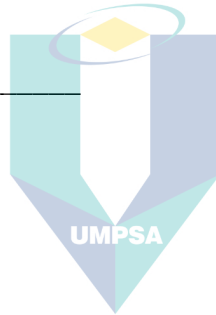
Wang Jing

(Student's Signature)

Full Name : WANG JING

ID Number : PCC17020

Date : 17/06/2024



اونيورسيتي مليسيا فهغ السلطان عبدالله
UNIVERSITI MALAYSIA PAHANG
AL-SULTAN ABDULLAH

MODEL-BASED HYBRID VARIATIONAL LEVEL SET METHOD APPLIED TO
OBJECT DETECTION IN GREY SCALE IMAGES



Thesis submitted in fulfillment of the requirements
اونيفورميتي مليسيا پاهانج عبدالله for the award of the degree of
UNIVERSITI MALAYSIA PAHANG AL-SULTAN ABDULLAH
Doctor of Philosophy/Master of Science

Faculty of Computing

UNIVERSITI MALAYSIA PAHANG AL-SULTAN ABDULLAH

JUNE 2024

ACKNOWLEDGEMENTS

I would like to express my gratitude to everyone who offered wisdom and moral support throughout my degree program. I am also grateful to my supervisors Dr. Liew Siau Chuin and Dr. Muhammad Nomani Kabir. Both of them do lots of efforts to help me finish my proposal and thesis. I am also grateful to the university and faculty staff. I am grateful to my siblings and mother, Shunyi, Yuanyi and Shufang Zhang, who have provided me through moral and emotional supports in my life. I am also grateful to my other family members and friends who have supported me along the way.



اونيورسيتي مليسيا قهغ السلطان عبدالله
UNIVERSITI MALAYSIA PAHANG
AL-SULTAN ABDULLAH

ABSTRAK

Pengesanan objek daripada imej berskala kelabu dengan tepat merupakan asas dalam pengkomputeran penglihatan dengan pelbagai aplikasi. Dalam pengimejan perubatan, ia membolehkan pengesanan tepat struktur anatomi, lesi, dan tumor daripada modaliti seperti CT, MRI, dan ultrabunyi untuk diagnosis, perancangan rawatan, dan pemantauan penyakit. Dalam pemeriksaan industri, algoritma pengesanan mengesan kecacatan produk, retak, atau anomali untuk kawalan kualiti dan keselamatan. Walau bagaimanapun, mencapai pengesanan tepat dalam imej berskala kelabu merupakan satu usaha yang mencabar disebabkan beberapa kerumitan semula jadi. Pencahayaan tidak sekata, isu biasa dalam senario pengimejan dunia sebenar, boleh menyebabkan variasi ketara dalam keamatan piksel, mengaburi sempadan objek dan merumitkan proses pengesanan. Tambahan pula, kehadiran hingar, sama ada daripada ketidaksempurnaan penderia atau faktor persekitaran, boleh mengurangkan kualiti imej dan memperkenalkan artifak yang menghalang pengesanan tepat. Selanjutnya, sempadan objek yang kompleks, terutamanya dalam adegan dengan halangan, bayang, atau bentuk rumit, menimbulkan cabaran besar bagi kaedah pengesanan tradisional. Kaedah ini sering kali gagal menggambarkan dengan tepat kontur rumit dan kawasan kepentingan, menyebabkan ralat bawah-segmen atau lebih-segmen. Untuk menangani cabaran ini, tesis yang dicadangkan memperkenalkan kaedah hibrid variasi aras set model berasaskan novel, digelar VKMHLS, yang dilaraskan khusus untuk pengesanan objek dalam imej berskala kelabu. VKMHLS menyederhanakan model Pengelompokan Keamatan Setempat (LIC) dan memperkenalkan fungsi tenaga novel berdasarkan fungsi tekanan wilayah, meningkatkan kecekapan pengesanan untuk imej berskala kelabu rendah. Tambahan pula, strategi pelaksanaan berangka pantas membolehkan pengesanan imej dan anggaran medan ofsét dengan cepat, meningkatkan kecekapan pengkomputeran keseluruhan dengan ketara. Untuk mensegmen struktur objek rumit dengan teguh dan tepat dalam set data berskala kelabu yang mencabar, VKMHLS menggunakan struktur aras set model berbilang lapisan dengan pengendali skala penyesuai. Pengendali ini menentukan bilangan lapisan optimum dan parameter skala tepat secara dinamik, mengatasi isu minima tempatan dan membolehkan pengendalian taburan berskala kelabu tidak sekata yang teruk. Di samping itu, tesis ini mencadangkan model kontur aktif inovatif dipanggil CER, yang menggabungkan unsur daripada model Chan-Vese (CV) dan model Region-Scalable Fitting (RSF) secara pintar. CER mengintegrasikan pengiraan entropi maklumat dan meminimumkan fungsi tenaga keseluruhan, membolehkan pengesanan berjaya kawasan dengan pinggir lemah, gangguan hingar kuat, dan variasi kecerahan tidak sekata merentas imej berskala kelabu. Untuk menangani cabaran berterusan mensegmen imej berskala kelabu dengan ciri-ciri tidak sekata dan tahap hingar tinggi, algoritma aras set hibrid berdasarkan metrik kernel diperkenalkan. Algoritma ini memanfaatkan penuras purata skala pelbagai yang ditingkatkan untuk mengurangkan ketidakseragaman berskala kelabu sambil mengurangkan kesan pemilihan parameter skala. Pengukuran kernel dan metrik kesamaan setempat menyekat pengaruh hingar, meningkatkan keteguhan. Tambahan pula, terma penyelarasan kecerunan kiraan mengurangkan kesan hingar lanjut, memastikan hasil pengesanan tepat. Penilaian eksperimen komprehensif menunjukkan bahawa VKMHLS mensegmen imej berskala kelabu dengan tepat yang dicirikan oleh ketidakseragaman dan pencemaran hingar, mempamerkan prestasi teguh merentas pelbagai jenis hingar. Ciri-ciri ini menjadikan VKMHLS alat yang amat bernilai untuk menangani cabaran pengesanan imej berskala kelabu dunia sebenar dan membolehkan pengesanan objek yang boleh dipercayai.

ABSTRACT

Accurate segmentation of objects from grayscale images is fundamental in computer vision with diverse applications. In medical imaging, it enables precise detection of anatomical structures, lesions, and tumors from modalities like CT, MRI, and ultrasound for diagnosis, treatment planning, and monitoring diseases. In industrial inspection, segmentation algorithms detect product defects, cracks, or anomalies for quality control and safety. However, achieving accurate segmentation in grayscale images is a challenging endeavor due to several inherent complexities. Uneven illumination, a common issue in real-world imaging scenarios, can lead to significant variations in pixel intensities, obscuring object boundaries and complicating the segmentation process. Additionally, the presence of noise, whether from sensor imperfections or environmental factors, can further degrade image quality and introduce artifacts that hinder accurate segmentation. Moreover, complex object boundaries, particularly in scenes with occlusions, shadows, or intricate shapes, pose significant challenges for traditional segmentation methods. These methods often struggle to accurately delineate the intricate contours and regions of interest, leading to under-segmentation or over-segmentation errors. To address these challenges, the proposed thesis introduces a novel model-based hybrid variational level-set method, termed VKMHLS, specifically tailored for object detection in grayscale images. VKMHLS simplifies the Local Intensity Clustering (LIC) model and introduces a novel energy functional based on the region-based pressure function, enhancing the efficiency of segmentation for low grayscale images. Furthermore, a fast numerical implementation strategy enables swift segmentation of images and estimation of the offset field, significantly improving overall computational efficiency. To robustly and accurately segment intricate object structures in challenging grayscale datasets, VKMHLS employs a multi-layer model-based level-set structure with adaptive scale operators. These operators dynamically determine the optimal number of layers and precise scale parameters, overcoming issues with local minima and enabling successful handling of severely uneven grayscale distributions. Additionally, the thesis proposes an innovative active contour model called CER, which intelligently combines elements from the Chan-Vese (CV) model and the Region-Scalable Fitting (RSF) model. CER integrates information entropy calculations and minimizes the overall energy functional, allowing successful segmentation of regions with weak edges, strong noise interference, and uneven brightness variations across grayscale images. To tackle the persistent challenge of segmenting grayscale images with both uneven characteristics and high noise levels, a hybrid level-set algorithm based on kernel metrics is introduced. This algorithm leverages an improved multi-scale mean filter to mitigate grayscale inhomogeneity while reducing the impact of scale parameter selection. Kernel measurements and local similarity metrics suppress noise influence, enhancing robustness. Furthermore, a count gradient regularization term further reduces noise impact, ensuring precise segmentation results. Comprehensive experimental evaluations demonstrate that VKMHLS accurately segments grayscale images characterized by both inhomogeneity and noise contamination, exhibiting robust performance across various noise types. These attributes make VKMHLS a highly valuable tool for tackling real-world grayscale image segmentation challenges and enabling reliable object detection.

TABLE OF CONTENT

| | |
|---------------------------------------|-------------|
| DECLARATION | |
| TITLE PAGE | |
| ACKNOWLEDGEMENTS | ii |
| ABSTRAK | iii |
| ABSTRACT | iv |
| TABLE OF CONTENT | v |
| LIST OF TABLES | x |
| LIST OF FIGURES | xi |
| LIST OF ABBREVIATIONS | xiii |
| LIST OF APPENDICES | xiv |
| CHAPTER 1 INTRODUCTION | 1 |
| 1.1 Introduction | 1 |
| 1.2 Background | 2 |
| 1.3 Problem Statement | 4 |
| 1.3.1 Uneven Gray Levels Problems | 5 |
| 1.3.2 Noise Problems | 8 |
| 1.3.3 Contour Initialization Problems | 11 |
| 1.4 Objectives | 14 |
| 1.5 Scope of The Research | 16 |
| 1.6 Chapter Organization | 17 |
| CHAPTER 2 LITERATURE REVIEW | 19 |
| 2.1 Introduction | 19 |

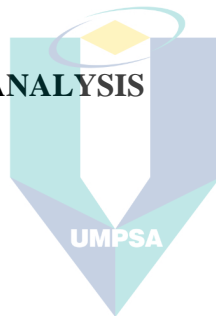


اونيورسيتي مليسيا قهغ السلطان عبدالله
UNIVERSITI MALAYSIA PAHANG
AL-SULTAN ABDULLAH

| | | |
|------------------------------|---|------------|
| 2.2 | Medical Image Segmentation Methods | 23 |
| 2.2.1 | Boundary-Based Segmentation Method | 24 |
| 2.2.2 | Threshold-Based Segmentation Method | 27 |
| 2.2.3 | Segmentation Method based on Regional Growth | 30 |
| 2.2.4 | Statistical based methods | 32 |
| 2.2.4.1 | Classifiers and clustering | 32 |
| 2.2.4.2 | The Random Field Method | 35 |
| 2.2.5 | Method based on Fuzzy Set Theory | 37 |
| 2.2.6 | Neural Network based Segmentation method | 39 |
| 2.3 | Image Segmentation for Energy Function | 42 |
| 2.3.1 | Energy Functions | 44 |
| 2.3.2 | Segmentation Method Based on Active Contour Model | 47 |
| 2.3.3 | Segmentation Method Based on Level Set | 50 |
| 2.3.4 | Information Theory-based Approach | 55 |
| 2.3.5 | Deep Learning-Based Level Set | 55 |
| 2.4 | Systematic Reviews for Related Works | 60 |
| 2.5 | The analysis of the Three Problems | 83 |
| 2.5.1 | The analysis of Uneven Gray Levels Problems | 86 |
| 2.5.2 | The analysis of Noise Problems | 92 |
| 2.5.3 | The analysis of Contour Initialization Problems | 99 |
| 2.6 | Brief Overview of the LIDC Dataset | 106 |
| 2.7 | The Summary | 112 |
| CHAPTER 3 METHODOLOGY | | 113 |
| 3.1 | Introduction | 113 |
| 3.2 | Scale Adaptive Fast Level-Set Image Segmentation Method | 113 |

| | | |
|-------|--|-----|
| 3.2.1 | Gray Uneven Image Model | 114 |
| 3.2.2 | Scale Adaptive Fast Level-Set Segmentation Algorithm | 117 |
| 3.2.3 | Area-based Pressure Function | 120 |
| 3.2.4 | Offset Field Initialization | 124 |
| 3.2.5 | Adaptive Scaling Operator | 127 |
| 3.2.6 | Numerical Realization | 130 |
| 3.2.7 | Multiphase Level-Set | 132 |
| 3.3 | Adaptive Multilayer Level-Set Image Segmentation Method | 133 |
| 3.3.1 | Improved Local Intensity Clustering Level-Set Segmentation Algorithm | 134 |
| 3.3.2 | Adaptive Scaling Operator | 134 |
| 3.3.3 | Improved Local Intensity Clustering Segmentation Algorithm | 137 |
| 3.3.4 | Simulation Experiment and Analysis | 139 |
| 3.3.5 | Adaptive Multi-Layer Level-Set Segmentation Algorithm | 145 |
| 3.3.6 | Adaptive Multilayer Level-Set Structure | 148 |
| 3.4 | Variational Level Set Method for Geometric Evolution of Curves | 153 |
| 3.4.1 | A General Equation for Geometric Evolution of Curves | 153 |
| 3.4.2 | Level Set Method for Curve Evolution | 154 |
| 3.4.3 | Improved Variational Level Set Method | 160 |
| 3.5 | Chan-Vese Model and Region-Scalable Fitting Model | 162 |
| 3.5.1 | CV Model | 162 |
| 3.5.2 | RSF Model | 165 |
| 3.6 | CER Model Based on Information Entropy | 169 |
| 3.6.1 | Information Entropy | 169 |
| 3.6.2 | Effects of Adding Information Entropy to RSF Model | 170 |
| 3.6.3 | CV- Entropy- RSF (CER) Model | 173 |

| | | |
|--|---|------------|
| 3.7 | Hybrid Level Set Image Segmentation Method Based on Kernel Metric | 174 |
| 3.7.1 | Kernel Measurement | 175 |
| 3.7.2 | Hybrid Level Set Segmentation Algorithm | 176 |
| 3.7.3 | Improved Multi-Scale Mean Filter | 176 |
| 3.7.4 | Energy Functional | 178 |
| 3.7.5 | Level Set Evolution and Numerical Realization | 181 |
| 3.7.6 | Multiphase Level Set | 185 |
| 3.8 | Level Set Image Segmentation Method and Variants | 192 |
| 3.9 | Lung Nodule Image Segmentation | 198 |
| 3.10 | Summary | 203 |
| CHAPTER 4 RESULTS AND ANALYSIS | | 207 |
| 4.1 | Introduction | 207 |
| 4.2 | Evaluation Criteria | 208 |
| 4.3 | Two-Phase Separation | 210 |
| 4.3.1 | Improve The Effectiveness of The Multi-Scale Mean Filter | 210 |
| 4.4 | Segmentation of Uneven Grayscale Images | 212 |
| 4.5 | Segmentation of Noisy Images | 219 |
| 4.6 | Multiphase Segmentation | 222 |
| 4.7 | Segmentation of Nodule Images | 228 |
| 4.8 | Conclusion | 228 |
| CHAPTER 5 CONCLUSION AND FUTURE WORKS | | 239 |
| 5.1 | Summary of Research Achievements | 239 |
| 5.2 | Research Contributions | 244 |
| 5.3 | Research Limitations | 248 |
| 5.4 | Recommendations for Future Works | 251 |



UNIVERSITI MALAYSIA PAHANG
AL-SULTAN ABDULLAH

REFERENCES

253

APPENDICES

274



اونيورسيتي مليسيا قهغ السلطان عبدالله
**UNIVERSITI MALAYSIA PAHANG
AL-SULTAN ABDULLAH**

LIST OF TABLES

| | | |
|-----------|---|-----|
| Table 2.1 | Processing stages included in each of the selected works | 65 |
| Table 2.2 | Computational techniques that have been used to carry out the automatic detection of pulmonary nodules in lung CT scan images | 69 |
| Table 2.3 | Computational classifiers that have been used for the false positive reduction task | 72 |
| Table 2.4 | Level set techniques for automatic detection of pulmonary nodules from lung CT images | 74 |
| Table 3.1 | Performance of various lung nodule segmentation methods under Jaccard overlap metric when available. | 201 |
| Table 4.1 | JS value of the image segmentation results of the seven models in Figure 4.6 | 216 |
| Table 4.2 | APD, DICE and calculation time of the seven models in the LVMR data set segmentation results | 217 |
| Table 4.3 | The JS value of the image segmentation results of the six models in Figure 4.8 | 220 |
| Table 4.4 | JS values of the four models on the image segmentation results in Figure 4.11 | 224 |
| Table 4.5 | JS values of the four models on the image segmentation results in Figure 4.12 | 224 |

LIST OF FIGURES

| | | |
|-------------|---|-----|
| Figure 2.1 | The sample of Medical Image Segmentation | 24 |
| Figure 2.2 | Boundary-Based segmentation example (a) left hand X-ray image, (b) the largest foreground region as the hand mask | 26 |
| Figure 2.3 | Threshold-Based Segmentation Method (a) original image, (b) apply global threshold function | 28 |
| Figure 2.4 | Segmentation method based on Regional Growth (a) Original image, (b) the result after process the starting point | 32 |
| Figure 2.5 | Fuzzy c Means Algorithm (a) Original image, (b) after apply double c means algorithm (c) enhancement filtration by opening structural element | 35 |
| Figure 2.6 | Fuzzy Set Algorithm (a) Original image (b) Ground truth (c) Fuzzy Set Segmentation | 38 |
| Figure 2.7 | The framework of CNN | 55 |
| Figure 2.8 | Image Segmentation of CNN | 57 |
| Figure 2.9 | Example images of lung nodules with different locations and shapes in CT: (a) common isolated nodule. (b) juxtapleural nodule. (c) cavitary nodule. (d) calcific nodule. (e) ground-glass opacity (GGO) nodule. | 57 |
| Figure 2.10 | Segmentation results visualization. | 59 |
| Figure 2.11 | Distribution of age and sex in the LIDC Dataset. | 108 |
| Figure 2.12 | The distribution of the spacing of pixels | 108 |
| Figure 2.13 | Distribution of annotation values for image features and malignancy. Note the excluded bin for the indeterminate malignancy value of 3 | 110 |
| Figure 3.1 | The effectiveness of the improved global adaptive operator | 141 |
| Figure 3.2 | Comparison of segmentation results under different initial contours | 142 |
| Figure 3.3 | Comparison of LICG, OLICG and OLICL segmentation results | 144 |
| Figure 3.4 | Local adaptive scale parameters | 145 |
| Figure 3.5 | OLICG and OLICL segmentation results | 146 |
| Figure 3.6 | The diagram of Scale Adaptive Fast Level-Set Image Segmentation Method | 186 |
| Figure 3.7 | The diagram of Adaptive Multilayer Level-Set Image Segmentation Method | 187 |
| Figure 3.8 | The diagram of Variational Level Set Method for Geometric Evolution of Curves | 188 |
| Figure 3.9 | The diagram of Chan-Vese Model and Region-Scalable Fitting Model | 189 |
| Figure 3.10 | The diagram of CER Model Based on Information Entropy | 189 |

| | | |
|-------------|--|-----|
| Figure 3.11 | The flowchart of Proposed Solution of Variational Kernel Metric Hybrid Level Set(VKMHLs) | 191 |
| Figure 3.12 | $u(x,y,t)=\exp(-(x-t)^2-(y-t)^2)+\exp(-(x+t)^2-(y+t)^2)-0.5$ is shown for $t = 0, 0.75, 1$. The zero-level curve is shown as a red line just below the surface. | 193 |
| Figure 3.13 | A solitary nodule in the lung parenchyma | 199 |
| Figure 4.1 | The offset field estimated by the improved multi-scale mean filter(the first line laid the original images, the second line laid the offset field images and the third line laid the correction images.) | 211 |
| Figure 4.2 | VKMHLs and VKMHLsO segmentation results of uneven grayscale images | 211 |
| Figure 4.3 | VKMHLs segmentation and offset field estimation of uneven grayscale images | 212 |
| Figure 4.4 | VKMHLs segmentation results under different initial contours | 213 |
| Figure 4.5 | VKMHLs segmentation results of images with different degrees of gray inhomogeneity | 213 |
| Figure 4.6 | Segmentation results of seven models on uneven grayscale images | 215 |
| Figure 4.7 | VKMHLs segmentation results of images with various noises | 218 |
| Figure 4.8 | Segmentation results of six models on images with various strong noises | 219 |
| Figure 4.9 | JS mean of image segmentation results with different levels of Gaussian noise | 221 |
| Figure 4.10 | Segmentation results of images with noise and gray inhomogeneity by six models | 222 |
| Figure 4.11 | The segmentation results of the four models on uneven grayscale MRI images | 223 |
| Figure 4.12 | The segmentation results of the four models on the MRI image with uneven grayscale with noise | 225 |
| Figure 4.13 | Segmentation results of eight models on the brain MRI slice dataset | 228 |
| Figure 4.14 | (a), (b) input image of LIDC-IDRI database; (c),(d) input image of SPIE-AAPM database; (e), (g) segmented lung (two lobes appear); (f),(h) segmented lung (only onelobe appear). | 229 |
| Figure 4.15 | First row shows the input image; second row depicts the tumor affected region (indicated using red arrow). | 229 |
| Figure 4.16 | (a),(b) show small and large ROI initialization around a low intensity nodule (c),(d) show small and large ROI initialization around a nodule with intensity inhomogeneity (e),(f),(g),(h) show segmentation results of (a),(b),(c) and (d) respectively | 230 |
| Figure 4.17 | The center slice of the 112 lung nodules from the testing dataset | 232 |

LIST OF ABBREVIATIONS

| | |
|-------|---|
| CNN | Convolutional Neural Network |
| PDE | Partial Differential Equations |
| KNN | K Nearest Neighbor |
| FCM | Fuzzy C-Means |
| EM | (Expectation-Maximization |
| MRF | Markov Random Field |
| MAP | Maximum A Posterior Probability |
| FB | Feedback Network |
| CHNN | Competing Hopfield Neural Networks |
| SOM | Self-Organization Map |
| SOPCA | Self-Organized Principal Components Analysis |
| AMSS | Affine Morphological Scale Space |
| CV | Mumford-Shah Model |
| DRL | Deep Reinforcement Learning |
| DNN | Deep Neural Network) |
| AI | Artificial Intelligence |
| PDE | the partial differential equation |
| FLSAS | Fast Level Set Method with Adaptive Scale Parameter |
| AMLLS | Adaptive Multilayer Level Set Method |
| LIC | local intensity clustering model |
| OLIC | Order Local Intensity Clustering |
| LBF | Local Binary Fitting |
| RSF | regional scale variable fitting |
| LVMR | Left Ventricle Magnetic Resonance |
| LUMR | Left ventricle magnetic resonance |
| JS | Jaccard Similarity |
| DSC | Dice Similarity Coefficient |
| APD | Average Perpendicular Distances |
| CJV | Coefficient of Joint Variation |
| WM | white matter |
| GM | gray matter |
| CSF | Cerebrospinal Fluid |
| MRI | magnetic resonance imaging |
| CFL | Courant-Friedrichs-Lewy |

LIST OF APPENDICES

| | |
|--|-----|
| Appendix A: TESTING RESULTS | 275 |
| Appendix B: NUMERICAL SCHEMES FOR THE LEVEL SET EVOLUTION EQUATION | 304 |
| Appendix C: STATISTICALLY-CALIBRATED LEVEL SET THEORY PROOFS | 304 |
| Appendix D: SEGMENTATION FEATURES | 304 |



اونيورسيتي مليسيا قهغ السلطان عبدالله
UNIVERSITI MALAYSIA PAHANG
AL-SULTAN ABDULLAH

CHAPTER 1

INTRODUCTION

1.1 Introduction

With the development of modern physics, imaging technology, computer technology, and communication technology, the application of X-ray in medical imaging has made great progress, mainly including PET tomography, MRI, DSA digital imaging, and CT. Image types such as tomographic imaging, microscopic imaging, MI molecular imaging. The images are mainly in DICOM format (Monteiro et al., 2017). With the development of various imaging technologies, in modern medicine, the use of imaging technology for disease diagnosis has become a development trend (Sumithra et al., 2015). The combination of graphic image technology and computer technology has affected the development of related industries in modern society, and it also has very important significance for the development of subject research.

In the study of medical images, authors have provided quantitative analysis and assistance for the diagnosis of medical conditions by observing the structure of tissues, anatomical structures, and applying modern techniques to analyze medical image data, locate lesions, segmentation, parameter analysis, and extract features (Bakas et al., 2017). Accurate analysis of medical images has a great effect on clinical diagnosis. Accurate data can greatly reduce misdiagnosis. Therefore, the analysis of medical images has become a focus area of many scholars (Bakas et al., 2017). The three levels of image processing, image analysis and image understanding constitute the main image research content (Bhattacharyya et al., 2017). Image segmentation belongs to the level of image analysis. The purpose is to divide the image target into a series of regions with different feature meanings, and identify the segmented regions (boundary curve, pixel feature points.). Image segmentation is an important part of the underlying visual application field, and is the basis of high-level image analysis and understanding, especially in the

fields of target tracking, target recognition, image feature analysis, medical image segmentation and reconstruction (Ghiasi and Fowlkes, 2016).

1.2 Background

The quality of the segmentation result has a direct impact on the success of picture interpretation and other related tasks since it acts as a bridge between the communication system's low-level pixel representation and its high-level semantic symbol representation. Image segmentation is often a necessary pre-processing step in a variety of different systems due to the reasons stated above. For example, text elements such as text, images, and tables are detected from images to lay the foundation for further pattern recognition. Obviously, with the development of computer intelligence, the high-level applications of various image data will be more and more, and image segmentation will continue to receive more attention because of its important position (Van et al., 2019). Image segmentation technology can automatically or semi-automatically extract regions of interest in an image that belong to the target region. This lays the foundation for higher-level image analysis and comprehension of the target of interest, such as model representation, parameter extraction, image recognition, and so on. Image segmentation technology can also extract regions of interest in an image that do not belong to the target region. In a similar vein, medical image segmentation is the essential technological component for the processing, reconstruction, analysis, and comprehension of medical images. Image registration, which is often used, 3D reconstruction, computer-aided diagnosis systems are inseparable from medical image segmentation technology (Tey et al., 2018). Medical image segmentation technology divides an image region with the same intensity, color or texture characteristics into several sub-regions, corresponding to different targets in the image, so that the medical volume data image pixels can be marked as specific tissues, organs or anatomical structures. Provide doctors with auxiliary judgments and help (Hung., 2018).

Medical image segmentation has been widely used in the research and practice of clinical diagnosis, pathological analysis, auxiliary surgery, medical image information processing., especially in the academic field of computer information processing and medical research. Volume. For example, it is necessary to extract the structural regions

of organ tissues in the image, which is convenient for doctors to analyze organ body data information, anatomical structure measurement, tissue structure cell identification. Medical image segmentation is medical image 3D reconstruction, image registration and assistance. The basic data of the diagnostic system provides reliable and complete data for intelligent analysis of images (Das et al., 2018). At the same time, it can be used to extract characteristic parameters of medical image target tissues, such as pathological information, time-dependent lesion geometry, physical structure Changes and the establishment of a relevant data repository to provide doctors with important information for the diagnosis of a particular condition. In the clinic, the extracted medical image target area is located and the segmented tissue is visualized for three-dimensional reconstruction, for surgery, specific medical treatment, computer-aided diagnosis, guidance for interventional surgery. To do accurate target positioning, which has been applied in modern medical surgery (Roth et al., 2018). Image segmentation technology also has application value in the digital storage of medical data. For the long-term preservation and management of medical image information resources, it is convenient for later search and Application, application segmentation of specific image targets, compression processing, image data better preservation, transmission, remote diagnosis services. Application of image segmentation technology to measure tissue, organ or lesion, calculate area, volume., before and after treatment Relevant quantification and analysis of image data can help doctors to develop more reasonable and targeted treatment plans according to the development of the disease, which is of great value to medical clinical applications.

Lung cancer, as one of the leading causes of cancer-related mortality worldwide, warrants detailed elucidation to provide readers with a clear understanding of its significance within the realm of medical imaging and the motivation behind the research (Biswas and Hazra, 2022).

In recent years, there has been a growing body of research focused on improving lung cancer detection and diagnosis, with an emphasis on the critical role played by medical imaging modalities such as computed tomography (CT) scans and magnetic resonance imaging (MRI). These imaging techniques are instrumental in the early detection and characterization of lung lesions, which is pivotal for timely intervention

and improved patient outcomes. The research on lung cancer imaging has been driven by the need for more accurate and efficient methods due to the sheer prevalence and lethality of the disease. According to recent statistics, lung cancer is responsible for a significant portion of cancer-related deaths globally (Wang et al., 2020; Yin et al., 2020).

Furthermore, contemporary research (Zhang et al., 2022; Srikanth and Bikshalu, 2022) has highlighted the specific challenges associated with lung cancer imaging, which include the heterogeneity of lung nodules, the presence of noise in medical images, and the necessity for precise contour initialization. These challenges underscore the importance of developing innovative image analysis and segmentation techniques, which is the core objective of the present research. Therefore, understanding the landscape of lung cancer imaging is essential for appreciating the relevance and significance of new methods in the context of lung cancer detection and diagnosis.

1.3 Problem Statement

Vision is an important way for humans to obtain information from the real world, to perceive and understand the world. However, limited by many factors, there are very few visual information that humans can personally acquire. As an important material carrier, the image can make up for this shortcoming. Humans use physical instruments such as optical devices to acquire images, and use digital technology to store and transmit images to achieve information visualization and information sharing. In the fields of astronomy, satellite remote sensing, military, small to medical, nanotechnology, and even entertainment industry and digital communication, images help humans to understand targets in different environments and at different scales, and to perceive the real world in different spaces and times. The various modes that help humans make optimal decisions and take the right actions (Liu and He., 2015). However, the original information contained in the image is often not directly used by humans, and the image processing science is thus produced. Even though this thesis already have a lot of research results, there are still some issues need to be solved. The problems are shown in below.

1.3.1 Uneven Gray Levels Problems

Due to defects in imaging equipment or changes in illumination, some grayscale images such as MRI, CT, and infrared will show uneven grayscale. The gray-scale distribution of uneven gray-scale images in different target areas overlaps seriously, which makes it difficult to segment the uneven gray-scale image correctly. As a solution to this issue, a number of researchers have presented a variety of level-set segmentation algorithms that are based on the various local areas. These researchers begin with the premise that the gray level of the picture is consistent within a given region (Li et al., 2007; Li et al., 2008; Wang et al., 2009; Zhang et al., 2010; Liu and Peng, 2012; Ji et al., 2015; Wang et al., 2017; Chen et al., 2017; Min et al., 2018). These techniques can segment pictures with an uneven grayscale, but they are prone to falling into local minima and are sensitive to the contour that is first drawn. In recent years, the approach to segmentation known as "offset correction level-set clustering," which is based on K-means clustering, has garnered a lot of interest (Li et al., 2011; Zhan et al., 2013; Zhang et al., 2014; Zhang et al., 2015; Huang and Zeng, 2015; Min et al., 2016; Cai et al., 2018; Wang et al., 2018). Estimating the offset field of the picture is possible with the help of this sort of approach, thanks to local K-means clustering. It achieves accurate segmentation of the picture despite the presence of gray inhomogeneity thanks to the offset correction and level-set approach, and obtain better segmentation performance than the local area-based method. However, it uses a finite difference strategy in its numerical implementation, and the time step needs to meet the CFL (Courant-Friedrichs-Lewy) condition (Weickert et al., 1998) to ensure the stability of level-set evolution. Therefore, it must be adopted A small time step leads to slow convergence and low segmentation efficiency. In addition, it uses local area information to estimate the offset field, this may quickly settle into a solution at a local minimum and is sensitive to the location of the starting contour. In addition, the scale parameter of the clustering kernel function is used by this sort of procedure in order to exercise control over the magnitude of the local region. The selection of the scale parameter affects the estimation accuracy of the migration field, and these methods use fixed scale parameters, which seriously affect their practical application.

Images that have broad gray-scale unevenness may be successfully segmented by using an offset correction level-set segmentation approach that is based on K-means clustering. On the other hand, since this thesis used a fixed scale in our clustering criterion, most methods are difficult to segment images with severely uneven gray levels. In response to this problem, researchers have proposed some adaptive scale parameter level-set segmentation methods (Cai et al., 2018; Piovano and Papadopoulos, 2008). Cai et al. used image entropy to automatically determine the scale parameters of the clustering kernel function (Cai et al., 2018). The previous method uses local variance to propose an adaptive scale operator. However, these methods use the same scale parameter at each pixel, leading to incorrect segmentation of some images with nonlinearity or severe gray-scale inhomogeneity. In addition, these approaches only employ local area information to segment the picture, which makes them sensitive to the initial contour of the image and makes it easy for them to fall into a solution that is a local minimum. In recent years, a number of multi-scale level-set approaches have been suggested (Wang et al., 2015; Min et al., 2016; and Zhang et al., 2017). In (Sui et al., 2012; Min et al., 2016) a set of scale parameters designed a multi-layer level-set structure, adaptively decide the scale parameters at each pixel, and maintain the ability to detect global contrast information in order to prevent slipping into local minima. It is difficult to provide appropriate scale parameters for segmenting images that have highly uneven gray levels because this method uses a series of fixed scale parameters and can only provide a limited number of candidate scales. In addition, this method only provides a small number of candidate scales.

The problem statement highlights several critical challenges in medical image segmentation, specifically related to uneven gray levels, and discusses the shortcomings of existing level-set segmentation algorithms (Li, et al., 2020; Yin et al., 2020). Understanding these issues is vital for appreciating the significance of innovations like the VKMHLS method.

Uneven Gray Levels Problems: Uneven gray levels in medical images can be attributed to various factors, including variations in imaging equipment quality, inconsistent illumination, or even inherent heterogeneity in the imaged tissue. These irregularities manifest as disparities in pixel intensities across the image, making it

difficult to distinguish between different structures accurately. For example, in lung CT scans, uneven gray levels might obscure the boundaries of nodules, which are critical for early cancer detection. Addressing this issue is essential for ensuring the accuracy of segmentation results.

Challenges with Existing Level-Set Algorithms: The statement rightly points out that existing level-set segmentation algorithms face significant challenges when dealing with images exhibiting uneven gray levels:

Prone to Local Minima: Level-set algorithms are optimization-based techniques that seek to minimize an energy functional to evolve contours and segment objects. However, they can often get stuck in local minima, resulting in suboptimal segmentations. This is particularly problematic when dealing with complex, unevenly lit medical images, as the algorithm may converge to an inaccurate segmentation.

Sensitivity to Initial Contour: Many level-set methods are highly sensitive to the initial contour or seed points provided by the user. In scenarios with uneven gray levels, slight variations in the initial contour placement can lead to vastly different segmentation results. This sensitivity requires users to have precise prior knowledge of the object's location, which is not always feasible in practical applications.

Limited Segmentation Efficiency: The requirement for a small time step in numerical implementations hinders the efficiency of existing level-set algorithms. This limitation arises from the need to maintain stability and convergence during the optimization process. Slower convergence rates can be especially problematic when dealing with large or high-resolution medical images, as it prolongs the segmentation process. In summary, the uneven gray levels problem in medical image segmentation poses significant challenges. It impacts the accuracy and efficiency of segmentation algorithms, which are critical for tasks like lung nodule detection. Furthermore, the susceptibility of existing methods to local minima and sensitivity to initial contours underscores the need for innovative solutions like VKMHLS. This method aims to overcome these limitations by introducing adaptive scale operators, novel energy functionals, and a multi-layer level-set structure. Through these advancements, VKMHLS seeks to provide more robust and accurate segmentations, even in the face of

uneven gray levels, ultimately contributing to improved medical image analysis and diagnosis.

Therefore, due to defects in imaging equipment or illumination changes, some grayscale images like MRI, CT, and infrared show uneven grayscale distributions, making it difficult to correctly segment the images. Most existing methods that use fixed scale parameters in clustering criteria are difficult to apply to images with severely uneven gray levels, leading to incorrect segmentations. Providing appropriate scale parameters is challenging when using fixed scales that offer limited candidate values. The problem statement emphasizes critical challenges with uneven gray levels and shortcomings of current level-set algorithms, underlining the need for innovative solutions to ensure accurate segmentation results.

1.3.2 Noise Problems

Many literatures have studied the level set segmentation methods of noisy images (Xie et al., 2014; Ali et al., 2018; He et al., 2012; Li et al., 2013; Guo et al., 2018; Miao et al., 2018; Wu et al., 2015; Liu et al., 2018; Yang et al., 2014; Niu et al., 2017; Yu et al., 2018; Duan et al., 2015; Wu et al., 2016; Liu et al., 2018). Some methods use the local similarity of pixels to reduce the influence of noise (Yang et al., 2014; Niu et al., 2017; Yu et al., 2018). These methods can deal with weak noise image, but it is difficult to correctly segment the image with strong noise. In addition, some new distance measurement methods and level set regularization methods are used to segment images with noise (Miao et al., 2018; Wu et al., 2015; Liu et al., 2018), (Duan et al., 2015; Wu et al., 2016; Liu et al., 2018). Liu et al. (2018) used kernel metrics and total variation rules to segment images with strong noise and proposed the KMD model, but this model cannot handle uneven grayscale images. Subsequently, Liu et al. proposed the LODL model (Liu et al., 2018) using the L_0 gradient and L_0 function regularization term. This model can accurately segment images with strong noise, but it is still difficult to deal with uneven grayscale images. The LIC model (Li et al., 2011) assumes that the offset field changes slowly in the image domain. Therefore, the MSF model (Wang et al., 2015) uses a multi-scale mean filter to estimate the offset field of the image to make the offset correction. The resulting image has slight gray-scale unevenness. Therefore, the segmentation

method using fixed scale parameters can correctly segment the corrected image, and can eliminate the influence of the scale parameter on the segmentation of the gray-scale uneven image. In recent years, some mixed level set models have been used to deal with uneven images (Wang et al., 2010; Wang et al., 2009; Shyu et al., 2012; Liu et al., 2013 ; Jiang et al., 2014; Wen, 2014; Wang et al., 2014; Wang et al., 2014; Wang et al., 2018; Li et al., 2015; Jiang et al., 2015; Zhou et al., 2016; Huang et al., 2015; Soomro et al., 2016; Shi and Pan, 2016; Mondal et al. al., 2016; Liu et al., 2017; Soomro et al., 2018; Wang et al., 2015; Cai et al., 2018). Liu et al., (2013) combined the LIC model based on local information (Li et al., 2011) with the CV model based on global information (Chan and Vese, 2001) and proposed the LIC-CV model (Liu et al., 2013). This model can handle slightly uneven grayscale images and is robust to the initial contour. The level set evolves quickly, but it is easily disturbed by noise.

The problem statement addresses a significant challenge in medical image segmentation, focusing on the detrimental impact of noise on existing level-set methods and emphasizing the need for more robust segmentation approaches (Yu et al., 2020; Wang et al., 2020; Biswas and Hazra, 2022; Zhang et al., 2022). This analysis explores the intricacies of the noise-related issues discussed in the statement.

Difficulty in Accurate Segmentation with Strong Noise: Noise in medical images can originate from various sources, including the imaging process itself and environmental factors. When noise levels are high, it becomes exceedingly challenging to accurately segment objects or regions of interest. The presence of noise introduces unwanted variations in pixel intensities, making it difficult for segmentation algorithms to distinguish between true object boundaries and noise-induced artifacts. This is particularly critical in medical imaging, where precise delineation of structures, such as tumors or organs, is essential for diagnosis and treatment planning.

Inability to Handle Combined Noise and Uneven Grayscale Levels: The statement highlights a particularly daunting scenario where medical images exhibit both strong noise and uneven grayscale levels simultaneously. This is a realistic challenge, as medical images are often prone to noise due to factors like low-dose acquisition or hardware limitations. When coupled with uneven grayscale levels, it becomes even more arduous

for traditional level-set segmentation methods to produce reliable results. Uneven grayscale levels, as discussed in the previous problem statement, further compound the complexity of the segmentation task.

Drawbacks of Existing Mixed Level-Set Models: The problem statement also alludes to existing mixed level-set models being easily disturbed by noise, leading to segmentation errors. Mixed level-set models combine different energy terms to balance various influences on the segmentation process. However, they can be sensitive to noise, as noise can significantly affect the energy landscape, leading to undesirable minima in the optimization process. This sensitivity undermines the robustness of the segmentation algorithm, particularly in the presence of noise.

In essence, the challenges related to noise in medical image segmentation are paramount. High noise levels degrade the quality of medical images, rendering conventional level-set methods less effective. Moreover, when combined with uneven grayscale levels, noise exacerbates the difficulties faced by segmentation algorithms. The mention of existing mixed level-set models being prone to noise disturbances underscores the urgency for innovative solutions.

Researchers have recognized the need to develop segmentation methods that are not only capable of handling noise effectively but can also address the complexities arising from uneven grayscale levels. Novel approaches, like VKMHLS, aim to mitigate these challenges by introducing adaptive mechanisms, advanced energy functionals, and noise-resistant techniques. By doing so, they strive to enhance the accuracy and reliability of medical image segmentation, ultimately benefiting clinical diagnosis, research, and treatment planning.

Therefore, some methods can deal with weak noise images, but it is difficult to correctly segment images with strong noise. Existing models that use new distance measurement methods and level set regularization to segment noisy images cannot handle uneven grayscale images. The problem statement highlights a daunting scenario where medical images exhibit both strong noise and uneven grayscale levels simultaneously, exacerbating the difficulties for traditional level-set methods. It also alludes to existing

mixed level-set models being easily disturbed by noise, leading to segmentation errors and undermining the robustness of the algorithms.

1.3.3 Contour Initialization Problems

The vast majority of the currently available models are only able to process basic picture types. What this indicates is that there is a distinct line separating the object from the backdrop. Real photographs are often more complicated than rendered ones because of the imaging technology and the many aspects in the actual world that contribute to ambiguity. For instance, medical photos often exhibit a significant amount of noise, poor edge definition, and uneven intensities across the image. The majority of the previous study consisted on less complicated picture analysis. In addition, existing level set segmentation methods can handle general uneven grayscale images according to level set segmentation features (Appendix D), but for severely uneven grayscale images, it is difficult to meet the assumption that the grayscale of the local area is approximately uniform due to the use of fixed-scale clustering criteria, resulting in segmentation errors. Second, the existing level set methods based on offset correction mostly use Euclidean distance to construct data items, but this measurement method is less robust to various types of noise, so it is difficult to deal with the simultaneous presence of strong noise and uneven grayscale. Image. In addition, for images with complex backgrounds, especially natural images, it brings great challenges to unsupervised level set segmentation methods, and further research is needed. Finally, the level set method itself also has some aspects that need to be improved, such as sensitivity to the initial contour, easy to fall into a local minimum solution, and slow level set evolution.

The majority of models (Chan and Vese, 2001; Liu et al., 2013), such as CV, have difficulties with their evolutionary pace. This is mostly a result of the fact that the great majority of theoretical outcomes of leveling are dependent, to some degree or another, on the degree to which the surface is smooth. In spite of this, the single-value surface is often seen as a product of the development process in applications that are based on the actual world. In order to ensure the smoothness criteria as well as the stability and effectiveness of the level set evolution, it is essential to often perform the reinitialization of the level set function. This is done in order to keep the leveling evolution smooth. The

procedure is carried out on a periodic basis in order to achieve this goal. This procedure requires a significant amount of time for computation. Researchers came up with a variety of innovative solutions to try to fix this issue. Nevertheless, these techniques can only be used to certain applications since they are only an upgrade tailored to the particular requirements of each mode. Thus, even enhanced acceleration algorithms have a limited capacity for adapting to new circumstances. As a result, it is essential to locate an algorithm that does not rely on a particular environment in particular, but instead expands the area of adaptability and effectively increases the pace of segmentation.

In a way that is analogous to the sensitivity of the RSF model in the process of picking the starting contour, Finding the numerical solution to partial differential equations that take into account beginning circumstances and boundary conditions is the fundamental objective of the overwhelming majority of models. This is the case for almost all of the models. This fundamental purpose is analogous to the sensitivity of the RSF model in the process of picking the starting contour. The initial conditions that were frequently supplied have a significant impact on the results of the segmentation that was performed. The vast majority of the models that are presently accessible provide an option for manually defining the starting form. As a result of this, the challenges of how to initialize the contours and where to initialize them have been established. The classic level-set segmentation methodology known as GAV requires the initialization level set to be specified in the form of a signed distance function. The no-initialization model has to define a piecewise constant function. In spite of the fact that they have to create several sorts of functions, they have to start by defining the initial contour first. Hence, finding a solution to the issue of contour initialization has been a significant focus in the most recent few years.

The problem statement addresses a set of challenges associated with contour initialization in the context of level-set segmentation methods (Srikanth and Bikshalu, 2022; Khosravanian et al., 2023), specifically focusing on the issues related to complex backgrounds, sensitivity to initial contours, and the computational inefficiency arising from frequent reinitialization.

Challenges with Complex Backgrounds: One of the fundamental challenges in image segmentation, especially in natural images, is the presence of complex backgrounds. These backgrounds can be intricate and varied, making it difficult for unsupervised level-set segmentation methods to distinguish between the foreground object of interest and the background clutter. This complexity arises in various domains, such as object recognition in outdoor scenes or medical image analysis, where objects are surrounded by anatomical structures or intricate textures. Handling such complexity effectively is crucial for achieving accurate and robust segmentation.

Sensitivity to Initial Contours: The problem statement highlights the sensitivity of level-set segmentation methods to the initial contour, which poses a risk of falling into a local minimum solution. In level-set-based segmentation, an initial contour is often provided as a starting point for the algorithm. The final segmentation result can vary significantly depending on the choice of this initial contour. Sensitivity to the initial contour means that small changes or inaccuracies in the initial contour can lead to suboptimal or incorrect segmentation results. This issue becomes particularly problematic when dealing with complex backgrounds, where it may be challenging to provide an accurate initial contour manually.

Slow Level-Set Evolution and Frequent Reinitialization: The level-set evolution process is a fundamental component of level-set segmentation methods. However, it can be computationally demanding and slow, especially in scenarios where smooth and accurate segmentations are required. To ensure that the level-set function remains well-behaved and maintains smooth contours, frequent reinitialization steps are often necessary. This process involves resetting the level-set function to its signed distance property and can significantly impact the computational efficiency of the segmentation algorithm. Slow evolution and frequent reinitialization can hinder the real-time or near-real-time application of level-set segmentation methods, which is essential in various domains like medical imaging or robotics.

Therefore, for images with complex backgrounds, especially natural images, it brings great challenges to unsupervised level set segmentation methods, and further research is needed. The problem statement highlights the sensitivity of level-set

segmentation methods to the initial contour, which poses a risk of falling into a local minimum solution. The level-set evolution process can be computationally demanding and slow, especially in scenarios requiring smooth and accurate segmentations. To maintain smooth contours, frequent reinitialization steps are often necessary, impacting the computational efficiency of the segmentation algorithm. Slow evolution and frequent reinitialization can hinder real-time or near-real-time applications of level-set segmentation methods.

In summary, the problem statement highlights the critical challenges associated with contour initialization in level-set segmentation methods. Complex backgrounds can confound the segmentation process, especially in natural images, where the object of interest is embedded in intricate surroundings. Sensitivity to initial contours can lead to suboptimal solutions, emphasizing the need for robust initialization methods. Additionally, the computational inefficiency arising from slow level-set evolution and frequent reinitialization limits the practical applicability of these methods, particularly in scenarios requiring real-time or near-real-time results. Addressing these challenges is vital for enhancing the usability and effectiveness of level-set segmentation techniques across a wide range of applications. Researchers and practitioners are continually working on innovative solutions to mitigate these issues, with the aim of making level-set segmentation more accessible and reliable in complex image analysis tasks.

1.4 Objectives

The proposed framework, based on entropy, is indeed designed to address all three of the identified problems simultaneously: Uneven Gray Levels Problems, Noise Problems, and Contour Initialization Problems. This comprehensive approach combines various techniques and strategies within a unified algorithm to tackle these challenges efficiently.

Uneven Gray Levels Problems: The framework employs an innovative approach to handle uneven gray levels. By utilizing logarithmic transformation, it can adapt to and enhance images with irregular grayscale distributions. This addresses the issue of varying intensities within the image and ensures that the segmentation process can effectively deal with uneven gray levels.

Noise Problems: Noise in medical images, such as those used in lung cancer detection, can be a significant obstacle to accurate segmentation. The proposed framework incorporates techniques like kernel measurement, local similarity measurement, and count gradient regularization. These elements collectively act as noise filters, ensuring that the algorithm can robustly handle images with strong noise, thus mitigating the Noise Problem.

Contour Initialization Problems: The contour initialization problem is tackled by providing an innovative method for initializing the migration field. This initialization approach likely contributes to more stable and accurate segmentation, addressing issues related to sensitivity to the initial contour and slow level-set evolution.

By combining these elements into a single algorithmic framework, the proposed method aims to provide a holistic solution to the stated problems. It leverages entropy-based principles and integrates them into the various stages of the image segmentation process. This unified approach is advantageous as it not only streamlines the segmentation process but also ensures that the algorithm remains robust and accurate in the presence of challenges related to uneven gray levels, noise, and contour initialization. However, a more detailed explanation and validation in the full paper would be necessary to comprehensively assess the effectiveness of this framework in addressing these issues.

The objectives can be described as:

- 1) **To Propose** an effective level-set segmentation method capable of handling images with uneven grayscale levels caused by imaging equipment defects and changes in illumination.
- 2) **To propose** techniques to handle images with both strong noise and uneven grayscale levels for enhancing the robustness of mixed level-set models to reduce the impact of noise and minimize segmentation errors.
- 3) Handling complex backgrounds, especially in natural images, **to improve** model-based level-set segmentation methods to reduce sensitivity to the initial contour, enabling more reliable segmentation results.

1.5 Scope of The Research

The study commenced with a comprehensive introduction to active contour models, elucidating their fundamental principles, applications, and significance in image segmentation. However, the research was limited to exploring active contour models rooted in image boundary features, excluding other types of active contour models. The research conducted a thorough analysis of the challenges prevalent in contemporary image segmentation techniques, with a specific focus on challenges related to uneven grayscale levels, noise, and contour initialization problems. Other challenges beyond these three areas were not be addressed in the current study. Furthermore, a pivotal segment of this study involved a meticulous investigation into the behaviour of the gradient vector flow field, a critical component in active contour models. The research undertook an exhaustive analysis of the gradient vector flow field, culminating in a significant discovery regarding the divergence of the flow field generated by the gradient vector. However, the analysis was limited to the theoretical aspects of the gradient vector flow field, without exploring its practical implementation or optimization.

Building upon the insights gained from the previous phases, the study focused on the development of a novel energy functional that serves as a measure of the flux of the gradient vector flow field through the active curve. This step was integral to ensuring precise and effective image segmentation. The research elucidated the methodology for quantifying the flux of the gradient vector flow field via the active curve, employing the newly developed energy function. In the final phase, the study culminated in the construction of an innovative active contour model, crafted by leveraging the gradient flow of the energy function discussed earlier. To rigorously assess the model's capabilities and effectiveness, it was tested on various datasets, including the Left Ventricle Magnetic Resonance (LVMR) dataset, continuous simulated brain MRI image slice datasets, and the LIDC-IDRI database. However, the testing and evaluation was limited to these specific datasets, and the model's performance on other datasets will not be explored in the current research. By defining the scope in this manner, the study acknowledges its limitations and provides a clear focus on specific objectives, including the analysis of active contour models, the investigation of the gradient vector flow field, the development of a novel energy functional, and the construction and testing of an

innovative active contour model. This revised scope ensures that the research remains focused, transparent, and aligned with the suggested boundaries outlined in the comment.

1.6 Chapter Organization

The main contributions of the dissertation are shown as below:

Chapter 1: The first chapter is an introduction. At the beginning, it described the fundamentals of images and image processing, which served as a foundation for the various medical picture segmentation techniques. In the second step of the image segmentation model development process, issue descriptions and goals were presented. Lastly, this thesis will discuss the primary body of our study.

Chapter 2: In this chapter, the mathematical notion that underpins the technique of image segmentation that is based on partial differential equations is explained. This chapter was titled "Picture Segmentation Based on Partial Differential Equations." This includes not only partial differential equations (PDE), but also the principles of the variational approach, as well as the variational level set method, plane curves, and the features of mathematical representation and curve development. In addition to that, the variational level set approach was covered in this chapter as well. In addition to this, it focused on many conventional models for image segmentation that are based on partial differential equations, the development of image segmentation, and the evolution of image segmentation and the most recent advancements in medical image segmentation algorithms using deep learning techniques. In conclusion, the SLR approach was used to provide a concise summary of the level set as well as the lung cancer detection algorithms that were employed in the process of establishing the database and testing methodologies.

Chapter 3: Both the Chan-Vese and RSF models have flaws, including a lack of capacity to segment grayscale images, sensitivity to the initialization contours, and poor noise immunity. Chapter 3 proposes the CER model as a solution to these problems so that the models will no longer have these problems. This model makes use of a local entropy weight, convolution neural networks, and reinforcement deep learning. And then, Scale adaptive fast level-set image segmentation method, Adaptive multilayer level-set

image segmentation method and Hybrid level set image segmentation method based on kernel metric were used to design the proposed method.

Chapter 4 is discussion of results. It presents the results of this study. According to research questions, it states main findings. Compared with former studies, results here are discussed, telling the common points and the difference with previous studies.

Chapter 5 has a summary of key findings. Based on these conclusion and future works of this research, it gives suggestions for researchers and operators of recommendations for further studies that are related to this thesis.



اونيورسيتي مليسيا قهغ السلطان عبدالله
**UNIVERSITI MALAYSIA PAHANG
AL-SULTAN ABDULLAH**

CHAPTER 2

LITERATURE REVIEW

2.1 Introduction

Image segmentation is a method and process that involves separating an object of interest from the rest of the picture based on color, intensity, texture. (Saba et al., 2018; Thilagamani and Kavya, 2018) Image segmentation is both the process and the method of dividing a picture into separate areas that don't overlap and have similar features. The segmentation of medical images has long been one of the most challenging aspects of image processing. This is because of the intricate backdrop, the wide variety of target elements, and the noise that might be present in the images. The manual segmentation stage is followed by the semi-automatic segmentation stage, and then lastly, the completely automated segmentation stage is reached. Manual segmentation is often carried out by qualified clinical professionals in accordance with the requirements of either scientific or clinical research, making use of specialized software to directly delineate the boundaries of the area of interest on the original picture.

At present, the accuracy of manual segmentation is the highest among all segmentation methods, and the semi-automatic or fully automatic segmentation method is generally evaluated as a gold standard. However, the manual segmentation method is time-consuming, laborious, and inefficient, and the segmentation result depends on the observer's knowledge and experience, and has certain subjectivity, so the repeatability is low. The semi-automatic segmentation method combines the powerful image data storage and processing capabilities of the computer with the operator's knowledge and experience, and completes the image segmentation process through human-computer interaction.

Compared with the manual segmentation method, the semi-automatic segmentation method has greatly improved the speed. However, the segmentation result still needs to rely on the operator's experience and knowledge, which limits the promotion

of the semi-automatic segmentation method in the clinic to some extent. application. The fully automatic segmentation method refers to the whole process of completely completing the image segmentation by using the computer completely, and the segmentation process is completely free from human interference. Since there is no influence of human factors in the automatic segmentation process, the segmentation result can be reproduced well, and the efficiency is high. Researching and developing effective automatic segmentation methods has been a hot topic in recent years for researchers to conduct image segmentation techniques. From the current development trend of medical image segmentation technology, the research on new segmentation methods usually targets the following aspects: Automatically, try to complete the target extraction process with minimal human-computer interaction; accurate, as close as possible to the target's anatomy Structure; fast, real-time processing in clinical applications as the ultimate goal; adaptability, different applications can self-learn; robustness, strong resistance to noise, offset field effects, blur. (Pham et al., 2018; Cao et al., 2018).

The comprehensive evaluation of medical image segmentation algorithms is of paramount importance as it ensures their robustness, generalizability, and clinical applicability. By subjecting these algorithms to rigorous testing on diverse datasets during viva voce examinations, researchers can gain invaluable insights into their performance across various imaging modalities, anatomical regions, and pathological conditions. The reasons can be summarized as:

Addressing Imaging Modality Variability. Medical imaging encompasses a wide range of modalities, each with its unique characteristics and challenges. Comprehensive evaluation during viva voce examinations involves testing segmentation algorithms on images acquired from different modalities, such as computed tomography (CT), magnetic resonance imaging (MRI), ultrasound, and X-ray. This diversity in imaging modalities introduces variability in terms of image quality, contrast, noise levels, and artifact patterns. By evaluating algorithms on multiple modalities, researchers can assess their ability to handle these variations and ensure their robustness across different clinical scenarios (Litjens et al., 2017).

Accounting for Anatomical Complexity. The human body is a complex structure with intricate anatomical features and variations across individuals. Effective medical image segmentation algorithms must be capable of accurately delineating structures and regions of interest in various anatomical regions, such as the brain, lungs, liver, heart, and musculoskeletal system. During viva voce examinations, candidates present their algorithms' performance on datasets encompassing diverse anatomical regions, demonstrating their ability to handle the unique challenges and complexities associated with each region (Heimann et al., 2009).

Addressing Pathological Variability. Medical images often capture pathological conditions, including lesions, tumors, and abnormalities, which can significantly impact the appearance and characteristics of anatomical structures. Comprehensive evaluation during viva voce examinations involves testing segmentation algorithms on datasets containing various pathologies to assess their ability to accurately segment diseased regions and maintain robustness in the presence of pathological variations (Cheplygina et al., 2019).

Validating Clinical Applicability. Ultimately, the goal of medical image segmentation algorithms is to facilitate accurate diagnosis and treatment planning in clinical settings. By evaluating algorithms on diverse datasets representative of real-world clinical scenarios, researchers can validate their applicability and potential impact on patient care. This comprehensive evaluation ensures that the algorithms can handle the variability and complexities encountered in clinical practice, increasing confidence in their use for decision-making and treatment planning (Heimann et al., 2022).

Enabling Algorithm Comparison and Benchmarking. Comprehensive evaluation provides a standardized platform for comparing the performance of different segmentation algorithms. By subjecting multiple algorithms to the same diverse datasets, researchers can objectively evaluate their strengths, weaknesses, and relative performance. This comparison and benchmarking process facilitate the identification of best-performing algorithms and guide future research efforts in the field (Maier-Hein et al., 2018).

Fostering Algorithm Improvement and Refinement. The comprehensive evaluation process often reveals limitations or shortcomings in segmentation algorithms. By analyzing their performance on diverse datasets, researchers can identify specific areas for improvement, such as handling specific imaging modalities, anatomical regions, or pathological conditions. This feedback loop enables researchers to refine their algorithms, incorporate new techniques or strategies, and iteratively enhance their performance, ultimately leading to more robust and reliable solutions (Jiang et al., 2021).

Facilitating Interdisciplinary Collaboration. Medical image segmentation is an interdisciplinary field that requires collaboration among researchers from various domains, including computer science, biomedical engineering, and clinical medicine. Comprehensive evaluation during viva voce examinations provides a common ground for researchers from different disciplines to engage in meaningful discussions, share insights, and collaborate on addressing the challenges and complexities of medical image analysis (Huo et al., 2021).

Promoting Reproducibility and Transparency. By adhering to comprehensive evaluation protocols and reporting standards, researchers can enhance the reproducibility and transparency of their work. This transparency allows other researchers to validate and build upon existing algorithms, fostering a collaborative and open research environment that drives scientific progress in medical image segmentation (Guo et al., 2020).

Facilitating Algorithm Deployment and Clinical Translation. The ultimate goal of medical image segmentation research is to develop algorithms that can be deployed in clinical settings and integrated into healthcare systems. Comprehensive evaluation during viva voce examinations provides evidence of an algorithm's robustness, generalizability, and applicability, which are crucial factors in gaining regulatory approval and facilitating clinical translation (Drozdal et al., 2021).

Driving Innovation and Advancing the Field. Comprehensive evaluation serves as a driving force for innovation and advancement in the field of medical image segmentation. By exposing the limitations of existing algorithms and identifying areas for improvement, researchers are motivated to explore new techniques, algorithms, and

approaches to address the challenges encountered during comprehensive evaluations. This iterative process of evaluation and innovation propels the field forward, enabling the development of more accurate, efficient, and reliable segmentation solutions (Nikolov et al., 2022).

Therefore, comprehensive evaluation plays a pivotal role in assessing the effectiveness, robustness, and generalizability of medical image segmentation algorithms. By subjecting these algorithms to rigorous testing on diverse datasets during viva voce examinations, researchers can gain invaluable insights into their performance across various imaging modalities, anatomical regions, and pathological conditions. This comprehensive approach not only ensures the clinical applicability of the developed algorithms but also fosters collaboration, promotes transparency, and drives innovation in the field of medical image analysis, ultimately contributing to improved patient care and advancing the frontiers of healthcare.

2.2 Medical Image Segmentation Methods

In the realm of image processing, the problem of medical image segmentation has been very popular but also quite challenging throughout the course of the previous two decades. There have been a significant number of people devoting their time and energy to the investigation of medical image segmentation techniques; nonetheless, the technology pertaining to segmentation has not yet reached the level of maturity. Researchers have suggested a vast number of different ways for the segmentation of medical images, including both newly developed ideas and methodologies from a wide variety of fields. The modern medical image segmentation method fully demonstrates the characteristics of multidisciplinary intersection, and is closely related to the development of mathematics, physics, optics, and computer science. Although there are many segmentation algorithms proposed at present, the limitations are also great, so medical image segmentation is still a challenging subject. Medical image segmentation is shown in Figure 2.1 and is a key link in the follow-up operation of normal tissue and diseased tissue visualization, three-dimensional reconstruction, quantitative analysis. It is also a bottleneck in clinical medical application and practice. The accuracy of segmentation seriously affects the doctor's diagnosis of the true condition of the disease. It is important to develop an accurate treatment plan (Nasrulloh et al., 2018).

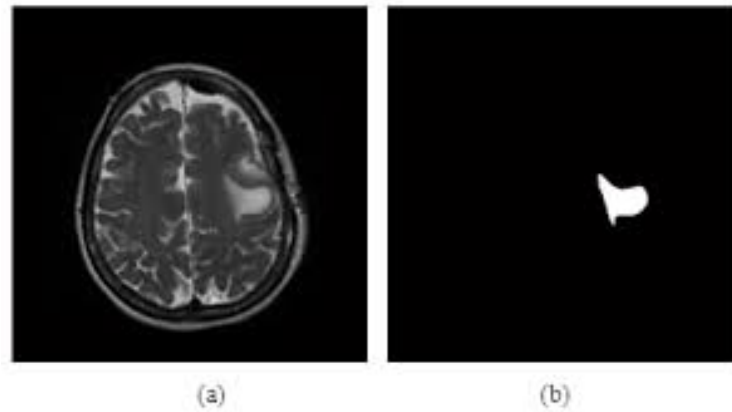


Figure 2.1 The sample of Medical Image Segmentation

Medical images themselves are characterized by their complexity. They are generally characterized by low resolution, low contrast, variability of anatomical tissues and organs, blurred boundaries between different soft tissues or soft tissues and lesions, shape structure and fineness. The structure (blood vessels, nerves) is complexly distributed, and the shape and characteristics of organs of different people are also greatly different. On the other hand, because of the imaging equipment that is now used in medical imaging (CT, MR, PET.), the medical pictures that are created contain a certain amount of noise, an offset field effect, and a partial volume effect. There is a possibility that the image's object edge contains ambiguity as well. The segmentation of medical images will be made more challenging as a result of these objective aspects (Drozdal et al., 2018). Therefore, there is no suitable and universal medical image segmentation theory and method in clinical application and practice, and satisfactory segmentation results can be obtained for all images. People can only make reasonable choices on the segmentation key indicators such as the accuracy, speed and robustness of the segmentation method for the specific segmentation problems and specific requirements faced in practical applications. For how to specifically classify medical image segmentation methods, so far this thesis have no unified standard (Yan and Wang., 2016). Below this thesis introduce several currently more classic or mature methods according to the theory or technology based on various algorithms.

2.2.1 Boundary-Based Segmentation Method

When a picture is broken up into subgraphs, there is often a distinct line delineating the border between each of the subimages that individuals get. The grayscale

amplitude is discontinuous because of the properties of the border pixels, which cause these characteristics. It is likely that this thesis will discover that the pixel characteristics on each side of the border exhibit discernible variations from one another. If this thesis can use some method to find the boundary and specify the direction of the boundary, then the pixels on one side of the boundary are divided into one sub-image, while the pixels on the other side belong to another sub-image. If this can be done, then the pixels on one side of the boundary belong to one sub-image, while the pixels on the other side belong to another sub-image. If there is a technique that can be used to locate the border and describe the direction that the boundary will go, then this thesis will be able to accomplish what needs to be done. This is something that this thesis could achieve if this thesis could utilize some mechanism to locate the border and indicate the direction in which the boundary runs. By proceeding in this manner, the process of picture segmentation has been completed. Figure 2.2 presents a number of different approaches that researchers and physicians have developed in order to determine the borders of the diagram. When manually determining the borders of an image, for instance, one may utilize devices such as a mouse and a light pen as determining instruments. The operator is now in a position to establish the location of the boundary by using the discontinuity of a particular feature of the boundary pixel in conjunction with their previous knowledge of the segmented picture. In addition, the preliminary boundary may be drawn by hand, or a number of boundary points can be determined, and then the final boundary can be corrected with the help of an algorithm. This is a technique that is only somewhat automated. In spite of the fact that the manual approach and the semi-automatic method both have drawbacks, such as low efficiency, poor repeatability, and a high dependency on subjective elements, the past information is contributed to the judgment process, particularly with respect to the segmented picture. Because of this applicable skill, manual segmentation may provide superior outcomes. Because of the complexity of a medical picture, it is occasionally necessary to use either a manual or a semi-automatic technique when attempting to determine the border of a target inside the image. In order to automatically establish the boundary, it is common practice to first identify the edge pixels and then, using a predetermined set of guidelines, link the edge pixels that meet the criteria to form the border.

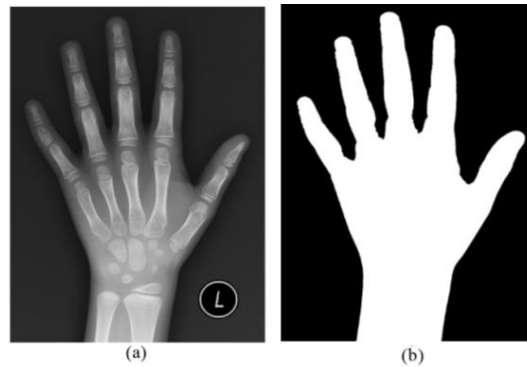


Figure 2.2 Boundary-Based segmentation example (a) left hand X-ray image, (b) the largest foreground region as the hand mask

The initial step in each of the boundary-based medical picture segmentation algorithms is to locate the pixel boundaries of the item to be segmented. In the spatial domain, the identification of an image target boundary pixel may be accomplished with the assistance of either an edge detection template or an edge detection operator. Edge extraction may be accomplished by using either the information about the picture's zero-crossing points in the second-order derivative or the extreme value of the first-order reciprocal of the image as the primary premise for doing so. To be more specific, in a region of the image where the rate of change is relatively slow, there is not a significant amount of change in the gray level of the adjacent pixels, and as a result, the gradient value is low. On the other hand, in the region of the image that is closest to the edge, there is a significant amount of change in the gray level of the adjacent pixels, and as a result, the gradient value is high. As a result, the location of the edge may be established by calculating the extent of the amplitude of the first derivative. In a similar manner, The sign of the second derivative can be used to determine whether or not a pixel is located on the bright side or the dark side of the edge, and the location of the zero crossing can be used to determine the precise location of the edge. Both of these factors can be used in conjunction with the location of the edge itself. First-order derivative edge operators include things like the Roberts gradient operator, the Sobel operator, the Prewitt operator, and a few others. On the other hand, the Gaussian Laplace operator is classified as a second-order derivative edge operator. In addition to the direction template and the edge detection technique of the statistical template, every edge detection operator has their own set of benefits and drawbacks that they bring to the table. However, because of the complexity of the edge, the edge of the image appears as an incoherence of gray in the

image. This is because the edge and the noise signal are both high-frequency signals, and high-frequency signals are easily confused with one another and are difficult to separate into their respective frequency bands. Image segmentation based on boundaries is necessary as a result. While there are still some obstacles to overcome with the technology, its relevance in the geometric analysis of medical pictures is quite significant.

2.2.2 Threshold-Based Segmentation Method

One of the most well-known and often used techniques for doing region-based parallel segmentation is known as the Threshold approach. The fundamental idea is to establish distinct feature thresholds for each class of image pixel point, and then partition the picture into many classes based on these thresholds. The fundamental idea behind threshold segmentation is to first determine the segmentation threshold based on a particular feature of the pixel, and then compare the feature value of the pixel to the segmentation threshold in order to determine which sub-image the pixel should be classified as belonging to. This is done so that the pixel can be assigned to the appropriate sub-image. This is done in order to determine which sub-image the pixel should be classified as belonging to. In most cases, the gray level of the pixel is used as the criteria for selecting the threshold. As a result, when people talk about threshold segmentation, they almost always mean grayscale threshold segmentation. Obviously, the threshold may also be chosen based on other characteristics, such as the grayscale gradient of the pixel. Nevertheless, this is not the only option.

Either the global information, which is the gray histogram of the whole picture, or the local information may be used as the basis for the determination of the Threshold. A context-based and non-context-based segmentation approach is what Taxt and colleagues mean when they talk about the threshold setting methodology, which is based on both local and global information (Sahare and Dhok. 2018). If during the process of segmentation, all of the pixels in the whole picture are compared and recognized by the same threshold, then the threshold segmentation in question is referred to as the global threshold segmentation. Local thresholding segmentation is a type of segmentation that can also be referred to as adaptive segmentation (Sahare and Dhok. 2018). This type of segmentation occurs when the image is divided into a number of distinct sub-regions during the process of segmentation, and then different thresholds are set for each of those

sub-regions in order to classify the image pixels. The threshold approach was developed by Verma and Parihar (2017) and Li et al. (2015). (Gao et al., 2018). The method of threshold segmentation may also be broken down further into single-threshold segmentation and multi-threshold segmentation. Images are separated into two categories in the single-threshold method: the target (shown as black) and the background (shown as white) in Figure 2.3.

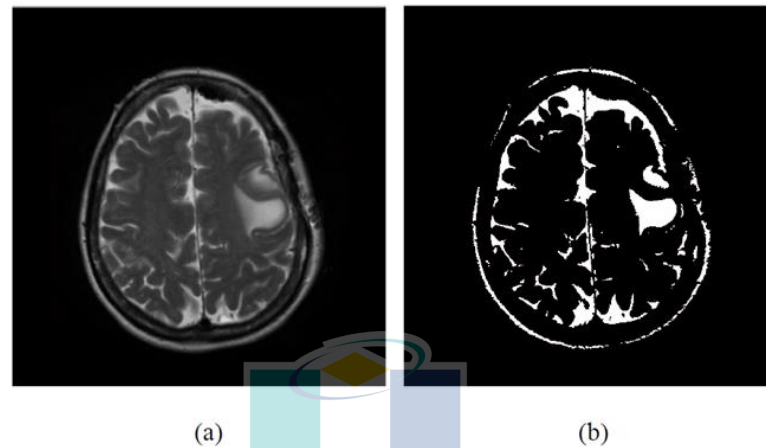


Figure 2.3 Threshold-Based Segmentation Method (a) original image, (b) apply global threshold function

It is necessary to use the Multi-threshold method in situations in which the image contains multiple objects, each of which has unique surface characteristics. These scenarios include images with uneven illumination, objects that have varying reflection coefficients, and images with varying depths of field. Under the context of this discussion, the threshold segmentation approach might be seen as a classification issue. All of the pixels in the picture are separated into two groups using the single-threshold segmentation technique: the target and the background. It was demonstrated by (Aja-Fernández et al., 2015) that the iterative threshold method that was proposed by (Deng et al., 2016) and (Bolourchi et al., 2016) can be viewed as a special case in the classical Bayesian criterion. These two papers were published in the journals (Deng et al., 2016) and (Bolourchi et al., 2016). The Bayesian allocation criteria may be written as a form that makes the threshold calculation easier, and the approach operates on the assumption that both the target and the background follow a normal distribution with the same variance (Bolourchi et al., 2016). Since the target and background pixels are both assigned the same prior probability distribution, the Bayesian formula used in the

technique described by only needs to compute the portion of the method that contains the threshold (Deng et al., 2016).

If the image contains areas with varying grayscale ranges, such as areas that are noticeably distinct from one another, The histogram of the picture will give the impression of having several peaks. Each peak in the histogram will be representative of a region in the picture, and the valleys that exist between any two peaks that are next to one another will be represented by peaks that are adjacent to one another in the histogram. Point apart. If the image target has a uniform gray value and is scattered over another background that likewise has a uniform gray value, then the gray histogram will have a pronounced double peak and a narrow trough. This will be the case if the histogram is plotted. This is because the two gray values will be additive. In this particular instance, the point at the bottom of the trough was selected as the threshold to use for differentiating between the target and the backdrop. As a result, when the gray histogram includes one (or more) narrow troughs, determining the threshold will be fairly straightforward, and the only point that has to be discovered is the valley point (Bolourchi et al., 2016).

The truth of the matter is, however, that photographs do not always seem to have clearly distinguishable objectives and backgrounds. Finding valley sites is not the only challenge involved in determining the appropriate threshold. The interference from the noise makes it impossible to pinpoint exactly where the valley is located. Researchers are looking for a mechanism to automatically establish the threshold in order to discover a solution to the issue (Li et al., 2015; Wang et al., 2016) Finding the ratio of the biggest inter-class variation to the local method is how researchers (Sun et al., 2017; Mousavirad and Ebrahimpour-Komleh, 2017; Bhandari, 2018; Park et al., 2018; Mousavirad and Ebrahimpour-Komleh, 2017) establish the threshold. Li et al., (2015) makes the assumption that the target and the background both follow the normal distribution with considerable differences between the mean and the variance, and they state that the threshold is found by locating the minimal amount of global misclassification error. The computation is somewhat difficult to understand. Bhandari, (2018) provided an approach that required a reasonably little amount of computing while operating on the premise that the same normal model was being used. They optimized the threshold of the average classification error for all pixels in order to locate the threshold at which the least amount

of error could be produced. (Park et al., 2018) used the assumption that both the target and the background follow the Poisson distribution, and they optimized the same criteria to find the threshold. The gray histogram of the picture is the sole piece of information that is used in threshold segmentation. The benefit is that the computation amount is relatively low and that it is simple to put into practice. Nevertheless, when there is no visible trough in the histogram, the threshold segmentation approach often does not have an appropriate threshold, which results in incorrect segmentation. Since spatial information is not taken into account, noise and inhomogeneity have the potential to create artifacts in the picture and ruin the grayscale distribution. The threshold segmentation approach is hence vulnerable to noise and unevenness.

2.2.3 Segmentation Method based on Regional Growth

The region expanding and splitting combining technique is a typical example of a serial method for segmenting regions, and the processing of the upcoming stages of the segmentation result is decided depending on the results of the steps that came before them. According to (Hole et al., 2016), the fundamental idea behind the region expanding technique is the act of aggregating picture pixels or sub-areas into bigger regions in accordance with a user-defined similarity function. This is the core theory behind the region growing method (Rajinikanth et al., 2018). During this step of the process, you will first locate a seed point (which can be a single pixel or a small area) as a growth point for each area that needs to be segmented. After that, you will search for its neighborhood, which in turn will have seed pixels in the neighborhood around the seed pixel depicted in Figure 2.4. Finally, you will segment the area based on the new growth points. To create a new growth starting point, pixels with the same or similar characteristics are merged together in the region where the seed pixel is situated. The steps described above are repeated until there are no more pixels that satisfy the condition, at which point the process ends and regions with distinct characteristics are formed. The approach for creating regions assumes that each pixel may be placed in just one of many categories. The most important thing to understand is that pixels of the same sort have certain characteristics that are comparable to one another according to a set of predetermined criteria. The term "feature vectors" refers to the collection of these attributes, which may include the grayscale values of the picture, the gradient values, the edge points, and so

on. In real-world applications, the regional growth method solves three fundamental problems: determining the number of regions to be created, choosing a set of seed points that accurately represent the region that is desired, and deciding on meaningful features, growth criteria, and criteria for terminating the process of growth. This algorithm's benefits include the ease with which it may be calculated, as well as its high accuracy and high efficiency when applied to uniform linked objects (Kalaiselvi and Nagaraja, 2015).

Nevertheless, in order to identify the seed pixels, the region growing technique involves interaction between a person and a machine. Moreover, in order to extract an area, a growth point has to be specified for that region. Moreover, it is sensitive to noise, which might cause a hole or even a disconnection in the region that is being removed. As a result, the region growth approach, much like the threshold segmentation method, is often not employed alone and instead has to be supplemented with additional image processing processes that are ideal for segmenting tumors and scars. The framework itself (Zhang et al., 2016; Drukker et al., 2018). While developing an algorithm for generating regions, it is possible to include statistical data and previous knowledge into the algorithm so as to eliminate the need for human selection of seed pixels. An adaptive region expanding approach was suggested by (Tan et al., 2017). This algorithm automatically learns to maximize homogeneity criteria depending on the form features of each segmentation area. (Tan et al., 2017) Using the sample sites in the area, which are chosen by random walks of the seed points, the parameters in the homogeneity criterion are calculated, and the homogeneity criteria are updated appropriately. When applied to the process of segmenting CT and MR images, the approach is not only easy to apply but also robust, and it may provide good results.

The concept behind the region merging approach is to first divide the complete picture into a number of smaller parts that are similar to one another, and then to combine the similar regions that are next to one another using some kind of evaluation criteria. By using the region splitting technique, the input picture is handled as an area, and the region is repeatedly divided into four smaller rectangular parts until a certain quality of the pixels included inside each of the little regions is identical. The split-merge process begins by partitioning the whole picture into separate sections, which are subsequently combined with those of their neighbors. The benefit of using the approach of area merging is that it

eliminates the need of doing a preliminary selection of seed spots (Rundo et al., 2016). The possibility that it may ruin the margins of the segmentation region is a drawback of this method.

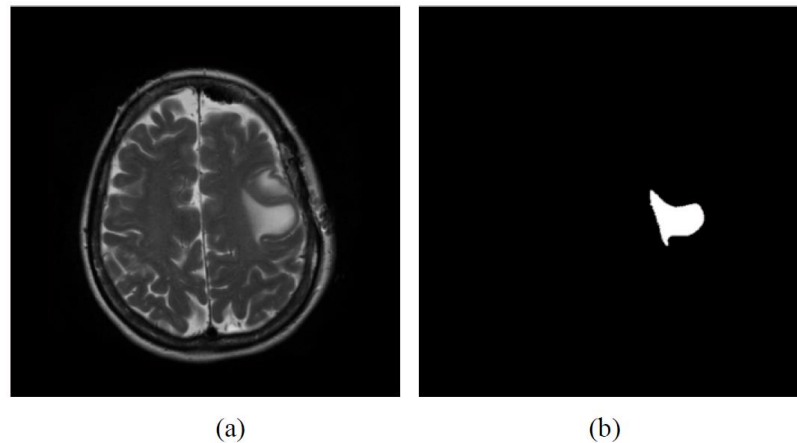


Figure 2.4 Segmentation method based on Regional Growth (a) Original image, (b) the result after process the starting point

2.2.4 Statistical based methods

The main idea behind the statistical method is to model the digital image from a statistical point of view and think of the feature value of each pixel in the image as a random variable with a certain probability distribution. This is done by treating the feature value of each pixel as if it were a probability distribution. This is done by treating the feature value of each pixel as if it were a probability distribution. To do this, the feature value of each pixel is modeled after a probability distribution. This ensures that accurate results are obtained. Image segmentation is carried out with the intention of determining, from a purely statistical standpoint, which of the many possible permutations of the image has the greatest probability of being actualized in practice. This is referred to as the most probable combination. Classifiers and clustering, as well as random field-based approaches, mixed distribution, and other methods similar to these are examples of common statistical methods.

2.2.4.1 Classifiers and clustering

Classification makes it possible to classify and discriminate samples with unknown category features; this is an essential component in the study of pattern

recognition. The fundamental concept here is to make use of the training sample set as a source of known category properties in order to locate points (in a one-dimensional space) and curves in the image's feature space. Image segmentation may be accomplished using dimensions, surfaces (3D), or hypersurfaces (high dimensions), according to (Shirly and Ramesh, 2019) and (Reboucas et al., 2018). Classifier-based image segmentation is a supervised statistical approach that needs the use of human labeling in order to produce a collection of training samples. These training samples are then utilized as a reference in order to automatically segment any new data. The classifier may be subdivided into a parameter (parametric) classifier and a nonparametric classifier. It is not necessary to have prior knowledge of the sample's statistical characteristics in order to use the nonparametric classifier. The nearest neighbor classifier is the simplest kind of nonparametric classifier. It assigns each pixel or voxel to a category that corresponds to the sample that has the gray level that is the most similar to the gray level in the data used for training. The K Nearest Neighbor (KNN) classifier is the closest neighbor classifier that is used the most often, and the pixels are categorized based on the votes of the k most recent training samples.

According to (Reboucas et al., 2018), the Parzen window approach is another example of a traditional non-parametric classifier. Its fundamental premise is to cast a vote based on a specified training sample inside a feature space window that is centered on an unknown pixel. The maximum likelihood approach, often known as the Bayesian classifier, is a popular choice for parameter classifiers. The parameter classifier makes the assumption that each gray pixel in the image represents a sample that is mutually independent inside a mixed model with a defined probability distribution (such as a Gaussian distribution). With the training set, one may first establish the prior probability of each component in the mixed model, and then one can apply the Bayesian formula to get the posterior probability of the unknown sample based on the prior probabilities. This is the core notion. The likelihood that the sample is representative of a certain class is referred to as the posterior probability, and the category that has the greatest a posteriori probability should be chosen as the one to focus on. The category into which the sample may be placed after being categorized.

Conventional classifiers need the structure to be segmented to have different features that can be quantitatively characterized in order to mark the training data. This is done so that the structure can be segmented correctly. The data from the marks may be converted into new data by the classifier so long as the feature space can clearly differentiate between each mark. The amount of computation required is quite low as compared to the threshold segmentation approach, and it may be used to pictures that include many channels. Classifiers often do not take into account the spatial properties of the picture, which means they do not obtain the required results when segmenting images with uneven intensity. This shortcoming of classifiers is one of its limitations (De et al., 2016). There is also the possibility of including information about the neighborhood and the geometry in the classifier in order to increase its accuracy (Guo et al., 2015). In addition to this, the human-computer interaction mode is required for the classification approach in order to collect the training set. The picture with fake labels is included in the training set. This process is very time-consuming and inefficient, and it is made worse by the fact that various human bodies have unique anatomical and physiological characteristics. Substantial mistakes or even inaccuracies in the segmentation results might occur when the same training set is used for a significant proportion of the recorded pictures.

The clustering algorithm is quite comparable to the classifier algorithm; however, in contrast to the classifier algorithm, the clustering algorithm does not need the use of training samples; hence, the clustering algorithm may be thought of as an unsupervised statistical approach. Because the clustering algorithm does not have any information on the training sample set, it performs iterative image classification and extracts the eigenvalues of each class (Mhiri et al., 2018). Because of this, the clustering algorithm can be thought of as a self-training classification algorithm.

Commonly used clustering algorithms include K-means (et al., 2018; Boutsidis et al., 2015), Fuzzy C-means (FCM) in Figure 2.5 (Aghabozorgi et al., 2015; Askari et al., 2017; Jiang et al., 2016), expectation-maximization (EM; Liu et al., 2018; Cho and Fessler 2015) algorithm. The K-means clustering algorithm, also known as the ISODATA algorithm, calculates the various types of grayscale mean values by iteratively, compares the image pixels with the distances of various centers, and divides the image

pixels into the center with the smallest distance from the pixel. That kind of class. The fuzzy C-means clustering method is an extended version of the K-means algorithm. It employs fuzzy set theory and makes it possible to do soft segmentation (Mendel, 2017). The expectation maximization algorithm operates under the presumption that the data follows the distribution of the Gaussian mixture model. This algorithm uses the same clustering criteria to iteratively calculate the posterior probability and makes use of the maximum likelihood estimation mean, covariance, and model mixing coefficients. Additionally, this algorithm employs clustering criteria to determine which variables should be clustered together. It is not necessary to have a training set in order for the clustering approach to perform; however, it does need a beginning segmentation or an initial parameter.

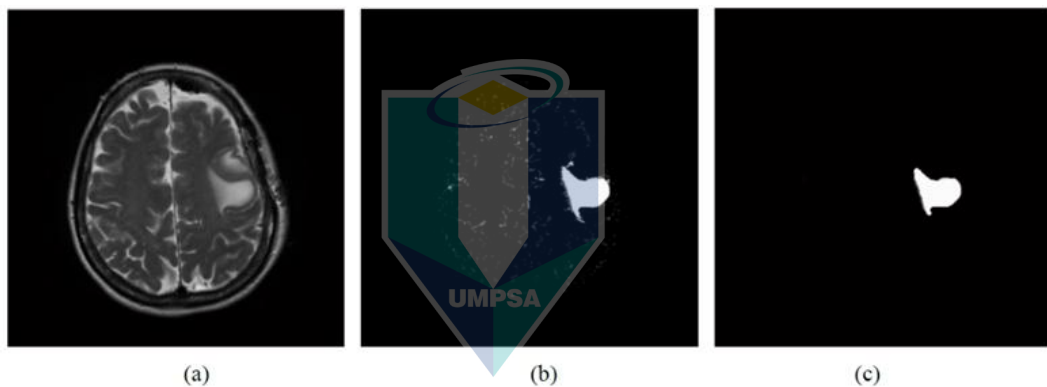


Figure 2.5 Fuzzy c Means Algorithm (a) Original image, (b) after apply double c means algorithm (c) enhancement filtration by opening structural element

Compared to K-means and FCM, The EM algorithm is more reliant on the starting settings than other algorithms. The clustering method, much like the classifier method, does not take into account spatial information. As a result, it can be quickly calculated, and the efficiency is relatively high (Drozdal et al., 2018). On the other hand, the clustering method is sensitive to noise and grayscale inhomogeneity.

2.2.4.2 The Random Field Method

One of the many methods of image segmentation that are now at one's disposal is the simulation of digital photographs using either a Markov random field (MRF) or a Gibbs random field. This technique, which makes it easier to include spatial information, is one of many options. One example of a conditional probability model is the MRF

model. In this model, the probability of each pixel is exclusively tied to the probabilities of the pixels that are located in its immediate vicinity. Modeling the properties of a large range of picture types may be accomplished via the use of local correlation as a solution. The MRF model is very useful for analyzing medical pictures since it takes into account the fact that most of the surrounding pixels have the same category as the pixel being analyzed. In their study on image processing (Blei et al., 2017), the authors suggested a hierarchical stochastic model called the Markov random field model. It is also possible to think of it as an algorithm for picture restoration. It begins with an overview of the MRF model's neighborhood system and then moves on to discuss the posterior probability. The Gibbs sampling method and other related problems, Simulated annealing has been shown to converge, which makes it possible for the MRF model to be used in the process of image segmentation. The simulated annealing algorithm is used to optimize the energy function, and it is shown that the simulated annealing method has converged. The energy function and the Gibbs sampling method are also discussed. The statistical approach of treating pictures as though they were Markov random fields is very prevalent. When the annealing approach is being used, the objective of the picture recovery process is not to obtain a maximum for the posterior probability at the local level, but rather at the global level. By obtaining the results of the image segmentation by the maximum a posterior probability (MAP), Derin and Elliott obtain suboptimal solutions by using simple assumptions in the model, which is equivalent to using dynamic programming. This is done in order to reduce the cumbersome computation of MAP estimation, which would otherwise be required. The approach is rather compact when it comes to solving the MAP issue (Tang et al., 2016).

Because of its theoretical perfection and its ability to accurately describe the spatial information contained within images, the MRF model has found widespread application in the fields of image segmentation and texture analysis, as well as the restoration of images that have been corrupted by noise. The parameter estimation issue is where the solution to the picture segmentation method based on the MRF model may be found. The precision of parameter estimate has a significant impact on the segmentation performance in many cases. The parameters may be calculated more precisely if there is sufficient previous information or a training picture collection; otherwise, a conflict between parameter estimation and segmentation would be

encountered. Because of this, the majority of the time, individuals will undertake iterative techniques by using segmentation and model parameter estimate (Shah and Chauhan, 2015).

The hybrid distribution approach is another strategy for segmenting medical images based on statistical analysis of the images themselves. The gray value of each pixel in the picture is evaluated using the hybrid distribution approach, which takes into account a mixture of multiple different probability distributions. The parameters of the probability distributions and the mixing between them may be calculated by optimizing a cost function based on the greatest a posteriori probability. This allows for the estimation of the mixing between the probability distributions as well. (Zhao et al., 2019) suggested a strategy for the Gaussian mixed distribution model that takes proportion into account. In order to determine the distribution of the target and the background, the approach first employs certain criteria to identify the edge points in the picture, and then it uses the gray value of the pixels that are located near these edge points. The histogram is used to provide a cutoff point for distinguishing between objects and backgrounds. In conclusion, a technique for estimating the parameters of a Gaussian mixed distribution is presented and investigated here.

2.2.5 Method based on Fuzzy Set Theory

In 2019, Zadeh presented the idea of fuzzy sets (Rubio-Manzano, 2019), which is a method for defining an occurrence that makes use of incomplete empirical information. At the moment, several academics are focusing their attention on the function of fuzzy theory within the context of the area of pattern recognition. The picture segmentation problem is an example of a common structural issue, and the fuzzy set may be used to reflect some degree of uncertainty that is brought on by the presence of information that is either missing, erroneous, or ill-conditioned. As a result, academics apply fuzzy set theory to the discipline of picture segmentation. The majority of the methods that go into fuzzy segmentation are known as fuzzy threshold segmentation, fuzzy cluster segmentation, and fuzzy connectivity segmentation.

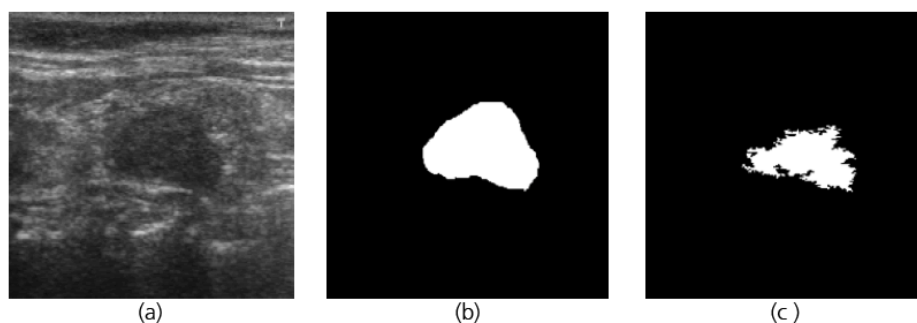


Figure 2.6 Fuzzy Set Algorithm (a) Original image (b) Ground truth (c) Fuzzy Set Segmentation

Both fuzzy and non-blurred histogram-based threshold segmentation approaches may reduce the grayscale differences (global entropy, fuzzy exponents) and geometric variability (fuzzy compactness) of pictures (Deng et al., 2016; Pavan et al., 2017). The fundamental concept behind the fuzzy threshold method is to first represent the fuzzy set through the use of a variety of S-type membership functions, followed by the definition of a cost function (such as the overall ambiguity of the entire image) on the fuzzy set, and finally the determination of the minimum through optimization of the cost function. An S function of uncertainty that is used in order to strengthen the connection that exists between the target and the pixels that are part of the target. The intersection of the estimated sigmoid function is the ideal threshold that must be reached in order for the threshold segmentation technique to be successful. The fuzzy threshold method may be extended to the multi-threshold segmentation approach; the sigmoid function can be asymmetric; the challenging aspect of this method is selecting a membership function that is appropriate, as well as the window and boundaries of the s-type function (Paul et al., 2017).

FCM is an unsupervised fuzzy clustering approach, which makes it particularly ideal for medical pictures containing ambiguities and uncertainties; as a result, it is commonly employed in medical image segmentation (Nida et al., 2019; He et al., 2016; Lu et al., 2019; Pang et al., 2015). To determine the degree of similarity that exists between picture pixels and the various cluster centers, an objective function is devised. The optimum cluster may be attained by continually and repeatedly optimizing the goal function until such time as it is reached. The fact that the FCM algorithm is entirely automated and does not need any kind of human intervention is one of its primary

advantages. The noise, the partial volume effect, and picture blur do not affect the segmentation process nearly as much as they used to. Yet, this technique requires a significant amount of computing, and it does not make use of any geographical information. In addition to having no real-time performance, the segmentation result has a tight relationship with the initial cluster center as well as the total number of clusters. Even though there is a lot of noise in the picture, the clustering result is still good. In the study by (Deng et al., 2016), the authors mapped the image gray space to the fuzzy feature space by using an asymmetric membership function G . The membership function and the enhancement operator are used in order to blur the picture while working inside the fuzzy space. Edges of the picture information that have been strengthened. After that, an inverse transformation of the picture in the airspace using the matching image, followed by an image edge detection using a simple spatial enhancement approach.

2.2.6 Neural Network based Segmentation method

The neural network is a model for large-scale modeling of the learning processes that occur in biological systems. A huge number of nodes make up it, and each individual node in the neural network is able to carry out a set of fundamental operations (Albanez et al., 2018). An adaptive allocation of the connection relationship between the nodes and the connection weights is conducted as the last step in the learning process. This brings the procedure to a close. The neural network technique has to take into account how stable the system is despite the presence of random noise. This technique makes an attempt to emulate the functioning of the human brain and nervous system so that it can satisfy the needs of real-time output. It is a network that is made up of a very large number of fundamental components that are able to change in response to their environment. The neural network is capable of teaching itself, modeling the process of data production, and predicting the output of variables whose values are unknown. One approach to machine learning is called a neural network. The neural network is often used as a classifier during the processing of medical pictures. This allows the training data set to be determined. Weights. It is well known that the process of identifying and labeling distinct anatomical organs and tissues in photographic pictures is the core of the medical image segmentation technique. As a result, neural networks have seen significant use in the field of medical picture segmentation (Oliveira et al., 2016). Unsupervised clustering may be

accomplished with the help of neural networks. The following are the three categories that may be used to classify neural network topologies:

1). Make an effort (FF). (Hertz, 2018) exhibited a multi-layer forward neural network that would be trained via the error back propagation method. Back propagation (BP) networks are the name that would be given to this kind of network, and it is presently the application that is having the greatest success. One of the models that use neural networks. It begins by choosing a few excellent examples of tissue classification samples, then applies the classifier to train itself on those samples, and finally classifies the images. After this, it chooses the additional points that are not classified within this range and adds them to the training group. The picture is split once again, and the classifier is trained once more as well. Therefore repeat till you have an appropriate segmentation result. The BP network has the capacity to learn and remember a significant number of input and output mode mapping associations. Nevertheless, the learning strategy of the BP algorithm is to utilize the gradient descent method to continuously update the weight and threshold of the network in order to minimize the square error of the network. This is done in order to get the best possible results from the BP algorithm. The BP network has the capacity to learn and remember a significant number of input and output mode mapping associations. BP networks are capable of having their input and output mode mapping relationships taught to them, which can then store the information they learn.

It is not possible to ensure that the connection weight will converge on the value that is optimum for the network as a whole. Since the learning rate of the algorithm is predetermined, the convergence speed of the network is somewhat sluggish, and the network often has a high degree of redundancy, the burden of network learning will be significantly increased.

2). System of feedback loops. It is also possible to refer to it as a self-associative memory network. The fundamental idea behind it is to construct a network that is capable of storing a collection of equilibrium points in such a way that it is able to operate independently after being provided with a set of beginning values. In the end, it all comes together to form the equilibrium of this design. The Hopfield network, which was suggested by the physicist Hopfield of the California Institute of Technology (DeGross, 2018) and has garnered the attention of a significant number of academics, is one of the

most common models of feedback networks. (Albanez et al., 2018) suggested a parallel unsupervised technique that achieves automated segmentation of medical pictures by using two competing Hopfield neural networks (CHNN). The Hopfield neural network algorithm is used in this strategy. Image segmentation is considered a pixel clustering issue, and an objective function is created for all different kinds of gray mean squared distance errors. CHNN assigns champions to collect all of the data (winner-take-all as the learning process for all). This makes it possible to skip the laborious work of finding weight coefficients, which in turn makes it possible for the algorithm to converge at a faster rate. As a result, the segmentation result is improved, and the noise is more robust.

3). a map of one's own self-organization (SOM). It is a network that clusters data without supervision. Learning from the organization is accomplished by the use of the input texture feature-based co-occurrence matrix. As a result, it is possible for it to be objective since the newly created cluster center may be mapped to a plane or surface without causing any changes to the topology. Taking into consideration the natural qualities of the target (El-Henawy et al., 2016). If the picture is extracted initially in the process of medical image segmentation, then the characteristics that were extracted will be mapped in order to accomplish image segmentation. A technique for defining CTIMRI brain pictures using feature extraction and unsupervised clustering was suggested by (Milletti et al., 2016). At various sizes, each voxel may be represented by a variety of patterns that maintain its geometric properties. While attempting to extract the characteristics of a picture, it is possible to employ two layers of self-organizing neural networks. The SOPCA network, which stands for self-organized principal component analysis, makes up the first layer. In order to map characteristics onto the primary axes, this network makes use of a technique called principal component analysis. To complete the process of picture segmentation, the second layer is a self-organized feature map. This map works by automatically clustering the feature vectors that are supplied to the system. This makes it possible to extract picture data with a limited number of dimensions.

Using a method that is based on neural networks, the problem of picture segmentation is first transformed into the problem of energy function optimization and classification. The neural network technology is then applied to the problem to solve it. The fundamental concept that underpins the neural network-based method is that first,

the neural network needs to be trained using the training sample set, then the connection relationship and connection weight between the nodes need to be adjusted, and finally, the trained neural network needs to be used to segment the new image data. This procedure is carried out several times until the desired outcomes are achieved. Before the neural network can be used for image segmentation, it must first be trained on a significant amount of image data. This must be done before it can be used.

Researchers have paid a significant amount of attention and conducted a significant amount of study on the fuzzy neural system, which combines neural networks with fuzzy systems. An adaptive fuzzy neural segmentation and edge detection system was suggested by (Hossain and Rahaman, 2018). This system is comparable to image segmentation utilizing a multi-layer perceptron network, and it automatically gets the adaptive image of the input picture via fuzzy labeling. A supervised forward neural network is used during the learning phase of this approach. A fuzzy set, which is capable of extracting border pixels, is used to represent the output of the network.

2.3 Image Segmentation for Energy Function

Picture segmentation is the activity in image processing that places the highest emphasis on the significance of the job. In recent times, a substantial improvement to the method of image segmentation known as partial differential equations has emerged as a result of research conducted in this area. The application of partial differential equations to the study of image processing began in the 1980s, which was the decade in which the 1980s took place. The method of partial differential equations has undergone rapid advancement and has resulted in the production of a substantial number of research results. The reason for this is because the field of partial differential equation, which is an important subfield of mathematics, has developed a robust theoretical foundation and solid numerical techniques. The technique for solving partial differential equations is created by using an enhanced Gaussian smoothing picture, which has the ability to strike a balance between the removal of noise and the preservation of features.

The following set of ideas underpins the application of partial differential equations to the process of picture segmentation. The theory of multiresolution analysis comes in at number one. Jiang et al., (2013) and Griffin (2019) offered a thorough theory

of multiresolution analysis, which was made available in the area of image processing. The theory of multiresolution analysis is now one of the foundations for the idea of partial differential equations, which previously did not incorporate this theory. The second equation is known as the Euler-Lagrange equation, and it is something that may be produced via the use of the variational model. When the issue is studied and a corresponding "energy" model is constructed, image processing becomes a problem of differentiable functional optimization. Image processing may be optimized in a number of different ways. This process takes place after the image processing problem has been changed. Calculating the extrema of the model using a variational model is the first step in obtaining the relevant Euler-Lagrange equation.

The difficulty with the picture processing may then be solved by using the reliable remedy. The level-set approach and the curve development theory make up the third possibility. While processing the image using this method, the image is thought of as either a series of horizontal curves or the surface of a high-dimensional space, depending on which interpretation is used. This is accomplished by deciding whether to direct the advancement of the horizontal lines or the surfaces or the surface of a high-dimensional space, depending on which interpretation is used. To do this, one must first choose whether to influence the progression of the horizontal lines or the surfaces. In contrast to the conventional approach to image segmentation, the technique of image segmentation that is based on partial differential equations has the following three characteristics (Cohen, 1991):

- 1). A continuous model for the direct analysis of pictures is provided by the partial differential equation model. Typically, the picture is filtered using continuous derivatives, and the discrete filtering is written as a continuous differential operator. This is not always the case, however. When discrete grids are used, it is much simpler to get an image that has undergone local processing and analysis;

- 2). The methodology that makes use of partial differential equations has a solid foundation in mathematics. Throughout this time, it is capable of providing a high level of stability for image segmentation. While doing numerical computations, using the level set approach may lead to the production of a result that is more accurate. In addition to

this, it is also capable of fixing the problem of the topological change that was brought about as a result of the target being merged and divided

3). The method of partial differential equations allows for greater flexibility in local adaptation. [Citation needed] [Citation needed] The partial differential equation employs a continuous picture model as its foundation. This model allows each image pixel's value to change in real time solely in relation to the other image pixels in its immediate vicinity.

The branch of mathematics known as partial differential equation has recently emerged as a hot issue in the disciplines that are connected to it. It already has a significant amount of research outcomes to its name. One may trace the origin of the concept of using partial differential equations to image processing all the way back to the study of (Kaynig et al., 2015). Nonetheless, the substantial advancement may be credited to (Griffin, 2019) and (Jiang et al., 2013). (Griffin, 2019) and inside introduced the concept that the convolution of the Gaussian function of the signal and the various scales is identical to the thermal diffusion equation with the signal as the starting value in 1984 and 1985, respectively. This notion was published in Griffin's work. The concept of multi-scale analysis serves as the foundation for this approach. (Alvarez et al., 1993) made a rational system as part of the process of deriving the AMSS (Affine Morphological Scale Space) equation. This equation marked the formal start of the field of image processing based on partial differential equations. This was the start of the formal development of the field of image processing, which is based on partial differential equations. This event marks the beginning of the formal establishment of the topic of image processing based on partial differential equations. At this point, image processing had only taken its first steps toward becoming an established academic discipline.

2.3.1 Energy Functions

Energy functions are a fundamental concept in medical image segmentation, serving as a mathematical framework that guides the optimization process towards accurate and meaningful segmentation results. By quantifying the quality of segmentation configurations, energy functions provide a principled approach to incorporating various constraints and prior knowledge, ultimately leading to segmentation solutions that align

with clinical objectives and anatomical realities. In this section, we delve deeper into the significance and applications of energy functions in medical image segmentation, highlighting their versatility and importance in addressing the complexities of this domain.

One of the key advantages of energy functions in medical image segmentation is their ability to incorporate domain-specific knowledge and prior information. By carefully designing the data and regularization terms, researchers can embed clinical expertise, anatomical constraints, and prior assumptions into the energy formulation. This integration of domain knowledge helps guide the segmentation process towards clinically relevant and anatomically plausible solutions (Frangi et al., 2021).

Medical images often depict intricate anatomical structures with varying degrees of complexity, such as intricate vascular networks, convoluted brain structures, or irregularly shaped tumors. Energy functions provide a flexible framework to capture and account for these complexities through appropriate data and regularization terms. By designing energy functions that incorporate shape priors, geometric constraints, or statistical models, researchers can effectively segment even the most challenging anatomical structures (Mukhopadhyay et al., 2021).

Medical images can exhibit significant variability and heterogeneity due to factors such as patient demographics, imaging protocols, and pathological conditions. Energy functions offer a versatile approach to addressing this variability by incorporating probabilistic models, intensity distributions, or texture descriptors into the data terms. This flexibility enables the development of robust segmentation algorithms that can adapt to diverse imaging scenarios and patient populations (Zheng et al., 2021).

In clinical practice, multiple imaging modalities are often utilized to gain complementary information about anatomical structures and pathologies. Energy functions can facilitate the integration of multi-modal data by incorporating terms that capture the unique characteristics of each modality. By combining modality-specific data terms and regularization constraints, energy functions enable the development of multi-modal segmentation algorithms that leverage the synergistic information from various imaging sources (Zhuang & Shen, 2020).

Energy functions provide a natural framework for incorporating user interactions and prior knowledge in interactive or semi-supervised segmentation approaches. By allowing users to provide seed points, contour initializations, or region annotations, energy functions can be adapted to incorporate these inputs as additional constraints or priors, enabling more efficient and accurate segmentation processes (Menze et al., 2023).

The quantitative nature of energy functions allows for objective evaluation and comparison of segmentation algorithms. By comparing the energy values associated with different segmentation configurations, researchers can assess the performance and accuracy of various algorithms, facilitating benchmarking and algorithm selection processes (Gholipour et al., 2022).

Energy functions serve as the objective functions that optimization algorithms aim to minimize during the segmentation process. By leveraging advanced optimization techniques, such as gradient descent, variational methods, or graph-based algorithms, researchers can efficiently find the segmentation configurations that minimize the energy function, leading to accurate and robust segmentation results (Gholipour et al., 2022).

The components of energy functions, such as data terms and regularization terms, provide a transparent and interpretable representation of the segmentation process. By analyzing the contributions of each term, researchers can gain insights into the factors that influence segmentation decisions, facilitating algorithm interpretation and explainability – a crucial aspect in the medical domain (Frangi et al., 2021).

Energy functions offer a versatile framework for incorporating prior knowledge and transferring learned representations across different tasks or domains. By designing energy functions that leverage pre-trained models or transfer learning techniques, researchers can achieve improved segmentation performance, even in scenarios with limited training data or domain shift (Zhuang & Shen, 2020).

The flexibility and generality of energy functions encourage researchers to explore new formulations, incorporate novel constraints, and develop innovative optimization strategies. This drives innovation and advancement in the field of medical image segmentation, enabling the development of more accurate, efficient, and clinically

relevant algorithms that can better assist in diagnosis, treatment planning, and patient care (Mukhopadhyay et al., 2021).

In conclusion, energy functions play a pivotal role in medical image segmentation by providing a principled mathematical framework for quantifying segmentation quality and guiding optimization processes towards accurate and clinically relevant results. Their ability to incorporate domain-specific knowledge, handle complex anatomical structures, address variability and heterogeneity, and facilitate multi-modal segmentation, among other advantages, makes them indispensable tools in the field of medical image analysis. As research in this domain continues to advance, energy functions will undoubtedly remain a cornerstone concept, driving innovation, enabling interpretability, and contributing to the development of more robust and reliable segmentation algorithms for improved patient care.

2.3.2 Segmentation Method Based on Active Contour Model

The active contour model is a method of image segmentation that was first suggested by (Kass et al., 1998) and was further developed by (Kasmi et al., 2016) and (Kass et al., 1998). (Pettersson et al., 2018). Researchers have shown a significant amount of interest in the active contour model in recent years. This model has a broad variety of applications, including visual tracking and picture segmentation, amongst others. The active contour model's central tenet is that it should optimize the curve to the goal boundary by, within those restrictions, maximizing the established energy function in the best possible way. Edge-based active contour models (Kass et al., 1998; Benninghoff and Garcke, 2016; Cuenca et al., 2018) and region-based active contour models (Zanetti and Bruzzone, 2017; Pratondo et al., 2017) are the two main categories that can be used to classify active contour models. Both of these categories can be broken down into subcategories based on the characteristics of the constraint terms (Niethammer et al., 2017).

According to (Kasmi et al., 2016), the edge-based active contour model extracts the target boundary by making use of the gradient information included within the picture. This approach may segment the picture using the edge stop function, which is sensitive to noise and relies on the starting contour position. The results of this segmentation are

dependent on the original contour position. The fact that it is not necessary to first establish global limits for the picture before beginning the segmentation process is the primary benefit of the edge-based active contour model. As a result, the approach can successfully segment pictures in certain circumstances, despite having an uneven target and backdrop, and the impact of the segmentation is excellent.

Recent research has recommended the use of a region-based active contour model that incorporates the regional competitiveness strategy (Zhang et al., 2015). This strategy makes use of the statistical data collected from both the target and background regions in order to generate an objective function that is tailored to the image. It also allows for control over the development of the curve, is resistant to noise, and can separate the weak boundary image. In addition to this, the approach is not affected by the location of the starting contour, and it is able to efficiently identify the borders of the target as well as the backdrop. (Zanetti and Bruzzone, 2017) and (Pratondo et al., 2017) proposed a simplified Mumford-Shah model (CV model), which is a region-information-based active contour model that is completely independent of gradient information, thereby overcoming edge-based active contours. (CV model) is an acronym for "complex variant of the Mumford-Shah model." The model has low global coverage, makes it difficult to segment weak edges, and is very susceptible to noise.

An excellent research tool in the area of image segmentation, the CV model is a kind of segmentation model that successfully increases the topology adaptive capacity of curve development. The CV model is capable of segmenting the segmentation constant picture in an exact manner. The CV model, on the other hand, is limited to the use of grayscale homogeneity as the only criteria for area separation. Moreover, the CV model is only applicable for high-contrast image segmentation that includes two distinct mean regions for the target and the background. When it comes to the segmentation of medical pictures that have considerable non-uniformity and structural complexity, the CV model is not the best option. The LBF (local binary fitting) model was proposed by the PS (piecewise smooth) model that was proposed by (Terbish et al., 2017) and (Ji et al., 2015). This model is an enhanced version of the CV model. (Terbish et al., 2017) and (Ji et al., 2015). The PS model is able to segment non-uniform pictures because it utilizes two piecewise smoothing functions rather of the CV model's two gray-scale mean constants.

The CV model was designed to segment uniform images. In contrast, the partial differential equations in the PS model are solved by repeatedly applying the same partial differential equation, which results in a vast number of calculations and a model that is very difficult to understand. In order to determine a region's binary fitting energy, the LBF model makes use of a kernel function. The segmentation method produces superior results than the CV model when used to the processing of non-uniform images. The model, on the other hand, does not differentiate between the gray inhomogeneity that may be found in various places; thus, it is still not insignificant to continually compute the image data and calculate the quantity, and the rate at which the curve evolves is sluggish, both of which work against the adoption of this technique in the segmentation of medical images.

Liu et al.(2017) came up with the idea for what is now known as the "Snake Model," which is also referred to as an "Active Contour Model" or a "Parametric Model".. When studying the development of the curve from a dynamical point of view, this approach is the one that is used since it provides the most accurate results. The energy function of the contour curve of the area is established by a concerted effort made by the internal force of the picture and the external force constraint provided by the image information. This effort is what determines the region's energy function. The energy function of the contour curve is the name given to this particular function. Both the target's interior forces and its outer forces, after being brought together by the combined action of the continuous movement, will finally converge around the perimeter of the object being targeted. It is feasible to extract the edge of the image area of interest with a degree of precision that may extend down to the sub-pixel level. This is attainable if the area of interest in the picture is large enough. The following is a list of some of the advantages that may be obtained using this model: (1) It does not make a difference how high the picture's quality is; this thesis will always be able to get a clean and closed target boundary. (2) It has a high degree of computational efficiency and is suitable for modeling due to its suitability. Furthermore, it is capable of obtaining any desired shape of the deformation profile. It is well suited for handling the individual variations that may be seen in photographs that have a high level of structural complexity. Because of the development of this model, the active contour model is rapidly becoming one of the most successful approaches for picture segmentation. After that, a number of other feature

models were developed, including surface flow, the deformable model, and deformation surfaces, amongst others. These models were built after that.

2.3.3 Segmentation Method Based on Level Set

The Level Set methodology was first proposed by (Osher, and Rudin 1990), and it was then developed and improved by (Romeny, 2013). They made a number of modifications and enhancements to the active contour model. The strategy was effectively used in a number of different fields, such as fluid dynamics and computer graphics, among others. (Caselles et al., 1993) and later (Caselles et al., 1996) included the level set technique into the active contour model (Malladi et al., 1994; Caselles et al. 1996) They have decided that the Level Set should be a representation of snakes. The curve was shown in a manner that did not make its status as a level set of higher dimensions of the surface explicitly clear (level set function). The methodology in issue is not analogous to the contour model in any way. The level set technique does not track the evolution of the curve at different periods in time. Several levels of the curve are considered. In order to recreate the progression of the curve, it is sufficient to simply fix it in the coordinate system. This will allow the level-setting function to be updated at a variety of different time intervals. The approach provided an efficient solution to the challenge of changing the topology of the mechanisms. Also, it contributed to the development of the theory of geometric contour models (Bernard et al., 2007; Lie et al., 2006; Xu et al., 2016; Tai et al., 2007). In 1995, Sapiro and colleagues came up with the idea for the Geodesic Active Contour model. In the Geodesic Active Contour model, the profile curve can only travel in one direction at a time, and the beginning location has a significant impact on the segmentation outcomes. If the contour curve has gone beyond the edge of the picture, it will be quite difficult to get back to the right place. In the end, the segmentation is unsuccessful. In order to resolve the issue with the Geodesic Active Contour model, Paragios integrated the notion of the regional competition presented in (Zhu and Yuille, 1996) with his own and created the Geodesic Active Area technique (Paragios and Deriche, 2000). The model is wholly dependant on the previous data for the picture region and the border rather than the beginning location, which has absolutely nothing to do with it. On the other hand, when the picture is segmented into numerous areas, it is essential to finish linking the different deformation models, which makes the

computation procedure more difficult. (Chan et al., 2005) conducted research to determine whether or not the existence solution requirements of the Total Variation model, which is based on L1 space, are indeed unique. Throughout the same calendar year, a method was presented by (Chan et al., 2006), and a global minimum was found using it (Chan et al., 2006). When it comes to image processing, this approach has the ability to convert nonconvex energy functional into convex energy functional. In order to locate the local optimal value, the authors made use of the conventional convex functional minimum solution.

Over the course of the last two decades, the geometric activity profile model has come to get a great deal of attention owing to the many advantages it provides. Hence, a variety of traditional segmentation models (Aubert and Kornprobst, 2006; Sapiro et al., 1995; Ni et al., 2016; Li et al., 2007; Li et al., 2008; Zhou et al., 2016) were proposed as possible solutions. The Active Contour model is capable of being segmented into three distinct subtypes if one wants to categorize it in accordance with the energy function that is represented by the edge map (Pratondo et al., 2016). This is a possibility since the energy function is determined by the edge map, which makes it conceivable for this to happen. The subtypes of active contour models that are included in this category include hybrid active contour models, active contour models that are based on area, and active contour models that are based on edge. A geodesic active contour is used as the basis for the edge-based active contour model. The edge indication function of the picture gradient puts a halt to the curve's development as it moves forward. It has the benefit of being able to detect numerous different regions at once, which is a distinct advantage. Unfortunately, this model has a number of drawbacks, the most notable of which are its sensitivity to noise and the need that the starting contour curve be defined manually. This paradigm is only useful in certain contexts. Since it makes use of the information that is global to the picture as a whole, the region-based active contour model is one way to combat the issue of susceptibility to noise. But, the calculating amount is really large, and it takes a significant amount of time to calculate. The edge and area information are both included into the mixed active contour model. When this thesis uses several types of initialization, this thesis get a variety of segmentation outcomes. Each of these types comes with both benefits and drawbacks of its own.

As a result, it is essential to choose the appropriate model in accordance with the particular picture and the requirements that are really being met. The process of acquiring medical pictures is distinct from the process of acquiring regular optical images. According to Aubert and Kornprobst (2006), the majority of medical pictures include the features of ambiguity and uneven grayness: (1) There is some fuzziness in the greyscale of the medical picture. There is a significant grayscale difference between the noise in the ultrasonic picture and its edges. There are a variety of distinct spots that may be seen in ultrasound pictures, particularly as a result of the nonuniformity of the imaging organ or tissue structure and the interference of acoustic signals. (2) Local body impact. Often frequently, the edge of a picture comprises both the border and the thing it surrounds. As a result of part of the sick tissue penetrating into the tissue that surrounds it, the border cannot be precisely delineated. (3) An absence of certainty In general, the structures that are present in a lesion that do not have a normal tissue or area present, such as the spurs on the surface of the bone, are referred to as abnormal structures. In addition, the look makes the construction of the model more complicated. This thesis noticed that in order to acquire the target region in the picture during the process of segmentation, this thesis needed to get rid of the noise that was in the image first. This was done so that this thesis could address a limitation of medical images. As a result, the reduction or removal of noise in medical pictures is of particular importance for the segmentation process. Since the Partial Differential Equation approach strikes a healthy balance between removing noise and preserving the qualities that define target features, it serves as the primary focus of our research in this method for the purpose of medical picture segmentation.

In recent years, the method of partial differential equation has become more popular for use in a number of image processing domains. These fields include image denoising, image magnification, image inpainting, and segmentation, to name just a few of the applications of this method. Not only is the model that is generated by partial differential equations more straightforward and easier to grasp, but it is also very simple to include partial differential equations with the traditional segmentation theory. This is due to the ease with which partial differential equations can be integrated. As a result, the process of creating a new model is rather straightforward.

The level set method, a powerful image segmentation technique based on partial differential equations, has seen rapid advancements driven by international collaborations and extensive research published in prestigious journals. Currently, substantial human and material resources are dedicated to investigating this topic in the United States. Major research centers focused on level set segmentation have been established at renowned universities such as Brown University, UCLA, and the University of Florida, among others. Researchers at these centers not only contribute to developing theoretical foundations but also actively participate in various image processing initiatives involving the level set method. Furthermore, the study of level set-based image segmentation encourages multidisciplinary research, bridging the fields of computer vision and biomedicine. The application of partial differential equations in this domain not only addresses numerous challenges in image segmentation but also contributes to the expansion of partial differential equation theory itself. Consequently, research in this area holds significant practical utility and scientific relevance. The level set method has emerged as a powerful tool for image segmentation, allowing for the accurate delineation of object boundaries and handling complex geometries and topological changes. By representing the evolving contour as the zero-level set of a higher-dimensional function, the level set method elegantly addresses the limitations of traditional segmentation techniques, such as the inability to handle topological changes or the requirement for explicit parametrization of the contour. Research efforts in level set segmentation have focused on developing robust energy functionals, efficient numerical schemes, and advanced regularization techniques to overcome challenges posed by noise, intensity inhomogeneities, and complex object shapes. Additionally, the incorporation of prior knowledge, such as shape priors or region-based statistics, has further enhanced the accuracy and robustness of level set-based segmentation methods. The multidisciplinary nature of this research has fostered collaborations between mathematicians, computer scientists, and medical experts, leading to novel applications in fields like medical imaging, computer vision, and pattern recognition. For instance, level set segmentation has played a crucial role in the analysis of medical images for disease diagnosis, treatment planning, and surgical guidance. As research in level set segmentation continues to advance, it holds the potential to address longstanding challenges in image analysis and

enable new applications in various domains, further solidifying its practical utility and scientific significance.

2.3.4 Information Theory-based Approach

The study of information and the transmission of information as a statistical phenomenon is accomplished by information theory through the use of probability theory and mathematical statistics. It offers a conceptual foundation for individuals to study information and the subjects that are connected to it. In the field of information theory, the most fundamental unit of measurement is called entropy. Medical image segmentation can be done using the theory of entropy in information theory (Oliveira et al., 2016). entropy is a representation of the statistical properties of images. In the threshold segmentation algorithm, one can select the most appropriate segmentation threshold by finding the extreme value of entropy. (Yang et al., 2016) proposed a minimax entropy formulation based on information theory to segment medical images. Threshold selection based on the maximum entropy principle is one of the most important threshold segmentation methods (Chen et al., 2018). The basic principle of this method is to divide the gray histogram of an image into two or more independent classes, and to maximize the total amount of entropy of each class. From the perspective of information theory, the determined threshold can get the maximum amount of information. In practical applications, the advantage of this method is that it utilizes the global objective property of a gray histogram. The limitation is that the search space is too large, the convergence speed is too slow, and the medical image with more complicated structure and loud noise is performed. The experimental results are not ideal when segmented.

There are many methods and literatures in the field of image segmentation. In addition to the more commonly used methods in the above categories, there are other segmentation methods, such as spectrum guidance theory and mathematical morphology methods. In order to effectively segment the vertebral body, brain tumor and myocardial septum, this paper focuses on the method based on graph theory and active contour model, and combines several classical image segmentation methods with single exponential fitting models to apply to the Mediterranean. Diagnosis and treatment of iron deposition in anemia patients.

2.3.5 Deep Learning-Based Level Set

Deep learning is a relatively recent development that has had a considerable influence on a variety of subfields within machine learning. As a result, the state of the art has been significantly elevated in areas such as object identification, voice recognition, and language translation. This may be explained by the fact that deep learning has been used for a greater variety of challenges (LeCun et al., 2015). Perhaps the single most important aspect of deep learning is the capacity of deep neural networks to automatically recognize condensed, low-dimensional representations (features) of high-dimensional input. This ability is known as feature extraction (e.g., images, text, and audio). Incorporating inductive biases into neural network designs, particularly those with hierarchical representations, has enabled practitioners of machine learning to make great progress in the battle against the so-called "curse of dimensionality" (Bengio et al., 2013).

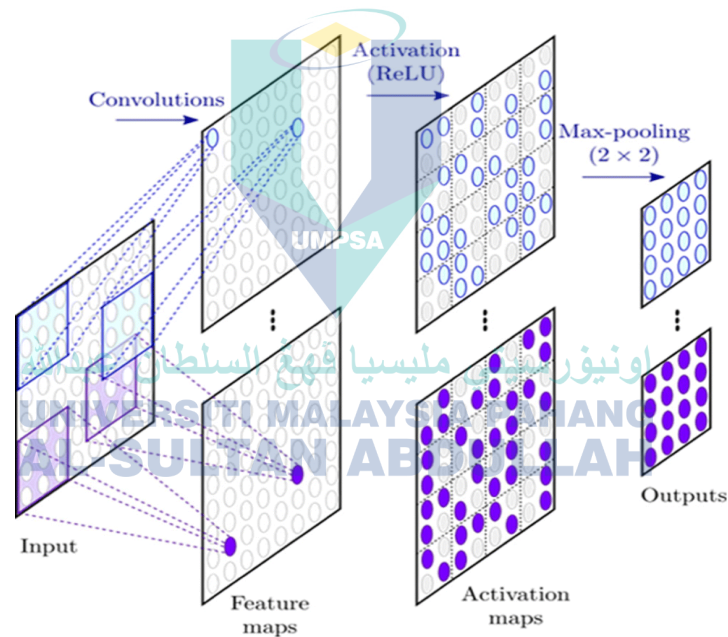


Figure 2.7 The framework of CNN

Techniques of Segmentation Based on Level Sets Instead of explicit (i.e., active contour models) models (Caselles et al., 1997; Kass et al., 1988) representations of curves, implicit representations of curves naturally manage complicated object topologies such as holes or splits. (Caselles et al., 1997; Kass et al., 1988). In the Level Set formulation (Caselles et al., 1997; Osher and ethian., 1988), the curve develops in an iterative manner by moving along the descent LevelSetvel set energy. This energy is

comprised of both the internal energy coming from the curve and the external energy coming from the edge based approaches (Caselles et al., 1993; Caselles et al., 1997; Kass et al., 1988). Most of the time, edge characteristics in the external energy are used by Kichenassamy et al., 1996, and Cohen, 1991, and an initial curve is evolved to suit object boundaries. To segment objects, region-based approaches (Chan and Chan, 2010; Paragios and Deriche, 1999; Ronfard, 1994) rely on the region's homogeneity rather than its edges (Chan and Chan, 2010; Paragios and Deriche, 1999). Using information about color, texture, and shape has also been the subject of a great deal of research (Cremers et al., 2007). In light of recent developments in the use of deep learning for picture segmentation (Bai et al., 2017; Chen et al., 2016; Chen et al., 2015; Long et al., 2015; Zhang et al., 2016).

Current work on picture segmentation has, among other things, integrated deep neural networks with the more conventional active contour models. They suggested combining a convolutional neural network with a well-planned level-set evolution method in order to take advantage of the benefits offered by both of these approaches. (Rupprecht et al., 2016) crop off sections surrounding the original curve and use a CNN to forecast the movement for curve development, patch by patch, in Figure 2.7. This is done in order to illustrate the results of their work. CNN characteristics are used by (Marcos et al., 2018) for the purpose of extracting the building footprint. These features are used to forecast the parameters of the active contour models shown in Figure 2.8. The authors suggest a structured prediction formulation as a means of training the model from beginning to finish by focusing on getting as close as possible to IoU. (Cheng et al., 2019) expand on this idea to suggest that the active contour should match the borders of the building. Unfortunately, these solutions require careful setup of the curve and suffer from the limitations that are characteristic of parametric curves, as seen in Figures 2.9 and 2.10. The research conducted by (Tang et al., 2017) employs level-set evolution as a postprocessing step for a CNN. The researchers trained their model using unlabeled data that was handled in a semi-supervised manner. In the study by (Hu et al., 2017), the level set energy was included in the loss function, and a convolutional neural network was used to directly predict the level set function for salient item recognition. Newer efforts have also used the mobility of pixels for the purpose of segmentation, which is analogous to the development of level sets. Deep convolutional neural networks (CNNs) are used in

(Liu et al., 2017) to train an affinity matrix, and spatial propagation is used to improve the segmentation output. (Januszewski et al., 2018) augment deep CNNs with a recurrent circuit and reconstruct brain cells by iterative extension. The authors of the study (Acuna et al., 2019) employ level set evolution during training in order to denoise the object annotations.

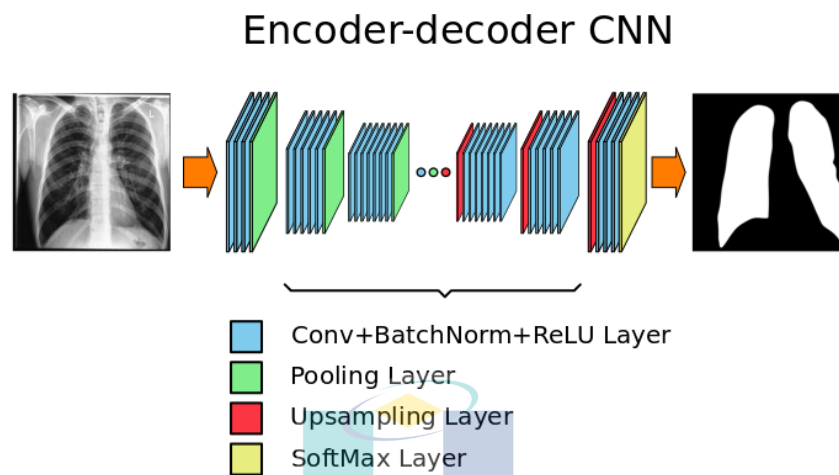


Figure 2.8 Image Segmentation of CNN



Figure 2.9 Example images of lung nodules with different locations and shapes in CT: (a) common isolated nodule. (b) juxtapleural nodule. (c) cavitary nodule. (d) calcific nodule. (e) ground-glass opacity (GGO) nodule.

In general, the reinforcement learning (RL) system has to be generalizable in order for it to be able to tackle increasingly complex problems at a level of performance comparable to that of humans. This is the most current development in the field of deep reinforcement learning (DRL). DRL is the merging of reinforcement learning with deep learning. The deep neural network (DNN) is used as a function approximation in the RL framework in this method, and gradient descent is used to optimize the loss function in relation to the neural network weights. DRL makes it possible for the agent to learn the meaningful representation directly from the raw inputs, minimizing the demand for

domain expertise and the necessity to handcraft features. In addition to this, it assists in scaling up the dimensionality of RL challenges. Deep reinforcement learning, also known as DRL, is a technique that has the potential to completely transform the artificial intelligence (AI) industry. It also represents a big breakthrough toward the creation of autonomous systems that have a better knowledge of the visual environment than was previously possible. RL, which was unable to solve some problems in the past, may now be applied to a wider range of issues thanks to deep learning. One example of this kind of problem is having to learn how to play video games by starting at the pixel level. DRL algorithms are also employed in robotics, which allows control methods for robots to be learned directly from camera inputs in the actual world. This is made possible by the fact that DRL algorithms are used. This is made possible thanks to the application of DRL algorithms.

Many distinct forms of DRL algorithms use approximations to model certain aspects of RL. The use of a neural network to approximate the value function, which is to estimate how beneficial the state or the state-action combination is, is one of the options available to you. The use of a neural network to approximate the policy, which is the method by which the agent selects an action in response to a given state, is still another option. The other option is to use the neural network to learn the dynamics of the model. As the components of RL are parametrized by the neural network, the frameworks may be trained by utilizing backpropagation and stochastic gradient descent to update the parameters, also known as the weights of the neural network. This allows the frameworks to become more accurate.

The conventional methods of reinforcement learning will always be doomed to be affected by the curse of dimensionality. As a consequence of this, they can only deal effectively with issues of relatively minor dimensions. Deep reinforcement learning algorithms, on the other hand, have been on the rise in recent years and make it possible to solve complicated issues with a high dimension. The training process, from beginning to conclusion, consists of several levels, as the term "deep" would imply. The term "deep reinforcement learning" refers to a methodology that combines "reinforcement learning" with "deep neural networks." In other words, apply deep learning algorithms within the framework of reinforcement learning by taking advantage of the function approximation

and representation learning capabilities of deep neural networks. For instance, one of our goals is to build a machine that can scare the birds away from a field of corn, then quickly escape and alert the people who are working in that facility. On the input side, the robot's footage is fed into a learning algorithm so that it may learn.

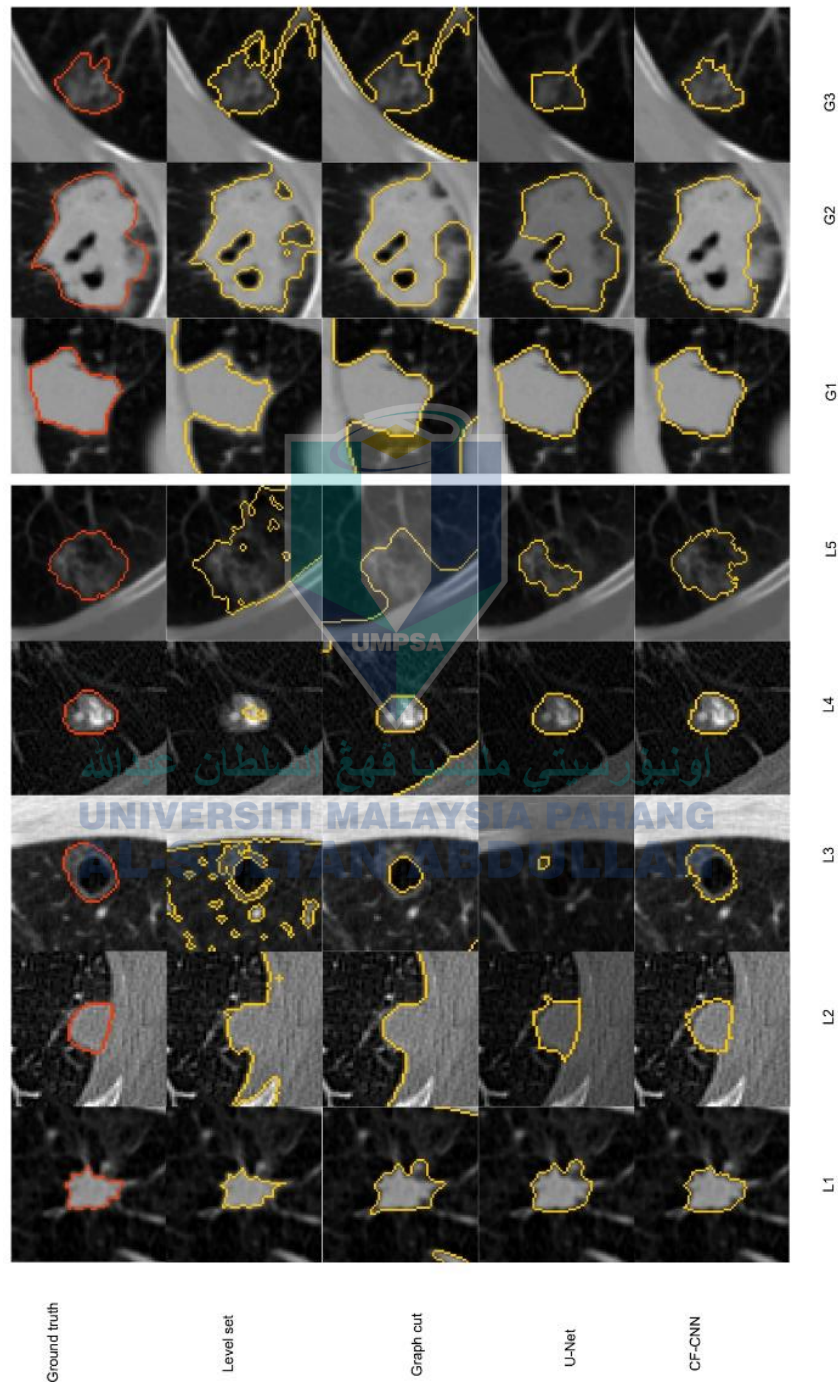


Figure 2.10 Segmentation results visualization.

In Figure 2.10, From top to bottom: nodule with ground truth, level set segmentation, graph cut segmentation, U-Net segmentation, and CF-CNN segmentation. L1-L5 are nodules of different types from the LIDC testing set. G1-G3 are nodules from the GDGH dataset.

A neural network is used to perform numerous levels of modification on the video, which initially contains high-dimensional pixels in each frame. This allows for the important low-dimensional properties of video frames to be extracted. On the basis of this information, the robot uses a technique called reinforcement learning to determine whether it should attack the item or flee from it. It has been shown that this kind of end-to-end learning, which makes use of high-dimensional data, presents astronomical processing complexity. Nevertheless, deep learning may be used to overcome this challenge.

In conclusion, it is important to note that despite the many examples of successful applications of deep reinforcement learning, this thesis still have a lot of work to do before this thesis can use this method to solve a broad variety of issues that occur in the real world. At this point in time, the community concerned with machine learning is doing research into a great many different aspects of this discipline, and the method as a whole is advancing on a daily basis.

2.4 Systematic Reviews for Related Works

This research presents a detailed overview of the approaches that may be utilized for the detection of lung nodules using computed tomography (CT) images. The study was carried out by the National Center for Biotechnology Information. Its primary goals are to conduct an investigation into the most recent technological developments that are being used in the process of creating computational diagnostic tools to facilitate the capture, storage, and, most importantly, the processing and interpretation of the biological data. This investigation will be conducted in order to fulfill its primary objectives. In addition to focusing on the achievements that have been made up to this point, the book analyzes the issues that still need to be resolved and provides an assessment of the potential outcomes of the situation in the future. This is the first time, as far as the authors are aware, that a review has been dedicated completely to left-set approaches for the

identification of pulmonary nodules from lung CT scans. This paper presents the findings of the first study to do so. This is the first time that such a review has been carried out; therefore, the very fact that it is being done offers this piece of work a great deal of value on its own. Throughout the course of the inquiry, each and every paper that had been published in the academic databases Web of Science, Scopus, Science Direct, PubMed, and IEEE Xplore up to the month of December 2016 was analyzed. Each individual piece of research that was found to have mentioned left-sided segmentation of the lungs was carefully examined in order to ascertain its objective, approach, and results. After an analysis of the works that were selected, it was decided that part of the research may be useful in the creation of medical diagnostic aid tools. This conclusion was reached as a result of the assessment that was carried out. However, there are certain aspects that still require attention, such as increasing the algorithm's sensitivity, reducing the number of false positives, improving and optimizing the algorithm's detection of different kinds of nodules with different sizes and shapes, and finally having the capability to integrate with electronic medical record systems as well as picture archiving and communication systems. These are just some of the things that still require attention. All of these are areas in which there is room for advancement. As a direct outcome of this investigation, this thesis is in a position to reach the following conclusions: (1) More study is needed to develop the approaches that are now being applied, and (2) new algorithms are essential to overcome the limitations that have been found in the existing methods.

This systematic review was conducted utilizing a method that included a total of six stages, which may be summarized as follows: (1) the creation of relevant search terms for the databases Web of Science, Scopus, Science Direct, and IEEE Xplore; (2) the execution of the database search; (3) the removal of duplicate works discovered; (4) the application of the inclusion criteria, which states that only set lung nodule segmentation techniques from CT images be left; and (5) the synthesis of the keywords obtained from the selected works and review of the terms with the highest incidence in obstructive pulmonary disease (COPD). The following logical expressions were used in order to carry out the search in the databases: ("level set" OR "level-set" OR "level sets") AND ("detection" OR "segmentation" OR "cad" OR "cade") AND ("lung" OR "lungs" OR "pulmonary" OR "chest") AND ("nodule" OR "nodules" OR "cancer" OR "tumor" OR "tumors"). These logical terms have been modified so that they are consistent with the

syntax of the search engines that are used by Web of Science, Scopus, Science Direct, PubMed, and IEEE Xplore, respectively. This was done in order to make the phrases searchable by those databases. The alterations were carried out in a manner that was compliant with the recommendations made available by each database. Only those works were selected for inclusion in the survey that was provided that had the logical words mentioned in their respective titles and abstracts. This was done in order to maintain consistency. During the initial stage of the investigation, this thesis amassed a total of 89 pieces of literature, of which 32 could be found in Web of Science, 22 could be found in Scopus, 10 could be found in IEEE Xplore, 15 could be found in PubMed, and 10 could be found in Science Direct. After doing the search, it was discovered that the databases included duplicates of 56 of these publications. After the identification and removal of works that were identical to others, a total of 22 works were chosen to proceed to the next step of the process. During the stage of analysis and classification, each item was examined on an individual basis in order to classify it according to its primary function, which included the following: correlated work (which describes a nodule segmentation or classification technique but is not applied to the study); and correlated work (which describes a nodule segmentation or classification technique but is not applied to the study); and correlated work (which describes a nodule segmentation or classification technique but is not applied to the study). automated algorithms to segment lung nodules in the leave-set; leave-set classification of lung nodules; a systematic literature review of segmentation and/or classification of lung nodules (which describes a nodule); any other works that cannot be classified in the previous categories (any other works that cannot be classified During the completion of this research, a total of 43 articles were discovered to include strategies using leave sets to segment lung nodules in CT images. Achieving this target was the primary focus of this specific piece of work. In conclusion, six of the studies do not relate in any way to the process of algorithm design. In addition, the next part will include a total of 37 items that will be discussed.

The collection of data, the pre-processing stage, the lung segmentation stage, the nodule identification stage, and the reduction of false positives stage are the five key phases that make up CADe systems in general. The LIDC and LIDC-IDRI programs were used during the whole process of data collection to carry out testing on the results a combined total of six and nine times, respectively. In the fourth chapter, this thesis are

going to put both datasets to use in order to test how well the proposal method works. The stages that were investigated by each of the selected studies for the purpose of the automated detection of pulmonary nodules in CT images of the lung are outlined in Table 2.1 below. At this point in the process, one of the tasks at hand is going to be collecting the images that the CAD program will ultimately end up using. In the best-case scenario, the PACS, electronic medical records, and computer-aided design (CAD) systems should all be connected to one another to ensure the success of the acquisition. Before the radiologist can do an analysis on the lung CT images, it is possible that the CAD system will perform some processing on them first. As a consequence of this, the interpretation of the inspection starts with the regions that the CADe system identifies as being potentially problematic. Because of the electronic medical record, the radiologist may also have access to extra clinical information that might be of assistance with the diagnosis (EMR). There are a few public databases that may be tapped into for the development, upkeep, and instruction of CAD systems. These databases are useful for the process of building and designing CAD systems and may be utilized in that context. These databases are deployed in the majority of instances to teach students, to serve as a repository for rare events, and to allow comparisons of the capabilities of different CAE systems. Preprocessing treatments are done to the CT slices (pictures) of the lung in order to improve the quality of the images obtained from the CT scan. When it comes to the identification of nodules, the results are therefore enhanced as a result of this. Since the lungs contain a multitude of structures that, at this phase, may be readily misinterpreted as nodules, this stage is critical. The process of lung segmentation is a necessary stage for any CAD system that hopes to aid in the early identification of lung diseases such as cancer and other lung ailments. This phase may be thought of as the backbone of the whole process. This attempt is made more challenging by the absence of heterogeneity in the area of the lung, the presence of structures with a comparable density, such as arteries, veins, bronchi, and bronchioles, and the use of a variety of imaging equipment with a variety of imaging procedures. The first step in the process of locating nodules using a CAD system is to define the search area of interest for the nodules. The process of nodule identification is the second step of the CAD system, which comes after the first step (for example, the segmented lung fields). The purpose of this stage is to identify whether or not any lung nodules are visible in the images that have been analyzed thus

far. In terms of their density, the shapes that they take, or the sites that they occupy, there is no comparison between the two. The existence of these obstacles adds to the difficulties associated with the process of identifying lung nodules. One of the most difficult features of these diagnostic tools is the relatively high number of false positives that are created by today's CAD systems. This is one of the most demanding parts. Due to the presence of these false positives, it could be more challenging to appropriately interpret the findings of medical examinations. The majority of the time, a substantial number of false positives will lead the radiologist in charge of interpretation to get confused, which will ultimately result in a reduction in the efficiency of the CAD system.

In Table 2.1, Firstly, many of the methods rely solely on CT scans from the LIDC/LIDC-IDRI datasets for evaluation. While these are useful standard datasets, relying too heavily on them risks overfitting models to these particular datasets. More diverse evaluation using different datasets would strengthen the validity of the methods. Only a few works used other datasets like JSRT, DIR-LAB, or their own clinical data. Using multiple datasets helps ensure the methods generalize well.

Secondly, most works focus on nodules larger than 3mm. Detecting smaller nodules is also critical for early diagnosis but is more challenging due to lower resolution and increased noise. Only Chung et al. and Song et al. evaluated on nodules smaller than 3mm. More research is still needed into precise segmentation of sub-3mm nodules.

Thirdly, several works did not provide key performance metrics like sensitivity, false positive rate, or computational time. These metrics are important for evaluating and comparing methods. Works that omit them make it difficult to critically judge the approach.

Fourthly, many methods are only evaluated qualitatively through visual inspection. Quantitative evaluation using metrics like sensitivity, accuracy and dice coefficient is needed to objectively compare techniques. Qualitative evaluation alone risks bias and makes fair comparison impossible.

Fifthly, most works focus on common solid nodules. Segmenting other types like juxtapleural, juxtavascular or ground glass opacity nodules is equally important but less

investigated. Only a few works by Wang et al., Roy et al., Shakir et al. and Kim et al. evaluated on these non-solid nodule types. More research should target precise segmentation of diverse nodule types.

Sixthly, many works do not discuss the clinical significance and potential real-world impact of their methods. Translating these techniques into clinical practice is the ultimate goal, yet few works provide clinical evidence like observer studies with radiologists or integration with hospital PACS systems. More evaluation in a clinical setting would strengthen the methods' potential for real-world lung cancer diagnosis.

Seventhly, several deep learning approaches have emerged recently but are still a minority compared to traditional methods. Deep learning has huge potential to leverage large datasets and extract semantic features automatically. But most works still use handcrafted features. More exploration of deep learning and neural networks for this application is warranted.

Finally, few works have investigated combining multiple methods to utilize complementary strengths. Hybrid approaches that integrate deep learning with traditional methods like level sets may outperform either alone. This is still an underexplored area with much promise.

Table 2.1 Processing stages included in each of the selected works

| Authors | Database Acquisition | Pre-processing | Lung Segmentation | Nodule detection | FP reduction |
|---------------------------------|----------------------|----------------|-------------------|------------------|--------------|
| (Wang, S., et al., 2017) | LIDC-IDRI | NI | YES | YES | YES |
| (Roy, R., et al., 2019) | LIDC-IDRI | YES | YES | YES | NI |
| (Li, Y., et al., 2018) | LIDC-IDRI | YES | YES | NI | NI |
| (Farhangi, M. M., et al., 2017) | LIDC-IDRI | YES | YES | YES | NI |

Table 2.1 Continued

| Authors | Database Acquisition | Pre-processing | Lung Segmentation | Nodule detection | FP reduction |
|-----------------------------------|--|----------------|-------------------|------------------|--------------|
| (Song, J., et al.,2016) | LIDC-IDRI | YES | YES | YES | YES |
| (Saïen, S., et al.,2018) | LIDC/LIDC-IDRI | YES | YES | YES | YES |
| (Abbas, Q. 2017) | LIDC/LIDC-IDRI | YES | YES | YES | NI |
| (Nithila, E. E., et al.,2019) | LIDC-IDRI/ SPIE- AAPM | YES | YES | YES | NI |
| (Zhang, W., et al.,2017) | LIDC-IDRI/ our own data sets | NI | YES | NI | NI |
| (Manickavasagam, R., et al.,2019) | LIDC | NI | YES | YES | NI |
| (Chunran, Y., et al.,2018) | LIDC | NI | YES | YES | NI |
| (Vishraj, R., et al.,2018) | LIDC | NI | YES | YES | YES |
| (Huidrom, R., et al.,2018) | LIDC and RIMS | YES | YES | YES | NI |
| (Chung, H., et al.,2018) | LIDC and WKUH | NI | YES | YES | YES |
| (Shakir, H., et al.,2018) | TCIA/CUM C/ RIDER/FD A/ LIDC in SU | YES | YES | YES | NI |

Table 2.1 Continued

| Authors | Database Acquisition | Pre-processing | Lung Segmentation | Nodule detection | FP reduction |
|--------------------------------------|---|----------------|-------------------|------------------|--------------|
| (Sargent, D., et al.,2017) | FDA lung phantom dataset/SPIE 2016 | YES | YES | YES | NI |
| (Liang, R., et al.,2017) | DIR-LAB | YES | YES | NI | NI |
| (Swierczynski, P., et al.,2018) | DIR-LAB | YES | YES | NI | NI |
| (Rebouças Filho, P. P., et al.,2019) | Lung CT images and Brain CT images | YES | YES | NI | NI |
| (Priyadharshini, F. A., et al.,2018) | Lung CT images and Brain CT images | YES | NI | NI | NI |
| (Siriapisith, T., et al.,2019) | 3D CT 1340 CT slices of | YES | NI | NI | NI |
| (Astaraki, M., et al.,2018) | eight OARs (organs-at-risk) | YES | YES | YES | NI |
| (Rebouças Filho, P. P., et al.,2017) | Database built from COPD, cystic fibrosis and | NI | YES | YES | NI |

Table 2.1 Continued

| Authors | Database Acquisition | Pre-processing | Lung Segmentation | Nodule detection | FP reduction |
|------------------------------------|---|----------------|-------------------|------------------|--------------|
| | healthy patients. | | | | |
| (Hooda, R., et al.,2019) | Publicly available JSRT | NI | YES | YES | NI |
| (Gong, J., et al.,2018) | LUNA16 and ANODE09 | YES | YES | YES | YES |
| (Samaghcheh, Z. N., et al.,2018) | CRPF from VIA/I-ELCAP | YES | YES | YES | NI |
| (Veduruparthi, B. K., et al.,2018) | CBCT | YES | YES | NI | NI |
| (Hao, R., et al.,2018) | PET-CT from a hospital in Shanxi, China | YES | YES | YES | YES |
| (Zhu, H., et al.,2017) | Shanghai Chest Hospital CT images | YES | YES | YES | NI |
| (Suárez-Mejías, C., et al.,2017) | Randomly of 26 cases | YES | NI | YES | NI |
| (Kim, Y. J., et al.,2016) | Four data sets | YES | YES | YES | NI |

Table 2.1 Continued

| Authors | Database Acquisition | Pre-processing | Lung Segmentation | Nodule detection | FP reduction |
|--------------------------------|-----------------------------|-----------------------|--------------------------|-------------------------|---------------------|
| (Zhuang, M., et al.,2016) | Clinical datasets | NI | YES | YES | NI |
| (Kronman, A., et al.,2016) | 28 CT scans of two common | YES | YES | YES | NI |
| (Soliman, A., et al.,2016) | 25 patients at EE-BH | NI | YES | YES | NI |
| (Saravanan, S., et al.,2017) | | YES | YES | YES | NI |
| (Pak, C.-H., et al.,2017) | | NI | YES | YES | NI |
| (Manoj Kumar, P., et al.,2016) | | NI | YES | YES | NI |

In Table 2.2, the computational methods that have been used to carry out the automated identification of pulmonary nodules in lung CT scan pictures are mentioned. This detection process has been carried out successfully. According to the reviewed papers, 8 papers are related to the Active Contour Method. 3 papers are related to Chan Vese (CV) model. As an accuracy segmented model, only two papers are mentioned to deep learning. Therefore, the proposed deep learning and level set algorithm is valuable to investigate.

Table 2.2 Computational techniques that have been used to carry out the automatic detection of pulmonary nodules in lung CT scan images

| Authors | Computational technique(s) |
|-----------------------------------|-----------------------------------|
| (Manickavasagam, R., et al.,2019) | Active Contour Model |
| (Nithila, E. E., et al.,2019) | Active Contour Model |

Table 2.2 Continued

| Authors | Computational technique(s) |
|--------------------------------------|---|
| (Zhang, W., et al.,2017) | Active Contour Model |
| (Zhuang, M., et al.,2016) | Active Contour Model |
| (Hao, R., et al.,2018) | LBF Active Contour Model |
| (Saravanan, S., et al.,2017) | DRLSE and Active contour |
| (Rebouças Filho, P. P., et al.,2019) | (OPS)-adaptive and active contour |
| (Rebouças Filho, P. P., et al.,2017) | 3D Adaptive Crisp Active Contour Method (3D ACACM) |
| (Farhangi, M. M., et al.,2017) | 3-D Active Contour Model |
| (Pak, C.-H., et al.,2017) | Chan-Vese model (CV model) and improved mean square error model (ME model) |
| (Swierczynski, P., et al.,2018) | Chan-Vese model |
| (Chung, H., et al.,2018) | Chan-Vese model |
| (Astaraki, M., et al.,2018) | level-set |
| (Shakir, H., et al.,2018) | level-set |
| (Saien, S., et al.,2018) | level-set |
| (Samaghcheh, Z. N., et al.,2018) | level-set |
| (Priyadharshini, F. A., et al.,2018) | Bat Algorithm (BA) and the Kapur's function level-set (DRLS) |
| (Li, Y., et al.,2018) | level-set |
| (Veduruparthi, B. K., et al.,2018) | gradient-based level-set (GB) and Local Rank Transform (LRT) |
| (Vishraj, R., et al.,2018) | Region-based level-set Method (rblsm) |
| (Liang, R., et al.,2017) | level-set |

Table 2.2 Continued

| Authors | Computational technique(s) |
|----------------------------------|---|
| (Zhu, H., et al.,2017) | Based on the super-pixels and the level-set segmentation methods |
| (Chunran, Y., et al.,2018) | Fully convolutional network (FCN), the level set method |
| (Wang, S. et al., 2017) | Multi-view convolutional neural networks |
| (Siriapisith, T., et al.,2019) | Iteratively alternating between two different segmentation techniques |
| (Manoj Kumar, P., et al.,2016) | Mostly watershed rule and multi-atlas segmentation method |
| (Gong, J., et al.,2018) | 3D tensor filtering algorithm and local image feature analysis |
| (Sargent, D., et al.,2017) | 3D extension of the 2D edge linking method |
| (Huidrom, R., et al.,2018) | Fully automated lung segmentation method |
| (Hooda, R., et al.,2019) | Shallow learning-based method |
| (Suárez-Mejías, C., et al.,2017) | continuous convex relaxation methodology |
| (Kim, Y. J., et al.,2016) | Five types of semi-automatic segmentation methods |
| (Abbas, Q. 2017) | New segmentation algorithm (propseg) |
| (Kronman, A., et al.,2016) | New geometry-based algorithm |
| (Soliman, A., et al.,2016) | New nonrigid registration methodology |
| (Song, J., et al.,2016) | Toboggan based growing automatic segmentation approach (TBGA) |

The computational classifiers that have been used in the false positive reduction step are indicated in Table 2.3. Most of models are classified by the traditional algorithms. Only two papers are related to deep learning classifiers for the segmentation application.

The following characteristics were included in order to make comparisons across the publications that were found during this review: sensitivity, false-positive rate (FP),

number of nodules used in the validation, size of the nodules, reaction time, and kinds of nodules. These characteristics may be found in the vast majority of the articles that were chosen. Table 2.4 provides a brief summary of the comparison.

For the segmentation techniques in Table 2.2, many rely solely on standard datasets like LIDC/LIDC-IDRI for evaluation. While useful benchmarks, over-dependence on these datasets risks overfitting and reduced generalizability. Testing on more diverse data from multiple sources would strengthen validity. Most works also focused on nodules >3mm. Detecting smaller nodules is critical but more challenging due to lower resolution and higher noise. Only Chung et al. and Song et al. evaluated on sub-3mm nodules. More research is still needed for precise segmentation of small nodules.

Table 2.3 Computational classifiers that have been used for the false positive reduction task

| Authors | Computational classifier |
|----------------------------|--|
| (Wang, S. et al., 2017) | Fully connected layer convolutional neural networks |
| (Saien, S., et al.,2018) | Hybrid undersampling/boosting algorithm Called rusboost |
| (Gong, J., et al.,2018) | CFS (Correlation Feature Selection) subset evaluator attribute selection method/Random forest classifier |
| (Chung, H., et al.,2018) | Bayesian approach |
| (Vishraj, R., et al.,2018) | Intuitionistic Fuzzy domain |
| (Hao, R., et al.,2018) | Information entropy and joint vector |
| (Song, J., et al.,2016) | Three-step framework |

Several works omit key metrics like sensitivity, false positives, and runtime. Without these metrics, it is difficult to critically evaluate and compare methods. Qualitative visual evaluation alone risks bias and lacks objectivity. Quantitative metrics using sensitivity, accuracy, dice coefficient. are essential for proper assessment.

The majority focus on common solid nodules. Segmenting other types like juxtaleural, juxtavascular or ground glass opacity nodules is equally important yet under-explored. Only Wang et al., Roy et al., Shakir et al. and Kim et al. evaluated such non-solid nodules. More work should target segmenting diverse, challenging nodule types.

Most works lack discussion of clinical relevance and real-world impact. Translating techniques into clinical practice is the ultimate goal, yet few works provide clinical validation like radiologist studies or integration with hospital PACS. More clinical evaluation would strengthen real-world utility.

Deep learning approaches are still a minority, with most using handcrafted features. Deep learning shows immense potential from large datasets and automated feature extraction. But this remains underexplored for this application.

Few works investigate combining methods to utilize complementary strengths. Hybrid approaches integrating deep learning and traditional techniques may outperform either alone. This fusion is still an open research area.

For the classifiers in Table 2.3, a key limitation is the reliance on conventional machine learning algorithms. Only Wang et al. and Saien et al. leverage deep learning for false positive reduction. Classical algorithms lack the representation learning capabilities of deep neural networks. Deep learning-based classifiers may offer improved generalization and performance, but remain under-studied.

Many traditional classifiers are also susceptible to overfitting on small, homogeneous datasets. Robustness to diverse samples is critical for real-world deployment. Deep learning can better capture feature representations to improve out-of-sample generalization, if sufficient training data is available.

Classical methods like Bayesian, fuzzy logic and random forests have limited capacity to model complex feature interactions. Deep neural networks can implicitly model intricate relationships through hierarchical feature extraction. This can better separate complex true and false positives.

Table 2.4 Level set techniques for automatic detection of pulmonary nodules from lung CT images

| Method | Sensitivity (%) | FP/exam | No of nodules | Size | Response time | Nodule types | No.of images |
|--------------------------------------|-----------------|--------------|---------------|------|---------------|----------------------------------|---------------------------------------|
| (Wang, S. Et al., 2017) | 83.72(20.71) | 77.58(15.83) | 893 | NI | NI | Juxta-pleural, cavitary/nonsolid | NI |
| (Manickavasagam, R., et al.,2019) | 92.17% | NI | NI | NI | NI | NI | 200 |
| (Siriapisith, T., et al.,2019) | NI | NI | NI | NI | NI | NI | Abdominal Aortic Aneurysms (20 cases) |
| (Swierczynski, P., et al.,2018) | NI | NI | NI | NI | NI | NI | 10 pairs of 4D CT lung scans |
| (Rebouças Filho, P. P., et al.,2019) | NI | NI | NI | NI | NI | lung and brain | 36(Normal, Fibrosis) |

Table 2.4 Continued

| Method | Sensitivity (%) | FP/exam | No of nodules | Size | Response time | Nodule types | No.of images and COPD) |
|--------------------------|--|---------|-------------------------------|---|--|---|------------------------|
| (Roy, R., et al.,2019) | The reduced error rate of isolated (8.33%) and pleural adhesion (11.76%) | NI | 38 solid 25/juxta pleural | CT image of the thorax with size 512 *512 | CNN (982 s) over 220 images DRL SE(418 s), WL SE(532 s), (Roy, R., et al.,2019) (456s) | Solid nodules and juxta-pleural nodules | NI |
| (Hooda, R., et al.,2019) | NI | NI | 154 lung nodules 4096 samples | 128 *128 Pixel size as 0.175 mm | 40.63s | NI | NI |

Table 2.4 Continued

| Method | Sensitivity (%) | FP/exam | No of nodules | Size | Response time | Nodule types | No.of images |
|-------------------------------|-----------------|---------|---------------|---|-------------------------------|---|--------------|
| (Nithila, E. E., et al.,2019) | NI | NI | NI | Thickness of slice varies from 1.25 to 2.5 mm range with the pixel size from 0.48 mm to 0.72 mm | Computation time of only 17 s | edge based and region based | NI |
| (Shakir, H., et al.,2018) | NI | NI | 72 | Any sizes | NI | Well-circumscribed nodules, juxta-vascular nodules, and juxta-pleural nodules | NI |

Table 2.4 Continued

| Method | Sensitivity (%) | FP/exam | No of nodules | Size | Response time | Nodule types | No.of images |
|----------------------------------|--|--------------|---------------|---------------|---|---------------------------------|--------------|
| (Saien, S., et al.,2018) | 92.22 | 2.4 per scan | 92 | 3mm or larger | It has shorter computational time compared to other methods | All type | NI |
| (Gong, J., et al.,2018) | 84.62 | 2.8 per scan | 39 | [3mm,30mm] | NI | Ball-like or dot-like structure | NI |
| (Samaghcheh, Z. N., et al.,2018) | NI | NI | 39 | NI | NI | NI | NI |
| (Chunran, Y., et al.,2018) | Accuracy of 100% and the dice overlap index of segmentation of 0.9 | NI | 1010 CT scans | [3mm,30mm] | NI | All types | 2000 |

Table 2.4 Continued

| Method | Sensitivity (%) | FP/exam | No of nodules | Size | Response time | Nodule types | No.of images |
|--------------------------------------|---|---------|------------------------|---------------------------------|---------------|--|--------------|
| (Huidrom, R., et al.,2018) | 0.99759 0.99204 | NI | 20 CT scans | NI | NI | Juxta-pleural nodules | NI |
| (Priyadharshini, F. A., et al.,2018) | NI | NI | NI | Size 630 * 630 pixels | NI | Brain and lung | NI |
| (Li, Y., et al.,2018) | NI | NI | 175 | Over3mm | NI | Juxta-pleural (JP) and pleural-tail (PT) nodules | NI |
| (Chung, H., et al.,2018) | 0.9785 | NI | 314/16873; 125/1766 | Smaller than 3mm | NI | Juxta-pleural nodule | NI |
| (Vishraj, R., et al.,2018) | NI | NI | NI | Ni | NI | Juxta-pleural nodules | NI |
| (Hao, R., et al.,2018) | 92.35% average dice similarity coefficient | NI | 400 | 2.19mm Hausdorff distance | Less time | Juxta-vascular pulmonary nodules | NI |

Table 2.4 Continued

| Method | Sensitivity (%) | FP/exam | No of nodules | Size | Response time | Nodule types | No.of images |
|--------------------------------|-----------------|---------|---------------|-------------------------------|--|---|--------------|
| (Zhang, W., et al.,2017) | NI | NI | 76 | NI | NI | Left and right lungs, juxta-pleural nodules | 60+60 |
| (Farhangi, M. M., et al.,2017) | NI | NI | 542 | Greater than or equal to 3 mm | NI | All types | NI |
| (Abbas, Q. 2017) | NI | NI | NI | (512 * 512) pixels | NI | Right or left lungs, lung nodules, human airwaysand pulmonary trees | 220 |
| (Liang, R., et al.,2017) | NI | NI | NI | NI | 67% of the time that LBF and DRLSE did | NI | NI |

Table 2.4 Continued

| Method | Sensitivity (%) | FP/exam | No of nodules | Size | Response time | Nodule types | No.of images |
|----------------------------------|-----------------------|---------|---------------|-----------------------|----------------------------------|--|---------------------|
| (Zhu, H., et al.,2017) | NI | NI | 104 groups | [3mm,50mm] | NI | Some are independent, and some are close to the lung wall or other biological tissue | NI |
| (Sargent, D., et al.,2017) | NI | NI | 80 | [8mm,10mm] | NI | Spherical, elliptical, speculated, and lobulated | NI |
| (Suárez-Mejías, C., et al.,2017) | 90 % | NI | NI | 512 * 512 pixels | 92.5 % lower than the time taken | Retroperitoneal tumors | 26 CT image volumes |
| (Kim, Y. J., et al.,2016) | Approximately 80%–90% | Tens | 40 | 512 * 512 with 12 b/p | Effective in terms of time | Persistent Ground Glass Nodules | NI |

Table 2.4 Continued

| Method | Sensitivity (%) | FP/exam | No of nodules | Size | Response time | Nodule types | No.of images |
|----------------------------|-----------------|--------------------|-------------------------|------------------------------|--|---|--------------|
| (Zhuang, M., et al.,2016) | NI | NI | 20+16 | NI | NI | Various lesion | NI |
| (Kronman, A., et al.,2016) | NI | NI | 28 CT scans | NI | 35.7 s (std = 2.7) and 41.1 s (std = 10.7) | Abdominal Aortic Aneurysms (AAA) and lung tumors | NI |
| (Soliman, A., et al.,2016) | NI | NI | 25 patients | NI | NI | NI | NI |
| (Song, J., et al.,2016) | 96.35% | 73 false positives | 850 lesions+121 lesions | [3mm,30mm] (average 9.80 mm) | Under 8s | Solid nodules, ground-glass opacities and cavities; Juxta-pleural and juxtavascular lesions | NI |

Most works evaluate classifiers in isolation, rather than end-to-end with the full segmentation pipeline. But classifier performance is highly dependent on the upstream steps. Joint end-to-end evaluation is needed for a true gauge of real-world viability.

Runtime is also rarely reported, but efficiency is important for real-time clinical use. Deep networks can leverage parallel GPU processing for fast inference unlike classical serial algorithms. But deep learning's superiority is not guaranteed and needs investigation.

In summary, while existing works have advanced lung nodule segmentation, several limitations around evaluation, metrics, nodule types, clinical relevance, deep learning fusion, generalization, feature modeling and efficiency warrant further investigation. But the field is advancing rapidly, with these gaps presenting exciting opportunities for future work. More diversity, combinatory techniques, clinical studies, neural networks and rigorous benchmarking will further enhance lung segmentation and its clinical impact. Critical analysis steers progress by identifying current weaknesses and motivating innovative solutions for real-world lung cancer care.

Accurate lung nodule segmentation from CT scans is an active area of research. U-Net (Ronneberger et al., 2015) is one of the most popular CNN architectures for biomedical segmentation. Huang et al. (2021) utilized a 3D U-Net model for lung nodule delineation, achieving 82.3% dice similarity. However, vanilla U-Net struggles with small nodules due to limited receptive field. Multi-scale approaches like nnU-Net (Isensee et al., 2021) integrate multiple U-Nets to capture both local and larger context. Chen et al. (2021) employed a nnU-Net pipeline for lung nodule segmentation, improving sensitivity to 82.4% for small nodules (<10mm).

Attention mechanisms are also promising to focus on salient nodule features. Wang et al. (2022) proposed a dual attention-guided U-Net for lung nodule delineation, outperforming U-Net and Attention U-Net. Dice scores reached 83.5% overall. Self-supervised methods like Contrastive Learning (CL) also boost performance by pre-training on unlabeled data before fine-tuning. Guo et al. (2022) applied CL to a U-Net-like model, achieving 85.2% dice on the LIDC dataset. Another trend is incorporation of shape/boundary priors into networks. Ravishankar et al. (2021) imposed shape

constraints within a convolutional LSTM model, improving contour regularization and dice score to 84.7%. Zhu et al. (2020) embedded a shape-aware loss function into a cascaded segmentation network, enhancing boundary adherence and reaching 81.6% dice accuracy. Weakly supervised methods using only bounding boxes or scribbles can reduce annotation burden. Zhou et al. (2021) trained a CNN weakly on just bounding boxes, achieving comparable accuracy to fully supervised models. Hu et al. (2022) introduced scribble annotations to progressively train a segmentation network, reaching 83.2% dice performance. Such methods show promise for reducing manual labeling effort. Efficient model design is also crucial for real-time inference. Liao et al. (2021) developed a compact segmentation network with just 1.8M parameters, delivering 79.2% dice while running over 80 FPS. Li et al. (2020) exploited model distillation techniques like knowledge transfer to compress U-Net by 4x with only a 1.2% drop in dice. These works demonstrate the potential for practical deployable segmentation. Segmentation consistency across datasets is another challenge. Standard datasets like LIDC have inherent biases that cause overfitting. Multi-dataset training can improve generalization, as explored by Gerard et al. (2020) using the LIDC, LUNA16 and NLST datasets. They achieved consistent dice scores around 83% across datasets using a 3D DualNet architecture. In summary, major advances in lung nodule segmentation leverage CNNs, attention mechanisms, shape/boundary constraints, weakly supervised learning, model compression and multi-dataset training. But several challenges remain around accuracy, efficiency, annotation burden and generalization. Continued research and benchmarking on diverse real-world data will further progress segmentation for clinical benefit.

2.5 The analysis of the Three Problems

The ability to perceive and understand the world around us is a fundamental aspect of human existence. Vision plays a crucial role in this process, allowing us to gather and interpret visual information from our surroundings. However, as the passage rightly points out, our individual capacity to acquire visual information is inherently limited by various factors (Liu and He, 2015). This limitation is where images emerge as invaluable tools, serving as material carriers that bridge the gap between the real world and our comprehension of it.

Images have become indispensable in numerous fields, ranging from astronomy and satellite remote sensing to medical imaging, nanotechnology, and even entertainment and digital communication (Liu and He, 2015). They enable us to perceive and understand targets in diverse environments and at different scales, transcending the boundaries of space and time. By capturing and preserving visual information, images facilitate information visualization and sharing, empowering humans to make informed decisions and take appropriate actions.

The passage emphasizes the importance of physical instruments, such as optical devices, in the acquisition of images (Liu and He, 2015). These instruments leverage advancements in technology to capture visual data that would otherwise be inaccessible to the naked eye. For instance, telescopes in astronomy allow us to observe celestial bodies and phenomena that are millions of light-years away, while microscopes in nanotechnology reveal the intricate details of structures at the nanoscale.

Moreover, the advent of digital technology has revolutionized the way we store, transmit, and process images (Liu and He, 2015). Digital imaging techniques have enabled the efficient storage and dissemination of visual information, facilitating collaboration and knowledge-sharing across diverse domains. From satellite imagery used for environmental monitoring and urban planning to medical imaging techniques like X-rays, CT scans, and MRI, digital images have become indispensable tools for understanding and decision-making.

However, as the passage aptly notes, the original information contained within an image is often not directly usable by humans (Liu and He, 2015). This limitation has given rise to the field of image processing, which aims to enhance, analyze, and extract meaningful information from digital images. Image processing techniques play a crucial role in various applications, such as medical diagnosis, object recognition, remote sensing, and scientific visualization. Despite the significant progress made in image processing research, the passage acknowledges that there are still unresolved issues that need to be addressed (Liu and He, 2015). These challenges may arise from factors such as noise, uneven illumination, complex backgrounds, or limitations in existing algorithms and methodologies. Overcoming these obstacles is essential for improving the accuracy,

robustness, and efficiency of image processing techniques, ultimately enhancing our ability to extract valuable insights from visual data.

One of the key challenges mentioned in the passage is the problem of uneven gray levels, which can significantly impact the accuracy of image segmentation algorithms (Liu and He, 2015). Uneven illumination or variations in imaging equipment can lead to non-uniform grayscale distributions within an image, making it difficult to distinguish between different structures or regions of interest. Addressing this issue requires the development of advanced segmentation algorithms that can effectively handle uneven grayscale levels, potentially through adaptive techniques or novel energy formulations. Another challenge highlighted is the presence of noise in images (Liu and He, 2015). Noise can originate from various sources, such as sensor imperfections, environmental conditions, or the imaging process itself. Noise can obscure important details, introduce artifacts, and degrade the overall quality of the image, negatively impacting subsequent processing and analysis tasks. Developing robust noise-reduction techniques and noise-resilient image processing algorithms is crucial for obtaining reliable and accurate results. Furthermore, the passage mentions the challenges posed by complex backgrounds, particularly in natural images or medical imaging scenarios (Liu and He, 2015). Complex backgrounds can make it difficult for segmentation algorithms to distinguish between the foreground object of interest and the background clutter. This challenge requires the development of advanced feature representations, machine learning techniques, or multi-scale approaches to effectively handle the complexity and variability present in real-world images.

In addition to these specific challenges, the passage also alludes to the need for improved computational efficiency and robustness in image processing algorithms (Liu and He, 2015). As imaging technologies continue to advance and the demand for real-time or near-real-time processing increases, it becomes crucial to develop algorithms that can efficiently handle large volumes of data while maintaining accuracy and reliability. By addressing these challenges, researchers and practitioners in the field of image processing can unlock the full potential of visual information, enabling more accurate and reliable analysis across a wide range of domains. Innovative solutions in image processing can have far-reaching implications, from enhancing medical diagnostics and

treatment planning to enabling advanced object recognition in autonomous systems or improving our understanding of the natural world through remote sensing and scientific imaging.

In conclusion, the part highlights the vital role of images in bridging the gap between the real world and human perception, while also acknowledging the necessity of image processing techniques to extract meaningful information from visual data (Liu and He, 2015). Despite the significant progress made in this field, there remain unresolved issues that require further research and innovation. By addressing these challenges, researchers and practitioners can unlock the full potential of visual information, enabling more informed decision-making and advancing our understanding of the world around us.

2.5.1 The analysis of Uneven Gray Levels Problems

Deep Medical image segmentation plays a crucial role in various clinical applications, such as disease diagnosis, treatment planning, and surgical guidance. However, achieving accurate segmentation is a challenging task, particularly when dealing with images exhibiting uneven gray levels. This issue arises due to defects in imaging equipment, inconsistent illumination, or inherent tissue heterogeneity (Li et al., 2020; Yin et al., 2020). The presence of uneven gray levels can obscure vital structures and hinder the correct delineation of regions of interest, leading to potential misdiagnosis or suboptimal treatment strategies.

This part highlights the shortcomings of existing level-set segmentation algorithms in handling images with uneven gray levels. These algorithms often suffer from limitations such as getting trapped in local minima, sensitivity to initial contour placement, and limited segmentation efficiency (Li et al., 2020; Yin et al., 2020). To address these challenges, researchers have proposed various approaches, each with its own strengths and weaknesses.

This section aims to provide an in-depth analysis of the Uneven Gray Levels Problems section, exploring the underlying causes, existing solutions, and their limitations. Furthermore, it will highlight the significance of innovations like the

VKMHLS method in overcoming these challenges and improving medical image segmentation accuracy.

1) Causes of Uneven Gray Levels in Medical Images

Uneven gray levels in medical images can arise from various sources, including defects in imaging equipment and variations in illumination conditions. Imaging modalities such as Magnetic Resonance Imaging (MRI), Computed Tomography (CT), and infrared imaging are particularly susceptible to this issue (Li et al., 2020; Yin et al., 2020).

Defects in imaging equipment can contribute to uneven gray levels due to factors such as sensor imperfections, non-uniform sensitivity, or improper calibration. For instance, in MRI, variations in the magnetic field strength or radio frequency coil sensitivity can lead to intensity inhomogeneities across the image (Belaroussi et al., 2006; Vovk et al., 2007).

Changes in illumination conditions can also result in uneven gray levels, particularly in optical imaging modalities like endoscopy or microscopy. Variations in lighting angles, intensity, or shadows can create intensity gradients and contrast differences within the image (Zhang et al., 2014; Wang et al., 2017).

Additionally, the inherent heterogeneity of biological tissues can contribute to uneven gray levels. Different tissue types, such as muscle, fat, or bone, exhibit varying degrees of signal attenuation and absorption, leading to intensity variations within the imaged region (Chen et al., 2017; Min et al., 2018).

2) Challenges with Existing Level-Set Segmentation Algorithms for Uneven Gray Levels

Existing level-set segmentation algorithms face significant challenges when confronted with images exhibiting uneven gray levels. The document highlights three main limitations:

Prone to Local Minima. In (Li et al., 2020; Yin et al., 2020), level-set algorithms are optimization-based techniques that seek to minimize an energy functional by evolving

contours to segment objects. However, in the presence of uneven gray levels, the energy landscape can become complex, with multiple local minima. This can lead to the algorithm converging to suboptimal solutions, resulting in inaccurate segmentations.

Sensitivity to Initial Contour. In (Li et al., 2020; Yin et al., 2020), many level-set methods require the user to provide an initial contour or seed points as a starting point for the segmentation process. In scenarios with uneven gray levels, slight variations in the initial contour placement can lead to vastly different segmentation results. This sensitivity demands precise prior knowledge of the object's location, which may not be feasible in practical applications.

Limited Segmentation Efficiency. In (Li et al., 2020; Yin et al., 2020), numerical implementations of level-set algorithms often require small time steps to ensure stability and convergence during the optimization process. This constraint leads to slow convergence rates, hindering the overall segmentation efficiency. As medical images continue to increase in size and resolution, this limitation becomes more pronounced, prolonging the segmentation process.

3) Existing Solutions and Their Limitations for Uneven Gray Levels

Researchers have proposed various approaches to address the challenges posed by uneven gray levels in medical image segmentation. These solutions can be broadly categorized into local area-based methods, offset correction level-set clustering methods, and adaptive scale parameter level-set methods.

Local Area-Based Methods. These methods are based on the assumption that the gray level within a given region remains consistent (Li et al., 2007; Li et al., 2008; Wang et al., 2009; Zhang et al., 2010; Liu and Peng, 2012; Ji et al., 2015; Wang et al., 2017; Chen et al., 2017; Min et al., 2018). While these techniques can segment images with uneven gray levels, they are prone to falling into local minima and are sensitive to the initial contour placement (Li et al., 2020; Yin et al., 2020).

Offset Correction Level-Set Clustering Methods. These methods, based on K-means clustering, have gained significant attention in recent years (Li et al., 2011; Zhan et al., 2013; Zhang et al., 2014; Zhang et al., 2015; Huang and Zeng, 2015; Min et al.,

2016; Cai et al., 2018; Wang et al., 2018). By estimating the offset field of the image through local K-means clustering, these approaches can achieve accurate segmentation despite gray inhomogeneity. However, they suffer from several limitations, including the use of finite difference strategies that require small time steps for stability, local minima trapping, sensitivity to the initial contour, and the use of fixed scale parameters (Li et al., 2020; Yin et al., 2020).

Adaptive Scale Parameter Level-Set Methods. To address the limitations of fixed scale parameters, researchers have proposed adaptive scale parameter level-set segmentation methods (Cai et al., 2018; Piovano and Papadopoulo, 2008). These approaches employ techniques such as image entropy or local variance to automatically determine the scale parameters of the clustering kernel function (Cai et al., 2018). While these methods represent an improvement, they still face challenges, such as using the same scale parameter at each pixel, leading to incorrect segmentations for images with severe gray-scale inhomogeneity or nonlinearity. Additionally, they solely rely on local area information, making them susceptible to local minima trapping and initial contour sensitivity (Li et al., 2020; Yin et al., 2020).

Multi-Scale Level-Set Approaches. In recent years, multi-scale level-set approaches have been proposed (Wang et al., 2015; Min et al., 2016; Zhang et al., 2017). These methods design multi-layer level-set structures with a set of scale parameters, adaptively deciding the scale parameters at each pixel and maintaining the ability to detect global contrast information to prevent local minima trapping (Sui et al., 2012; Min et al., 2016). However, these approaches face limitations in providing appropriate scale parameters for segmenting images with highly uneven gray levels, as they use a series of fixed scale parameters and can only offer a limited number of candidate scales (Li et al., 2020; Yin et al., 2020).

While these existing solutions have made significant contributions, they still face challenges in accurately segmenting medical images with severe uneven gray levels, demonstrating the need for more robust and adaptive approaches.

4) Significance of the VKMHLs Method for Uneven Gray Levels Issues

The part highlights the importance of the VKMHLS (Variational K-means and Multi-layer Hybrid Level-Set) method as a novel approach designed to address the complexities of lung nodule segmentation and overcome the limitations of existing algorithms (Li et al., 2020; Yin et al., 2020).

5) The VKMHLS method introduces several key innovations:

Simplification of the Local Intensity Clustering (LIC) model. By simplifying the LIC model and introducing a novel energy functional based on the region-based pressure function, VKMHLS enhances segmentation efficiency for low gray-scale images (Li et al., 2020; Yin et al., 2020).

Fast Numerical Implementation Strategy. VKMHLS employs a fast numerical implementation strategy that swiftly segments images and estimates the offset field, significantly improving overall segmentation efficiency (Li et al., 2020; Yin et al., 2020).

Adaptive Multi-layer Level-Set Structure. To address the complexities of lung nodule segmentation and achieve robust and accurate results in challenging medical image datasets, VKMHLS extends its capabilities through a multi-layer model-based level-set structure (Li et al., 2020; Yin et al., 2020). This structure employs two specially designed scale operators that adaptively determine the optimal number of layers and the precise scale parameters for each layer. This adaptive multi-layer approach overcomes local minima challenges during segmentation, enabling VKMHLS to handle images with severely uneven gray level distributions successfully.

Integration of the CER Active Contour Model. VKMHLS introduces an innovative active contour model, CER, which intelligently combines elements from the well-established Chan-Vese (CV) model and the Region-Scalable Fitting (RSF) model (Li et al., 2020; Yin et al., 2020). CER integrates information entropy calculations and minimizes the overall energy functional, allowing it to successfully segment regions with weak edges, strong noise interference, and uneven brightness variations across the medical image. This robust approach enhances the accuracy of delineating target boundaries, proving particularly valuable for segmenting structures in magnetic resonance and ultrasonic imaging modalities.

Hybrid Level-Set Algorithm Based on Kernel Metrics. To tackle the persistent challenge of segmenting images with both uneven gray-scale characteristics and high levels of noise contamination, VKMHLS incorporates a hybrid level-set image segmentation algorithm based on kernel metrics (Li et al., 2020; Yin et al., 2020). This algorithm leverages an improved multi-scale mean filter to effectively mitigate gray-scale inhomogeneity across the image while reducing the impact of scale parameter selection on the final segmentation accuracy. Kernel measurement techniques and calculations of local similarity metrics are employed to suppress the influence of noise, enhancing the robustness of the method. Additionally, a count gradient regularization term is incorporated to further reduce noise impact, ensuring more precise segmentation results.

Through these innovations, VKMHLS aims to provide more robust and accurate segmentations, even in the face of uneven gray levels and noise contamination, ultimately contributing to improved medical image analysis and diagnosis.

6) Experimental Validation and Significance

The document highlights that comprehensive experimental evaluations demonstrate VKMHLS's ability to accurately segment images characterized by both gray-scale inhomogeneity and noise contamination, exhibiting robust performance across various types of noise distributions (Li et al., 2020; Yin et al., 2020). These attributes make VKMHLS a highly valuable tool for tackling real-world image segmentation challenges and enabling reliable nodule detection in lung cancer applications. The significance of VKMHLS lies in its potential to address the longstanding challenges associated with uneven gray levels and noise in medical image segmentation. By providing a robust and accurate segmentation solution, VKMHLS can facilitate earlier and more precise diagnosis of lung cancer, as well as improve treatment planning and patient outcomes. Furthermore, the innovative techniques introduced in VKMHLS, such as the adaptive multi-layer level-set structure and the integration of kernel metrics, may inspire further research and development in the field of medical image analysis. These advancements can potentially be applied to other imaging modalities and clinical applications, extending the impact of VKMHLS beyond lung cancer detection.

Therefore, the Uneven Gray Levels Problems section of the document highlights a critical challenge in medical image segmentation, specifically related to the presence of uneven gray levels in imaging modalities like MRI, CT, and infrared. Existing level-set segmentation algorithms face significant limitations in handling these irregularities, including susceptibility to local minima trapping, sensitivity to initial contour placement, and limited segmentation efficiency. While researchers have proposed various solutions, such as local area-based methods, offset correction level-set clustering methods, adaptive scale parameter level-set methods, and multi-scale level-set approaches, these techniques still face challenges in accurately segmenting medical images with severe uneven gray levels. The VKMHLS method, introduced in this research, represents a novel and innovative approach designed to address the complexities of lung nodule segmentation. Through its simplification of the LIC model, introduction of a novel energy functional, adaptive multi-layer level-set structure, integration of the CER active contour model, and hybrid level-set algorithm based on kernel metrics, VKMHLS aims to enhance segmentation accuracy and stability, even in the presence of uneven gray levels and noise contamination.

Experimental results demonstrate VKMHLS's robustness and improved accuracy over existing benchmarks, validating its effectiveness as a powerful tool for lung cancer detection in challenging medical imaging scenarios. The significance of VKMHLS lies not only in its potential to improve lung cancer diagnosis and treatment but also in its ability to inspire further research and development in the field of medical image analysis. As medical imaging technology continues to advance and the demand for accurate and reliable segmentation techniques grows, approaches like VKMHLS will play a crucial role in revolutionizing clinical practices and enhancing patient care.

2.5.2 The analysis of Noise Problems

Noise is a ubiquitous challenge in medical image segmentation, arising from various sources such as the imaging process itself, environmental factors, and hardware limitations (Yu et al., 2020; Wang et al., 2020). The presence of noise can significantly degrade the quality of medical images, making it difficult for segmentation algorithms to accurately delineate structures of interest, such as tumors or organs. This issue is particularly critical in applications like cancer diagnosis and treatment planning, where

precise segmentation is essential for optimal patient outcomes (Biswas and Hazra, 2022; Zhang et al., 2022).

The document highlights the detrimental impact of noise on existing level-set segmentation methods and emphasizes the need for more robust approaches to address this challenge. It discusses the difficulties in accurate segmentation with strong noise, the inability to handle combined noise and uneven grayscale levels, and the drawbacks of existing mixed level-set models in the presence of noise disturbances.

This section aims to provide an in-depth analysis of the "Noise Problems" section, exploring the underlying causes and consequences of noise in medical image segmentation, evaluating the strengths and limitations of existing methods, and highlighting the potential of novel approaches like VKMHLS to mitigate these challenges.

1) Sources and Types of Noise in Medical Imaging

Noise in medical images can originate from various sources, each contributing to different types of noise patterns and intensities. Understanding these sources is crucial for developing effective noise-resistant segmentation techniques.

Imaging Process Noise. The imaging process itself can introduce noise due to factors such as quantum fluctuations in photon detection (e.g., in X-ray or PET imaging), thermal noise in electronic components, or imperfections in the analog-to-digital conversion process (Aja-Fernández et al., 2015; Motwani et al., 2020). These sources can result in additive white Gaussian noise or speckle noise in the acquired images.

Environmental Noise. External factors like electromagnetic interference, vibrations, or ambient light can contribute to noise in medical images (Weiskopf et al., 2014; Kozubski and Kozinski, 2019). These sources can lead to structured noise patterns that may be difficult to model and remove.

Low-Dose Acquisition. In modalities like CT or PET, reducing the radiation dose to minimize patient exposure can result in increased noise levels in the acquired images (Nasirudin et al., 2017; Ghafarian et al., 2021). This trade-off between image quality and

patient safety necessitates robust segmentation techniques that can handle noisy low-dose images accurately.

Hardware Limitations. Imperfections or limitations in imaging hardware, such as sensor noise, electronic noise, or non-uniform sensitivity, can contribute to various types of noise in medical images (Aja-Fernández et al., 2015; Kozubski and Kozinski, 2019).

The presence of these diverse noise sources and patterns poses significant challenges for existing level-set segmentation methods, as they can introduce unwanted variations in pixel intensities, making it difficult to distinguish true object boundaries from noise-induced artifacts.

2) Challenges in Accurate Segmentation with Strong Noise

The document highlights the difficulty in accurately segmenting objects or regions of interest when medical images exhibit strong noise levels (Yu et al., 2020; Wang et al., 2020; Biswas and Hazra, 2022; Zhang et al., 2022). This challenge arises due to the fundamental principles underlying level-set segmentation algorithms.

Level-set methods are optimization-based techniques that seek to evolve contours or surfaces to segment objects by minimizing an energy functional (Osher and Sethian, 1988; Sethian, 1999). However, in the presence of strong noise, the energy landscape can become highly complex and riddled with local minima, leading to suboptimal or incorrect segmentations.

Noise can introduce artificial edges or intensity variations that can be mistakenly interpreted as object boundaries by the segmentation algorithm. Additionally, it can obscure or distort the true boundaries, making it challenging for the algorithm to accurately delineate the desired structures (Duan et al., 2015; Wu et al., 2016; Liu et al., 2018).

Moreover, strong noise can significantly impact the convergence behavior of level-set algorithms, as the energy minimization process becomes more susceptible to local minima trapping. This can result in the algorithm converging prematurely to an

inaccurate segmentation or failing to converge altogether (Yang et al., 2014; Niu et al., 2017; Yu et al., 2018).

3) Existing Solutions and Their Limitations for Solving Noise Problems

Researchers have proposed various approaches to address the challenges posed by noise in medical image segmentation, primarily focusing on local similarity measures, distance measurement methods, and level-set regularization techniques.

Local Similarity-Based Methods. Some methods utilize the local similarity of pixels to reduce the influence of noise during segmentation (Yang et al., 2014; Niu et al., 2017; Yu et al., 2018). These techniques estimate local intensity statistics or employ kernel-based similarity measures to identify and suppress noise while preserving true object boundaries. However, these methods may struggle with accurately segmenting images with strong noise, as the local similarities can be distorted or obscured by the high noise levels.

Distance Measurement and Regularization Methods. Other approaches employ novel distance measurement methods or level-set regularization techniques to segment noisy images (Miao et al., 2018; Wu et al., 2015; Liu et al., 2018; Duan et al., 2015; Wu et al., 2016; Liu et al., 2018). For instance, the KMD model (Liu et al., 2018) uses kernel metrics and total variation regularization to segment images with strong noise. The LODL model (Liu et al., 2018) incorporates L0 gradient and L0 function regularization terms to improve noise robustness. While these methods can achieve accurate segmentations in the presence of strong noise, they may still face challenges when dealing with uneven grayscale images, as highlighted in the document.

Offset Correction and Mixed Level-Set Models. The document discusses the LIC model (Li et al., 2011) and the MSF model (Wang et al., 2015), which employ offset correction and multi-scale mean filtering techniques to mitigate the impact of gray-scale unevenness on segmentation accuracy. These methods allow for the use of fixed scale parameters in segmenting the corrected images, reducing the influence of scale parameter selection on uneven grayscale images.

Additionally, the document mentions the use of mixed level-set models that combine local and global information to handle uneven images (Wang et al., 2010; Wang et al., 2009; Shyu et al., 2012; Liu et al., 2013; Jiang et al., 2014; Wen, 2014; Wang et al., 2014; Wang et al., 2018; Li et al., 2015; Jiang et al., 2015; Zhou et al., 2016; Huang et al., 2015; Soomro et al., 2016; Shi and Pan, 2016; Mondal et al., 2016; Liu et al., 2017; Soomro et al., 2018; Wang et al., 2015; Cai et al., 2018). For example, the LIC-CV model (Liu et al., 2013) combines the LIC model with the CV model (Chan and Vese, 2001) to handle slightly uneven grayscale images while being robust to initial contours. However, the document notes that these mixed models can still be easily disturbed by noise, leading to segmentation errors.

While these existing solutions have made significant contributions, they often face limitations in accurately segmenting medical images with both strong noise and uneven grayscale levels simultaneously. This highlights the need for more robust and adaptive approaches that can effectively handle the combined challenges posed by noise and gray-scale inhomogeneities.

4) Potential of the VKMHLS Method for Noise Issues

The document emphasizes the potential of the VKMHLS (Variational K-means and Multi-layer Hybrid Level-Set) method to mitigate the challenges related to noise and uneven grayscale levels in medical image segmentation. VKMHLS introduces several innovations that can contribute to improved noise robustness and accuracy:

Adaptive Multi-layer Level-Set Structure. VKMHLS employs an adaptive multi-layer level-set structure that uses specially designed scale operators to determine the optimal number of layers and scale parameters for each layer (Li et al., 2020; Yin et al., 2020).

Integration of CER Active Contour Model. The CER (Combining Elements from CV and RSF) active contour model introduced in VKMHLS integrates elements from the Chan-Vese (CV) and Region-Scalable Fitting (RSF) models (Li et al., 2020; Yin et al., 2020). CER utilizes information entropy calculations and energy functional minimization to segment regions with weak edges, strong noise interference, and uneven brightness

variations across the medical image. This robust approach can enhance the accuracy of delineating target boundaries, even in the presence of noise and intensity inhomogeneities.

Hybrid Level-Set Algorithm Based on Kernel Metrics. To tackle the combined challenge of uneven grayscale characteristics and high noise levels, VKMHLS incorporates a hybrid level-set algorithm based on kernel metrics (Li et al., 2020; Yin et al., 2020). This algorithm employs an improved multi-scale mean filter to mitigate grayscale inhomogeneity while reducing the impact of scale parameter selection on segmentation accuracy. Additionally, kernel measurement techniques and local similarity metrics are used to suppress noise influence, enhancing the method's robustness. Furthermore, a count gradient regularization term is incorporated to further reduce noise impact, ensuring precise segmentation results.

These innovations in VKMHLS aim to address the limitations of existing methods by providing an adaptive, robust, and efficient approach to medical image segmentation in the presence of both noise and uneven grayscale levels.

5) Significance and Potential Impact for Noise Issues

The significance of the VKMHLS method lies in its potential to overcome the longstanding challenges associated with noise and uneven grayscale levels in medical image segmentation. By achieving accurate and reliable segmentations, even in the presence of these complicating factors, VKMHLS can contribute to improved clinical diagnosis, treatment planning, and patient outcomes across various medical domains.

Improved Early Detection and Diagnosis. Accurate segmentation of tumors, lesions, or other abnormalities is crucial for early detection and diagnosis of diseases like cancer. VKMHLS's ability to handle noisy and unevenly lit images can enable more precise identification and delineation of these structures, facilitating earlier intervention and potentially improving patient prognosis.

Enhanced Treatment Planning and Guidance. In radiotherapy, surgical planning, and image-guided interventions, accurate segmentation of target structures and surrounding anatomical features is essential for optimal treatment delivery and minimizing collateral damage. VKMHLS's robust segmentation capabilities can

contribute to more accurate treatment planning, reducing the risk of complications and improving overall treatment efficacy.

Advancement of Medical Image Analysis Research. The innovations introduced in VKMHLS, such as the adaptive multi-layer level-set structure and the integration of kernel metrics, can inspire further research and development in the field of medical image analysis. These advancements can potentially be applied to other imaging modalities and clinical applications, extending the impact of VKMHLS beyond its initial scope.

Facilitation of Automated and Semi-Automated Segmentation. By providing accurate and reliable segmentations, even in challenging scenarios with noise and intensity inhomogeneities, VKMHLS can facilitate the development of automated or semi-automated segmentation pipelines. This can streamline the segmentation process, reduce the need for manual intervention, and enhance the efficiency of medical image analysis workflows.

Enabling Advanced Image Analytics and Quantification. Accurate segmentation is a prerequisite for many advanced image analytics techniques, such as quantitative analysis, feature extraction, and machine learning-based classification or prediction models. VKMHLS's robust segmentation capabilities can enable more reliable and precise quantification of anatomical structures, pathological features, and disease progression, contributing to improved diagnostic and prognostic models.

As medical imaging technology continues to evolve, and the demand for accurate and efficient image analysis increases, approaches like VKMHLS will play a crucial role in advancing clinical practices, research, and patient care.

Therefore, the Noise Problems section of the document highlights the significant challenges posed by noise in medical image segmentation, particularly when combined with uneven grayscale levels. Noise, originating from various sources, can degrade image quality, obscure object boundaries, and introduce unwanted artifacts, making it difficult for existing level-set segmentation methods to achieve accurate and reliable results. While researchers have proposed various solutions, such as local similarity-based methods, distance measurement and regularization techniques, and mixed level-set

models, these approaches often face limitations in handling strong noise or the combined effects of noise and uneven grayscale levels simultaneously.

The VKMHLS method, proposed in this research, represents a promising and innovative approach to address these challenges. By incorporating an adaptive multi-layer level-set structure, the CER active contour model, and a hybrid level-set algorithm based on kernel metrics, VKMHLS aims to enhance segmentation accuracy, robustness, and efficiency in the presence of noise and gray-scale inhomogeneities. The significance of VKMHLS lies in its potential to improve early disease detection, enhance treatment planning and guidance, advance medical image analysis research, facilitate automated and semi-automated segmentation pipelines, and enable advanced image analytics and quantification techniques. By overcoming the limitations of existing methods, VKMHLS can contribute to improved clinical practices, patient outcomes, and the overall advancement of medical imaging and analysis. As the demand for accurate and reliable medical image segmentation continues to grow, approaches like VKMHLS will play a crucial role in revolutionizing clinical practices, research, and patient care. By addressing the longstanding challenges of noise and uneven grayscale levels, VKMHLS represents a significant step forward in the field of medical image analysis, paving the way for more accurate diagnostics, personalized treatment strategies, and ultimately, better patient outcomes.

2.5.3 The analysis of Contour Initialization Problems

Contour initialization is a critical step in level-set segmentation methods, as it significantly influences the accuracy and convergence behavior of the algorithm. The problem statement highlights several challenges associated with contour initialization, including the presence of complex backgrounds, sensitivity to the initial contour placement, and computational inefficiencies arising from frequent reinitialization (Srikanth and Bikshalu, 2022; Khosravanian et al., 2023).

In many real-world scenarios, such as medical image analysis or object recognition in natural scenes, images often exhibit intricate backgrounds, noise, and uneven intensity distributions. These factors pose significant challenges for unsupervised level-set segmentation methods, as they can obscure the object of interest and make it

difficult to distinguish between the foreground and background (Srikanth and Bikshalu, 2022; Khosravanian et al., 2023). Additionally, the sensitivity of level-set methods to the initial contour placement can lead to suboptimal or incorrect segmentation results, particularly when dealing with complex backgrounds or uneven grayscale levels (Srikanth and Bikshalu, 2022; Khosravanian et al., 2023). Small variations or inaccuracies in the initial contour can cause the algorithm to converge to local minima, resulting in segmentation errors. Furthermore, the level-set evolution process itself can be computationally demanding and slow, especially when smooth and accurate segmentations are required. Frequent reinitialization steps are often necessary to ensure the stability and well-behaved nature of the level-set function, further impacting the computational efficiency of the algorithm (Srikanth and Bikshalu, 2022; Khosravanian et al., 2023).

This section aims to provide an in-depth analysis of the "Contour Initialization Problems" section, exploring the underlying challenges, evaluating existing approaches, and highlighting the importance of innovative solutions to address these issues effectively.

1) Challenges with Complex Backgrounds

One of the fundamental challenges in image segmentation, particularly in natural or medical images, is the presence of complex backgrounds (Srikanth and Bikshalu, 2022; Khosravanian et al., 2023). These backgrounds can be intricate and varied, with various textures, structures, and intensity variations, making it difficult for unsupervised level-set segmentation methods to distinguish between the foreground object of interest and the background clutter.

In medical imaging, for instance, objects such as tumors or organs may be surrounded by intricate anatomical structures or textures, making it challenging to accurately segment the target region (Srikanth and Bikshalu, 2022; Khosravanian et al., 2023). Similarly, in natural scenes, objects of interest may be embedded in complex outdoor environments, with varying illumination conditions, shadows, and background objects.

Traditional level-set methods often assume that the object of interest can be easily distinguished from the background based on intensity differences or edge information (Chan and Vese, 2001; Liu et al., 2013). However, in the presence of complex backgrounds, these assumptions may not hold true, leading to inaccurate segmentation results or the algorithm becoming trapped in local minima (Srikanth and Bikshalu, 2022; Khosravanian et al., 2023).

2) Sensitivity to Initial Contours

The problem statement highlights the sensitivity of level-set segmentation methods to the initial contour placement (Srikanth and Bikshalu, 2022; Khosravanian et al., 2023). This sensitivity can pose significant challenges, as small variations or inaccuracies in the initial contour can lead to vastly different segmentation results or cause the algorithm to converge to local minima, resulting in suboptimal or incorrect segmentations.

In level-set-based segmentation, an initial contour is often provided as a starting point for the algorithm, either manually or through automated techniques (Srikanth and Bikshalu, 2022; Khosravanian et al., 2023). The final segmentation result is highly dependent on this initial contour, as the algorithm evolves and deforms the contour based on various energy functionals and constraints.

When dealing with complex backgrounds or uneven grayscale levels, it can be challenging to provide an accurate initial contour manually, as the boundaries between the object of interest and the background may not be clearly defined (Srikanth and Bikshalu, 2022; Khosravanian et al., 2023). Even slight inaccuracies in the initial contour placement can lead the algorithm astray, causing it to converge to an incorrect solution or become trapped in local minima.

This sensitivity to initial contours can be particularly problematic in applications where prior knowledge of the object's location or shape is limited, such as in medical image analysis or object detection in natural scenes (Srikanth and Bikshalu, 2022; Khosravanian et al., 2023). Reliance on manual initialization can introduce human biases and errors, further compounding the challenges associated with contour initialization.

3) Slow Level-Set Evolution and Frequent Reinitialization

The level-set evolution process is a fundamental component of level-set segmentation methods, where the contour is iteratively deformed and evolved based on various energy functionals and constraints (Osher and Sethian, 1988; Sethian, 1999). However, the problem statement highlights the computational inefficiency associated with this process, particularly in scenarios where smooth and accurate segmentations are required (Srikanth and Bikshalu, 2022; Khosravanian et al., 2023).

One of the key reasons for slow level-set evolution is the need for frequent reinitialization steps (Srikanth and Bikshalu, 2022; Khosravanian et al., 2023). As the level-set function evolves, it can become irregular or lose its signed distance property, leading to numerical instabilities and potential convergence issues. To address this, the level-set function is periodically reinitialized, ensuring that it remains well-behaved and maintains smooth contours.

However, this reinitialization process can be computationally expensive, particularly for large or high-resolution images (Srikanth and Bikshalu, 2022; Khosravanian et al., 2023). It involves solving additional partial differential equations, further increasing the overall computational complexity and slowing down the segmentation process.

Slow level-set evolution and frequent reinitialization can hinder the real-time or near-real-time application of level-set segmentation methods, which is essential in various domains such as medical imaging, robotics, or video processing (Srikanth and Bikshalu, 2022; Khosravanian et al., 2023). In scenarios where rapid segmentation and analysis are required, such as in image-guided interventions or autonomous systems, the computational inefficiency of traditional level-set methods can pose significant limitations.

4) Existing Approaches and Their Limitations for Initialization Problems

Researchers have proposed various approaches to address the challenges associated with contour initialization in level-set segmentation methods. These approaches can be broadly categorized into techniques for handling complex

backgrounds, methods for mitigating sensitivity to initial contours, and strategies for improving computational efficiency.

Handling Complex Backgrounds. To tackle the challenges posed by complex backgrounds, researchers have explored techniques such as incorporating texture information, shape priors, or machine learning-based approaches (Srikanth and Bikshalu, 2022; Khosravanian et al., 2023). For example, incorporating texture features into the energy functional or using shape models can aid in distinguishing the object of interest from the background clutter. Additionally, deep learning-based methods have shown promise in automatically identifying and segmenting objects in complex scenes. However, these approaches often require additional training data, which may not be readily available in all domains, or rely on specific assumptions about the object's shape or texture, limiting their generalization capabilities (Srikanth and Bikshalu, 2022; Khosravanian et al., 2023).

Mitigating Sensitivity to Initial Contours. To address the sensitivity of level-set methods to initial contour placement, researchers have explored techniques such as multiphase level-set methods, region-based approaches, or incorporating prior information (Srikanth and Bikshalu, 2022; Khosravanian et al., 2023). Multiphase level-set methods can segment multiple objects simultaneously, reducing the reliance on accurate initial contours for each object. Region-based approaches segment images based on regional statistics rather than edge information, potentially mitigating the impact of initial contour placement. However, these methods often introduce additional complexities or require prior knowledge about the number of objects or regions to be segmented, which may not be available in all scenarios (Srikanth and Bikshalu, 2022; Khosravanian et al., 2023).

Improving Computational Efficiency. To address the computational inefficiency associated with slow level-set evolution and frequent reinitialization, researchers have explored techniques such as adaptive time-stepping schemes, parallel computing, and hardware acceleration (Srikanth and Bikshalu, 2022; Khosravanian et al., 2023). Adaptive time-stepping schemes can adjust the time step dynamically, potentially reducing the need for frequent reinitialization while maintaining numerical stability. Parallel computing and hardware acceleration, such as leveraging graphics processing

units (GPUs), can significantly improve the computational performance of level-set algorithms. However, these approaches may introduce additional complexities or require specialized hardware, potentially limiting their applicability in resource-constrained environments or legacy systems (Srikanth and Bikshalu, 2022; Khosravianian et al., 2023).

Despite these efforts, the challenges associated with contour initialization in level-set segmentation methods remain significant, and no single approach has been able to comprehensively address all the issues simultaneously. The presence of complex backgrounds, sensitivity to initial contours, and computational inefficiencies continue to be active areas of research, with ongoing efforts to develop more robust, accurate, and efficient segmentation algorithms.

5) The Importance of Innovative Solutions for Initialization Problems

Given the limitations of existing approaches, the development of innovative solutions to address the contour initialization problems in level-set segmentation is of paramount importance. Overcoming these challenges can unlock the full potential of level-set methods in various domains, enabling more accurate and reliable image analysis and understanding.

Accurate Segmentation in Complex Environments. Accurate segmentation in complex environments, such as medical imaging or natural scenes, is essential for various applications, including disease diagnosis, treatment planning, object recognition, and autonomous systems (Srikanth and Bikshalu, 2022; Khosravianian et al., 2023). By addressing the challenges posed by complex backgrounds, level-set segmentation methods can provide more reliable and accurate results, enabling better decision-making and enhancing the performance of downstream tasks.

Robustness to Initial Contour Placement. Developing level-set segmentation methods that are robust to initial contour placement can significantly improve the usability and reliability of these techniques (Srikanth and Bikshalu, 2022; Khosravianian et al., 2023). By reducing the sensitivity to initial contours, these methods can minimize the need for manual intervention or prior knowledge, enabling more automated and consistent segmentation results across a wide range of applications.

Real-time or Near-real-time Segmentation. Improving the computational efficiency of level-set segmentation methods is crucial for enabling real-time or near-real-time applications, such as image-guided interventions, autonomous systems, or video processing (Srikanth and Bikshalu, 2022; Khosravanian et al., 2023). By addressing the issues of slow level-set evolution and frequent reinitialization, innovative solutions can unlock the potential of level-set methods in time-critical scenarios, enabling rapid decision-making and enhancing the responsiveness of various systems.

Innovative solutions to the contour initialization problems in level-set segmentation methods can take various forms, including advanced mathematical formulations, novel energy functionals, machine learning-based approaches, or hybrid techniques that combine different strategies (Srikanth and Bikshalu, 2022; Khosravanian et al., 2023). Additionally, leveraging emerging technologies, such as parallel computing, hardware acceleration, or distributed computing, can further enhance the computational efficiency and scalability of these solutions.

Therefore, the Contour Initialization Problems section of the provided document highlights critical challenges associated with level-set segmentation methods, including handling complex backgrounds, sensitivity to initial contours, and computational inefficiencies arising from slow level-set evolution and frequent reinitialization (Srikanth and Bikshalu, 2022; Khosravanian et al., 2023). These challenges can significantly impact the accuracy, robustness, and efficiency of segmentation results, limiting the practical applicability of level-set methods in various domains. While existing approaches have attempted to address these issues, they often introduce additional complexities, require specific assumptions or prior knowledge, or face limitations in terms of generalization or scalability (Srikanth and Bikshalu, 2022; Khosravanian et al., 2023). Consequently, the development of innovative solutions to tackle the contour initialization problems remains an active area of research, with ongoing efforts to develop more robust, accurate, and efficient segmentation algorithms.

By overcoming these challenges, innovative solutions can unlock the full potential of level-set segmentation methods, enabling accurate segmentation in complex environments, reducing the reliance on manual intervention or prior knowledge, and enabling real-time or near-real-time applications (Srikanth and Bikshalu, 2022;

Khosravanian et al., 2023). These advancements can have far-reaching implications across various domains, including medical imaging, object recognition, autonomous systems, and beyond. As imaging technologies continue to evolve and the demand for precise and reliable segmentation grows, the importance of addressing the contour initialization problems in level-set segmentation methods will only increase. Collaborative efforts among researchers, practitioners, and industry partners will be essential in driving innovation and developing practical solutions that can be seamlessly integrated into real-world applications, ultimately enhancing our ability to extract valuable insights from complex and diverse image data.

2.6 Brief Overview of the LIDC Dataset

The LIDC dataset (Armato et al., 2021) is a collection of 1018 lung CT scans that were gathered from a variety of colleges and organizations and are now accessible to the public. In addition to the CT image data, this thesis give handwritten comments for every scan, which were contributed by unnamed radiologists from four different locations. Annotations of this kind are produced with regard to the following categories of structures:

- (i). Lung nodules with a diameter that is more than 3 millimeters at their greatest point.
- (ii). Lung nodules that are smaller than 3 millimeters in diameter at their greatest point.
- (iii). Non-nodule formations with a diameter that is bigger than three millimeters in its biggest dimension.

When it comes to each of these different kinds of structures, the location of the structure is described using picture coordinates, as established by each of the four medical professionals. According to the findings of each of the four physicians, there was no consensus reached on the existence of these buildings or the coordinates that indicated their location. There was no coercive agreement reached about the existence of these buildings or the location of those structures. In this research, the first group of structures that this thesis explore is made up of lung nodules that have a maximum size of less than three millimeters. These nodules have been shown to be associated with an increased risk of developing lung cancer. Each of the same radiologists working at the four separate

sites provides additional comments for this specific type of structure. These annotations include hand-drawn outlines of the nodule borders in the CT scan slices, quantified values for a range of nodule attributes, and a quantified value of the evaluation of the nodule's malignancy at the time that the assessment was performed. All of these annotations can be found in the image file. All of these annotations can be found in the image file. It is very important not to forget that the quantifications are radiological interpretations of the presence of the different physical properties. Keeping this in mind is very vital. This thesis would like to bring attention to the fact that the malignancy quantification is not supported by pathological evidence in the vast majority of the nodules. In spite of this, there is some follow-up information available for a limited number of the nodules that are part of the dataset (but this thesis has not considered this data in our study).

This thesis presents a summary of some of the patient demographic information and scan information in Figures 2.11 and 2.12, respectively. These figures may be seen below. Reviewing the data included inside the DICOM file that was extracted from the LIDC dataset allowed for the collection of this information. There is no information on the subject's age or gender included in any of the 734 scans. The remaining 284 occurrences that have gender information (DICOM Tag ID: 0010,0040) accessible are made up of a 49.3% male population and a 50.7% female population. When age information (DICOM Tag ID: 0010, 1010) is also given, Figure 2.2 reveals that the median age is 61 years old. There is a possibility that this may be a value for the tag. There is never a situation in which information about a person's age is known but not their gender. This is because the two pieces of information are mutually exclusive.

Figure 2.12 is an illustration of the distribution of the spacing of pixels within a slice of the scan (DICOM Tag ID: 0028, 0030) and of the thickness of each slice (DICOM Tag ID: 0018, 0050), with medians of 0.7 mm and 2.0 mm, respectively. These values represent the middle value of each distribution. These values are based on the middle value of the distribution. The units of measurement for each of these dimensions are millimeters.

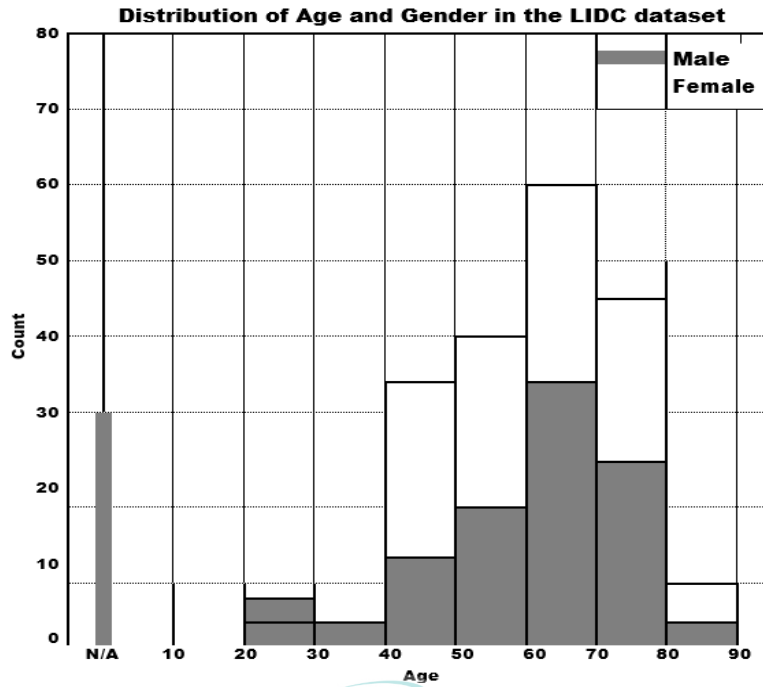


Figure 2.11 Distribution of age and sex in the LIDC Dataset.

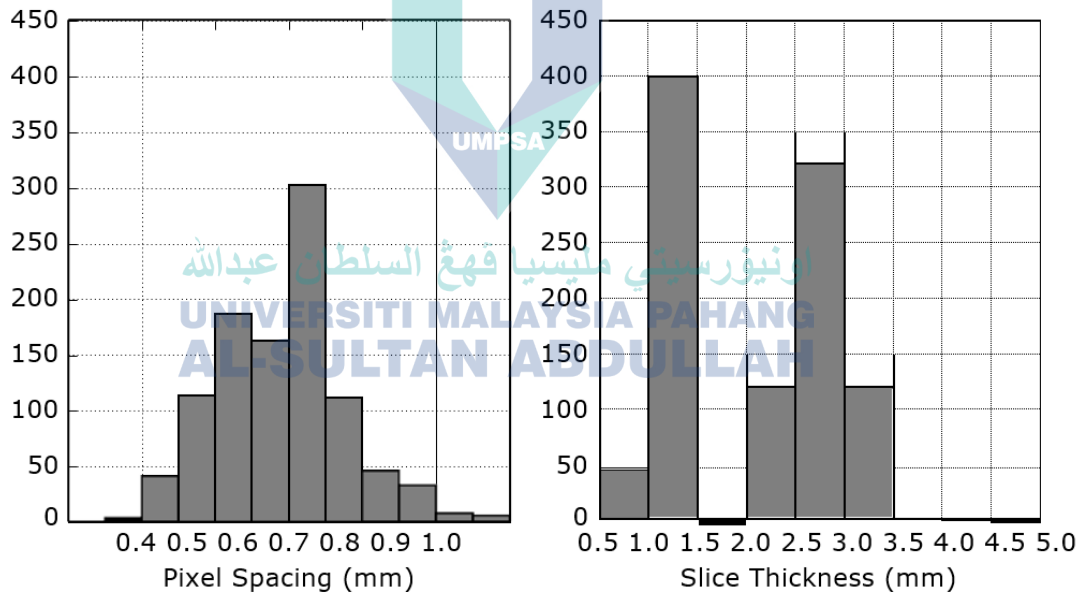


Figure 2.12 The distribution of the spacing of pixels

Figure 2.12 illustrates the distributions of scanner resolutions that were discovered in the LIDC dataset. A distribution of the pixel spacing within the slice can be seen on the left, with a median value of 0.7 millimeters. A distribution of the slice thickness of CT scan image volumes can be seen on the right, with a median value of 2.0 millimeters or less. This number indicates that most of the slices are thinner than this.

There are a few important aspects that are worth addressing in relation to the values and scales that were utilized for the spiculation and lobulation feature values, and this thesis will do so in this section. The first description (McNitt-Gray et al., 2007) of the grading systems that were used to measure these qualities stipulated that a value of 1 would represent extremely spiculated (lobulated), and a value of 5 would represent missing spiculation. This was based on the fact that a value of 1 would represent extremely spiculated (lobulated), and a value of 5 would represent missing spiculation (lobulation). On the other hand, the current scoring system inverts this description (Shen et al., 2019), which means that it gives a score of 1 for a low presence of the trait and a score of 5 for a strong presence of the feature. In other words, the score increases as the degree of presence of the trait increases. In addition, it has been said that there are 399 known examples in the LIDC dataset, and that a subset of 100 of these may have been marked using the conflicting grading techniques for spiculation and lobulation. This is something that has been alleged to have occurred. It has been hypothesized that this may be the case, but it has not been shown (Shen et al., 2019). This data was extracted from a previously published article, which assigned a value of 1 to indicate a weak presence of the characteristic and a value of 5 to indicate a significant presence of the feature. In addition, it has been said that there are 399 known examples in the LIDC dataset, and it is possible that a subset of one hundred of these cases were marked using the conflicting grading techniques for spiculation and lobulation. This is something that has been speculated about (Shen et al., 2019). This information was taken from a publication that was just published. It is not feasible to tell with absolute confidence which one hundred of the three hundred and ninety-nine examples may have had ratings that were assigned inconsistently (i.e., with a 1 as high and a 5 as low). As a result of this, this thesis has made the decision not to include these 399 cases in our study and analysis. Nevertheless, this thesis has noted that there are a number of studies that have been published that incorporate these physician-quantified labelings of spiculation and lobulation from the LIDC dataset. These labelings come from the dataset. However, none of these articles discuss the possibility of mislabelings in the dataset, nor do they mention the exclusion of these 399 cases from their respective studies. Neither of these topics is brought up in any of the articles (Horsthemke et al., 2008; Opulencia et al., 2011; Raicu et al., 2010;

Wiemker et al., 2009; Wiemker et al., 2009b; Zinovev et al., 2009; Opulencia et al., 2011; Raicu et al., 2010; Zinovev et al., 2011).

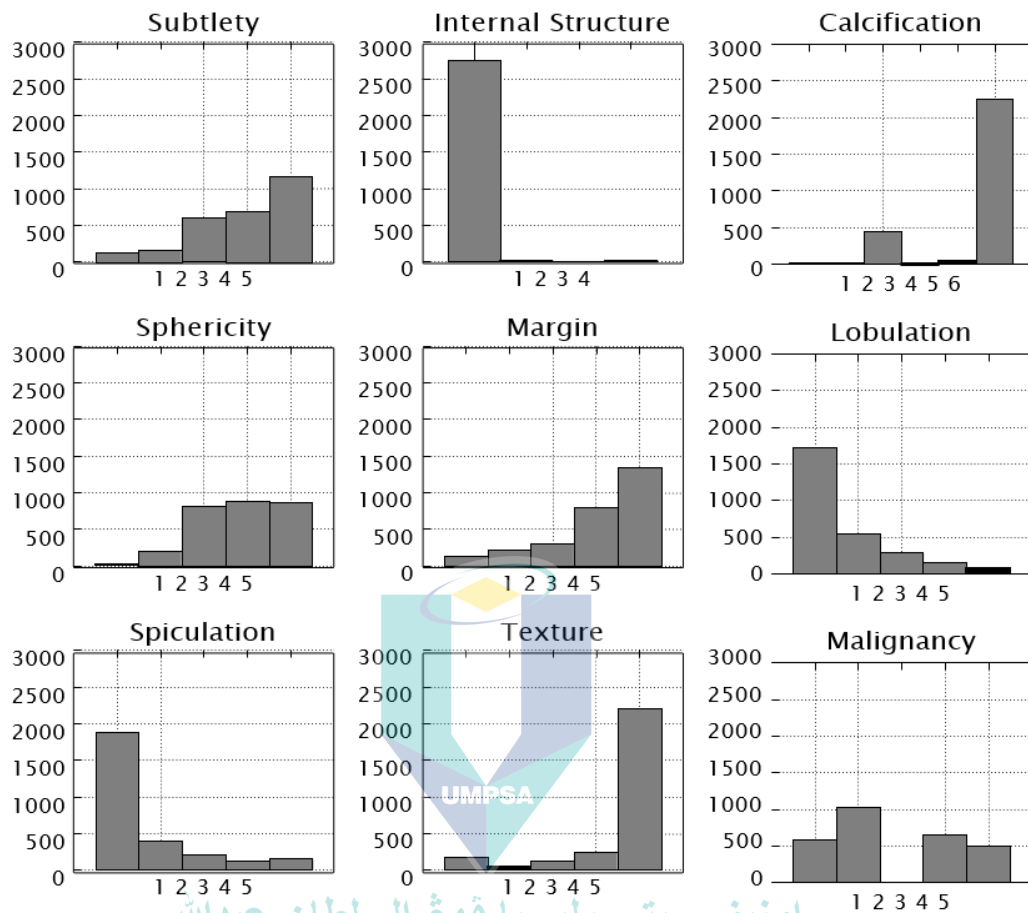


Figure 2.13: Distribution of annotation values for image features and malignancy. Note the excluded bin for the indeterminate malignancy value of 3

After removing these 399 instances from the calculation, this thesis are left with 4384 nodule annotations that have been labeled in the same manner throughout. In order to eliminate uncertain circumstances, the total number of annotations that were used was cut even further from 4384 down to 2817 (as described in the following section). The degree of consensus reached by the four individuals who annotated a nodule as belonging to the first kind of structure determined the number of annotations that were given to each nodule, which might have ranged from one to four in total. Since the physical nodules do not have a universally unique identification among the numerous annotations, it is difficult to tell which annotations correspond to the same physical nodule in a scan without rigorous visual examination. This is because a scan contains a large number of annotations. Because of this, it is very difficult to identify which annotations on a scan

relate to the same physical nodule. By comparing the coordinates of the annotations with one another and seeing where they overlap, it is able to approximately establish which annotations relate to the same nodules using an algorithm. On the other hand, in order to identify whether or not several annotations may in fact be referring to the same nodule, this procedure requires making certain decisions that are fairly arbitrary. For instance, One would have to decide at what percentage of overlap, or at what average distance between annotation coordinates, a number of annotations would be deemed to correspond to the same physical nodule. This would be a choice that would have to be made. This decision would need to be made before a physical nodule could be located. Because of these factors, this thesis consider each annotation to be its own individual sample inside our dataset in Figure 2.13.

To be more specific, this thesis take into account the quantitative qualities to be random vectors, which are represented by the letter X, and the malignancy values to be random variables, which are represented by the letter Y. In addition, this thesis consider every annotation to be a distinct draw taken from the combined distribution, which is symbolized by the letter Y. (X, Y). As a consequence of this, it is feasible that many samples from different datasets relate to the same physical nodule. Yet, this thesis still regard these occurrences as distinct manifestations of the random quantity (X, Y), where the source of randomness is noise (for example, as a result of inadvertent mislabeling) and the natural changes of the quantified feature values. To phrase it another way, this thesis consider each of these cases to be a unique manifestation of the random amount. To put it another way, this thesis consider every one of these instances to be a unique occurrence of the random quantity (e.g., due to varying annotator experience and training). As a direct result of this, a viewpoint on the facts that is consistent throughout may be established. After that, the statistical learning algorithms will model the conditional probability distribution of malignancy, if there is one. which is symbolized by the symbol $P(Y | X)$, based on the quantified feature values. This will take place once the feature values have been characterized. In the next section, this thesis will talk about the methodology in addition to detailing the two statistical learning approaches that this thesis use here.

2.7 The Summary

This chapter presents a literature review on image segmentation methods applied to lung cancer detection in computed tomography (CT) images. It begins by introducing image segmentation and its importance for medical image analysis and interpretation. The manual, semi-automatic, and fully automated segmentation approaches are discussed. The challenges of medical image segmentation are outlined, including complexity of structures, noise, blurring, variability across images and patients. An overview of major segmentation methods is then provided, categorized as boundary-based (using edge detection), thresholding, region-based (region growing, splitting and merging), statistical learning (classifiers, clustering), random field models, fuzzy set theory, partial differential equations (PDEs), active contours, level sets, and deep learning. Key papers utilizing PDEs and active contour models for lung nodule segmentation are highlighted as most relevant to the thesis focus. Public datasets for algorithm training and testing are noted, with a detailed summary of the LIDC dataset used later in this work. The lung nodule annotation process in LIDC is described, along with the exclusion of uncertain cases, leaving 2817 useable nodule annotations. The chapter concludes with a discussion of remaining challenges and limitations of current segmentation methods, motivating the development of the proposed hybrid PDE and deep learning approach to improve lung nodule detection performance. Overall, this chapter provides a comprehensive overview of medical image segmentation, lung CT analysis, relevant datasets, and gaps in existing methods to set the stage for the novel contributions of this thesis.

CHAPTER 3

METHODOLOGY

3.1 Introduction

The most basic and essential component of image processing is image segmentation, which involves the removal of elements from a picture that are of importance to the viewer. After many decades of study, development, and invention in the area, image segmentation approaches that are based on a range of different theories have finally been developed. In recent years, a key development in the field of image segmentation has been the rise of the active contour model as a strategy for separating images. This model uses the variational approach in addition to the level-set method as its foundation. This example shows the advantages of using a method that processes photos by employing partial differential equations. Its major concentration is on the idea of dynamic evolution, and it has had a considerable influence on the research into various methods for the segmentation of pictures. This chapter proposes the CER model as a solution to the problems that the Chan-Vese and RSF models have, which include sensitivity to the initialization contours, poor noise immunity, and an inability to segment grayscale images. In order to implement this solution, the CER model makes use of a local entropy weight, convolutional neural networks, and reinforcement learning. All of these techniques are combined with reinforcement learning. The suggested technique was designed using the scale adaptive fast level-set image segmentation method, the adaptive multilayer level-set image segmentation method, and the hybrid level-set image segmentation method based on kernel metric.

3.2 Scale Adaptive Fast Level-Set Image Segmentation Method

Through offset correction and level-set method, it can correctly segment the image with gray inhomogeneity, and obtain better segmentation performance than the local area-based method. However, it uses a finite difference strategy in its numerical

implementation, and the time step needs to meet the CFL (Courant-Friedrichs-Lewy) condition (Weickert et al., 1998) to ensure the stability of level-set evolution. Therefore, it must be adopted A small time step leads to slow convergence and low segmentation efficiency. In addition, it uses local area information to estimate the offset field, This may quickly settle into a solution at a local minimum and is sensitive to the location of the starting contour. In addition, the scale parameter of the clustering kernel function is used by this sort of procedure in order to exercise control over the magnitude of the local region. The selection of the scale parameter affects the estimation accuracy of the migration field, and these methods use fixed scale parameters, which seriously affect their practical application.

This approach presents a rapid leveling set method with an adjustable scale in order to tackle the challenges that have been outlined above (Fast Level Set Method with Adaptive Scale Parameter, FLSAS). At the beginning, in order to build the energy function, a pressure function that is determined by regional information is suggested in accordance with the gray, inhomogeneous picture model and applied. After that, a quick segmentation of the gray inhomogeneous picture and an estimate of its offset field are carried out with the help of approaches that minimize the energy functional and provide a rapid numerical realization. In addition, a brand new strategy for initializing the migration field is presented as a means of enhancing the algorithm's resilience in relation to the initial contour. In addition, a clustering kernel function with an adaptive scale operator is constructed by making use of the local variance of the picture. This operator is able to properly estimate the image's offset field. The suggested technique for segmentation is first provided in the form of a two-phase level-set segmentation, and it is subsequently expanded to include support for many phases of segmentation.

3.2.1 Gray Uneven Image Model

Gray unevenness is usually described as a smooth spatial variation function (Vovk et al., 2007), called an offset field, which changes the gray level of the original gray uniform image. The uneven gray scale image can be described as the addition or multiplication of the offset field and the original image. Because it is consistent with the uneven sensitivity of the receiving device, the product model is usually used to model the gray uneven image. The noise of the uneven grayscale image mainly includes the

scanning noise caused by the imaging device and the noise of each target area itself, and usually only one kind of noise is modeled.

Since the scanning noise has nothing to do with the unevenness of the grayscale of the image, the first model of the uneven grayscale image can be obtained by modeling the scanning noise:

$$I = bJ + n_1 . \quad 3.1$$

Among them, I is the image gray level, b is the offset field, J is the original image, and n_1 is assumed to be Gaussian noise.

The noise n_2 of each target area is modeled to obtain the second gray-scale uneven image model:

$$I = b(J + n_2) . \quad 3.2$$

Among them, n_2 is assumed to be Gaussian noise.

Through logarithmic transformation, the product model is converted to an additive model, and the third type of gray inhomogeneous image model can be obtained:

$$\log I = \log b + \log J + n_3 . \quad 3.3$$

Among them, n_3 is still assumed to be Gaussian noise.

These three models are widely used to model uneven grayscale images. In this study, this thesis use the first model to describe gray-scale uneven images. Because the logarithmic transformation serves an important purpose in converting the product model of gray-level inhomogeneity to an additive model, which is more amenable to processing and analysis (Li et al., 2011; Vovk et al., 2007; Wang et al., 2015). Specifically, gray-level inhomogeneity arises due to a smooth spatial variation function called the offset field $b(x)$, which modulates the true image $J(x)$ to generate the observed image $I(x)$. A common model is the product model $I(x) = b(x)J(x)$, representing the pixel-wise multiplication of the offset field and true image. However, this product model poses

difficulties for image processing algorithms due to its nonlinearity. The logarithmic transformation provides a clever way to convert this into a more tractable additive model (Vovk et al., 2007): $\log(I(x)) = \log(b(x)J(x)) \implies \log(b(x)) + \log(J(x))$. Here, the multiplicative inhomogeneity has been converted into an additive inhomogeneity $\log(b(x))$, which is typically easier to estimate and correct for using methods like low-pass filtering. The log-transformed image can then be processed more effectively.

Several researchers have utilized this logarithmic transformation technique in developing algorithms for gray-level inhomogeneity correction. Li et al. (2011) applied it in their formulation of a Local Intensity Clustering (LIC) model for image segmentation. By converting to an additive model, they were able to apply clustering techniques more readily to group image pixels and estimate the offset field. Vovk et al. (2007) also used the logarithmic transform similarly to derive an effective correlation mapping algorithm for correcting inhomogeneity in MRI images. More recently, Wang et al. (2015) employed the logarithm conversion as a preprocessing step in their bias field estimation method using a pulse-coupled neural network. The additive model enabled easier integration of their neural network architecture for offset field estimation. The authors reported improved performance over methods operating directly on the product model.

The logarithmic transformation plays an important role in converting the multiplicative gray-level inhomogeneity into an additive inhomogeneity. This additive model enables easier application of linear filtering techniques and clustering/classification algorithms for estimating the offset field. It transforms the problem into a more convenient form for analysis and processing. By using this transformation, the proposed method can also leverage a range of techniques like clustering and low-pass filtering to effectively correct for the bias field and thereby enable accurate image segmentation.

There are many image enhancement techniques that can be applied to improve uneven grayscale images, such as histogram analysis, contrast stretching, filtering, and local adaptive filtering (Gonzalez & Woods, 2018; Pratt, 2007). However, this study utilizes a logarithmic transformation approach due to its specific advantages for enabling more effective segmentation algorithms to be applied.

The key motivation is that the logarithmic transform converts the multiplicative gray-level inhomogeneity into an additive inhomogeneity model (Li et al., 2011; Vovk et al., 2007). This additive model is more convenient and amenable to processing using methods like clustering, thresholding, and low-pass filtering to estimate and correct for the intensity inhomogeneity or bias field. As Li et al. (2011) discuss, the product model $I(x) = b(x)J(x)$ is problematic for segmentation algorithms due to its nonlinearity. By applying $\log(I(x)) = \log(b(x)) + \log(J(x))$, the multiplicative bias field is transformed into an additive bias that is easier to model and correct. This then facilitates segmentation using approaches like their Local Intensity Clustering method. Vovk et al. (2007) also utilized the logarithmic transformation to convert the product model into an additive one, allowing application of correction techniques like homomorphic filtering on the log-transformed image. This greatly improved the ability to compensate for inhomogeneities compared to directly filtering the product model image. More recently, Wang et al. (2015) employed the logarithmic transform similarly to convert the model into a more convenient additive form that enabled easier integration of their pulse-coupled neural network architecture for bias field correction.

Thus, the key advantages of using the logarithmic transform are: 1) It converts the model into a more mathematically convenient, additive form; 2) This additive form allows application of linear filtering, clustering, and classification techniques for bias estimation and correction; 3) Correcting the bias facilitates more accurate segmentation of the image into distinct regions. Without this transform, directly applying enhancement techniques on the product model image is prone to suboptimal performance and segmentation inaccuracies due to the multiplicative gray-level nonuniformity. The logarithm conversion elegantly circumvents this problem.

3.2.2 Scale Adaptive Fast Level-Set Segmentation Algorithm

This section first proposes a pressure function based on regional information based on the LIC model, and uses a fast numerical implementation strategy to quickly segment the gray-scale uneven image. Next, in order to make the algorithm more resistant to changes in the initial contour, an innovative way for initializing the migration field is provided. In addition to this, the construction of a clustering kernel function with an adaptive scale operator is carried out.

The problem of uneven gray levels in images poses significant challenges for segmentation algorithms. As discussed in Chapter 3, the author applies a logarithmic transformation technique to convert the multiplicative gray level inhomogeneity into an additive inhomogeneity model (Section 3.2.1). However, solely utilizing an existing approach like logarithmic transformation has limitations that need to be addressed.

Several researchers have applied logarithmic transforms for gray level inhomogeneity correction (Li et al., 2011; Vovk et al., 2007; Wang et al., 2015). But a key research gap is that these methods typically treat the correction as a pre-processing step and do not tightly couple and optimize it jointly with the segmentation algorithm. As Pham et al. (2000) discuss, independent bias correction and segmentation steps can lead to suboptimal performance. To address this gap, the author proposes an integrated optimization framework that simultaneously estimates the inhomogeneity offset and performs segmentation by iteratively minimizing an energy functional (Section 3.2.2). Instead of using logarithm transform as a fixed pre-processing, it becomes an integral part of the variational level set formulation.

Specifically, the proposed method introduces a bias field variable $b(x)$ directly into the energy functional and alternates between optimizing the level set function ϕ and estimating b . The offset field estimation utilizes the logarithmic transformation model $\log(I(x)) = \log(b(x)) + \log(J(x))$ within the energy minimization framework. This enables tighter coupling between bias correction and segmentation. Moreover, the method uses a scale-adaptive clustering technique to estimate $b(x)$, avoiding pre-fixed approaches like low-pass filtering which may not effectively capture variations. The cluster-based offset modeling coupled with integrated optimization improves accuracy.

While a logarithmic transform can help convert multiplicative inhomogeneity into an additive form, limitations exist when used as a pre-processing step. The proposed integrated optimization framework addresses this by making bias modeling an adaptive, optimized part of level set energy minimization. This achieves tighter coupling and improves segmentation accuracy for uneven gray level images.

In addition, while logarithmic transformation is a useful technique that can convert multiplicative inhomogeneity into an additive model, utilizing it purely as a pre-

processing stage has limitations. As demonstrated by Pham et al. (2000), typical strategies of performing bias correction separately prior to segmentation can result in suboptimal performance.

The key innovation in the proposed method is the integration of bias field modeling and correction within the segmentation formulation itself, rather than treating it as an independent pre-processing step. Specifically, a bias field variable is introduced directly into the energy functional optimized through the level set framework. By iteratively alternating between estimation of the offset field and evolution of the level set contour, the technique achieves tighter coupling between inhomogeneity correction and segmentation.

Incorporation of the logarithmic transform within this integrated optimization framework allows it to adaptively estimate and compensate for intensity variations during the segmentation process, rather than applying it in a pre-determined manner. This addresses the limitations of conventional approaches that treat correction and segmentation independently.

In this section, it introduces a novel strategy for initializing the migration field $b(x)$ to improve robustness of the level set segmentation to the initial contour. The key steps of this technique are:

Preprocess the input image $I(x)$ using median and bilateral filtering to obtain $I_1(x)$.

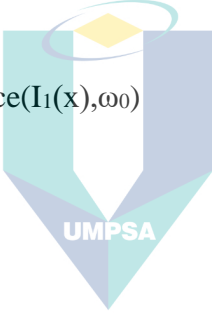
Estimate the object boundary C_L using Laplacian of Gaussian edge detection on $I_1(x)$.

Define the smooth region Ω_s as pixels sufficiently away ($>\omega_0$) from the edge C_L .

Compute the local variance $D(x)$ for each pixel in the smooth region Ω_s using neighboring squares of size $(2\omega_0+1) * (2\omega_0+1)$.

Initialize the migration field as $b_0(x) = K * I_1(x) / N_0$, where K is a kernel function and N_0 is the average gray level of $I_1(x)$.

As Li et al. (2011) discuss, the key idea is to use the spatial variation trends in the image itself to approximate the offset field, since inhomogeneity induces smooth changes in gray levels. The local variance in smooth regions ignores edges and captures this variation. The algorithm can be outlined as follows:

| | |
|---|--|
| <p>Input: Image $I(x)$</p> <p>Output: Initialized migration field $b_0(x)$</p> <p>1: $I_1(x) = \text{Preprocess}(I(x))$</p> <p>2: $C_L = \text{EdgeDetect}(I_1(x))$</p> <p>3: $\Omega_s = \{x : \text{dist}(x, C_L) > \omega_0\}$</p> <p>4: for each x in Ω_s do</p> <p>5: $D(x) = \text{LocalVariance}(I_1(x), \omega_0)$</p> <p>6: end</p> <p>7: $N_0 = \text{Mean}(I_1(x))$</p> <p>8: $b_0(x) = \text{Filter}(I_1(x)/N_0)$</p> |  <p>اونيورسيتي مليسيا قهغ UNIVERSITI MALAYSIA PAHANG</p> |
|---|--|

This initialization provides a better starting point for the migration field compared to constant initialization, improving convergence and robustness. The model is still iteratively refined after initialization.

3.2.3 Area-based Pressure Function

The LIC model is a classic K-means clustering offset correction level-set segmentation method (Li et al., 2011), which is based on the gray inhomogeneous image model of equation (3.1). The original image J makes more specific assumptions:

Assumption 1. The offset field b changes slowly in the image domain Ω ;

Assumption 2. In each disjoint area, J can be approximated as a constant, that is, for $\chi \in \Omega_i$, $J(\chi) \approx c_i$ holds, where $\{\Omega_i\}_{i=1}^N$ is the partition of the image domain Ω .

Let χ be any pixel in the image domain, within the circular neighborhood $O_\chi \triangleq \{y: |y - \chi| \leq \rho\}$ with a radius of ρ , the offset field b is approximately unchanged. Therefore, the circular neighborhood O_χ can be divided into N clusters with cluster centers $b(\chi)c_i$, $i = 1, 2, \dots, N$. Using K-means clustering to classify the image and expand it to the entire image domain, the energy term of LIC can be obtained as:

$$E(\phi, c, b) = \int \left(\sum_{i=1}^N \int K(\chi - y) |I(y) - b(\chi)c_i|^2 M_i(\phi(y)) dy \right) d\chi . \quad 3.4$$

In Equation 3.4, $K(\chi - y)$ refers to the Gaussian kernel function centered at pixel y with scale parameter σ , as defined in Equation 3.5. This kernel function is used for density estimation at each pixel. $I(y)$ refers to the image gray level intensity at pixel y . The key idea is that the energy term in Equation 3.4 uses clustering and the kernel function K to model the image intensity distribution locally around each pixel, taking into account the offset field $b(\chi)$. To improve robustness to initial contour, the method proposes a new strategy to initialize the offset field $b(\chi)$ based on the image gray level variation trends. This initialization provides a better starting point for $b(\chi)$ compared to constant initialization in traditional methods. With proper offset field initialization, the evolving contour can progress stably towards the object boundaries even from different initial contours. Therefore, the kernel-based clustering model coupled with the proposed offset field initialization technique helps improve robustness to initial contour placement compared to standard methods. The contour evolution depends less on initial placement and can converge to correct segmentation from varied starting locations.

Among them, $M_i(\phi)$ is the membership function, and the Gaussian kernel function $K(\cdot)$ is defined as:

$$K(u) \begin{cases} \frac{1}{a} e^{-u^2/(2\sigma^2)}, & |u| \leq 2\sigma \\ 0, & \text{other} \end{cases} . \quad 3.5$$

Among them, a is the normalization constant and σ is the standard deviation (or scale parameter) of the kernel function.

When $N = 2$, the gradient descent flow equation of the energy functional in formula (3.4) is:

$$\begin{aligned} & \frac{\partial \phi}{\partial t} \\ &= -\delta(\phi) \left(\int_{\Omega} K(\chi - y; |I(y) - b(\chi) c_1|^2 - |I(y) - b(\chi) c_2|^2) d\chi \right) \quad 3.6 \\ &= -\delta(\phi) \left(2I(K * b)(c_2 - c_1) + (K * b^2)(c_1 - c_2)(c_1 + c_2) \right). \end{aligned}$$

Since the convolution operation can be regarded as the process of obtaining the weighted average, and according to the assumption 1 in the LIC model, this thesis can obtain $|K * b^2 - (K * b)^2| < \xi$, where ξ is a sufficiently small positive number. Therefore, if this thesis assume $K * b^2 \approx (K * b)^2$, the above formula can be rewritten as:

$$\frac{\partial \phi}{\partial t} \approx \delta(\phi) \alpha \left(I - (K * b) \left(\frac{c_1 + c_2}{2} \right) \right). \quad 3.7$$

Among them, $\alpha = 2(K * b)(c_1 - c_2)$.

It can be seen that when c_1 and c_2 are fixed, the LIC model mainly drives zero level-set based on the difference between the image gray level I and $u = (K * b)(c_1 + c_2)/2$. Perform evolution to achieve image segmentation. Similar to the model in the literature (Wu and He, 2015), this thesis propose a region-based pressure function:

$$\begin{aligned} & S(\chi) \\ &= I(\chi) - u(\chi) \quad 3.8 \\ &= I(\chi) - (K * b) \left(\frac{c_1 + c_2}{2} \right). \end{aligned}$$

It can be seen from the above formula that $\mu(\chi)$ represents the lower limit of the gray level of the target or background of the gray uneven image at each pixel, and the proposed pressure function $S(\chi)$ can drive the contour to the gray value. The boundary of the area larger than μ moves to realize the segmentation of the gray-scale uneven image.

Using the above formula to construct a new energy functional is:

$$E(\phi, c, b) = - \int \left(I(\chi) - (K * b) \left(\frac{c_1 + c_2}{2} \right) \right) M_1(\phi(\chi)) d\chi . \quad 3.9$$

Similar to the LIC model, the optimal c and b are:

$$c_i = \frac{\int (K * b) I M_i(\phi) d\chi}{\int (K * b)^2 M_i(\phi) d\chi}, i = 1, \dots, N ; \quad 3.10$$

$$b = \frac{(IJ^{(1)}) * K}{J^{(2)} * K}, J^{(1)} = \sum_{i=1}^N c_i M_i(\phi), J^{(2)} = \sum_{i=1}^N c_i^2 M_i(\phi) . \quad 3.11$$

Among them, $M_1(\phi) = H(\phi)$, $M_2(\phi) = 1 - H(\phi)$, $H(\phi)$ is defined as:

$$H(\phi) = \begin{cases} 1, & \phi > 0 \\ 0, & \text{other} \end{cases} . \quad 3.12$$

The gradient descent flow equation of the energy functional in formula (3-9) is:

$$\frac{\partial \phi}{\partial t} = \delta(\phi) \left(I - (K * b) \left(\frac{c_1 + c_2}{2} \right) \right). \quad 3.13$$

Minimizing the energy functional in equation (3.9) will prompt the active contour to move to the boundary of the image region with a gray value greater than u , while ensuring that $c_1 > c_2$. The proposed model can obtain a gradient descent flow equation similar to the LIC model. The essence is to simplify the LIC model.

The proposed region-based pressure function in this study is similar to the model presented by Wu and He (2015). However, there are some key differences in the method compared to their approach. For formulation of the energy functional, Wu and He (2015)

minimize an energy with global intensity fitting term only. This study proposes a simplified energy with region-based pressure function term. For Offset field estimation, Wu and He (2015) use zonal average filtering to estimate offset field. This study uses clustering-based estimation adapted via scale parameter. For contour evolution, Wu and He (2015) use traditional level set PDE for contour evolution. This study uses a fast numerical scheme with multiple iterations between offset estimation. For Initialization, Wu and He (2015) use constant initialization of level set function. This study presents a new initialization technique using image gray level trends. While the region-based pressure function is similar in spirit to Wu & He's model, there are significant differences in the overall energy functional, offset field estimation, contour evolution, and initialization. The proposed modifications help improve efficiency and robustness of the segmentation. The key novelty lies in the fast numerical scheme and integrated offset field estimation.

3.2.4 Offset Field Initialization

For any pixel $\chi \in \Omega$ in the image, the LIC model initializes the offset field to $b(\chi) = 1$. The LIC model will eventually degenerate into a CV model at the very first iterative operation that is performed. The CV model is a method for segmentation that is dependent on global information and is unable to handle grayscale pictures with uneven tones. As a consequence of this, after the first iterative operation, the zero level can be located quite some distance from the real boundary of the target, which would lead to segmentation problems. In order to remedy this deficiency, this thesis has come up with a novel approach to the initialization of the offset field.

In level set methods, the contour delineating the segmentation is represented implicitly as the zero level set of a higher dimensional function $u(x,y)$. In traditional methods, the offset field $b(x)$ is often initialized to a constant (e.g. $b(x) = 1$). With this constant initialization, after the first iteration of gradient descent on the energy, the zero level set of $u(x,y)$ can evolve and move significantly from its initial position. Since the initial constant offset field estimate is inaccurate, the zero level set after the first iteration may end up quite far from the real object boundary. This then leads to poor convergence and incorrect segmentation, as the contour is starting too far away from the true edges we

want to delineate. In contrast, the proposed method in the paper initializes $b(x)$ based on image gray level trends to better approximate the true offset field. This helps keep the zero level set after the first iteration much closer to the real boundaries compared to constant initialization. The key advantage is that by preventing the zero level set from deviating too far after the first step, the proposed initialization improves convergence and segmentation accuracy. Therefore, with constant offset field initialization, the zero level set can move significantly away from the real boundary after the first iteration, leading to poor convergence. The proposed initialization prevents this issue by keeping the contour closer to the true edges.

In each target area of the image, the image offset field causes the image grayscale to change. In this way, the change trend of the image gray level is similar to the change trend of the offset field. Therefore, by extracting the image gray change trend, the offset field of the image can be better estimated. According to the gray inhomogeneous image model in equation (3.1) and the assumption 1 in the LIC model, this thesis initialize the offset field as:

$$b_0 = K * (I / N_0) . \quad 3.14$$

Among them, N_0 represents the average gray value of the image. It can be seen that the proposed initial offset field can approximate the image offset field and improve the robustness to the initial contour.

In (3.14), K is the smoothing kernel (e.g. Gaussian) and refers to the kernel function used for density estimation and smoothing. It is typically implemented as a Gaussian kernel. I is the image intensity at pixel x and refers to the input image intensity function $I(x)$. And b_0 refers to the initial estimate of the offset field, denoted as $b_0(x)$, that is computed using Equation 3.14. N_0 is the average intensity of the image. So, K smooths the image intensity, and $I(x)$ provides the intensity value at each pixel. Dividing by the average intensity N_0 normalizes the values. $b_0(x)$ is then the smoothed, normalized intensity which approximates the offset field.

The offset field introduces spatial variations in gray levels across the image, causing the image intensity to change smoothly between different regions. These

intensity changes represent important information about the underlying offset field. Specifically, areas with similar offset values will have similar intensity changes, while transitions between offset regions will exhibit more rapid gray level changes. Thus, the spatial trends and transitions in image intensity, as characterized by gradients and local variance, provide cues to the underlying offset field structure. By analyzing the image's intensity change patterns, the offset field can be approximated by extracting information about where intensity is changing rapidly versus remaining relatively homogeneous. In essence, while the offset field is not directly observable, its structure is reflected in the image intensity variations it introduces. By intelligently analyzing the image's gray level change trends using techniques like local variance, we can estimate a good approximation of the latent offset field.

The image after offset correction is:

$$J_0 = \frac{I}{b_0} = N_0 \frac{I}{K * I} \quad 3.15$$

J_0 refers to the image after approximated offset correction, calculated as: $J_0(x) = I(x) / b_0(x)$. Where, $I(x)$ is the original input image $b_0(x)$ is the initial estimate of the offset field from Equation 3.14. So $J_0(x)$ represents the image after dividing out the estimated offset field $b_0(x)$. The intention is that $J_0(x)$ will have reduced intensity inhomogeneity compared to the original $I(x)$. The form (N_0/K) in Equation 3.15 is likely a typo or mistake in the text. It should simply be: $J_0(x) = I(x) / b_0(x)$. To summarize: $J_0(x)$ is the image after initial offset correction using $b_0(x)$. Dividing by $b_0(x)$ aims to reduce inhomogeneity and normalize intensity. The $((N_0/K)$ term in the text is likely an error.

Generally, the gray scale changes of the target boundary area image are large, and the gray scale changes of other areas are small. Near the target boundary, the corrected image gray level J_0 will be greater than or less than N_0 , while in other areas it is approximately equal to N_0 . The boundary area is generally much smaller than the entire image field. Therefore, for the initial contour at any position, the proposed initial offset

field can ensure $(c_1 + c_2)/2 \approx N_0$. In this way, in the first time In the iteration, the pressure function can be expressed as:

$$S = I - K * (K * I) . \quad 3.16$$

Where, K is a Smoothing kernel. I(x) is Input image intensity. $(K * I)$ is Smoothed image intensity. S(x) is a pressure function based on difference between original and smoothed intensity. The key idea is that S(x) will have larger values at image edges and transitions, thereby providing an edge-driving force for the level set evolution.

The pressure function only has a greater driving force in areas where the gray level changes greatly, as is seen in Figure 3.1 (d). Since the grayscale of the picture of the actual boundary region of the target often shifts quite a little, it is possible to segment the image of the real boundary area of the target first. The level-set function has developed to the point that it now encompasses the whole of the picture domain. As a result, the migration field initialization strategy that has been provided has the potential to increase the algorithm's resilience to the starting contour location.

3.2.5 Adaptive Scaling Operator

In the level-set segmentation approach that is based on K-means clustering, it is expected that the picture in the local neighborhood is roughly uniform. The size of each local neighborhood is controlled by the scale parameter of the clustering kernel function. In most cases, the scale parameter has to have an adequate value chosen for it in accordance with the amount of grayscale unevenness present in the picture. (Li et al., 2011). However, the real area of each target cannot be obtained in advance, and it is difficult to measure the degree of grayscale unevenness of the image. According to the gray inhomogeneity image model of equation (3.1) and the assumptions 1 and 2 in the LIC model, it can be obtained that the gray inhomogeneity causes the smooth area of the image gray to change slowly in each target area, and the target boundary. The gray level change at the position is mainly caused by the image itself, and the change is drastic. The key idea is that at the boundary between two image regions, there is typically a more rapid transition in gray levels compared to within homogeneous regions. For example,

consider an image with a bright object on a dark background. At the object's edges, the intensity changes quickly from bright to dark over a short distance. This rapid spatial change in intensity is caused inherent edges in the image itself, rather than being due to the smooth intensity variations from the offset field. In contrast, within a homogeneous region (e.g. fully inside the object or background), the intensity changes more slowly and smoothly due to the offset field variations. So, at region boundaries in the image, there are inherently rapid gray level changes over a short distance. This is intrinsic to the image content rather than the smooth offset field effects. Within homogeneous regions, intensity changes more slowly due to offset field variations. Therefore, this thesis removed the boundary region, use the image local variance information of the smooth region in each target to measure the degree of local gray-scale inhomogeneity of the image, and use the image local variance to design an adaptive scale operator for the clustering kernel function.

Firstly, the image is preprocessed by median filtering and bilateral filtering to reduce the influence of noise. The preprocessed image grayscale is I_1 . Then, it is necessary to obtain a smooth area Ω_s without the true boundary of the target. Using the Laplace operator to detect the boundary of the target, the smooth area Ω_{s_0} can be obtained as:

$$\Omega_{s_0} = \{\chi \mid |F(\chi)| < T \& \chi \in \Omega\} \quad (3.17)$$

Among them, $F = K_1 * I_1$, $T = \tau \cdot \min(\max|F|), T_0)$, τ is a constant, T_0 is a constant threshold, K_1 represents a Laplacian with eight neighborhoods.

The greater the change in the image gray level of the local area, the greater the absolute value of F , and vice versa. The image gray scale changes slowly in the smooth area, while most of the pixels in Ω_{s_0} belong to the smooth area, and the offset field changes slowly in the image domain. Therefore, the value of F in Ω_{s_0} approximately obeys Gaussian distributed. In order to further eliminate the boundary and noise area, remove the pixels far away from the mean value in Ω_{s_0} to obtain a more accurate smooth area Ω_s as:

$$\Omega_s = \{\chi | \max(c_F - 1.5\sigma_F, -T) < F(\chi) < \min(c_F + 1.5\sigma_F, T)\} \& \chi \in \Omega_{s_0}\} . \quad 3.18$$

In 3.17, Ω_{s_0} - This refers to an initial estimate of the smooth image region, without edges or noise. $F = K_1 * I_1$ - This is the result of applying a Laplacian filter K_1 to the preprocessed image I_1 . $T = \tau * \min(\max|F|)$ - A threshold value calculated based on the Laplacian response. So Ω_{s_0} excludes pixels where the Laplacian response $|F|$ exceeds the threshold T , indicating likely edges. In 3.18, $F(x)$ - The Laplacian response at pixel x , $F = K_1 * I_1$. c_F - The mean value of $F(x)$ in Ω_{s_0} . σ_F - The standard deviation of $F(x)$ in Ω_{s_0} . Ω_s - The final estimated smooth region after excluding any high Laplacian values far from the mean c_F . $F(x)$ measures edge strength via the Laplacian. Pixels with $|F(x)|$ much above the mean c_F are excluded to get the final smooth region Ω_s . This removes any remaining edges or noise from the smooth region.

Among them, c_F and σ_F represent the mean and standard deviation of F in Ω_{s_0} , respectively.

After obtaining the smooth area Ω_s , calculate the $(2\omega_0 + 1) \times (2\omega_0 + 1)$ square neighborhood $R^{\omega_0}(\chi)$ as the center in the image I_1 . The local variance of χ is $D(\chi)$. If there is a larger degree of unevenness in the picture gray, then there will be a bigger variation in the local region. As a result, the scale parameter will need to be decreased in order to satisfy the assumption that the image in the immediate vicinity is relatively uniform. As a result, the scale parameter is inversely proportional to the local variance of the image, which is used to measure the degree of the overall grayscale inhomogeneity of the image. This is because the mean value of the local variance of the image in the smooth area is used to determine how much grayscale inhomogeneity there is in the image. The kernel function's adaptive scaling operator, which was constructed, is as follows:

$$\sigma_b = \frac{\beta}{\sqrt{c_D}} . \quad 3.19$$

The key idea is that c_D , the average local variance in the smooth region Ω_s , provides a data-dependent measure of the image's gray level inhomogeneity. Higher c_D

indicates more inhomogeneity, while lower c_D implies a more homogeneous image. While β is a constant, c_D adapts to each input image based on the measured inhomogeneity. Since σ_b is inversely proportional to $\sqrt{c_D}$, it will take on larger values for images with less inhomogeneity (smaller c_D), and smaller values for images with more inhomogeneity (larger c_D). This enables σ_b to adaptively set the kernel scale based on the input image characteristics, rather than using a fixed value unsuitable for all images. In summary, c_D captures inhomogeneity via local variance in smooth regions. σ_b adapts inversely to $\sqrt{c_D}$ to set appropriate kernel scale. Images with more inhomogeneity get smaller σ_b , and vice-versa. It's the data-dependent c_D that enables adaptation in σ_b .

Among them, β is a constant parameter, and c_D represents the average value of $D(\chi)$ of the image I_1 in the area Ω_s .

Based on the formula shown above, it is clear that the degree of unevenness of the gray level of the picture will have a direct impact on the size of the scale parameter that is derived, and vice versa. As a result, the proposed adaptive scale operator has the capability to adaptively pick suitable scale parameters for the kernel function based on the degree of gray inhomogeneity present in the picture.

3.2.6 Numerical Realization

Through standardized scaling, $\delta(\phi)$ can be replaced with $|\nabla\phi|$ (Vese and Chan, 2002). In this way, the steady-state solution of the gradient descent flow equation in equation (3.13) is equivalent to the following equation:

$$\frac{\partial\phi}{\partial t} = |\nabla\phi| \left(I - (K * b) \left(\frac{c_1 + c_2}{2} \right) \right). \quad 3.20$$

In addition, in order to prevent the level-set function from being too steep or flat in the evolution process, the condition $|\nabla\phi| = 1$ (Fedkiw and Osher, 2002) must be satisfied, then the above formula is simplified to:

$$\frac{\partial\phi}{\partial t} = I - (K * b) \left(\frac{c_1 + c_2}{2} \right). \quad 3.21$$

Use an explicit finite difference strategy to discretize the formula (3.21):

$$\frac{\phi^n - \phi^{n-1}}{\Delta t} = I - (K * b) \left(\frac{c_1 + c_2}{2} \right). \quad 3.22$$

Where c_1 and c_2 refer to the cluster centers estimated via K-means clustering of the image intensities. Specifically, c_1 is Cluster center for intensities inside the object region. c_2 is Cluster center for intensities outside the object region. So c_1 and c_2 represent the modeled average intensities on either side of the evolving contour. Among them, Δt is the time step and n is the number of iterations.

It is clear from the preceding formula that the right side of the equal sign does not have anything to do with phi, and it is possible to choose a reasonably big time step in order to accelerate the algorithm's process of convergence by doing so. In fact, the estimation procedure for the offset field consumes the majority of the time during each iteration. Additionally, when the offset field is fixed, the level set cannot reach a stable state after one iteration. As a result, multiple iterations are required to evolve the level-set function, which, in turn, can reduce the number of estimation times for the offset field and effectively accelerate the speed at which the algorithm converges. In addition, in order to guarantee the consistency of the numerical realization, the iterative procedure makes use of gaussian filtering to regularize the level-set function. This is done in order to assure the stability of the numerical realization (Zhang et al., 2010).

In the experiment, when the change of the level-set function is less than the given threshold η , that is,

$$\int |\phi^n(\chi) - \phi^{n-1}(\chi)| d(\chi) < \eta. \quad 3.23$$

The algorithm stops iterating.

The main steps of the scale-adaptive fast level-set segmentation algorithm (FLSAS) are as follows:

Step 1. Obtain the initial offset fields b_0 and σ_b according to equations (3.14) and (3.19) respectively, and initialize the level-set function ϕ_0 as a binary function:

$$\phi_0(\chi) = \begin{cases} -1, & \chi \in \text{inside}(\Omega_0) \\ 1, & \text{other} \end{cases} .$$

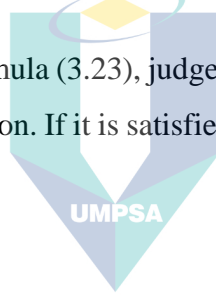
Among them, Ω_0 is a subset of the image domain Ω ;

Step 2. For $K=1:m$

- 1) Calculate c_i according to formula (3.10);
- 2) Evolve the level-set function ϕ according to formula (3.22);
- 3) Use Gaussian filter to regularize the level-set function;
- 4) If $\phi > 0$, then $\phi = 1$; otherwise, $\phi = -1$.

Step 3. Calculate the offset field b according to formula (3.11);

Step 4. According to formula (3.23), judge whether the level-set function ϕ meets the threshold of stopping evolution. If it is satisfied, the algorithm ends, otherwise, return to step 2.



3.2.7 Multiphase Level-Set

The model that was provided above is a two-phase level-set segmentation form. As this form is unable to segment pictures that include multiple target regions, the model that was proposed needs to be expanded to a multi-phase level-set segmentation form. Using k level-set functions to describe the target area $\Omega_i, i = 1, 2, \dots, N$, The membership function M_i of Ω_i is expressed as:

$$\begin{aligned} & M_i(\Phi(\chi)) \\ & = M_i(\phi_1(\chi), \phi_2(\chi), \dots, \phi_K(\chi)) = \begin{cases} 1, & \chi \in \Omega_i \\ 0, & \text{other} \end{cases}, i = 1, 2, \dots, N . \end{aligned} \quad 3.24$$

Among them, $\Phi = (\phi_1, \phi_2, \dots, \phi_K)$.

When $N=4$, use level-set functions ϕ_1 and ϕ_2 to define the four target areas of the image, and the membership functions are expressed as: $M_i(\Phi) =$

$H(\phi_1)H(\phi_2)$, $M_2(\Phi) = H(\phi_1; 1 - H(\phi_2))$, $M_3(\Phi) = (1 - H(\phi_1); 1 - H(\phi_2))$ and $M_4(\Phi) = (1 - H(\phi_1)S) H(\phi_2)$. Assuming $c_1 > c_2 > c_3 > c_4$, the two-phase energy in equation (3.11) The functional is transformed into a multiphase energy functional:

$$\begin{aligned}
 & E(\Phi, c, b) \\
 &= -\int_{\Omega} \sum_{i=1}^{N-1} (S_{i,i+1} \sum_{j=1}^i M_j(\Phi)) d\chi \\
 &= -\int_{\Omega} (S_{1,2}H(\phi_1)H(\phi_2) + S_{2,3}H(\phi_1) + S_{3,4}(1 - H(\phi_2) \\
 &\quad + H(\phi_1)H(\phi_2)))d\chi .
 \end{aligned} \tag{3.25}$$

The area-based pressure function $S_{i,i+1}$ is defined as:

$$S_{i,i+1} = I - (K * b) \left(\frac{c_i + c_{i+1}}{2} \right), i = 1,2,3 . \tag{3.26}$$

Among them, c_i and b can be calculated according to formula (3.10) and formula (3.11) respectively.

Relative to the energy functional E in the minimization equation (3.25) of ϕ_1 , the gradient descent flow equation can be obtained as:

$$\frac{\partial \phi_1}{\partial t} = (S_{1,2} + S_{3,4})H(\phi_2) + S_{2,3} . \tag{3.27}$$

Similarly, relative to ϕ_2 minimize the energy functional E in equation (3.25), the gradient descent flow equation is obtained as:

$$\frac{\partial \phi_2}{\partial t} = (S_{1,2} + S_{3,4})H(\phi_1) - S_{3,4} . \tag{3.28}$$

3.3 Adaptive Multilayer Level-Set Image Segmentation Method

In recent years, a number of multi-scale level-set approaches have been suggested (Wang et al., 2015; Min et al., 2016; and Zhang et al., 2017). (Sui et al., 2012). Min et al. (2016) In order to avoid falling into local minima, it is important to create a multi-layer

level-set structure using a set of scale parameters, make decisions about the scale parameters at each pixel using an adaptive method, and keep the capacity to detect global contrast information. Because this method uses a series of fixed scale parameters and can only provide a limited number of candidate scales, it is difficult to provide appropriate scale parameters for segmenting images that have highly uneven gray levels. This is because this method can only provide a limited number of candidate scales. Moreover, this approach only offers a limited selection of possible scales to choose from.

An adaptive multi-layer level-set picture segmentation technique is proposed in this paragraph as a solution to the challenges outlined above (Adaptive Multilayer Level Set Method, AMLLS). First, make use of the image's local variance to design an improved global adaptive scale operator as well as a local adaptive scale operator. Next, propose an improved local intensity clustering segmentation algorithm, but keep in mind that it is easy for the algorithm to fall into a local minimum solution. In order to accomplish this, it is extended to a multi-layer level-set form, and then the two adaptive scale operators that were designed are used to adaptively determine the number of layers and the scale parameters of each layer. Finally, an adaptive multi-layer level-set structure is constructed, and it is passed. The segmentation and offset field estimation of very uneven grayscale pictures are both made possible using the dual reduction of energy functionals. In addition, a hybrid offset field initialization strategy is offered as a means of enhancing the algorithm's already impressive degree of resilience.

3.3.1 Improved Local Intensity Clustering Level-Set Segmentation Algorithm

This part of the analysis utilizes the image's local variance in order to determine the level of gray inhomogeneity that exists in the surrounding area. Moreover, it creates a local adaptive scale operator in addition to an enhanced global adaptive scale operator for the clustering kernel function. Finally, it combines the LIC model (Li et al., 2011) to propose an improved local strength cluster segmentation algorithm.

3.3.2 Adaptive Scaling Operator

An improved local intensity clustering (OLIC) model is presented in Section 3.3.1 to handle gray level inhomogeneity. This uses adaptive scale parameters and altered

optimization order. Section 3.3.2 extends this to a multi-layer level set formulation (AMLLS) to improve convergence and avoid local minima. Multiple scale layers are used with adaptive determination of parameters. A hybrid offset field initialization is proposed in Section 3.3.3 to improve robustness. This initializes each level's offset field as a blend of constant and previous iteration's estimate. The function of equations in this section was described as:

Eq 3.29-3.30: Compute adaptive global and local scale parameters σ_G and σ_L based on image local variance statistics.

Eq 3.31: Discretize σ_L into intervals σ_D for simpler optimization.

Eq 3.32: OLIC energy functional using discrete σ_D .

Eq 3.33-3.36: Update cluster centers c_i and offset field b by minimizing energy.

Eq 3.37: OLIC level set evolution equation.

Eq 3.42-3.45: Define multi-layer scale parameters $\sigma_{ML}^{(j)}(\chi)$ adapted to image inhomogeneity.

Eq 3.48: Multi-layer energy function.

Eq 3.56-3.59: Update parameters by minimizing multi-layer energy.

Eq 3.61: Hybrid offset field initialization.

3.3.2.1 Improved Global Adaptive Scaling Operator

The previous study provided a global adaptive scale operator and utilized the local variance of the smooth area of the picture to evaluate the degree of local gray inhomogeneity. Nevertheless, this method is subject to noise interference when it is used to calculate the smooth area of the image. As a result, this thesis make improvements to the global adaptive scale operator by reducing the complexity of the approach for getting the smooth area.

First, use median filtering and bilateral filtering to preprocess the image I , and the preprocessed image gray level is I_1 . Then, use the Laplacian of Gaussian to estimate the boundary C_L of the target. The local area of pixels near the target boundary may will contain the target and background pixels. Therefore, remove the pixels whose distance C_L is less than $\omega_0 + 1$ to obtain the final smooth area Ω_s ,

$$\Omega_s = \{\chi | \text{dist}(\chi, C_L) > \omega_0 + 1\}, \chi \in \Omega. \quad 3.29$$

Among them, ω_0 is a constant parameter, and $\text{dist}(\chi, C_L)$ is the Euclidean distance between the pixel χ and the nearest pixel in C_L .

After obtaining the smooth area Ω_s , calculate the local variance $D(\chi)$ of the $(2\omega_0 + 1) \times (2\omega_0 + 1)$ square neighborhood $R^{\omega_0}(\chi)$ centered on χ on the image I_1 . The global adaptive scaling operator of the previous methods is extended to a more general form, which is suitable for different types of kernel functions, and an improved global adaptive scaling operator σ_G is proposed:

$$\sigma_G = \frac{\alpha}{(\sqrt{C_D})^\rho}. \quad 3.30$$

Among them, α and ρ are constant parameters, and C_D is the mean value of $D(\chi)$ of image I_1 in the area Ω_s .

3.3.2.2 Local Adaptive Scaling Operator

It is difficult to cope with non-linear gray-scale uneven pictures when using the enhanced global adaptive scale operator, despite the fact that it gives uniform scale parameters for all pixels. In actual reality, the scale parameter of each pixel has to be updated in an adaptive manner so that it corresponds to the degree of local gray-scale unevenness. Therefore, this thesis use the image local variance $D(\chi)$ to measure the degree of local gray inhomogeneity, and propose a local adaptive scale operator σ_L :

$$\sigma_L(\chi) = \begin{cases} 0.5\sigma_G, & \chi \notin \Omega_s \text{ \& } D(\chi) > 4C_D \\ \sigma_G - \frac{2\sigma_G}{\pi} \arctan\left(\frac{\sqrt{D(\chi)} - \sqrt{C_D}}{\varsigma + \sqrt{C_D}}\right), & \text{other} \end{cases} \quad 3.31$$

Among them, ς is a constant parameter.

The σ_L in formula (3.31) can adaptively provide a suitable scale parameter between zero and $2\sigma_G$ for each pixel according to the degree of local gray inhomogeneity of the image, and avoid excessive or excessive scale parameters. The occurrence of minor situations. The larger the local variance, the smaller the scale parameter, and vice versa. In addition, in the target boundary area, the local variance of the image is large, and the gray scale of the target boundary area is approximately uniform. Therefore, the minimum scale parameter of the non-smooth area is limited to $0.5\sigma_G$. In this way, on the one hand, it avoids the slow level-set convergence caused by the too small scale parameter; on the other hand, it can effectively improve the segmentation accuracy of the boundary area.

3.3.3 Improved Local Intensity Clustering Segmentation Algorithm

This thesis updated the LIC model in order to address the issue that the local intensity clustering model (LIC; Li et al., 2011) has with being sensitive to the starting contour and setting scale parameters. To begin, modify the order of level-set evolution and migration field estimate, also known as the OLIC (Order Local Intensity Clustering) model, so that the resilience to the starting contour may be improved. The segmentation performance of highly uneven grayscale pictures is then enhanced by combining an improved version of the global adaptive scale operator (OLICG) with an improved version of the local adaptive scale operator (OLICL).

The OLICG model is similar to the LIC model and is easy to implement. Only the OLICG model is introduced here, and its energy functional is:

$$E^{OLICL} = \int (\sum_{i=1}^N \int K_{\sigma_L}(y - \chi) |I(\chi) - b(y) c_i|^2 M_i(\phi(\chi)) d\chi) dy. \quad 3.32$$

Due to the selection of different scale parameters at each pixel, the algorithm implementation is more complicated. For this reason, the scale parameters can be

discretized at equal intervals to simplify the calculation. The discrete scale parameter is expressed as:

$$\sigma_D^{(j_0)} = \min(\sigma_L) + (j_0 - 0.5) \cdot \tau, j_0 = 1, 2, \dots, m_1 . \quad 3.33$$

Among them, $\tau = (\max(\sigma_L) - \min(\sigma_L)) / m_1$, m_1 real constant.

Using discrete scale parameters, the energy functional of the OLICG model can be expressed as:

$$E^{OLICL} = \sum_{i=1}^N \int \left(\sum_{j_0=1}^{m_1} \int \delta_0(L_{\sigma_D}(y) - j_0) K_{\sigma_D^{(j_0)}}(y - \chi) |I(\chi) - b(y) c_i|^2 M_i(\phi(\chi)) d\chi \right) dy . \quad 3.34$$

Among them, $L_{\sigma_D} = \lceil \sigma_L - \min(\sigma_L) \rceil / \tau$ If $\chi = 0$, then $\delta_0(\chi)$ is 1, otherwise it is 0.

Similar to the LIC model, the optimal c_i and b are:

$$c_i = \frac{\int \sum_{j_0=1}^{m_1} ((b * K_{\sigma_D^{(j_0)}}) \delta_0(L_{\sigma_D}(\chi) - j_0)) I M_i(\phi) d\chi}{\int \sum_{j_0=1}^{m_1} ((b^2 * K_{\sigma_D^{(j_0)}}) \delta_0(L_{\sigma_D}(\chi) - j_0)) M_i(\phi) d\chi} . \quad 3.35$$

$$b = \frac{\int ((\sum_{i=1}^N c_i M_i(\phi) I) * K_{\sigma_D^{(j_0)}} \delta_0(L_{\sigma_D}(\chi) - j_0))}{\int ((\sum_{i=1}^N (c_i)^2 M_i(\phi)) * K_{\sigma_D^{(j_0)}} \delta_0(L_{\sigma_D}(\chi) - j_0))} . \quad 3.36$$

Considering the two-phase segmentation and introducing the rule term and length term in the LIC model, the final gradient descent flow equation is:

$$\frac{\partial \phi}{\partial t} = -\delta(\phi)(e_1 - e_2) + \mu \left(\nabla^2 \phi - \text{div} \left(\frac{\nabla \phi}{|\nabla \phi|} \right) \right) + \nu \delta(\phi) \text{div} \left(\frac{\nabla \phi}{|\nabla \phi|} \right) . \quad 3.37$$

Among them, $\mu \geq 0$, $\nu \geq 0$, e_i are:

$$e_i(\chi) = \sum_{j_0=1}^{m_1} \int \delta_0(L_{\sigma_D}(y) - j_0) K_{\sigma_D^{(j_0)}}(y - \chi; I(\chi) - b(y) c_i)^2 dy. \quad 3.38$$

In the numerical implementation, an explicit finite difference strategy is used to discretize equation (3.37):

$$\frac{\phi^n - \phi^{n-1}}{\Delta t} = \frac{\partial \phi^{n-1}}{\partial t}. \quad 3.39$$

Among them, Δt is the time step and n is the number of iterations. The Heaviside function is regularized into the following form:

$$H_\varepsilon(\phi) = \frac{1}{2} \left[1 + \frac{2}{\pi} \cdot \arctan \left(\frac{\phi}{\varepsilon} \right) \right]. \quad 3.40$$

Among them, ε is a constant parameter. $\delta(\cdot)$ is approximately:

$$\delta_\varepsilon(\phi) = H'_\varepsilon(\phi) = \frac{1}{\pi} \frac{\varepsilon}{\varepsilon^2 + \phi^2}. \quad 3.41$$

3.3.4 Simulation Experiment and Analysis

This section verifies the performance of the improved local intensity clustering segmentation algorithm through experiments on synthetic and real images. The experimental platform used is the same. In the experiment, the parameters are set as: $\omega_0 = 1$, $\alpha = 5.2$, $\rho = 1.25$, $\zeta = 1$, $m_1 = 6$, $\Delta t = 0.1$, $\varepsilon = 1$, $v = 1$ and $\mu = 0.0001 \times 255^2$.

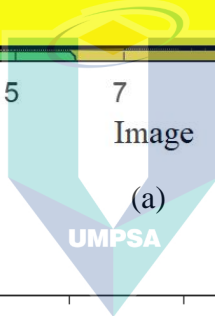
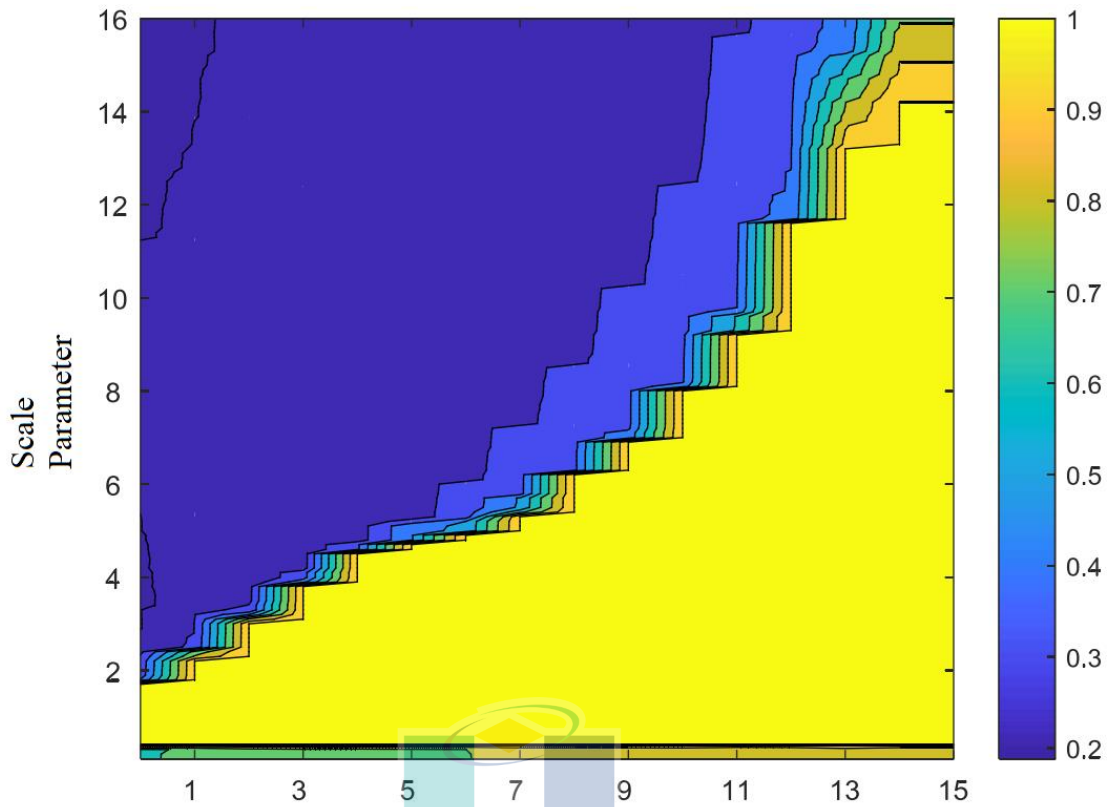
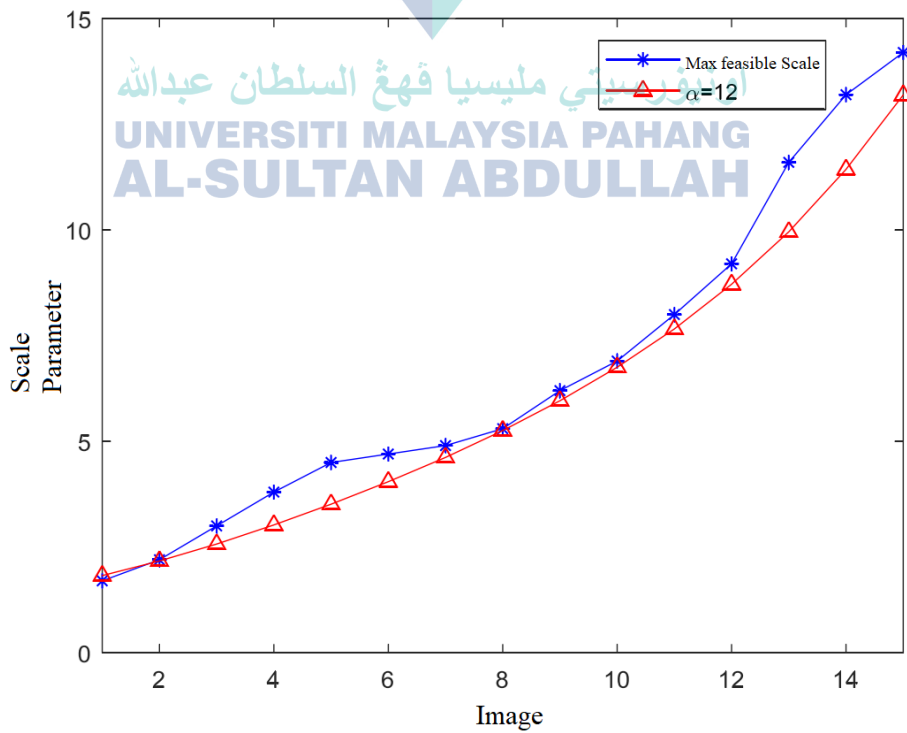


Image
(a)



(b)

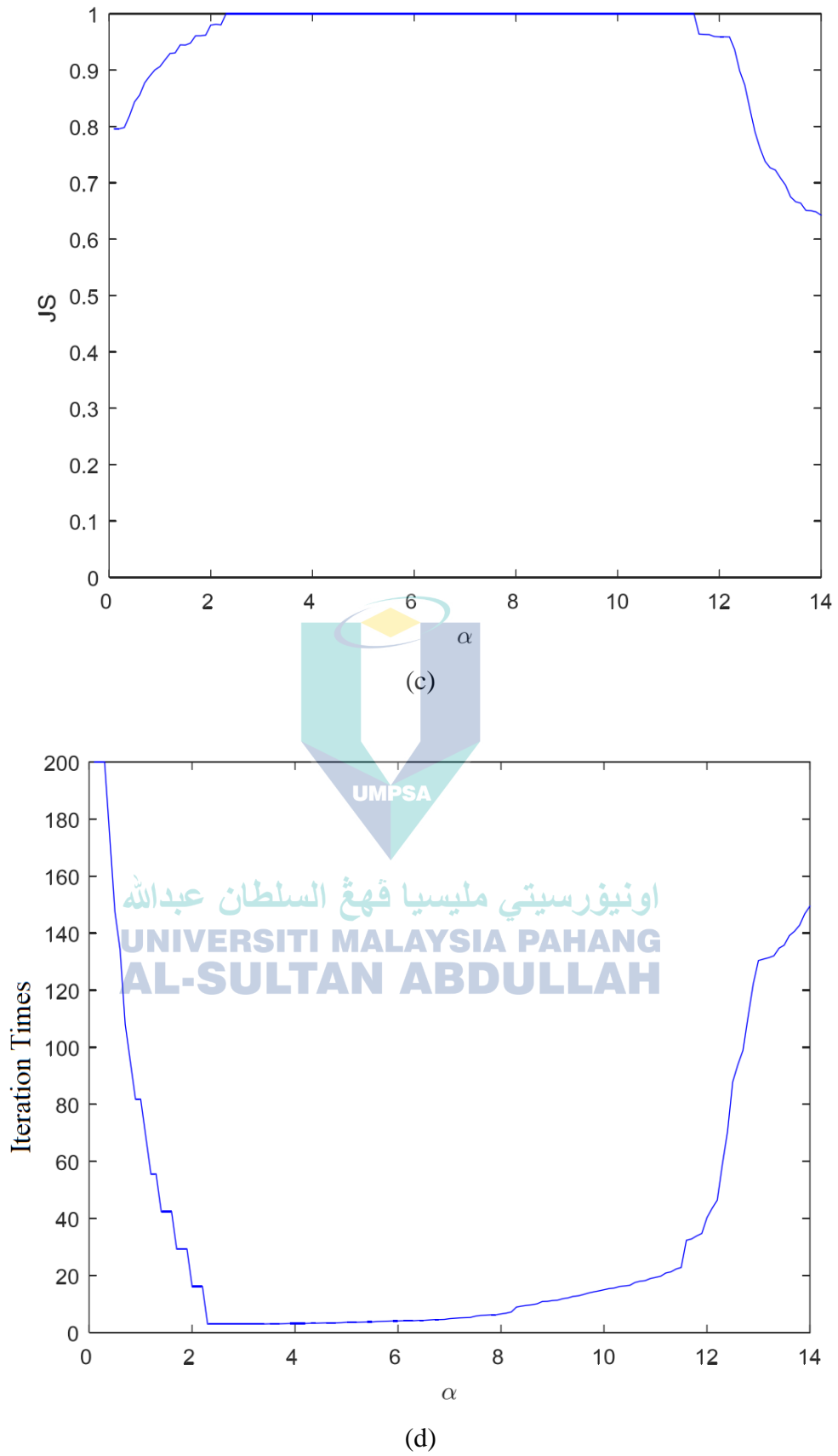


Figure 3.1 The effectiveness of the improved global adaptive operator

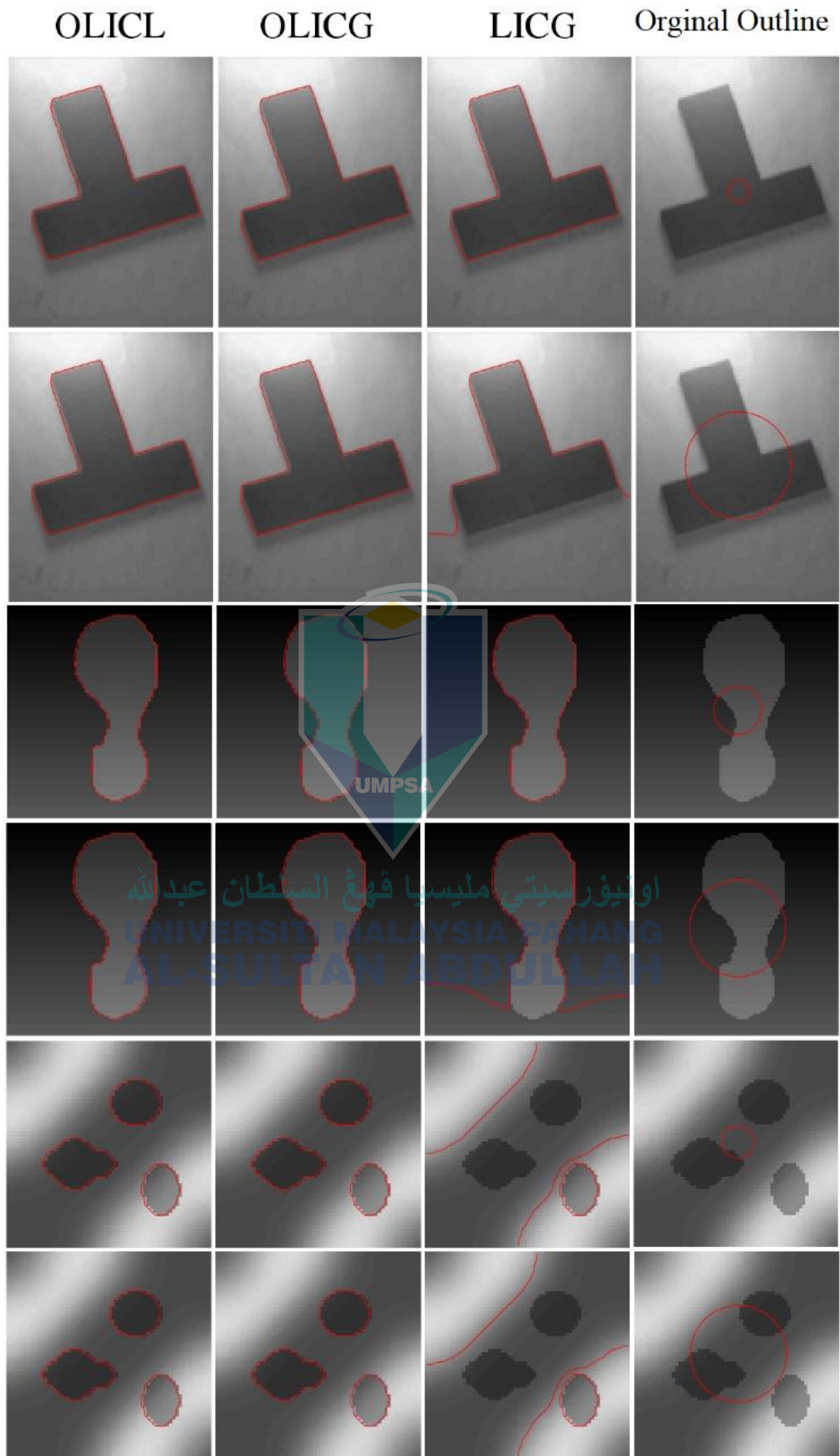


Figure 3.2 Different initial contours-state the difference in the caption

Figure 3.1 shows the effectiveness analysis of the improved global adaptive operator. Put the OLIC model in the composite image, including 15 images, and the gray-scale unevenness of the image gradually decreases. In the experiment, μ is set to zero to remove the length term, and the initial contour is set near the actual boundary of the target to reduce the influence of the initial contour on the model. It can be seen from Figure 3.1(a) that images with different gray-scale inhomogeneities require different scale parameters. Figure 3.1(b) shows the comparison between the adaptive scale operator when $\alpha=12$ and the maximum feasible scale parameter (the maximum scale parameter whose JS value is 1 in the segmentation result of the OLIC model). It can be seen that the proposed adaptive scale operator is very close to the maximum feasible scale parameter. It can be seen from Figure 3.1(c) that when $\alpha \approx 2.3\sim 11.5$, the OLIC model can segment all images correctly. Figure 3.1(d) shows the average number of iterations required by the OLIC model under different α . Considering the accuracy and efficiency of the algorithm, α is set to 5.2 in the experiment.

Figure 3.2 shows the segmentation results of the LIC model (LICG), OLICG and OLICL combined with the global adaptive scale operator under different initial contours for the gray-scale uneven image. It can be seen that different initial contours lead to different segmentation results for LICG, while OLICG and OLICL can both obtain the same and correct segmentation accuracy, indicating that OLICG and OLICL have strong robustness to the initial contour.

Figure 3.3 shows the segmentation results of LCG, OLICG and OLICL on uneven grayscale images. In the experiment, for the four images, μ is set to 0.001×255^2 , 0.0003×255^2 , 0.001×255^2 and 0.0001×255^2 . It can be seen that it is difficult for LICG to segment images with severely uneven gray levels. The segmentation performance of OLICG is higher than that of LICG, but the segmentation accuracy is worse in weak boundary regions. However, OLICL obtains accurate segmentation results for all images, indicating that OLICL can accurately segment images with severely uneven grayscale.

Figure 3.4 shows the local adaptive scale parameters of the first and third images in Figure 3.3. It can be seen that for the first image with slightly uneven grayscale, the

scale parameter of the smooth area is larger. For the second image with severely uneven gray scale, the scale parameter of the smooth area is smaller. It demonstrates that the proposed local adaptive scale operator is able to give appropriate scale parameters at each pixel based on the degree of local gray inhomogeneity present in the picture. In addition, the target boundary area is on a smaller scale, which, when combined with the smaller scale, has the potential to significantly increase the border area's segmentation accuracy.

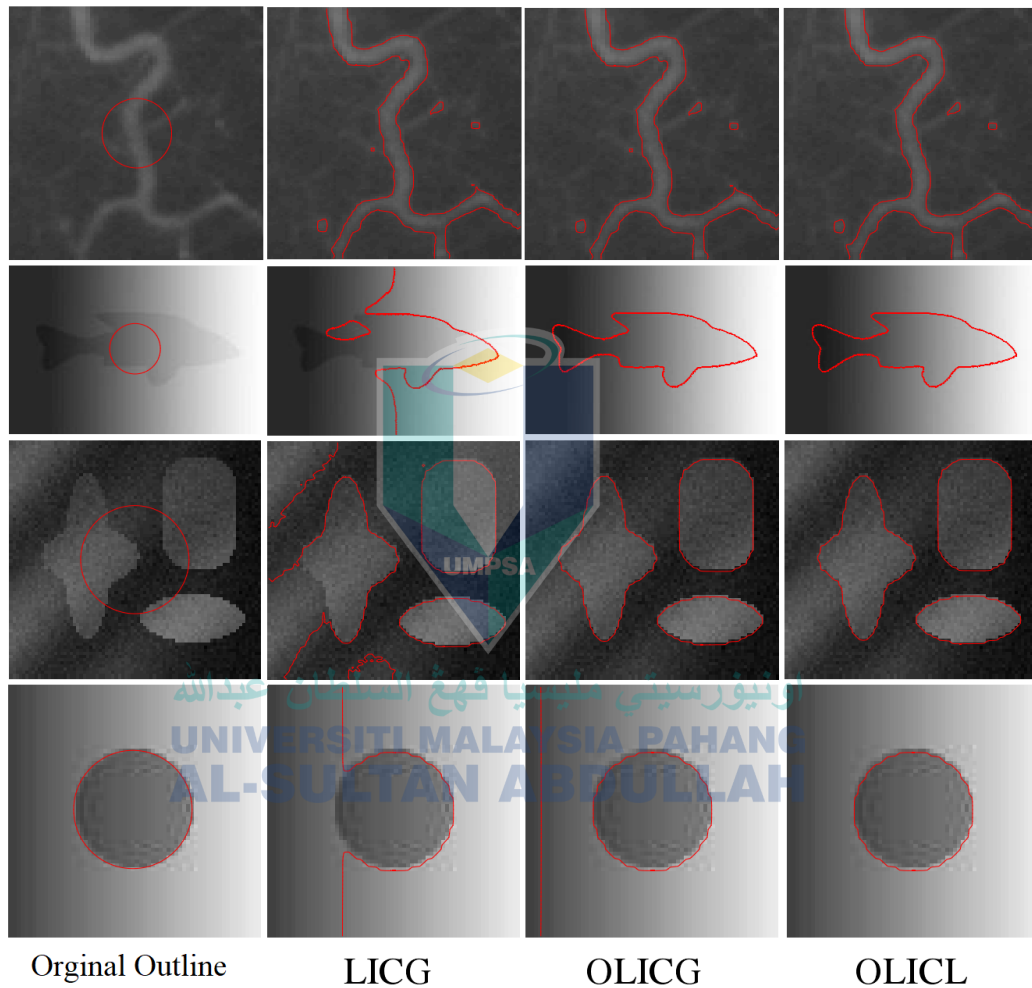


Figure 3.3 Comparison of LICG, OLICG and OLICL segmentation results

Figure 3.5 shows the segmentation results of OLICG and OLICL for severely uneven grayscale images. It can be seen that changing the position of the initial contour will lead to incorrect segmentation, indicating that OLICG and OLICL will still fall into a local minimum solution.

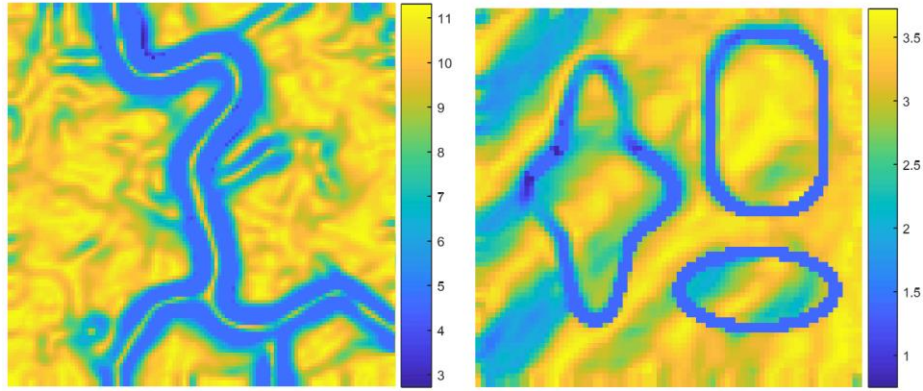


Figure 3.4 Local adaptive scale parameters

Aiming at the problem that the algorithm falls into a local minimum solution, the improved local strength clustering segmentation algorithm in section 4.2 is extended to a multi-level level-set form, and the multi-level level-set structure is constructed using the proposed global and local adaptive scale operators, Propose an adaptive multi-layer level-set segmentation algorithm.

3.3.5 Adaptive Multilayer Level-Set Structure

The low-level energy items in the multi-layer level-set structure (Min et al., 2016) primarily represent the local gray distribution information of the picture, but the high-level energy items include more information on the image's global contrast. Because the proposed local adaptive scale operator is obtained according to the degree of the image's local gray inhomogeneity, it is possible to use it to construct the first layer of a multi-layer level-set structure. This is because of the way that the proposed local gray inhomogeneity is measured. The following are the scale parameters that are specified for the first layer:

$$\sigma_{ML}^{(l)}(\chi) = \beta \cdot \sigma_L(\chi) + 1. \quad 3.42$$

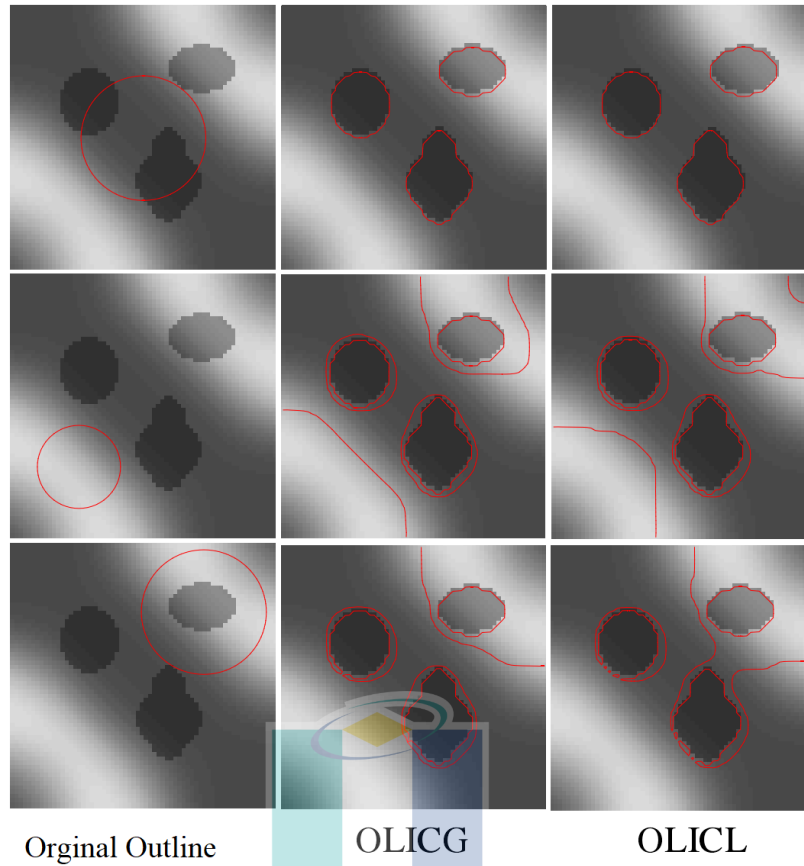


Figure 3.5 OLICG and OLICL segmentation results

Among them, β is a constant parameter. At the same time, since the proposed global adaptive scale operator is obtained according to the degree of the overall grayscale inhomogeneity of the image, it can be used to construct the scale parameters of other layers of the multi-layer level-set structure. The scale parameter of layer j ($j > 1$) is defined as:

$$\sigma_{ML}^{(j)}(\chi) = \Delta s \cdot j + 1 = \beta \cdot \sigma_G \cdot j + 1 \quad 3.43$$

It can be seen from the above formula that the scale difference between adjacent layers in the multi-layer level-set structure $\Delta s = \beta \cdot \sigma_G$ changes adaptively with the degree of global gray-scale inhomogeneity of the image. A uniform image provides a smaller Δs , while a slightly uneven grayscale image provides a larger Δs . In addition, the maximum scale of the multilayer level-set structure must be sufficient to cover the image to detect the global contrast information of the image. In this way, this thesis can define

the number of layers m of the multilayer level-set structure according to Δs and the size of the image:

$$m = \text{round}(\min((\frac{N_0}{\pi})^{0.5}/(4 \cdot \Delta s), \frac{T}{\Delta s})) + 1 \quad 3.44$$

Among them, T is a constant parameter, used to limit the maximum value of the scale, and N_0 is the number of pixels of the image. It can be seen from the above formula that for images with severely uneven grayscale, the value of m is larger, this might give a greater number of potential scales for the picture processing. When dealing with photos that have grayscale that is somewhat uneven, using a lower value for m may help speed up the convergence time of the method.

The scale parameter of the j -th layer of the adaptive multi-layer level-set structure is defined as:

$$\sigma_{ML}^{(j)}(\chi) = \begin{cases} \beta \cdot \sigma_L(\chi) + 1, & j = 1 \\ \beta \cdot \sigma_G \cdot j + 1, & j = 2, 3, \dots, m \end{cases} \quad 3.45$$

It can be seen from the above formula that the scale parameters and the number of layers of the adaptive multi-layer level-set structure can be adjusted adaptively according to the degree of gray-scale inhomogeneity of the image. For images with severely uneven gray-scale, it can be automatically selected. More layers and denser candidate scales can better estimate the offset field of the image and achieve accurate image segmentation. For images with slightly uneven gray scales, choosing a sparse candidate scale and fewer layers is conducive to fast image segmentation.

Then, a series of Gaussian kernel functions are constructed using the scale parameters in equation (3.45). The Gaussian kernel function of the j -th layer is:

$$K_{\sigma_j}(u) = \begin{cases} \frac{1}{a} e^{-u^2/(2\sigma_j^2)}, & |u| \leq \sigma_j, j = 1, 2, \dots, m \\ 0, & \text{other} \end{cases} \quad 3.46$$

The energy term of the adaptive multilayer level-set structure can be described as:

$$E_M = \{E_M^{(1)}, E_M^{(2)}, \dots, E_M^{(j)}, \dots\}, j = 1, 2, \dots, m \quad 3.47$$

$$E_M^{(j)} = \sum_{i=1}^N \lambda_1 \iint K_{\sigma_{ML}^{(j)}} \cdot (I(\chi) - b^{(j)}(y)c_i^{(j)})^2 M_i(\phi(\chi)) dy d\chi \quad 3.48$$

In the first layer, each pixel is assigned a different scale parameter. Therefore, using the same method as the OLICL model, $\sigma_{ML}^{(1)}$ is discretized at equal intervals to calculate $E_M^{(1)}$, the detailed process Refer to section 3.3.1.

3.3.6 Level-Set Evolution and Numerical Calculation

3.3.6.1 Energy Functional

The difference between the cluster center and the image gray level estimated by the adaptive multi-layer level-set structure at each pixel, that is, the multi-layer gray level difference, is defined as:

$$DI_i^{(j)}(\chi) = \begin{cases} \sum_{j_0=1}^{m_1} \int \delta_0(L_{\sigma_D}(y) - j_0) K_{\sigma_D^{(j_0)}}(y - \chi; I(\chi) - b^{(1)}(y) c_i^{(1)})^2 dy, & j = 1 \\ (I(\chi) - b^{(j)}(\chi) c_i^{(j)})^2, & j = 2, \dots, m \end{cases} \quad 3.49$$

At each pixel, the layer corresponding to the smallest multi-layer grayscale difference is the optimal evolution layer. Generally, the image gray scale of the target boundary area is approximately uniform. Therefore, using smaller scale parameters in the target boundary area can improve the segmentation accuracy of the algorithm. Set the optimal evolution layer of the estimated non-smooth area of the image as the first layer, so that the optimal evolution layer of the adaptive multi-layer level-set structure is:

$$L_i(\chi) = \begin{cases} 1, & \chi \notin \Omega_s \\ \arg \min_j (DI_i^{(j)}(\chi)), & \chi \in \Omega_s \end{cases}, \quad i = 1, \dots, N. \quad 3.50$$

Using the optimal evolution layer in formula (3.50), the optimal gray level difference can be obtained:

$$Z_i(\chi) = DI_i^{(L_i(\chi))}(\chi), i = 1, \dots, N. \quad 3.51$$

The final level-set energy functional is:

$$E_D = \sum_{i=1}^N \lambda_1 \int_{\Omega} Z_i(\chi) \cdot M_i(\phi(\chi)) d\chi. \quad 3.52$$

In addition, the level-set function needs regularization (Li et al., 2010), (Li et al., 2008), (Zhang et al., 2012) to ensure its stability. This thesis introduce the length term and regularization term in (Li et al., 2008) into the proposed algorithm. When $N = 2$, the level-set energy functional is:

$$E = \lambda_1 \int_{\Omega} Z_1(\chi) H(\phi(\chi)) d\chi + \lambda_2 \int_{\Omega} Z_2(\chi; 1 - H(\phi(\chi))) d\chi + \mu \int_{\Omega} |\nabla H(\phi)| d\chi + \nu \int_{\Omega} \frac{1}{2} (|\nabla \phi| - 1)^2 d\chi. \quad 3.53$$

Among them, $\mu \geq 0, \nu \geq 0$.

Extend the two-phase division form to the polyphase form, and use k level-set functions $\phi_1, \phi_2, \dots, \phi_k$ to represent the area $\Omega_i, i = 1, 2, \dots, N$, then the membership function of the area Ω_i for:

$$M_i(\Phi(\chi)) = M_i(\phi_1(\chi), \phi_2(\chi), \dots, \phi_k(\chi)) = \begin{cases} 1, & \chi \in \Omega_i \\ 0, & \text{other} \end{cases}. \quad 3.54$$

Among them, $\Phi = (\phi_1, \phi_2, \dots, \phi_k)$. When $N = 3$, two level-set functions ϕ_1 and ϕ_2 are used to define the partitions in the image domain Ω , and the membership function is expressed as: $M_1(\Phi) = H(\phi_1)H(\phi_2)$, $M_2(\Phi) = H(\phi_1; 1 - H(\phi_2))$ and $M_3(\Phi) = 1 - H(\phi_1)$. Multiphase energy functional representation for:

$$E = \sum_{i=1}^N \lambda_1 \int_{\Omega} Z_i(\chi) \cdot M_i(\phi(\chi)) d\chi + \mu \cdot \sum_{q=1}^k \int_{\Omega} |\nabla H(\phi_q)| d\chi + v \cdot \sum_{q=1}^k \int_{\Omega} \frac{1}{2} (|\nabla \phi_q| - 1)^2 d\chi . \quad 3.55$$

3.3.6.2 Minimize Energy

According to formula (3.53) or formula (3.55), the energy functional E is minimized for each variable, and the closed solution of each variable can be obtained. Fixing ϕ and $b^{(j)}$, the optimal $c_i^{(j)}$ can be obtained by minimizing the energy term $E_M^{(j)}$ in equation (3.48):

$$c_i^{(j)} = \frac{\int (b^{(j)} * K_{\sigma_{ML}}^{(j)} \cdot I \cdot M_1(\Phi)) d\chi}{\int (b^{(j)})^2 * K_{\sigma_{ML}}^{(j)} \cdot M_1(\Phi) d\chi} , j = 2, \dots, m . \quad 3.56$$

$c_i^{(1)}$ can be obtained according to formula (3.35).

When fixing ϕ and $c_i^{(j)}$, the optimal $b^{(j)}$ can be obtained by minimizing the energy term $E_{M^{(j)}}$ in equation (3.48):

$$b^{(j)} = \frac{(I \cdot (\sum_{i=1}^N c_i^{(j)} M_i(\Phi))) * K_{\sigma_{ML}}^{(j)}}{(\sum_{i=1}^N (c_i^{(j)})^2 M_i(\Phi)) * K_{\sigma_{ML}}^{(j)}} , j = 2, \dots, m . \quad 3.57$$

$b^{(1)}$ can be obtained according to formula (3.36).

When $N=2$, fix $b^{(j)}$, $c_i^{(j)}$ and L_i , and minimize the energy functional in equation (3.53) with respect to the level-set function Φ to obtain the gradient descent flow equation:

$$\frac{\partial \phi}{\partial t} = -\frac{\partial E}{\partial \phi} = -\delta(\phi) \lambda_1 Z_1 - \lambda_2 Z_2 + \mu \delta(\phi) \operatorname{div} \frac{\nabla \phi}{|\nabla \phi|} . \quad 3.58$$

Among them, $div(\cdot)$ is the divergence operator, ∇ is the gradient operator, and $\delta(\cdot)$ is the Dirac function.

When $N > 2$, fix $b^{(j)}$, $c_i^{(j)}$ and L_i relative to the variable $\Phi = (\phi_1, \phi_2, \dots, \phi_K)$. Minimize the formula (3.55) middle Energy functional, get gradient descent flow equation:

$$\begin{aligned} \frac{\partial \phi_q}{\partial t} = -\frac{\partial E}{\partial \phi_q} = & -\sum_{i=1}^N \lambda_1 Z_i \frac{\partial M_i(\Phi)}{\partial \phi_q} + \mu \delta(\phi_q) \operatorname{div} \frac{\nabla \phi_q}{|\nabla \phi_q|} \\ & + v(\nabla^2 \phi_q \operatorname{div} \frac{\nabla \phi_q}{|\nabla \phi_q|}), \quad q = 1, \dots, k. \end{aligned} \quad 3.59$$

In the numerical implementation, the explicit finite difference strategy is also used to discretize equations (3.58) and (3.59):

$$\frac{\phi_q^n - \phi_q^{n-1}}{\Delta t} = \frac{\partial \phi_q^{n-1}}{\partial t}. \quad 3.60$$

Among them, Δt is the time step and n is the number of iterations.

3.3.6.3 Initialization of Mixed Offset Field

The level-set segmentation method realizes image segmentation through the evolution of level-set, which is an interactive iterative process. Before each iteration, the offset field $b^{(j)}$ estimated in the previous iteration is usually used to initialize the offset field of the multi-layer level-set structure, which can promote the smooth convergence of the algorithm, but also cause the algorithm to fall into Local minimum solution. The DM model (Min et al., 2016) uses a simple offset field initialization operation, that is, $b_0^{(j)}(\chi) = 1, \chi \in \Omega$, although the DM model can accurately and efficiently segment some gray levels Inhomogeneous images, but for images with large overlaps in the gray distribution of the inner and outer regions of the target, the segmentation will be unstable and inaccurate. In order to make the algorithm more robust, a hybrid offset field is constructed by estimating the overlap degree of the gray distribution of the inner and

outer regions of the segmentation contour, and the offset field before each iteration is initialized.

For the n th iteration, the mixed offset field of the j th layer of the multilayer level-set structure is:

$$hb_n^{(j)}(\chi) = (1 - \omega_n)b_0^{(j)}(\chi) + \omega_nb_{n-1}^{(j)}(\chi), i = 1, 2, \dots, m. \quad 3.61$$

Among them, $b_0^{(j)} = 1$ is the initial offset field, $b_{n-1}^{(j)}(\chi)$ is the estimated offset of the i -th layer of the multilayer structure after $n-1$ iterations Field, the weight ω_n is designed as:

$$\omega_n = 1 - \exp(-CJV(\phi^{n-1})^2/4). \quad 3.62$$

Among them, ϕ^{n-1} is the level-set function after $n-1$ iterations, and the definition of $CJV(\Phi; Vovk \text{ et al., 2007})$ is:

$$\omega_n = 1 - \exp(-CJV(\phi^{n-1})^2/4), \quad 3.63$$

$$\Omega_1 = \{\chi \in \Omega | \Phi(\chi) < 0\}, \Omega_2 = \{\chi \in \Omega | \Phi(\chi) \geq 0\}. \quad 3.64$$

Among them, $c(\cdot)$ and $\sigma(\cdot)$ respectively represent the average gray value of the image in the area and standard deviation.

The main steps of the proposed adaptive multilayer level-set image two-phase segmentation algorithm (AMLLS) are as follows:

Step 1. Calculate σ_G and σ_L according to formula (3.30) and formula (3.31);

Step 2. Construct $\sigma_{ML}^{(j)}$ according to formula (3.45);

Step 3. Initial $b_0^{(j)}(\chi) = 1, n=1$ and $\phi^0(\chi) = \begin{cases} -1, & \chi \in \Omega_0 \\ 1, & \text{other} \end{cases}$, where Ω_0 is a subset of

Ω ;

Step 4. Calculate $hb_n^{(j)}$ according to formula (3.61), and use it to initialize the offset field $b^{(j)}$;

Step 5. Calculate $c_i^{(j)}$ according to formula (3.35) and formula (3.56);

Step 6. Calculate $b^{(j)}$ according to formula (3.36) and formula (3.57);

Step 7. Calculate L_i according to formula (3.50), and calculate Z_i according to formula (3.51);

Step 8. Evolve the level-set function according to formula (3.58) and formula (3.60);

Step 9. When the maximum number of iterations is reached or the level-set function converges, the algorithm ends, otherwise, let $n=n+1$ and return to step 4.

3.4 Variational Level Set Method for Geometric Evolution of Curves

3.4.1 A General Equation for Geometric Evolution of Curves

First, this thesis consider a closed curve sequence $C(p, t)$, $t \geq 0$ that follows the following PDE evolution:

$$\frac{\partial C(p, t)}{\partial T} \equiv V = \alpha(p, t)T + \beta(p, t)N, C(p, 0) = C_0(p), \quad 3.65$$

where α and β are the tangential velocity and the normal velocity respectively. The value of y of a curve can be expressed as a function of x , $y = r(x)$. That is, the curve C is represented by x as a parameter, $C(x) = (x, r(x))$. So, the tangential vector is $C_x = (1, r_x)$.

The unit tangent vector and the normal vector are $T = \frac{(1, r_x)}{\sqrt{1+r_x^2}}$ and $N = \frac{(r_x, -1)}{\sqrt{1+r_x^2}}$.

Therefore, when the curve C is evolved, x and y at any point will move in accordance with the following equations:

$$\frac{\partial C(p, t)}{\partial T} \equiv V = \alpha(p, t)T + \beta(p, t)N, C(p, 0) = C_0(p).$$

Given that:

$$\begin{aligned} \frac{dy}{dt} &= r_x \frac{dx}{dt} + r_t \rightarrow r_t = \frac{dy}{dt} - r_x \frac{dx}{dt} \\ &= \alpha \frac{r_x}{\sqrt{1+r_x^2}} + \beta \frac{1}{\sqrt{1+r_x^2}} - \alpha \frac{r_x}{\sqrt{1+r_x^2}} + \beta \frac{r_x^2}{\sqrt{1+r_x^2}} = \beta \sqrt{1+r_x^2}. \end{aligned}$$

This formula demonstrates that the modification of the geometric shape of the curve is exclusively connected to the normal β of V and not to the tangential α of the velocity of motion. So, when this thesis talk about the development of geometric curves, the only thing this thesis need to take into consideration is the normal velocity. In this manner, the overall equation for the progression of curves may be made more straightforward.

$$\frac{\partial C}{\partial t} \equiv \beta N.$$

3.66

3.4.2 Level Set Method for Curve Evolution

3.4.2.1 Basic concept

It has been pointed that a closed plane curve can adopt implicit expression, which is defined as a level set of a two-dimensional function $u(x, y)$, i.e. $C = \{(x, y), u(x, y) = c\}$. Then, if C has any kind of changes, then this thesis can say function $u(x, y)$ has corresponding changes. More precisely, the closed curve that changes with time can be expressed as a level set of a 2D function $u(x, y)$ that changes with time, namely $C = \{(x, y), u(x, y, t) = c\}$. So, how does the embedding function $u(x, y, t)$ evolve when the curve $C(t)$ evolves? Taking the derivative du/dt for the function u in the above equation, using the chain rule of the composite function, this thesis have $\frac{du}{dt} = \frac{\partial u}{\partial t} + \nabla u \cdot \frac{\partial(x,y)}{\partial t} = 0$. It obtains

$$\frac{\partial u}{\partial t} = -\nabla u \cdot \frac{\partial(x, y)}{\partial t} = -\nabla u \cdot V = -|\nabla u| \frac{\nabla u}{|\nabla u|} \cdot V = |\nabla u| N \cdot V = \beta |\nabla u|, \quad 3.67$$

where $\beta = N \cdot V$ is the normal component of the motion velocity. equation (3.67) is the basic equation of curve evolution level set method.

It has been assumed in the preceding derivation that $u(x, y)$ is more than c for (x, y) that are outside the closed curve C ; $u(x, y)$ is less than c for (x, y) that are within the closed curve C ; and $u(x, y)$ is equal to c for (x, y) that are on the closed curve C . In addition, it should be pointed out that the derivation of equation (3.67), which is shown below, is not reliant on the value of the constant C . Because of this, the convenient equation $c = 0$ is often used. In other words, the curve that is of interest to us is the zero level set of the embedded function.

This thesis can see that the evolution of equation 3.66, under the initial condition C_0 of the closed curve C , is equivalent to the evolution of the embedding function $u(x, y)$, according to equation 3.67, under the given initial value u_0 condition. This is because both equations describe the same thing: the evolution of the closed curve C . This is because equation 3.67 describes the development of equation 3.66 given the starting condition C_0 of the closed curve C . The reason for this is because equation 3.67 is a given. (The value C_0 is equivalent to the zero level of u_0 .) That is to say, the current curve $C(t)$ may be recognized at any moment t by taking the level set of $u(x, y, t) = 0$. This is done in order to avoid any confusion. To put it another way, what this indicates is that it is possible to ascertain the current curve at any given time.

3.4.2.2 Variational level set method

When curve evolution is applied to image processing issues, a curve motion equation often originates from an energy functional that minimizes a closed curve C . This is the case because closed curves have the least amount of energy. As an example, the goal of the well-known geodesic active contour model for picture segmentation is to minimize the following functional.

$$E(C) = \oint g(|\nabla I[C(s)]|) ds . \quad 3.68$$

Now this thesis will describe this theory and prove (Dakai et al., 2008) that the descent gradient of equation (3.82) is

$$\frac{\partial C}{\partial t} = [g(c)\sigma - \nabla g \cdot N]N . \quad 3.69$$

(1) Selection of energy functional

In the field of optics, the theorem of Fermat states that when light passes through a material that is not homogeneous, the route of the light will not be in a straight line; rather, the path of the light will be decided by the path that is the shortest. If the material has a refractive index of $n(x, y, z)$, then the path that light takes to go from A to B must fulfill an optical path such that it achieves its minimum,

$$L_R = \int_A^B n(s) ds \quad 3.70$$

where ds in the formula is the length of an arc defined by Euclidean geometry. That is to say, light will always be transmitted via the neighborhood with the lowest value of n . Within the realm of geometrical optics, the Fermat principle may be used to provide an explanation for optical phenomena such as refraction and reflection. This concept is congruent with the assumption that the local minima on the active contour should be achieved by the local minimizing of $g(|\nabla I|)$ in the image segmentation snake model. The idea of this principle is as follows: (Liu et al., 2017). Consequently, in Sapiro et al. (1995), it is proposed that the active contour may be determined by minimizing the energy functional:

$$L_R(C) = \int_0^{L(C)} g(|\nabla I[C(s)]|) ds , \quad 3.71$$

where $L(C)$ represents the arc length of the closed curve C and $L_R(C)$ is the weighted arc length.

This equation can also be written as

$$E(C) = \oint g(|\nabla I[C(s)]|) ds \quad 3.72$$

(2) Prove equation (3.69)

Using the parametric representation of a curve, the closed curve C is expressed as $C(p): [0,1] \rightarrow R^2$, $C(0) = C(1)$. Given that $ds = |C_p| dp$, equation (3.72) can be rewritten into

$$E(C(p)) = \int_0^1 g(C(p) |C_p(p)|) dp \quad 3.73$$

In order to derive the gradient descent flow of this formula, the auxiliary variable t must first be put into C before the formula can be recast into its final form.

$$E(C(p, t)) = \int_0^1 g(C(p, t) |C_p(p, t)|) dp \quad 3.74$$

So this thesis have

$$\begin{aligned} E(C(p, t)) &= \int_0^1 g(C(p, t) |C_p(p, t)|) dp \\ \frac{dE}{dt} &= \int_0^1 \left\{ \frac{d}{dt} g(C(p, t) |C_p(p, t)|) \right\} dp \\ &+ \int_0^1 g(C(p, t) \left\{ \frac{d}{dt} |C_p(p, t)| \right\}) dp \\ &= \int_0^1 \{ \nabla g(C(p, t) \cdot C_t(p, t)) |C_p(p, t)| \} dp \\ &+ \int_0^1 g(C(p, t) \{ C_{pt}(p, t) \cdot T \}) dp \end{aligned} \quad 3.75$$

In the equation, the letter T stands for the unit tangent vector of the letter C. When the technique of partial integration is used on the second component of the equation (3.75), and when it is taken into consideration that C is a closed curve, then this thesis obtain

$$\begin{aligned} \int_0^1 g(C(p, t))\{C_p(p, t) \cdot T\}dp &= - \int_0^1 \{g(C(p, t))T\}_p C_t(p, t)dp \\ &= - \int_0^1 \{\nabla g(C(p, t)) \cdot C_p(p, t)\}[C_t(p, t) \cdot T]dp \\ &\quad - \int_0^1 [g(C(p, t))]T_p \cdot C_t(p, t)dp . \end{aligned}$$

Substituting it into equation (3.75) and using s to replace the parameters p in the above equation, and $|C_s(s, t)| \equiv 1$, this thesis have

$$\begin{aligned} \frac{dE}{dt} &= \int_0^{L(C)} \{\{\nabla g(C(s, t)) \cdot C_t(s, t)\} - \{\nabla g(C(s, t)) \cdot T\}[T \cdot C_t(s, t)]\} ds \\ &\quad - \int_0^{L(C)} \{g(C(s, t))\}T_p \cdot C_t(p, t)\} ds \\ &= \int_0^{L(C)} \{\nabla g(C) - [\nabla g(C) \cdot T]T - g(C)T_s\} \cdot C_t ds \end{aligned}$$

Because $\nabla g(C) - [\nabla g(C) \cdot T]T = [\nabla g(C) \cdot N]N$ and $T_s = \sigma N$, this thesis have

$$\frac{dE}{dt} = \int_0^{L(C)} \{\nabla g(C) \cdot N - \nabla g(C)\sigma\}N \cdot C_t ds$$

In order to make $\frac{dE}{dt} < 0$, C_t should satisfy $\cdot C_t = \nabla g(C)\sigma - \nabla g(C) \cdot N$. Now the equation (3.68) is approved.

(3) Variational level set representation

If the level set method discussed above is used, then the corresponding PDE for the embedded function is

$$\frac{\partial u}{\partial t} [g\sigma - \nabla g \cdot N] |\nabla u| \operatorname{div} \left(g \frac{\nabla u}{|\nabla u|} \right) \quad 3.76$$

Terbish et al. (2017) present a novel level set approach for the curve evolution issue that they name the variational level set method. Their method is developed from the energy functional minimization of curves. To begin, this thesis make use of the specialized functions that are described below (called heavyside functions),

$$H(z) = \begin{cases} 1, & z \geq 0 \\ 0, & z < 0 \end{cases}$$

The loop integral formula equation (3.68) along the C can be rewritten as an area division $\oint_C g(C) ds = \iint_{\Omega} g(x, y) |\nabla H(u)| dx dy$. Because $\nabla H(u) = \delta(u) \nabla u$, $\delta(z) = \frac{d(H(z))}{dz}$, equation (3.68) can be rewritten as the functional of imbed function u

$$J(u) = \iint_{\Omega} g(x, y) \delta(u) |\nabla u| dx dy. \quad 3.76a$$

Using the variational method, the gradient descent flow of the upper type can be obtained

$$\frac{\partial u}{\partial t} = \delta(u) \operatorname{div} \left(g \frac{\nabla u}{|\nabla u|} \right) \quad 3.77$$

In order to make it a computable PDE, δ in the formula needs to be approximated by regularization δ_r , that is equation (3.77) can be rewritten as

$$\frac{\partial u}{\partial t} = \delta_r(u) \operatorname{div} \left(g \frac{\nabla u}{|\nabla u|} \right) \delta_r = \frac{dH_r(z)}{dz}. \quad 3.78$$

Here, $H_r(z)$ is called the regularized Heaviside function. In principle, it can be any function that satisfies the following conditions: $H_r(z) \xrightarrow{z=0} H(z)$.

PDEs (3.76) and (3.78) look like the same. The difference is just $|\nabla u|$ and $\delta_r(u)$. Nonetheless, there is a significant difference between the two PDEs from a mathematical standpoint. The hyperbolic type is represented by the equation 3.77, whereas the parabolic type is represented by the equation 3.78 is represented by the equation 3.77,

whereas the parabolic type is represented by the equation 3.78. The latter one has a greater degree of stability than the one that came before it. Hence, The numerical implementations need a larger time step, and in many instances, this may be done without the need for the embedded function to be re-initialized. The application of the variational level set technique to the problem of curve development is predicated on the idea that the issue is caused by a decrease in the "energy" functional $J(C)$ of the C curves. This idea underlies the use of the variational level set approach. This does not, however, suggest that the variational level set approach may serve as a suitable replacement for the level set method. In order to do this, first the embedded function u is presented, and then the Heaviside function is used to transform $J(C)$ into $J(U)$. The procedure that is used in order to get the PDE for u is known as the calculus of variations. The energy function of C is first minimized using the variational technique, and then the equation of motion for C is generated using the information gained from that process. This is what the procedure for establishing levels consists of. After this, the embedded function will be called into play so that the PDE may be retrieved on your behalf. The problem is that the evolution of curves and surfaces is not completely derived from the process of minimizing energy consumption. This is the source of the difficulty.

In fluid mechanics, the material sciences, and a wide variety of other domains, there are many different sorts of interface evolution issues. In situations like these, the evolution equation (PDE) of the interface may be simply determined from the physical principles that govern it. In situations like this, the use of level-set approaches is possible. Consequently, the level-set approach is superior to the variational level-set method in terms of suitability.

3.4.3 Improved Variational Level Set Method

In order to completely avoid re-initialization, an improved variational level set method is proposed in (Li et al., 2008) by adding an item in the "energy" functional related to the embedded function u , i.e. $P(u) = \iint_{\Omega} \frac{1}{2} (|\nabla u| - 1)^2 dx dy$. Its gradient descent flow is $\frac{\partial u}{\partial t} = [\nabla^2 u - \text{div}(\frac{\nabla^2 u}{|\nabla u|})]$. Obviously, minimizing $P(u)$ means that the requirement of $|\nabla u| = 1$, that is, the embedded function u should be kept as a distance

function as far as possible in the evolution process. The above equation can be rewritten as

$$\frac{\partial u}{\partial t} = \operatorname{div} \left[\left(1 - \frac{1}{|\nabla u|} \right) \nabla u \right]. \quad 3.79$$

This is a nonlinear heat conduction equation with a conductivity rate of $\alpha = 1 - \frac{1}{|\nabla u|}$. Obviously when $|\nabla u| > 1$ and $\alpha > 0$, the heat is conducted to the outside, and $|\nabla u|$ is reduced; The other way around, when $|\nabla u| > 1$ and $\alpha < 0$, $|\nabla u|$ is increased. As a result, any deviation from the local $|\nabla u| = 1$ will be corrected in the subsequent evolution. Thus, re-initialization is not necessary at all.

For example, after adding $P(u)$ to the functional of equation (3.4a), this thesis have

$$J(u) = \mu \iint_{\Omega} \frac{1}{2} (|\nabla u| - 1)^2 dx dy + \iint_{\Omega} \frac{1}{2} g(x, y) \delta(u) |\nabla u| dx dy \quad 3.80a$$

The Corresponding gradient descent flow is

$$\frac{\partial u}{\partial t} = \mu \left[\nabla^2 u - \operatorname{div} \left(\frac{\nabla u}{|\nabla u|} \right) \right] + \delta_r(u) \operatorname{div} \left(g \frac{\nabla u}{|\nabla u|} \right), \quad 3.81b$$

where μ is a chosen constant.

The advantage of the improved variational level set method is that it not only completely avoids the problem of re-initialization, but also simplifies the work of initializing the embedded function $u_0(x, y)$. Since the model itself has the ability to automatically approximate the embedded function u as a distance function, initialization does not necessarily strictly require that $u_0(x, y)$ be a distance function C^0 . Based on this consideration, (Liu et al., 2017) proposed the below initialization scheme

$$u_0 = \begin{cases} -\alpha, & (x, y) \in \text{internal of } C_0 \\ 0, & (x, y) \in C_0 \\ \alpha, & (x, y) \in \text{external of } C_0 \end{cases}, \quad 3.82c$$

where $\alpha \approx r$, and r is the parameter of regularized Heaviside function.

3.5 Chan-Vese Model and Region-Scalable Fitting Model

3.5.1 CV Model

The following descriptors may be used for the CV model: The picture set I that is supplied is cut in half by the active contour C , and these halves are recorded as the inner (C) and outside (O) of the model, respectively (C). The average value of the curve's internal gray level is represented by the symbol c_1 , and the average value of the curve's exterior gray level is represented by the symbol c_2 ; these two values are individually represented by the symbols c_1 and c_2 . According to the definition of the fitting energy function that was provided by Ni et al. (2016), it is defined as follows:

$$E^{CV}(c_1, c_2, C) = v \cdot \text{Length}(C) + \mu \cdot \text{Area}(\text{inside}(C)) + \lambda_1 \int_{\text{inside}(C)} |1 - c_1|^2 dx dy + \lambda_2 \int_{\text{outside}(C)} |1 - c_2|^2 dx dy, \quad 3.83$$

where $\text{Length}(C)$ is the length of the contour curve which plays a role of regularization, $\text{Area}(\text{inside}(C))$ is the internal area of the contour curve, $\mu > 0$ and $v > 0$ are two parameters, λ_1 and λ_2 are two weight coefficients, and λ_1 and $\lambda_2 > 0$. The first two terms on the right-hand side of the formula are referred to as the "fitting" terms. These terms are mostly used to regulate the fitting error for the contour curve fit edge. The other two terms are referred to as the "smooth" words because they allow for the evolution process to proceed along a smooth curve. With the process of reducing the energy functional, one is able to derive the ultimate location of the contour curve.

Let the level set function u be represented by the following formula:

$$\begin{cases} u(x, y) = 0, & (x, y) \in C \\ u(x, y) > 0, & (x, y) \in \text{internal of } C \\ u(x, y) < 0, & (x, y) \in \text{external of } C \end{cases} \quad 3.84a$$

In order to apply the level set method, the Heaviside function is introduced

$$H(x) = \begin{cases} 1, & x \geq 0 \\ 0, & x < 0 \end{cases}$$

The Dirac function is

$$\delta(x) = \frac{d}{dx} H(x)$$

The Heaviside function is used in this approach to split the area of evolution, and the Dirac function is used to determine the value of evolution around the zero-level set function. Together, these functions are referred to as the Heaviside-Dirac method. Here,

$$\text{Length}(C) = \int_0^{L(C)} 1 \cdot ds = \int_{\Omega} \delta(u) |\nabla u| dx dy$$

$$\text{Area}(\text{inside}(C)) = \int_{\Omega} H(u) dx dy$$

$$\int_{\text{inside}(C)} |I(x, y) - c_1|^2 dx dy = \int_{\Omega} |I(x, y) - c_1|^2 H(u) dx dy . \quad 3.85b$$

The regularized Heaviside function is often used in the numerical calculation as

$$H_r = \frac{1}{2} \left[1 + \frac{1}{\pi} \arctan \left(\frac{x}{r} \right) \right].$$

For the constant r , the corresponding Dirac function is

$$\delta_r(x) = \frac{1}{\pi} \cdot \frac{r}{x^2 + r^2} .$$

The goal is to expand the capture range and to prevent the occurrence of singular cases. Thus, the energy functional of the level set function is obtained as

$$\begin{aligned} E_r^{CV}(c_1, c_2, C) &= \int_{\Omega} \delta_r(u) |\nabla u| dx dy + \int_{\Omega} H_r(u) dx dy \\ &+ \int_{\Omega} |I(x, y) - c_1|^2 H_r(u) dx dy \\ &+ \int_{\Omega} |I(x, y) - c_2|^2 (1 - H_r(u)) dx dy . \end{aligned} \quad 3.86$$

At this point, the level set of the image $I(x, y)$ is

$$I(x, y) = c_1 H_r(u) + c_2 (1 - H_r(u)) .$$

Fixing u and minimizing the energy functional $E_r^{CV}(c_1, c_2, C)$, one has

$$\begin{aligned} c_1 &= \frac{\int_{\Omega} I(x, y) H_r(u(x, y)) dx dy}{\int_{\Omega} H_r(u(x, y)) dx dy} , \\ c_2 &= \frac{\int_{\Omega} I(x, y) (1 - H_r(u(x, y))) dx dy}{\int_{\Omega} (1 - H_r(u(x, y))) dx dy} \end{aligned} \quad 3.87$$

In the CV model, this thesis usually set $v = 0$. The energy functional $E_r^{CV}(c_1, c_2, C)$, is minimized using the variation method and the gradient descent flow technique and Euler-Lagrange equation is obtained as

$$\frac{\partial u}{\partial t} = v \delta_r(u) \operatorname{div} \left(\frac{\nabla u}{|\nabla u|} \right) + \delta_r(u) (\lambda_2 (1 - c_2)^2 - \lambda_1 (1 - c_1)^2) \quad 3.88(a)$$

According to (Gu et al., 2017), the Dirac function has a tight definition, which restricts the globality of the edge of the picture. Moreover, the function cannot be recognized reliably since the target edge is located outside of the closed curve. The CV

model solely uses information about the global region in order to optimize c_1 and c_2 . It does not take into account any changes that may have occurred to the grey value of the target or the background region of the picture. As a result, the CV model is unable to segment the picture because of the uneven grayscale. The solution to equation (3.88(a)), which includes a curvature element, is very difficult to obtain. In order to preserve numerical consistency, this thesis are going to need to use a certain numerical procedure. Moreover, in order to preserve the numerical stability of the CV model, During each update, the level set function $u(x,y,t)$ has to be reinitialized after first being set up as a symbol distance function during the initialization process. When this is happening, reinitialization might induce a movement in the location of the zero level set. Also, it raises the total amount of calculation and takes up a considerable amount of additional time. The iterative equation (3.88(b)) is shown below:

$$H(x) = \begin{cases} \varphi_t = \text{sign}(u(t)(1 - |\nabla\varphi|)) \\ \varphi(0, \cdot) = u(t, \cdot) \end{cases} \quad 3.89(b)$$

3.5.2 RSF Model

The well-known RSF model, which is based on variable region fitting energy functions, was presented by Li et al. as a solution to the issues that were caused by the CV model (Xu et al., 2015). Another name for this model is the LBF (local binary fitting) model (Li et al., 2007). The RSF model makes use of two local fitting functions called $f_1(x)$ and $f_2(x)$ in order to obtain an approximation of the local area's average gray-value on both sides of the target.

For any point $x \in \Omega$ in the image area and contour curve C , and the fitting energy is

$$E_x^{RSF}(f_1, f_2, C) = \lambda_1 \int_{\text{inside}(C)} K_\sigma(x-y) |I(y) - f_1(x)|^2 dx dy + \lambda_2 \int_{\text{outside}(C)} K_\sigma(x-y) |I(y) - f_2(x)|^2 dx dy , \quad 3.90$$

where λ_1 and λ_2 are two positive constant numbers (usually fixed to constant 1), The gray fitting values of the picture at location x are denoted by the expressions $f_1(x)$ and $f_2(x)$.

The gray value $I(y)$ is only calculated for a small region that is centered on the point x ; the size of this region is determined by the kernel function K . Hence, equation (3.69), which is also mentioned in (Xu et al., 2015), as a regional scale variable fitting (RSF) energy of contour C at point x . $K : \mathbb{R}^2 \rightarrow \mathbb{R}$ is a kernel function. It is satisfied the local property.

1. $K(u) = K(|u|)$;
2. If $|u| < |v|$, then $K(u) \geq K(v)$, meanwhile $\lim_{|u| \rightarrow \infty} K(u) = 0$
3. $\int_{\mathbb{R}^2} K(u) = 1$

Due to the fact that the kernel function $K(u)$ has locality (attribute 2), $f_1(x)$ and $f_2(x)$ are mostly decided by the gray values that are in close proximity to one another. It possesses traits that are considered "local." It should come as no surprise that picking the appropriate kernel function for the RSF model is of the utmost significance. There are a lot of kernel functions that can meet these requirements for the local environment. The initial study (Li et al., 2007) and the subsequent study (Xu et al., 2015) both make use of the Gaussian kernel function.

$$K_{\sigma}(u) = \frac{1}{\sqrt{2\pi}\sigma} e^{-\frac{|u|^2}{2\sigma^2}}, u \geq 0,$$

where, $\sigma > 0$ is a scale parameter.

Let u be the level set function of the contour curve C . Using the level set method, one has

$$E_x^{RSF}(f_1, f_2, C) = \lambda_1 \int_{inside(C)} K_{\sigma}(x - y) |I(y) - f_1(x)|^2 H(u) dy + \lambda_2 \int_{outside(C)} K_{\sigma}(x - y) |I(y) - f_2(x)|^2 (1 - H(u)) dy \quad 3.91$$

The total fitting energy function is

$$E^{RSF} = \int_{\Omega} E_x^{RSF} dx .$$

In order to avoid periodic initialization of the level set, the RSF model combines the methods that do not need reinitialization (Li et al., 2008). Adding the set regularization $\int_{\Omega} \frac{(|\nabla u|-1)^2}{2} d\sigma$ term, the total energy functional of the RSF model is

$$\begin{aligned} E_x^{RSF}(f_1, f_2, u) = & \lambda_1 \int_{inside(C)} K_{\sigma}(x-y)|I(y) - f_1(x)|^2 H(u) dy dx \\ & + \lambda_2 \int_{outside(C)} K_{\sigma}(x-y)|I(y) - f_2(x)|^2 (1 \\ & - H(u)) dy dx + v \int_{\Omega} |\nabla H(u(x))| dx \\ & + \mu \int_{\Omega} \frac{(|\nabla u| - 1)^2}{2} dx \end{aligned} \quad 3.92$$

Firstly, fixing u in above formula, after minimizing the energy functional $E_x^{RSF}(f_1, f_2, u)$ with respect to $f_1(x)$ and $f_2(x)$, this thesis have

$$\begin{aligned} f_1(x) &= \frac{\int_{\Omega} K_{\sigma}(x-y)I(y)H(u(y))dy}{\int_{\Omega} K_{\sigma}(x-y)H(u(y))dy} \\ f_2(x) &= \frac{\int_{\Omega} K_{\sigma}(x-y)I(y; 1-H(u(y)))dy}{\int_{\Omega} K_{\sigma}(x-y; 1-H(u(y)))dy} \end{aligned}$$

In fact, the fitting function $f_1(x)$ and $f_2(x)$ are the weighted averages of the image grey values $I(y)$ in area inside(C) and outside(C). The weight is $K_{\sigma}(x-y)$. Due to the local character of the Gaussian kernel K_{σ} , the effect of the gray value $I(y)$ on $f_1(x)$ and $f_2(x)$ decreases as the distance between y and x increases. When $|x-y| > 3\sigma$, the effect of $I(y)$ is almost reduced to zero. Therefore, the values of the fitting functions $f_1(x)$ and $f_2(x)$ are determined primarily by the gray value of point y in $\{y: |x-y| < 3\sigma\}$.

Then fixing the fitting factors $f_1(x)$ and $f_2(x)$, after minimizing the energy functional E^{RSF}

with respect to u , the evolution equation of the energy functional E^{RSF} is obtained using a gradient descent flow:

$$\frac{\partial u}{\partial t} = -\delta_r(\lambda_1 e_1 - \lambda_2 e_2) + \mu \left[\nabla^2 u - \operatorname{div} \left(\frac{\nabla u}{|\nabla u|} \right) \right] + v \delta_r(u) \operatorname{div} \left(\frac{\nabla u}{|\nabla u|} \right), \quad 3.93$$

where $e_1 = \int_{\Omega} K_{\sigma}(x - y) |I(y) - f_1(y)|^2 dy$, $e_2 = \int_{\Omega} K_{\sigma}(x - y) |I(y) - f_2(y)|^2 dy$.

The RSF model is the energy functional, which is defined by the local binary fitting energy based on Gaussian kernel function. The functions $f_1(x)$ and $f_2(x)$ are a local energy which are related to variance. As a result, the RSF model is capable of segmenting the picture with inhomogeneous intensity more effectively. In addition, the RSF model utilizes integrated models that do not need reinitialization in order to circumvent the need for periodic initialization of the level set function (Li et al., 2008). The pace of evolution has substantially accelerated as a result. Although the RSF model is capable of better segmenting the picture with intensity inhomogeneity, it is still very sensitive to the beginning location of the active contour in the image. It is simple to descend to the level of least value in a given area when the original contour selection is inappropriate. The outcome of the segmentation will be incorrect if this happens. The local peculiarities of the RSF model are the primary contributors to the occurrence of this phenomenon. The fitting functions $f_1(x)$ and $f_2(x)$ in the model are fitted to the local grayscale of the image. Therefore, the different fitting values obtained at different locations results in that the RSF model being sensitive to the initial contour position.

One of the probable explanations for this is that energy $E_x^{RSF}(f_1, f_2, u)$ only takes into account the spatial information of the picture pixel and ignores the information on the grayscale variation of the pixel. This thesis combined the CV model and the RSF model with information entropy and developed a new local fitting energy function to replace the ones that were present in the CV model and the RSF model. This was done on the basis of an analysis of the benefits and drawbacks of the CV model and the RSF model, which can be found above. Finally, this thesis came up with a brand new CER model in an effort to enhance both the CV model, which is incapable of segmenting an image with an uneven grayscale, and the RSF model, which is sensitive to the initial

position and has a high level of noise. In order to do this, this thesis developed a new CER model.

3.6 CER Model Based on Information Entropy

3.6.1 Information Entropy

Entropy may be thought of as the amount of disorder that exists inside a system. It finds significant use in domains like cybernetics, number theory, astronomy, the biological sciences, and many more. Moreover, more particular definitions may be found throughout several fields of study. In many different areas of study, entropy serves as a crucial metric. Rudolf Clausius is the one who first suggested the concept of entropy. The earliest use of it may be found in thermodynamics. After that, Lombardi (2016) generalized Boltzmann's formula and came up with the idea of information entropy. The entropy of the information is a description of the unpredictability of the source. It represents the typical quantity of information that can be found for each target inside the source. The fundamental concept underlying information theory is that of entropy, which may be thought of as either a random event of uncertainty or the amount of information measured. In information theory, the fundamental idea is referred to as "the quantity of information." The entropy of the information is calculated by taking into consideration the statistical qualities of the whole source. It is a measurement of the entire information source based on the mean, and it is used to estimate how random the information is. Entropy increases in direct proportion to the degree to which a variable is subject to uncertainty. The establishment of entropy as the scientific theoretical underpinning of contemporary information theory was a major step toward the advancement of information theory, which was substantially aided by the introduction of this concept. Image processing received an introduction to the idea of entropy thanks to the work of (Bera et al., 2016). The process of picture segmentation currently relies heavily on its effectiveness as a tool. The image entropy may be stated as the average amount of information contained inside the picture's information source. It is represented as the number of bits that make up the image's grayscale set. Based on Shannon's information theory, if p_i is a given distribution of a given image $I = (I_i)$, then image entropy is:

$$E_l = - \sum_i p_i \log_2 p_i , \quad 3.94$$

where the likelihood that a certain grayscale is present in the picture is represented by the distribution function p_i of the image. The definition of the distribution function p_i might be a number of different things; how it is defined is determined by the technique that was used to segment the picture. As an example, in the process of edge extraction, in order to take into account the tonal range of the picture, Shiozaki (Wang et al., 2018) defined the p_i as the grey scale distribution $p_i = I_i / \sum_j I_j$ in the image, where I_i is the grayscale of pixel i . In the image thresholding method (Fortin et al., 2017), distribution function p_i can be approximately obtained from a given histogram. In this section, our distribution function is obtained through the image histogram.

The purpose of the entropy-based picture segmentation approach is to reduce the amount of image information that is lost. Because of this, this thesis are able to employ image entropy to fix the backdrop. In the meanwhile, the entropy of the picture represents the degree to which the grayscale of the image is scattered. A high entropy value is present in an image with a reasonably uniform distribution of gray tones across the picture. On the other hand, the entropy is low when the gray distribution of the picture has greater discreteness. Entropy is the product of the dynamic relationship that exists between all of the image's pixels. It is not sensitive to noise that originates from a single spot. As a consequence of this, it is equipped with anti-noise and filtering capabilities. The global entropy is represented as a value, whereas the local entropy is represented as a matrix. Image entropy saves a significant amount of time when contrasted with the convolution process that is performed on the matrix.

3.6.2 Effects of Adding Information Entropy to RSF Model

The CV model is a kind of model that is based on the global property of the picture, as was mentioned earlier on in the discussion. The CV model's most significant shortcoming is that it is unable to segment a picture with an uneven grayscale. The fact that the CV model does not take into account the difference in gray value between the target and the background region of the picture is the primary cause of this problem. On

the other hand, the RSF model, also known as the LBF model, is a model that is constructed using the image's local information. It has the ability to segment the uneven grayscale picture successfully. Such as a picture from an MRI. Yet, due to the fact that the model is localized, it is relatively simple for the model to enter the local extremum, which results in the model being very sensitive to the contour initialization. The RSF model, on the other hand, does not have a particularly high resilience to noise. The main reason for these problems is that the gray value change of the image is not considered when the local fitting energy $E_x^{RSF}(f_1, f_2, C)$ is defined. In order to overcome the above shortcomings of the RSF model, this thesis introduce the concept of information entropy (see equation (3.38)), the energy functional in the RSF model is rewritten as follows:

$$E_x^{RSF}(f_1, f_2, C) = \int_{\Omega} E_t(x) E_t(f_1(x), f_2(x), C) dx \quad 3.95$$

A new model is formed by combining the global energy and the local energy. In equation (3.74),

$E_t(x) = E(x, B(x, t))$ is the local information entropy of point $x \in \Omega$, where $B(x, t) = \{y: |x - y| \leq t\}, t > 0$ is the circle centered on point x with radius t .

In addition, the smoothness of the image contour C is ensured by controlling its length $|C|$. So combining with the above formula, the new energy functional can be written as the following:

$$\begin{aligned} E^{ZRSF1}(f_1, f_2, C) &= E^{ZRSF}(f_1, f_2, C) + v|C| \\ &= \sum_{i=1}^2 \lambda_i \int_{\Omega} E_t(x; \int_{\Omega} K_{\sigma}(x - y) |I(y) - f_i(x)|^2 dy) dx \\ &\quad + v|C| \end{aligned} \quad 3.96$$

Using Heaviside function, the energy function can be expressed as follows:

$$\begin{aligned}
E^{ZRSF1}(f_1, f_2, u) &= E^{ZRSF}(f_1, f_2, u) + v \int_{\Omega} |\nabla H(u(x))| dx \\
&= \sum_{i=1}^2 \lambda_i \int_{\Omega} E_t(x; \int_{\Omega} K_{\sigma}(x \\
&\quad - y) |I(y) - f_i(x)|^2 M_i(u(y)) dy) dx \\
&\quad + v \int_{\Omega} |\nabla H(u(x))| dx ,
\end{aligned} \tag{3.97}$$

where $M_1 = H(u(x))$, $M_2 = 1 - H(u(x))$, $\int_{\Omega} |\nabla H(u(x))| dx$ is the length of the contour C (i.e. the zero level set of u), and $\delta(\cdot)$ is the derivative of $H(\cdot)$.

Meanwhile, in order to avoid the periodic initialization of the level set function, this thesis consider an internal energy term for the level set function in the energy functional $E^{ZRSF1}(f_1, f_2, u)$ of equation (3.41):

$$P(u) = \int_{\Omega} \frac{1}{2} |\nabla u(x) - 1|^2 dx \tag{3.92a}$$

When $\nabla u(x) = 1$, $P(u)$ is kept to a minimum. This means that the level set function must, to the greatest extent feasible, maintain its status as a sign distance function while the evolution is taking place. Hence, the level set of the energy functional that is based on information entropy is

$$\begin{aligned}
E^{ZRSF1}(f_1, f_2, u) &= E^{ZRSF}(f_1, f_2, u) + v \int_{\Omega} \delta(u(x)) |\nabla(u(x))| dx \\
&\quad + \mu \int_{\Omega} \frac{1}{2} |\nabla u(x) - 1|^2 dx \\
&= \sum_{i=1}^2 \lambda_i \int_{\Omega} E_t(x; \int_{\Omega} K_{\sigma}(x \\
&\quad - y) |I(y) - f_i(x)|^2 M_i(u(y)) dy) dx \\
&\quad + v \int_{\Omega} \delta(u(x)) |\nabla(u(x))| dx + \mu \int_{\Omega} \frac{1}{2} |\nabla u(x) - 1|^2 dx ,
\end{aligned} \tag{3.93a}$$

where $\mu > 0$ is weight parameter.

3.6.3 CV- Entropy- RSF (CER) Model

A weighted RSF model that is based on local entropy has been presented up there in order to improve the original model's resilience with regard to the starting contour location and the level of noise that is there. In fact, owing to the heterogeneity of the gray scale, the difference in gray scale across various places in a picture that has an uneven distribution of gray is often varied. This is because a picture with an uneven distribution of gray contains a picture that has an uneven distribution of gray. This thesis creates a new local fitting energy function to replace the ones that are in the CV model and the LBF model. This is done in order to better deal with the phenomenon of intensity inhomogeneity and to take into consideration the benefits and drawbacks of the CV model and the RSF model (Akram et al., 2017). Because of this, we will be able to deal with the phenomenon of intensity inhomogeneity in a more effective manner. The following is a definition of the new energy functional:

$$E^{CER}(f_1, f_2, c_1, c_2, C) = \omega E^{CV}(c_1, c_2, C) + (1 - \omega)E^{ZRSF}(f_1, f_2, C) , \quad 3.98$$

where the range of $0 \leq \omega \leq 1$. constants c_1, c_2 are the average gray values in the inside and the outside of evolution curve of the original image area, respectively, and f_1, f_2 are the fitting value of the image at the point x . Using Heaviside function $H(u)$, the level set of energy function is:

$$\begin{aligned} E^{CER}(f_1, f_2, c_1, c_2, C) &= \omega E^{CV}(c_1, c_2, C) \\ &+ (1 - \omega)E^{ZRSF}(f_1, f_2, C)v \int_{\Omega} \delta(u(x))|\nabla(u(x))|dx \\ &+ \mu \int_{\Omega} \frac{1}{2} |\nabla u(x) - 1|^2 dx \\ &= \omega \left[\lambda_1 \int_{inside(C)} |I(x, y) - c_1|^2 dx dy \right. \\ &\left. + \lambda_2 \int_{outside(C)} |I(x, y) - c_2|^2 dx dy \right] + (1 \\ &- \omega) \sum_{i=1}^2 \lambda_i \int_{\Omega} E_t(x) \int_{\Omega} K_{\sigma}(x \\ &- y) |I(y) - f_i(x)|^2 M_i(u(y)) dy) dx + H(u, v) \end{aligned} \quad 3.99$$

Where, $H(u, v) = v \int_{\Omega} \delta(u(x)) |\nabla(u(x))| dx + \mu \int_{\Omega} \frac{1}{2} |\nabla u(x) - 1|^2 dx$.

3.7 Hybrid Level Set Image Segmentation Method Based on Kernel Metric

The pervious part discusses the segmentation method of uneven grayscale images, and does not pay attention to the effect of noise on segmentation. In reality, images are often interfered by noise during the process of acquisition and transmission, which seriously reduces image quality. The segmentation method based on offset correction level set usually uses Euclidean distance to construct data items, but the noise robustness of this measurement method is poor. For an image with gray unevenness and noise at the same time, the local grayscale changes in each target area are caused by the gray unevenness and noise. In this way, the local image variance cannot be used to measure the degree of gray-scale unevenness of the image. The adaptive scale operator proposed by the pervious part will be invalid, affecting the estimation of the offset field and reducing the segmentation accuracy of the gray-scale uneven image.

In recent years, some mixed level set models have been used to deal with uneven images ((Wang et al., 2010; Wang et al., 2009; Shyu et al., 2012; Liu et al., 2013 ; Jiang et al., 2014; Wen, 2014; Wang et al., 2014; Wang et al., 2014; Wang et al., 2018; Li et al., 2015; Jiang et al., 2015; Zhou et al., 2016; Huang et al., 2015; Soomro et al., 2016; Shi and Pan, 2016; Mondal et al. al., 2016; Liu et al., 2017; Soomro et al., 2018; Wang et al., 2015; Cai et al., 2018). Liu et al. (2013) combined the LIC model based on local information (Li et al., 2011) with the CV model based on global information (Chan, and Vese, 2001) and proposed the LIC-CV model (Liu et al., 2013). This model can handle slightly uneven grayscale images and is robust to the initial contour. The level set evolves quickly, but it is easily disturbed by noise.

As a solution to the issues mentioned above, this technique suggests using a hybrid level-setting method that is based on kernel metric (KMHLs). First, an enhanced multi-scale mean filter is put to use in order to make an estimate of the picture's offset field. Then, an offset correction is applied to the image in order to lessen the gray level inhomogeneity that the image has. After that, the kernel measurement technique is used to construct energy items using local and global information in the appropriate

proportions. As an additional measure, the local similarity measurement approach has been included in the energy term in order to reduce the impact of noise. In order to develop a hybrid energy function, a new weight function is used to adaptively alter the weight coefficients of the two different energy components. In conclusion, the count gradient regularization term is implemented in order to further lessen the impact that noise has. After first being provided in the form of a two-phase level-set segmentation, the suggested method for segmentation is later modified to support several phases of the process.

3.7.1 Kernel Measurement

The offset correction level set method based on K-means clustering usually uses Euclidean distance to construct data items, but this measurement method lacks robustness to noise and outliers, and severely reduces the segmentation accuracy of noisy images. Therefore, the L_2 norm can be replaced by a non-linear distance metric. Usually, the kernel method is used for nonlinear distance measurement. The commonly used kernel function can be expressed as (Wu et al., 2015):

$$K(\mathbf{a}, \mathbf{b}) = \langle \varphi(\mathbf{a}), \varphi(\mathbf{b}) \rangle = \varphi(\mathbf{a})^T \varphi(\mathbf{b}) \quad 3.100$$

Among them, \mathbf{a} and \mathbf{b} are vectors with the same dimension, $\varphi(\cdot)$ represents the non-linear mapping from the original data space to the feature space, $\langle \cdot, \cdot \rangle$ represents the inner product operation, and T represents the transpose operation.

The Gaussian radial basis function is a commonly used kernel function (Wu et al., 2015), expressed as:

$$K(a, b) = \exp\left(-\frac{(a - b)^2}{\sigma}\right). \quad 3.101$$

Among them, the parameter σ represents the bandwidth of the kernel function, and $K(a, a) = 1$. Then, the non-Euclidean distance metric in the feature space is expressed as (Wu et al., 2015):

$$\begin{aligned}
\| \varphi(a) - \varphi(b) \|^2 &= (\varphi(a) - \varphi(b))^T \varphi(a) - \varphi(b) \\
&= K(a, a) + K(b, b) - 2K(a, b) \\
&= 2 - 2K(a, b)
\end{aligned}
\tag{3.102}$$

3.7.2 Hybrid Level Set Segmentation Algorithm

This section first uses an improved multi-scale mean filter to estimate the offset field of the image to reduce the gray-scale unevenness of the image. Then, the kernel metric and local similarity metric are used to suppress the influence of noise. Finally, the count gradient regularization term is used to further reduce the influence of noise.

3.7.3 Improved Multi-Scale Mean Filter

The MSF model (Wang et al., 2015) uses a multi-scale mean filter to estimate the offset field of the gray inhomogeneous image. However, this model uses a fixed number of scales. For some small-sized images, a larger scale will cause the offset field to be excessively smooth, and the local grayscale change information of the image cannot be obtained, leading to incorrect segmentation. Therefore, this thesis propose an improved multi-scale mean filter, which can approximate the offset field of the image and obtain more local variation information of the offset field.

The higher the degree of unevenness of the gray level of the image, the more severe the local gray level changes in the smooth area of the image. Therefore, try to use small-scale mean filtering to estimate the offset field of the image to obtain more local change information, which is beneficial to remove the serious grayscale inhomogeneity of the image, and only retains the slight grayscale inhomogeneity. The scale number k of the multi-scale mean filter is defined as:

$$k = \min (\text{round} (\sqrt{N_0/(4\pi)}), k_{max}) \tag{3.103}$$

Among them, N_0 is the number of pixels of the image I , and k_{max} is a positive integer, which represents the maximum number of scales of the multi-scale mean filter.

In this way, the i scale parameter of the multi-scale mean filter is expressed as:

$$r_i = i, i = 1, 2, \dots, k \quad 3.104$$

In addition, by weighting the image gray level to reduce the influence of salt and pepper noise and singular values, the mean filter with a scale of r_i is defined as:

$$AF_i(x) = \frac{\sum_{y \in R_{x,i}} I(y) \cdot w(y)}{\sum_{y \in R_{x,i}} w(y)} \quad 3.105$$

Among them, $R_{x,y} = \{y: |y - x| \leq r_i\}$ represents a partial circular area with x as the center and radius r_i . $w(\cdot)$ is the weight function of image gray level, defined as:

$$AF_i(x) = \frac{\sum_{y \in R_{x,i}} I(y) \cdot w(y)}{\sum_{y \in R_{x,i}} w(y)} \quad 3.106$$

Among them, $*$ is a convolution operator, K_0 is a normalized mean filter with a size of $(2w_0 + 1) \times (2w_0 + 1)$, and σ_0 is:

$$\sigma_0 = \left(\frac{1}{N_0 - 1} \sum_{j=1}^{N_0} (d(x_j) - \bar{d})^2 \right)^{0.5} \quad 3.107$$

Among them, $d(x) = |I(x) - \bar{I}|$, \bar{I} represents the average gray value of image I , and \bar{d} represents the average value of $d(x)$.

Then, the approximate estimation of the offset field of the uneven grayscale image is:

$$B_0(x) = \frac{1}{k} \sum_{i=1}^k AF_i(x) / \bar{I} \quad 3.108$$

According to the uneven gray scale image model, through offset correction, the image I_1 after offset correction is obtained as:

$$I_1(x) = \frac{I(x)}{B_0(x)}, x \in \Omega \quad 3.109$$

The improved multi-scale averaging filter can well eliminate the unevenness of slightly uneven grayscale images, while for severely uneven grayscale images, it can greatly reduce the unevenness, leaving only slight grayscale unevenness. At the same time, the filter has strong robustness to noise.

3.7.4 Energy Functional

The image I_1 after the offset correction generally has slight grayscale unevenness. The LIC-CV model (Liu et al., 2013) can segment images with slight gray unevenness quickly, accurately and robustly. Therefore, this thesis use the LIC-CV model to construct the energy functional, and can use fixed scale parameters. The kernel function estimates the offset field and eliminates the influence of scale parameters on the segmentation of uneven grayscale images. At the same time, this thesis introduce the kernel metric method into the LIC-CV model, and replace the Euclidean distance metric in the energy functional with the kernel metric to improve the robustness to noise. In this way, the energy term based on local area information is expressed as:

$$E^{local}(\phi, b, c) = \sum_{i=1}^N \lambda_i \int (1 - K_L(I_1, b, c_i)) M_i(\phi(x)) dx \quad 3.110$$

Among them, $M_i(\phi)$ is the membership function, and $K_L(I_1, b, c_i)$ is defined as the form of the kernel metric:

$$K_L(I_1, b, c_i) = \exp \left(- \int K_\sigma(y - x; (I_1(x) - b(y)c_i)^2 / \sigma_1) dy \right) \quad 3.111$$

Among them, σ_1 can be obtained by using image I_1 and formula (5-8), $k_\sigma(\cdot)$ is a Gaussian kernel function with a standard deviation of σ .

The energy item based on the global area information is:

$$E^{global}(\phi, c^{cv}) = \sum_{i=1}^N \lambda_i \int (1 - K_G(I_1, c_i^{cv})) M_i(\phi(x)) dx \quad 3.112$$

Among them, $K_G(I_1, c_i^{cv})$ is defined as the form of nuclear metric:

$$K_G(I_1, c_i^{cv}) = \exp\left(-\frac{(I_1(x) - c_i^{cv})^2}{\sigma_1}\right) \quad 3.113$$

Secondly, considering the spatial relationship between the center pixel and its neighborhood, this thesis use the local block similarity (Yu et al., 2018) to further reduce the impact of noise, and the local and global energy terms can be converted into:

$$K_G(I_1, c_i^{cv}) = \exp\left(-\frac{(I_1(x) - c_i^{cv})^2}{\sigma_1}\right) \quad 3.114$$

$$E^{global}(\phi, c^{cv}) = \int \sum_{i=1}^N \lambda_i \int Z(|z - x|) (1 - K_G(I_1, c_i^{cv})) M_i(\phi(x)) dx dz \quad 3.115$$

Among them, the kernel function $Z(\cdot)$ is defined as:

$$Z(u) = \begin{cases} \frac{1}{2} \exp\left(-\frac{u^2}{h}\right), & |u| \leq r \\ 0, & other \end{cases} \quad 3.116$$

Among them, h is the bandwidth and r is the scale parameter.

In addition, this thesis suggest a novel weight function as a means of dynamically modifying the relative importance of regional and international energy variables. The weight of the global energy item is automatically adjusted according to the degree of gray-level unevenness of the image, whereas the weight of the local energy item is automatically adjusted according to the gray-level uniformity of the image. This is because the global energy item can only handle the gray-level uniform image, whereas the local energy item can handle the gray-level uneven image. The gray-level unevenness of the picture may be described using the offset field b , as stated by the gray-level uneven

image model (Li et al., 2011). The offset field value of the gray-level uniform image is 1, and the farther b deviates from 1, the image The more significant the unevenness in the gray scale. Hence, a new weight function is constructed by making use of the estimated offset field while the algorithm is going through the iteration process:

$$\omega(x) = v \exp(-l(b(x) - 1)^2) \quad 3.117$$

Among them, v and l are constant parameters.

v For the two-phase segmentation, that is, $N=2$, this thesis use a binary step function to represent the inner and outer regions of the evolution curve C , which is defined as:

$$\phi(x) = \begin{cases} -1, & x \in \text{inside}(C) \\ 1, & x \in \text{outside}(C) \end{cases} \quad 3.118$$

Then the membership function of each subregion is expressed as: $M_1(\phi(x)) = (1 + \phi(x))/2$ and $M_2(\phi(x)) = (1 - \phi(x))/2$. Using the weight function in formula (3.111) to combine the local and global energy terms, the mixed energy function is obtained as:

$$\begin{aligned} E^H(\phi, b, c, c^{cv}) &= \int \sum_{i=1}^2 \lambda_i \int (1 \\ &\quad - \omega(x)) Z(|z - x|) (1 - K_L(I_1, b, c_i)) M_i(\phi(x)) dx dz \quad 3.119 \\ &\quad + \int \sum_{i=1}^2 \lambda_i \int \omega(x) Z(|z - x|) (1 \\ &\quad - K_G(I_1, c_i^{cv})) M_i(\phi(x)) dx dz \end{aligned}$$

In addition, this thesis introduce the length term and rule term (Liu et al., 2018) based on L_0 regularization to regularize the level set function to ensure the stability of the level set evolution and further suppress the influence of noise. A weighted RSF model that is based on local entropy has been established at the top in order to increase the original model's robustness with respect to the beginning contour position and

considerable noise. This is a very important development. In fact, owing to the heterogeneity of the gray scale, the difference in gray scale across various places in a picture that has an uneven distribution of gray is often varied. This is because a picture with an uneven distribution of gray contains a picture that has an uneven distribution of gray. This thesis creates a new local fitting energy function to replace the ones that are in the CV model and the LBF model. This is done in order to better deal with the phenomenon of intensity inhomogeneity and to take into consideration the benefits and drawbacks of the CV model and the RSF model (Akram et al., 2017). Because of this, we will be able to deal with the phenomenon of intensity inhomogeneity in a more effective manner. The definition of the new energy function is as follows: (3.119). The final mixed energy functional may be written using the heavy function $H(u)$:

$$E^{CER} = \gamma E^H(\phi, b, c, c^{cv}) + \mu C(\nabla\phi) + \nu C(\phi + 1) \quad 3.120$$

Among them, γ , μ and ν are constant parameters, $C(\cdot)$ represents the L_0 counting operator, and $C(\phi + 1)$ represents the number of pixels satisfying $|\phi + 1| \neq 0$.

3.7.5 Level Set Evolution and Numerical Realization

By minimizing the energy function in equation (3.114), image segmentation can be achieved and the offset field can be estimated at the same time. Using the alternate iterative minimization method to solve, the energy functional E is minimized relative to each variable in the formula (3.114), and the closed solution of each variable M can be obtained:

$$c_i = \frac{\int (b * K) I_1 M_i(\phi) W_i^L dx}{\int (b^2 * K) M_i(\phi) W_i^L dx}, i = 1, \dots, N \quad 3.121$$

$$b = \frac{(I_1 J^{(1)}) * K}{J^{(2)} * K} \quad 3.122$$

$$= \frac{\int_{\Omega} I_1(x) M_i(\phi(x)) W_i^G dx}{\int_{\Omega} M_i(\phi(x)) W_i^G dx}, i = 1, \dots, N, \quad 3.123$$

among them, $J^{(1)} = \sum_{i=1}^N W_i^L c_1 M_i(\phi)$, $J^{(2)} = \sum_{i=1}^N W_i^L c_1^2 M_i(\phi)$, $W_i^L = \exp(-(I_1 - b c_1)^2 / \sigma_1)$, $W_i^G = \exp(-(I_1 - c_i^{cv})^2 / \sigma_1)$.

When c_i , b, s and c_i^{cv} are fixed, the relative level set function ϕ minimizes the energy function. However, two counting operators are introduced in the mixed energy functional, namely $C(\nabla\phi)$ and $C(\phi + 1)$, which cannot be solved directly by the gradient descent method. To this end, auxiliary variables are introduced, and the level set function is evolved using the alternate iteration optimal method (Liu et al., 2018). Similar to the LODL model, the mixed energy function is discretized, and three auxiliary variables φ , ξ and ψ are introduced for $\partial_x \phi_p$, $\partial_y \phi_p$ and ϕ respectively, the final discrete energy functional can be obtained as:

$$E = \gamma E^H(\phi, b, c, c^{cv}) + \mu C(\varphi, \xi) + \nu C(\psi) + \alpha \sum_p ((\partial_x \phi_p - \phi_p)^2 + (\partial_y \phi_p - \xi_p)^2) + \beta \sum_p (\phi_p + 1 - \psi_p)^2 \quad 3.124$$

among them, $C(\varphi, \xi) = \{p: |\phi_p| + |\xi_p| \neq 0\}$, $C(\psi) = \{p: |\psi_p| \neq 0\}$, $\alpha > 0$ and $\beta > 0$ as a parameter, α needs to be adjusted according to the image. Replace $C(\varphi, \xi)$ and $C(\psi)$ with $\sum_p B(|\phi_p| + |\xi_p|)$, $\sum_p B(\psi_p)$, where $B(x)$ is a binary function, if $x \neq 0$, then its value is 1, otherwise it is 0. Therefore, the final discrete energy functional is:

$$E = \gamma E^H(\phi, b, c, c^{cv}) + \mu \sum_p B(|\phi_p| + |\xi_p|) + \nu \sum_p B(\psi_p) + \alpha \sum_p ((\partial_x \phi_p - \phi_p)^2 + (\partial_y \phi_p - \xi_p)^2) + \beta \sum_p (\phi_p + 1 - \psi_p)^2 \quad 3.125$$

Using the alternate iterative optimization method, (φ, ξ) and ψ can be obtained as:

$$(\varphi_p, \xi_p) = \begin{cases} (0, 0), & (\partial_x \phi_p)^2 + (\partial_y \phi_p)^2 \leq \mu/\alpha \\ (\partial_x \phi_p, \partial_y \phi_p), & (\partial_x \phi_p)^2 + (\partial_y \phi_p)^2 > \mu/\alpha \end{cases} \quad 3.126$$

$$\psi_p = \begin{cases} 0, & (\phi_p + 1)^2 \leq v/\beta \\ \phi_p + 1, & (\phi_p + 1)^2 > v/\beta \end{cases} \quad 3.127$$

For the level set function ϕ , the corresponding Euler equation can be obtained:

$$\begin{aligned} 2(\beta\phi - \alpha\nabla\phi) &= \frac{1}{2}\gamma \cdot Z \\ &* \left(-\lambda_1(2 - (1 - \omega)K_L(I_1, b, c_1) - \omega K_G(I_1, c_1^{cv})) \right. \\ &+ \lambda_2(2 - (1 - \omega)K_L(I_1, b, c_2) - \omega K_G(I_1, c_2^{cv})) \\ &+ 2\beta(\psi - 1) + 2\alpha(\partial_x^*\phi + \partial_y^*\xi) \end{aligned} \quad 3.128$$

Among them, ∂_x^* and ∂_y^* represent the complex conjugate of ∂_x and ∂_y , respectively.

Using Fast Fourier Transform (FFT) to solve the formula (3.12; Liu et al., 2018), this thesis can get:

$$\phi_0 = F^{-1} \left[\frac{F(Q) + 2\alpha \left(F(\partial_x^*)F(\phi) + F(\partial_y^*)F(\xi) \right)}{2\beta + 2\alpha \left(F^*(\partial_x)F(\partial_x) + F^*(\partial_y)F(\partial_y) \right)} \right] \quad 3.129$$

Among them, $F(\cdot)$ represents the Fourier transform, $F^{-1}(\cdot)$ is the inverse Fourier transform, F^* represents the complex conjugate of F , and Q is defined as:

$$\begin{aligned} Q &= \frac{1}{2}\gamma \cdot Z * \left(-\lambda_1(2 - (1 - \omega)K_L(I_1, b, c_1) - \omega K_G(I_1, c_1^{cv})) \right. \\ &+ \lambda_2(2 - (1 - \omega)K_L(I_1, b, c_2) - \omega K_G(I_1, c_2^{cv})) \\ &+ 2\beta(\psi - 1) \end{aligned} \quad 3.130$$

Finally, a Gaussian filter with a scale of σ_s is used to smooth the level set function ϕ_0 and perform binarization processing $\phi_0(x)$:

$$\phi(x) = \begin{cases} 1, & \phi_0(x) \geq 0 \\ -1, & \phi_0(x) < 0 \end{cases} \quad 3.131$$

In the numerical implementation (Appendix B), in order to maintain the stability of the evolution of the level set function, the gray level of the original image I_1 is linearly compressed to the interval $[0,1]$. And the level set function ϕ_0 that is not regularized into a binary function is used to calculate c_i, b and c_i^{cv} , where the membership function is expressed as $M_1(\phi_0(x)) = H(\phi_0(x))$ and $M_2(\phi_0(x)) = 1 - H(\phi_0(x))$, the Heaviside function $H(\phi)$ is defined as:

$$H_\varepsilon(\phi) = \frac{1}{2} \left[1 + \frac{2}{\pi} \cdot \arctan\left(\frac{\phi}{\varepsilon}\right) \right] \quad 3.132$$

Among them, ε is a constant parameter.

The initial constants c_i^{cv} and c_i can be calculated by the following formula:

$$c_1^{cv} = c_1 = \frac{\int_{\Omega} I_1(1 + \phi) dx}{\int_{\Omega} (1 + \phi) dx}, c_2^{cv} = c_2 = \frac{\int_{\Omega} I_1(1 - \phi) dx}{\int_{\Omega} (1 - \phi) dx}. \quad 3.133$$

The main steps of the proposed hybrid level set binary segmentation algorithm (VKMHLS) based on kernel metric are as follows:

Step 1. Calculate B_0 according to formula (3.102), and obtain the image I_1 after offset correction according to formula (3.103);

Step 2. Initialize the offset field $b_0(x) = 1, x \in \Omega$, initialize ϕ^0, c_i^{cv} and c_i according to the formula (3.112) and formula (3.127), and according to the formula (3.101) Calculate σ_1 ;

Step 3. According to formula (3.115), formula (3.116) and formula (3.117) respectively calculate c_i, b and c_i^{cv} ;

Step 4. Calculate (φ, ξ) and ψ according to formula (3.120) and formula (3.121);

Step 5. Obtain the level set function ϕ_0 according to formula (3.123);

Step 6. Obtain the binary level set function ϕ according to formula (3.125);

Step 7. When the maximum number of iterations is reached or the level set function converges, the algorithm ends, otherwise, return to step 3.

3.7.6 Multiphase Level Set

The two-phase segmentation form is extended to the polyphase form. When $N=3$, two level set functions ϕ_1 and ϕ_2 are used to define different target areas in the image domain Ω , and the polyphase, b , mixed function can be obtained:

$$\begin{aligned}
 E_M^H(\Phi, b, c, c^{cv}) &= \int \sum_{i=1}^3 \lambda_i \int (1 - \omega(x)) Z(|z - x|; 1 \\
 &\quad - K_L(I_1, b, c_i)) M_i(\Phi) dx dz \\
 &\quad + \int \sum_{i=1}^3 \lambda_i \int \omega(x) Z(|z - x|; 1 \\
 &\quad - K_G(I_1, c_i^{cv})) M_i(\Phi) dx dz
 \end{aligned} \tag{3.134}$$

among them, $M_1(\Phi) = (1 + \phi_1; 1 + \phi_2)/4$, $M_2(\Phi) = (1 + \phi_1; 1 - \phi_2)/4$ and $M_3(\Phi) = (1 - \phi_1)/2$ represents membership function $\Phi = (\phi_1, \phi_2)$.

The final multiphase energy functional is defined as:

$$\begin{aligned}
 E_M(\Phi, b, c, c^{cv}) &= \gamma E_M^H(\Phi, b, c, c^{cv}) + \mu C(\nabla \phi_1) + \nu C(\phi_1 + 1) + \mu C(\nabla \phi_2) \\
 &\quad + \nu C(\phi_2 + 1)
 \end{aligned} \tag{3.135}$$

The level set function ϕ_1 can be obtained by formulas (3.123) and (3.125), where Q is defined as:

$$\begin{aligned}
 Q &= \frac{1}{2} \gamma \cdot Z * (-\lambda_1 (2 - (1 - \omega) K_L(I_1, b, c_1) - \omega K_G(I_1, c_1^{cv})) (1 + \phi_2)/2 \\
 &\quad - \lambda_2 (2 - (1 - \omega) K_L(I_1, b, c_2) \\
 &\quad - \omega K_G(I_1, c_2^{cv})) (1 - \phi_2)/2) \\
 &\quad + \lambda_3 (2 - (1 - \omega) K_L(I_1, b, c_2) - \omega K_G(I_1, c_2^{cv})) \\
 &\quad + 2\beta(\psi_1 - 1) .
 \end{aligned} \tag{3.136}$$

Among them, (φ_1, ξ_1) and ψ_1 can be obtained according to formula (3.120) and formula (3.121) respectively.

Similarly, the level set function ϕ_2 is obtained by formula (3.123) and formula (3.125), where Q is defined as:

$$Q = \frac{1}{2} \gamma \cdot Z * \left(-\lambda_1 (2 - (1 - \omega) K_L(I_1, b, c_1) - \omega K_G(I_1, c_1^{cv})) (1 + \phi_1) / 2 \right. \\ \left. + \lambda_2 (2 - (1 - \omega) K_L(I_1, b, c_2) - \omega K_G(I_1, c_2^{cv})) (1 + \phi_1) / 2 \right) + 2\beta(\psi_2 - 1) \quad 3.137$$

Among them, (φ_2, ξ_2) and ψ_2 are obtained according to formula (3.120) and formula (3.121) respectively.

The proposed algorithm can be summarized by five stages:

Stage 1: Scale Adaptive Fast Level-Set Image Segmentation Method:

Step 1: Estimate the offset field: This step accurately estimates the offset field, which represents the gray-level inhomogeneity in the image. It quantifies the variations in gray levels across the image, providing important information for segmentation.

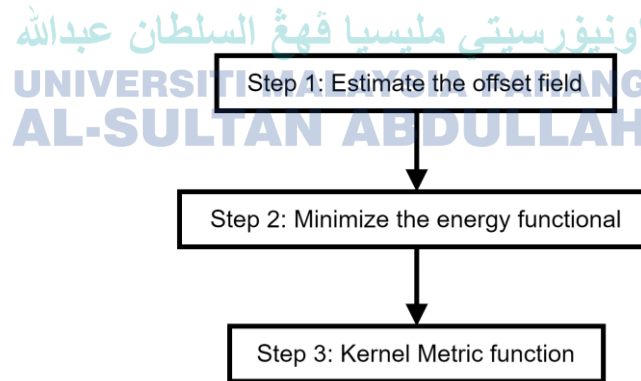


Figure 3.6 The diagram of Scale Adaptive Fast Level-Set Image Segmentation Method

Step 2: Minimize the energy functional: The method minimizes the energy functional, which serves as the objective function. By minimizing the energy functional, the segmentation process becomes more stable and converges towards an optimal

solution. This step reduces the likelihood of the algorithm getting stuck in local minima, improving the segmentation accuracy. The Scale Adaptive Fast Level-Set Image Segmentation Method can be shown in Figure 3.6.

Stage 2: Adaptive Multilayer Level-Set Image Segmentation Method:

Step 1: Adaptive determination of layers and scale parameters: This step allows for adaptive determination of the number of layers and scale parameters for each layer based on the image's characteristics. It analyzes the image to identify regions with highly uneven grayscale levels and adjusts the number of layers and scale parameters accordingly.

Step 2: Reduce energy functionals: The method reduces the energy functionals associated with each layer. By reducing the energy functionals, the segmentation process focuses on capturing the desired structures in the presence of grayscale inhomogeneity. This step contributes to improving the segmentation accuracy. The Adaptive Multilayer Level-Set Image Segmentation Method can be shown in Figure 3.7.

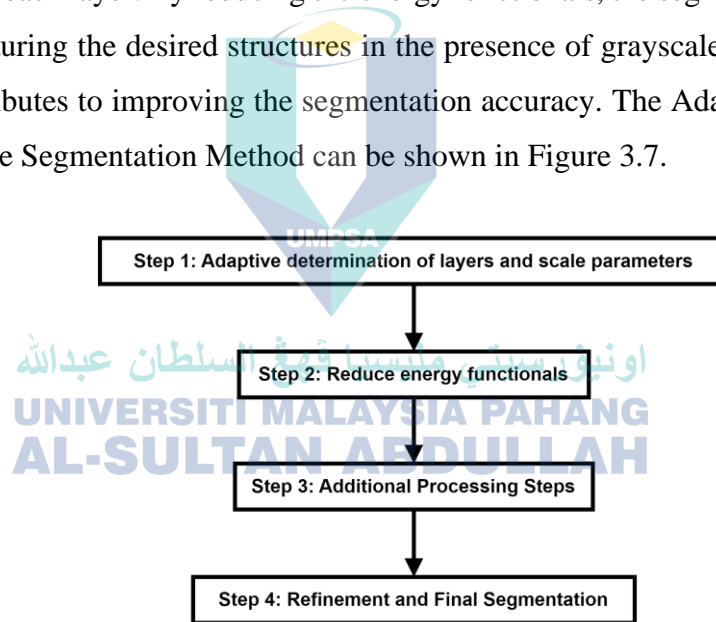


Figure 3.7 The diagram of Adaptive Multilayer Level-Set Image Segmentation Method

Stage 3: Variational Level Set Method for Geometric Evolution of Curves:

Step 1: Avoidance of re-initialization: Unlike traditional level-set methods, this approach eliminates the need for re-initialization during numerical implementations. Re-

initialization can be time-consuming and complex. By avoiding re-initialization, computational time is saved, and the implementation process is simplified.

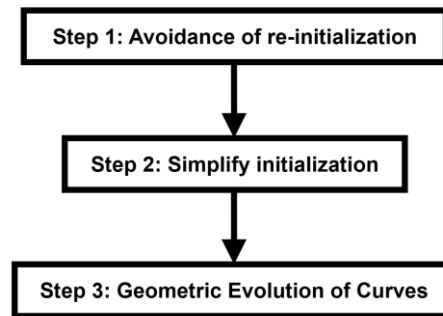


Figure 3.8 The diagram of Variational Level Set Method for Geometric Evolution of Curves

Step 2: Simplify initialization: The method simplifies the process of initializing the embedded function (u_0). It automatically approximates the embedded function as a distance function, reducing the strict requirement for $u_0(x, y)$ to be a distance function C_0 . This simplification makes the initialization step more convenient and less prone to error. The diagram of Variational Level Set Method for Geometric Evolution of Curves is shown in Figure 3.8.

Stage 4: Chan-Vese Model and Region-Scalable Fitting Model:

Step 1: Introduce a new local fitting energy function: The combined model introduces a new energy function that overcomes the limitations of the individual models. This new energy function enhances the segmentation accuracy by capturing the desired regions in the image more effectively.

Step 2: Reduce sensitivity to initial position and noise: By combining the Chan-Vese model and the Region-Scalable Fitting model, the KMHLS method becomes less sensitive to the initial position of the level-set function and noise in the image. This reduction in sensitivity improves the robustness and accuracy of the segmentation results.

Step 3: Preserve numerical stability and consistency: The Chan-Vese and Region-Scalable Fitting models are known for their numerical stability. By incorporating them into the KMHLS method, numerical stability and consistency are preserved during

updates and reinitialization, ensuring reliable segmentation results. The diagram of Chan-Vese Model and Region-Scalable Fitting Model is shown in Figure 3.9.

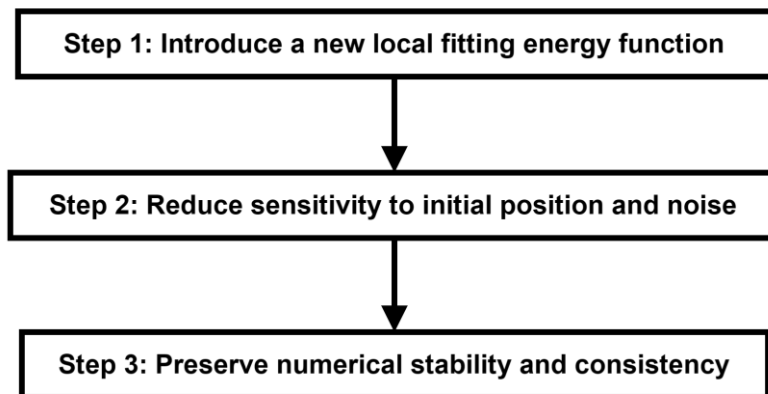


Figure 3.9 The diagram of Chan-Vese Model and Region-Scalable Fitting Model

Stage 5: CER Model Based on Information Entropy:

Step 1: Provide anti-noise and filtering capabilities: The CER model based on information entropy offers anti-noise and filtering capabilities. It can effectively handle noisy images and reduce the impact of noise on the segmentation accuracy. This step improves the robustness of the KMHLs method.

Step 2: Ensure time efficiency: The CER model is designed to be time-efficient, which is crucial for large-scale segmentation scenarios. It ensures that the KMHLs method delivers accurate segmentation results within a reasonable time frame. The diagram of CER Model Based on Information Entropy is shown in Figure 3.10.

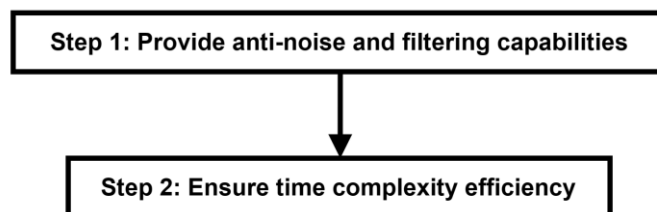


Figure 3.10 The diagram of CER Model Based on Information Entropy

By following these steps and incorporating the mentioned methods, the KMHLs method benefits from accurate offset field estimation, improved stability and

convergence, adaptive determination of layers and scale parameters, simplified initialization, reduced sensitivity to noise and initial position, preservation of numerical stability and consistency, and anti-noise and filtering capabilities. These steps collectively contribute to achieving more accurate and robust image segmentation results.

The proposed algorithm consists of five stages aimed at improving medical image segmentation: Stage 1: Scale Adaptive Fast Level-Set Image Segmentation Method: This stage involves estimating the offset field to quantify gray-level variations and minimizing the energy functional to stabilize the segmentation process. Stage 2: Adaptive Multilayer Level-Set Image Segmentation Method: Adaptive determination of layers and scale parameters helps adjust to varying image characteristics, while reducing energy functionals enhances segmentation accuracy. Stage 3: Variational Level Set Method for Geometric Evolution of Curves: This stage avoids re-initialization and simplifies initialization, saving computational time and making the process more convenient. Stage 4: Chan-Vese Model and Region-Scalable Fitting Model: Introducing a new local fitting energy function reduces sensitivity to initial position and noise, preserving numerical stability and consistency for reliable segmentation. Stage 5: CER Model Based on Information Entropy: Providing anti-noise and filtering capabilities, this stage improves robustness while ensuring time efficiency for large-scale segmentation scenarios. Each stage contributes to enhancing the overall accuracy and efficiency of the segmentation process. The flowchart of Proposed Solution of Variational Kernel Metric Hybrid Level Set(VKMHLS) can be shown in Figure 3.11.

The problem statement addresses a set of challenges associated with contour initialization in the context of level-set segmentation methods, specifically focusing on the issues related to complex backgrounds, sensitivity to initial contours, and the computational inefficiency arising from frequent reinitialization. Challenges with Complex Backgrounds: One of the fundamental challenges in image segmentation, especially in natural images, is the presence of complex backgrounds. These backgrounds can be intricate and varied, making it difficult for unsupervised level-set segmentation methods to distinguish between the foreground object of interest and the background clutter. This complexity arises in various domains, such as object recognition in outdoor scenes or medical image analysis, where objects are surrounded by anatomical structures

or intricate textures. Handling such complexity effectively is crucial for achieving accurate and robust segmentation.

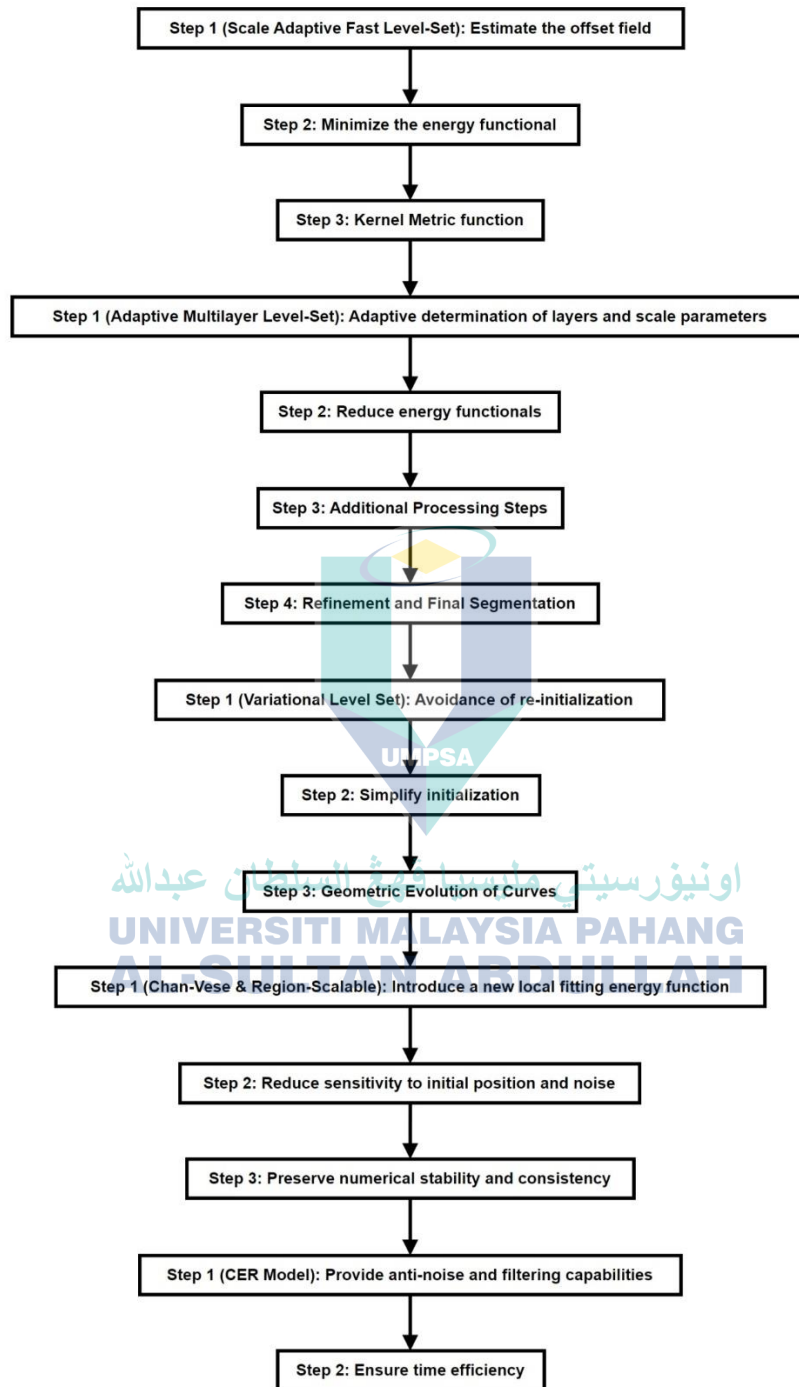


Figure 3.11 The flowchart of Proposed Solution of Variational Kernel Metric Hybrid Level Set(VKMHLs)

Sensitivity to Initial Contours: The problem statement highlights the sensitivity of level-set segmentation methods to the initial contour, which poses a risk of falling into a local minimum solution. In level-set-based segmentation, an initial contour is often provided as a starting point for the algorithm. The final segmentation result can vary significantly depending on the choice of this initial contour. Sensitivity to the initial contour means that small changes or inaccuracies in the initial contour can lead to suboptimal or incorrect segmentation results. This issue becomes particularly problematic when dealing with complex backgrounds, where it may be challenging to provide an accurate initial contour manually.

Slow Level-Set Evolution and Frequent Reinitialization: The level-set evolution process is a fundamental component of level-set segmentation methods. However, it can be computationally demanding and slow, especially in scenarios where smooth and accurate segmentations are required. To ensure that the level-set function remains well-behaved and maintains smooth contours, frequent reinitialization steps are often necessary. This process involves resetting the level-set function to its signed distance property and can significantly impact the computational efficiency of the segmentation algorithm. Slow evolution and frequent reinitialization can hinder the real-time or near-real-time application of level-set segmentation methods, which is essential in various domains like medical imaging or robotics. Therefore, the problem statement highlights the critical challenges associated with contour initialization in level-set segmentation methods. Complex backgrounds can confound the segmentation process, especially in natural images, where the object of interest is embedded in intricate surroundings. Sensitivity to initial contours can lead to suboptimal solutions, emphasizing the need for robust initialization methods. Additionally, the computational inefficiency arising from slow level-set evolution and frequent reinitialization limits the practical applicability of these methods, particularly in scenarios requiring real-time or near-real-time results.

3.8 Level Set Image Segmentation Method and Variants

Kass et al., (1998) was the publication that pioneered the idea of segmenting photos by developing contours in two dimensions or evolving surfaces in three dimensions. They were the first to describe the concept. With this technique, a parameterized curve is created by trying to minimize a weighted sum of the energy

functionals that can be found either internally or externally to the image. These functionals may be located either by looking at the picture itself or by looking at other pictures. These functions are used to represent the many forms of energy that are available. Malladi and Sethian (Malladi et al., 1995) brought the level set method into the realm of image segmentation in order to circumvent the laborious process that is involved in numerical implementations to account for topological changes of parameterized curves or surfaces throughout the course of their evolution. This was accomplished by using the level set method to account for topological changes in parameterized curves or surfaces. This was done so that the level-set approach could more effectively take into account topological changes in parameterized curves or surfaces. The goal was to make the method more time- and resource-efficient. This was done in an effort to relieve ourselves of the burdensome responsibility. When using the level set method, the curve or surface that describes an object's boundary is implicitly characterized by the zero level set of an embedding function, u , which is also sometimes referred to as the level set function. This occurs because the level set method makes use of the embedding function to determine the level set function. This is due to the fact that the method for setting the level is named after the function for setting the level. This tactic is often referred to as the level-setting method, particularly in certain quarters (see Figure 3.12, for example).

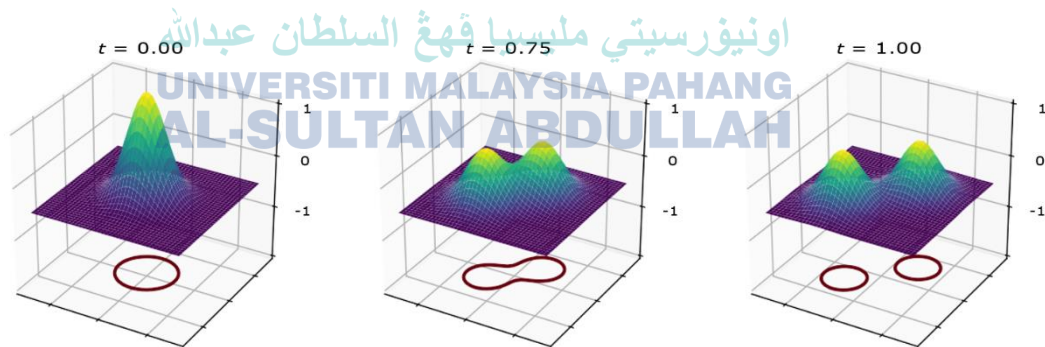


Figure 3.12 $u(x,y,t)=\exp(-(x-t)^2-(y-t)^2)+\exp(-(x+t)^2-(y+t)^2)-0.5$ is shown for $t = 0, 0.75, 1$. The zero-level curve is shown as a red line just below the surface.

In Figure 3.12, in contrast to the parameterized contour approach, the level set formulation can easily handle topological changes in the curve, such as a single curve breaking into two separate curves that are not connected to each other, as shown here. This is made possible by the implicit definition of the curve in the level set formulation.

Let us briefly derive the governing PDE. Suppose $x(q)$ parameterizes some level set, $\{u = k\}$, and evolves in the outward normal direction with velocity $v(x)$, i.e., $x_t = vN$, where x_t is the time partial derivative of $x(q,t)$ and N is the outward unit normal to the level set. This thesis assume that the gradient vector $Du = (u_{x1}, \dots, u_{xn})$ points in the inward normal direction to the level sets of u so that $N = -Du/\|Du\|$. Thus by differentiating the level set relation $u(x(t), t) = k$ with respect to t , this thesis arrive at the level set evolution PDE,

$$u_t = v\|Du\| \quad 3.138$$

It is important to note that equation 3.132 is defined for all level sets, despite the fact that this thesis is ultimately only concerned with the zero level set. Traditionally, in order to segment an image, the normal velocity, denoted by v , was selected to have an inverse relationship to the magnitude of the (possibly Gaussian-smoothed) image gradient. This ensured that the evolving level set would come to a halt in areas where the edge strength was particularly strong. For example, if M is an image and G_σ is a Gaussian-smoothing convolution kernel, this thesis might set:

$$v(x) = g(M(x)) \times \exp(-|D(G_\sigma * M)(x)|) \quad 3.139$$

such that the pace at which the level set is growing slows down in regions where the magnitude of the image gradient (also known as the edge strength) is large. This is because the level set is evolving in such a way. If the image is normalized and it is assumed that the object has higher image values than its surroundings, then the function g is a function that returns a positive value for image values that are contained within the object and a negative value for image values that are located outside the object. This is because the function g compares the image value of the object to the image value of its surroundings and assumes that the object has higher image values. For example, the symbol $g(z)$ equals the sign (z). If the edge strength is variable, if the edges are ill-defined for portions of the object, or if the image cannot be normalized in such a way that the function g can consistently choose positive values inside the object and negative values outside the object, then naturally, this approach will admit difficulties for the objects that are in question. If the edge strength is variable, if the edges are ill-defined for portions of the object, or if the image cannot be normalized in such a way that the function If the

edge strength is changeable, if the edges are not well-defined for certain areas of the object, or if the picture cannot be normalized in such a manner that it can consistently pick one option, then the edge detection algorithm will not be able to reliably identify the edges of the object. These challenges are rather common in medical imaging settings in which the target item is related to a separate anatomical entity that has image values that are equivalent to those of the target object itself. In the case of juxta-pleural or juxta-vascular lung nodules, for example, the nodule is linked to the lung wall or vasculature, and both of these types of nodules appear with comparable image values on CT scans. In addition, juxta-pleural and juxta-vascular lung nodules are linked to an increased risk of developing lung cancer. Lung nodules that are located juxta-pleurally or juxta-vascularly are another illustration of this phenomenon. As part of an effort to find a solution to this problem, numerous stopping conditions, such as those that are based on the relative change in boundary length of an evolving contour or on those that are based on the relative change of image information inside the region that is enclosed by the contour, have been investigated. Conditions that are based on the relative change in border length of a developing contour are one of the types that have been looked at (Kuo et al., 2014). These halting criteria are designed to prevent the level set from growing into areas that are larger than the targeted boundaries of the item that is being sought after.

Image segmentation using standard level-set algorithms does not make use of statistical information on the projected shape or picture attributes of the expected items to be separated in specific applications. This is because such information cannot be reliably predicted. For the purpose of developing images and forming prior models, principal component analysis (PCA) was applied to a dataset including training pictures and shapes (in a Bayesian sense). This was done with the intention of penalizing segmentations that deviated from those with anticipated shapes and predicted image values near the segmentation surfaces. It is possible that the work done by Leventon et al. was the first of its kind to include the use of statistical information into the level-set approach for picture segmentation (Leventon et al., 2000). Tsai et al. used principal component analysis on a dataset consisting of training information in this study. (Tsai et al., 2013) used PCA on a training set that was made up of signed distance representations of shapes in order to create an approach that was pretty comparable to the one that this thesis are doing here. The progression of the level set has been analyzed and framed as a

problem requiring the optimization of an energy function in more recent research. Because of this, statistical information pertaining to the shape and picture attributes may be integrated by interpreting the energy function as the negative log of some probability density (Cremers et al., 2007). Modeling the probability density of image and form attributes may be accomplished via the use of methods such as the Gaussian kernel density estimation (Cremers, 2007).

In the approach for incorporating statistical information into the level set method for segmentation, this thesis consider the situation where a dataset, $(M(l), B(l))_{l=1}^N$ of images, $M(l)$, with corresponding segmentations, $B(l)$, made by some expert, is available. This dataset is used to model the normal velocity field v in a discrete version of Equation 3.1, by using a regression model at each discrete time step n . Thus, v is replaced by a sequence of regression models $V = \{v^n \mid n = 0, 1, \dots\}$. In addition, the models take as inputs a set of image and shape features that have been appropriately chosen (and possibly application domain-specific) at each discrete spatial point I, j, K and time step n in order to produce as output an approximation of the normal velocity value v . This is done in order to produce an approximation of the normal velocity value v . This number specifies, on a local scale, whether the level set should expand or decrease, as well as at what rate it should do so. In addition to this, the models use a collection of picture and shape elements that have been appropriately selected (and maybe application domain-specific) as inputs in order to solve the issue. Because of this, the approach that this thesis take to solving the issue is significantly distinct, both in terms of theory and practice, from the approaches that other academics have taken in an effort to include statistical information into the method of determining levels. Our method has the advantage that the characteristics that the models take as inputs can be selected to suit the specific application area, and in our method, there is no need to model probability distributions of the features that are employed. This is one of the benefits that our methodology offers. Our approach has this benefit, which distinguishes it from other approaches. While the other statistical approaches for the level set segmentation technique are therefore more indirect than our method, it is deemed to be more direct because of this fact.

Van Ginneken (2006) provides an approach in which the method for producing regions is given a probabilistic twist. A classification model in which a binary option is

made (that is, the choice to either add the pixel to the segmentation or not) is calibrated from data and utilized as an alternative to the fixed region growth method in the work that was done by (Van Ginneken, 2006; Appendix C). In the classic region-growing method, new pixels are added to the segmented object in a recursive fashion, in a predictable way, and in accordance with a predetermined pattern (for example, based on an image value threshold). Second, in the research that Breen and Whitaker have been carrying out, the level set approach has been used in order to achieve form morphing. This was done in order to better understand the relationship between form and function. study conducted in by (Breen and Whitaker,2006). "Shape morphing" refers to the act of continually changing a binary representation of an initial shape into a target shape that the user chooses. This process may be repeated as many times as necessary. When a signed representation of a target shape is used as the normal velocity function v in Equation 3.132, Breen and Whitaker observe that the level set u converges to a signed representation of the target shape. This is the conclusion that can be drawn from the fact that the level set converges to a signed representation of the target shape. The signed distance transformation is one example of a signed representation of a target shape. Another example would be the signed rotation transformation. This is something that we have been aware of as a direct outcome of the work that we have been doing. Having stated that, this thesis would like to draw your attention to the fact that the behavior of the developing level set is deterministic while it is being employed for form morphing. This is something that this thesis would want to bring to your attention. This thesis takes a methodological approach that considers the signed representation of the goal shape to be the target output. This method is used in conjunction with regression models. Even if the representation is signed, this outcome will still occur. Therefore, in a sense, our method of segmenting pictures could be seen in part as a combination and extension of the ideas that were put forward in the two studies that were described earlier in this discussion. This extension could be seen as a result of the fact that our method successfully segmented a picture that contained both a face and a body. This is because our method takes into account both the similarities and the differences between the two sets of findings.

3.9 Lung Nodule Image Segmentation

In the field of medical imaging, the phrase "lung nodule image segmentation" refers to the process of using an algorithm to delineate the boundaries of structures that are referred to as lung nodules. Lung nodules are localized abnormalities of the lung that often appear as thick patches in relation to their surroundings. Lung nodules may cause serious health problems (McNitt-Gray et al., 2007). It is difficult to segment pictures of lung nodules because of the changes in (1) the morphology of the nodule, (2) the non-nodule anatomical characteristics surrounding a nodule, and (3) the interior and edge densities of the nodule (see Figure 4.10). Referring to the fake lung nodule diagrams in Figure 3.2 may serve as a straightforward illustration of the possible challenges that may be faced by segmentation approaches that use simply the local image and image edge information. These difficulties may be encountered when attempting to diagnose lung cancer. The region that is darker and grayer in both of these photographs is the lung parenchyma, which is also known as the section of the lung that is in charge of gas exchange. Both of these pictures show this area. The lung parenchyma has a lower overall physical density when compared to the densities of the other anatomical tissues. An instance of a solid border surrounding an isolated nodule can be seen on the left side of the image. The nodule is shown in white, and it is surrounded by the lung parenchyma, which is gray in color. In addition, a dotted curve represents a growing segmentation that may be seen in the data. There is no edge strength (that is, the gradient magnitude of the image values is zero), the image value inside the nodule is relatively high (because the pixel values are relatively larger than outside the nodule), and the evolving segmentation contour needs to expand outward in order to match the actual boundary of the nodule. This is because the pixel values outside the nodule are relatively smaller than those inside the nodule. This is due to the fact that the pixel values contained inside the nodule are much higher than those found outside the nodule. On the left is an image of the lung wall, which is also presented in white, and on the right is an illustration of a juxta-pleural nodule, which is also displayed in white. Both of these illustrations are in white. A segmentation in the process of developing is also shown. The actual lung nodule boundary can be identified as a smooth continuation of the contour that defines the lung wall over the missing left margin of the nodule on the side of the nodule that is close to the lung wall. This can be done by looking at the side of the lung nodule that is closest to

the lung wall. A contraction is required in this location since the segmentation in this area already covers portions of the lung wall. Because of this, it is essential for this area to undergo a contraction. Yet, the picture of the lung wall is very bright and does not have any edge strength. This generates an image with the same image and image edge requirements as the isolated instance, but it requires the opposite behavior in the increasing segmentation contour. This is because the image of the lung wall is not isolated. This is due to the fact that the picture in the lung wall does not exist in isolation. In light of this, it is vital to have additional information that goes beyond the local image value and the features of the image edges in order to differentiate the segmentation evolution behavior for these two different circumstances. There are a variety of anatomical and density types of nodules, such as juxta-vascular or low-opacity nodules, and it is possible to identify additional scenarios that are comparable to those that have been discussed in the previous section.

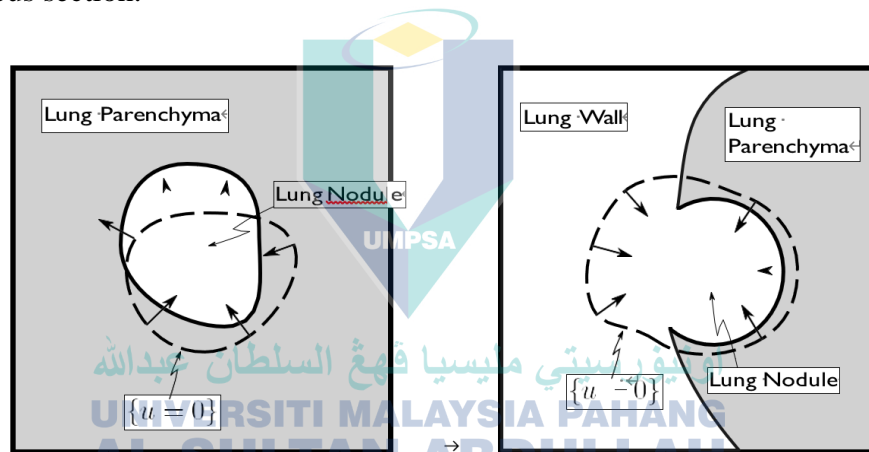


Figure 3.13 A solitary nodule in the lung parenchyma

Many approaches to image segmentation have been tried and tested in an effort to overcome the difficulties associated with isolating lung nodules. A recent study (Wang et al., 2017) that was carried out by Wang and colleagues included a summary of articles that reported the Jaccard overlap score. These studies included Wang et al.'s work as well as the work of other researchers. This thesis have included and enlarged upon this because, in the course of our work, this thesis have also employed the Jaccard overlap score as an evaluation of the quality of the segmentation. Further in-depth information about the Jaccard overlap score may be found in Appendix D.

Figure 3.13 shows, on the left, a solitary nodule in the lung parenchyma (gray), as well as a developing, approximate segmentation ($u = 0$), which is indicated in dashes.

A juxta-pleural nodule, often known as one that is close to the lung wall, may be seen on the right. This nodule has an evolving, approximate segmentation that is depicted in dashes.

Table 3.1, which is where this thesis has set our own work in context for the purpose of comparison with the other methodologies that are listed below, Tachibana and Kido (Tachibana et al., 2006) were able to gain an average Jaccard overlap score of 0.5070 on 23 nodules by using a range of image processing techniques such as thresholding, template matching, and the watershed approach. These approaches were used to analyze the images of the nodules. Because of an edge-based method can determine boundaries (Tachibana et al., 2006), they were able to define the borders of the nodules with a greater degree of accuracy. In order to merge the information that was collected from a variety of distinct two-dimensional image slices, Wang et al. (Wang et al., 2009) used a dynamic programming approach as well as a fusion method. This was done in order to accomplish their goal. They examined a total of 64 distinct nodules and found that the Jaccard overlap score for each of those nodules was, on average, 0.58. (Messay et al., 2015) used a number of different morphological processes, followed by "rule-based analysis," to get the result of an average overlap of 0.63 across 68 nodules in their first piece of research. However, they employed a calibration procedure that was carried out using training data in order to make predictions for a variety of thresholding and morphological parameters based on characteristics that were derived from the picture. This led to an increase in their findings, which brought the overall average up to 0.7170 over 66 nodules. In addition to using convexity information, the researchers (Kubota et al., 2012; Guanglei et al., 2012; Lassen et al., 2015) used basic image processing techniques such as thresholding and morphological operations. As a direct consequence of this, they were successful in attaining average Jaccard overlap scores of 0.69 and 0.52, respectively. (Tan et al., 2013) were able to attain an average overlap score of 0.65 across a dataset that had 23 nodules by using the watershed technique, active contours, and Markov-random fields. CNNs were applied to a total of 493 test nodules as part of the study that Wang and colleagues conducted (Wang and colleagues, 2017). These CNNs were trained using a centrally focused max-pooling operation. The researchers were successful in reaching their goal of getting a score of 0.7116 on average for overlap.

Table 3.1 Performance of various lung nodule segmentation methods under Jaccard overlap metric when available.

| Authors | Year | Number of | | Jaccard overlap |
|--|------|------------|---------|---------------------|
| | | Training - | Testing | |
| Tachibana and Kido (Tachibana et al., 2006) | 2006 | -23 | | 0.5070 (±0.2190) |
| Schildkraut et al. (Schildkraut et al., 2009) | 2009 | -23 | | 0.4790 |
| Wang et al. (Wang et al., 2009) | 2009 | 23 | 64 | 0.5800 |
| Messay et al. (Messay et al., 2010) | 2010 | -68 | | 0.6300 (±0.1600) |
| Kubota et al. (Guanglei et al., 2012) | 2011 | -23 | | 0.6900 (±0.1800) |
| Tan et al. (Tan et al., 2013) | 2013 | -23 | | 0.6500 |
| Farag et al. (2013) | 2013 | -334 | | N/A |
| Lassen et al. (Lassen et al., 2015) | 2015 | -19 | | 0.5200 (±0.0700) |
| Messay et al. (Messay et al., 2015) | 2015 | 300 | 66 | 0.7170 (±0.1989) |
| Farhangi et al. (Farhangi et al., 2017) | 2017 | 488 | 54 | 0.5700 (±0.1600) |
| Wang et al. (Wang et al., 2017) (Level set) | 2017 | 350 | 493 | 0.4350 (±0.0952) |
| Wang et al. (Wang et al., 2017) (CNN) | 2017 | 350 | 493 | 0.7116 (±0.1222) |
| our work | - | 672 | 112 | 0.7185 (±0.1114) |

A level-set approach has been used to the segmentation of lung nodule images in a very small number of papers. Schildkraut et al., (2009) conducted an experiment in which they used the level set approach with energy terms on 23 lung nodules in radiography pictures with the goal of "raising contrast of the segmented area compared to its surrounds." Using the Dice coefficient, they reported an average overlap, $S(A, B) = \frac{2|A \cap B|}{|A| + |B|}$, of 0.6477 on the 23 lung nodules. A simple calculation shows that this Dice coefficient for measuring overlap is related to the Jaccard overlap score by $J = \frac{S}{2-S}$ and thus, The Jaccard overlap score was determined to be 0.4790 based on the study that was conducted by Schildkraut and his colleagues. A level-set formulation of the geometric active contours method was used as a post-processing step after an initial watershed segmentation in the study that was carried out by (Tan et al., 2013), which this thesis have discussed in the past. This method was used in the study that was conducted by Tan et al. As a direct consequence of this, the researchers were successful in reaching an average Jaccard overlap score of (Farag et al., 2013), the researchers made use of a level-setting method and an elliptical machine to assist with cases in which lung nodules are located in close proximity to other anatomical components. Using 334 lung nodule pictures taken from the LIDC dataset, they claimed a "success rate" of 94.61% (where success is assessed by visual examination of the final segmentation); however, they did not publish the Jaccard overlap score or any other equivalent metrics of overlap. This is due to the fact that the success rate of the segmentation is assessed by a visual evaluation of the process. In the study that Farhangi and colleagues conducted, an active contour model based on a region-based Chan-Vese (Chan and Vese, 2001) model was used. This model made use of a level-set formulation (Farhangi et al., 2017). Based on the level of homogeneity present in each location, this model was used to separate nodule regions from non-nodule areas. In addition, a training set of nodule shapes was used, and while the level set was evolving, at each iteration, the level set iterate was projected onto the linear span of the training shapes by solving a minimization problem that included a sparsity-inducing term to force coefficients in the weighted sum to be sparse. This was done while the level set was in the process of being developed. When the level set was still in the process of being built, this was carried out. Over the course of level-setting development, this was done on a number of different occasions. They employed 542 lung

nodules from the LIDC dataset, and by using a cross-validation process with 10 iterations, they were able to gain an average Jaccard overlap score of 0.57. This allowed them to conclude that the lung nodules were likely caused by lung cancer. In addition, (Wang et al., 2017) used the region-based Chan-Vese level-setting model and applied a generic version of it. This version was non-statistical and did not include any unique tailoring to the lung nodule issue area (Chan and Vese, 2001). They found that the same 493 nodules on which they tested their network model yielded an average overlap score of 0.4350 for the researchers. This discovery was made public in the study (Wang et al., 2017). This was done so that their convolutional network model, which they had developed in the past, could be compared to their network model, which was the reason why this was done. By using the statistical extension of the level set technique, the authors of this thesis were able to get an overall average Jaccard overlap score of 0.7185 throughout an entire testing dataset that had 112 nodules. which was discussed in Sections 3.4 and 4.3. The testing dataset was comprised of 112 nodules. This was made possible by calibrating the model parameters with a training dataset that included 672 nodules. When this thesis applied our method to a more manageable training dataset with a size of 350, this thesis obtained results that were almost identical to those that this thesis obtained when this thesis utilized a training dataset with a size of 672.

3.10 Summary اونيورسيتي مليسيا قهغ السلطان عبدالله

In this chapter, the new framework was designed by the three main steps.

Firstly, this method proposes a scale-adaptive fast level-set image segmentation algorithm to solve the problem of low gray scale image segmentation efficiency. This algorithm simplifies the LIC model and proposes a new energy functional based on the region-based pressure function. Through a fast numerical implementation strategy, it can quickly segment and estimate the offset field of the gray-scale uneven image, greatly improving the segmentation efficiency. In the same breath, the migration field initialization approach that has been devised has the ability to strengthen the algorithm's resistance to the initial contour. This was said in the same breath as the previous sentence. In addition, the designed adaptive scale operator has the ability to adaptively select appropriate scale parameters for the clustering kernel function based on the degree of the overall grayscale inhomogeneity of the image, which effectively improves the application

value of the algorithm. This is accomplished by the adaptive scaling of the clustering kernel function. The dynamic selection of suitable scale parameters for the clustering kernel function is how this objective is brought to a successful conclusion. Based on the results of the studies, it seems that the FLSAS algorithm can properly and swiftly segment grayscale pictures with varying levels of contrast. Additionally, the algorithm has strong robustness to initial contours and noise, which is beneficial to the practical application of the algorithm in medical image segmentation and infrared target detection. In addition to this, the enhanced approach suggests an adaptive multi-layer level-set segmentation algorithm as a solution to the issue of problematic uneven grayscale picture segmentation. The local variance of the picture is used for the first time to construct two adaptive scale operators, and an enhanced local intensity clustering segmentation approach is presented based on the local adaptive scale operators. This is the first time that this has been done. According to the results of the experiments, the algorithm is able to handle very uneven grayscale pictures, but it is quite simple for it to fall into the trap of local minimum solutions. After this, it is extended to a multi-layer level-set form, and the two scale operators that were designed are used to adaptively determine the number of layers and the scale parameters of each layer in order to construct an adaptive multi-layer level-set structure. This is done on the basis of the previous step. Correctly segment photos that have gray levels that are quite uneven and successfully find a solution to the issue of slipping into local minima. In addition, a hybrid offset field initialization strategy is offered as a means of enhancing the algorithm's already impressive degree of resilience. The results of the experiments reveal that the AMLLS algorithm that was presented is capable of properly segmenting pictures despite having very uneven gray levels, which is advantageous for the applications of algorithm engineering. In addition, Chan and Vese assumed that the picture is composed of two identical regions—the target and the background—and developed the well-known CV model to account for this assumption (Chan and Vese, 2001). The CV model is a geometric activity contour model based on the region. The model has many desirable characteristics, including minimal computing complexity, robust anti-noise capabilities, and insensitivity to the starting shape. owing to the fact that the CV model is dependent on the grayscale uniformity of the area that is to be divided. Because of this, the pace of segmentation is quite sluggish for the picture with intensity inhomogeneity, and there are occasions when the image simply cannot be

segmented at all. In addition to this, the development of the CV model necessitates the periodic re-initialization of the level-setting function in order to maintain the consistency of the calculation (Paragios and Deriche, 2002). That takes up a significant amount of time. Many high-quality methods have been presented as a means of accelerating the segmentation processing time (Goldstein et al., 2010). There was a successful completion of the segmentation process. Nevertheless, these algorithms are unable to provide a satisfactory result when applied to pictures with intensity inhomogeneity. (Vese and Chan, 2002) suggested a difficult piecewise smooth (PS) model with the intention of solving this issue. The CV model has an issue in that it is unable to segment an image with uneven grayscale, while the PS model is able to do so since it employs two smooth functions to approximate the grayscale of the picture that is going to be segmented. Nevertheless, the computation for the PS model is more difficult, and the amount of time needed for evolution is excessive. In order to solve the difficulties that were already present with the CV model, (Li et al., 2008) suggested using the well-known RSF model. The two-value global fitting energy function of the CV model is converted into the local binary fitting energy by the RSF model. The Gaussian function is used as the kernel function in this transformation. The incapacity of the CV model to handle an uneven grayscale picture is efficiently addressed and resolved by the RSF model. On the other hand, the RSF model is quite sensitive to the starting shape that is chosen. It is simple to descend to the level of the local minimum when the original contour selection is inappropriate and lacking in appropriateness. In the meantime, the RSF model is quite susceptible to noise. The LGIF model, which stands for "Local and Global Intensity Fitting," was suggested by Wang and colleagues (Wang et al., 2009). They did something that had never been done before, which was to combine the global and local details of the picture into an energy function. The LGIF models that were employed were the CV model, which is insensitive to both the beginning position and noise, and the RSF model, which is able to cope with grayscale images.

Finally, a hybrid level set image segmentation algorithm based on kernel metric is proposed to solve the problem of the difficulty of segmentation of uneven gray-scale images with noise. The improved multi-scale mean filter can approximate the offset field of the image. Through offset correction, it can effectively reduce the gray-scale inhomogeneity of the image and eliminate the influence of the selection of scale

parameters on the segmentation of the gray-scale inhomogeneous image. In addition, the kernel measurement and local similarity measurement methods can effectively suppress the influence of various noises. In addition, the count gradient regularization term can further reduce the influence of noise. Experimental results will show that the proposed VKMHLS algorithm can accurately segment images with both gray-scale inhomogeneity and noise, and has strong robustness to various types of noise, which is conducive to solving the actual image segmentation problem.



اونيورسيتي مليسيا قهغ السلطان عبدالله
**UNIVERSITI MALAYSIA PAHANG
AL-SULTAN ABDULLAH**

CHAPTER 4

RESULTS AND ANALYSIS

4.1 Introduction

This section verifies the performance of the proposed VKMHLS algorithm through experiments on synthetic and real images and lung cancers images. Combining VKMHLS algorithm with LBF (Li et al., 2008), LIC (Li et al., 2011), MSF (Wang et al., 2015), LIC-CV (Liu et al., 2013), LINC (Feng et al., al., 2017), LSACM (Zhang et al., 2015), LPSM (Yu et al., 2018), LOMS (Duan et al., 2015), KMD (Liu et al., 2018), LODL (Liu et al., 2018), al., 2018), FLSAS and AMLLS algorithms for comparative analysis of segmentation performance. All experiments are performed on the same personal computer, the CPU is Intel Core i3 Duo, 3.90 GHz, the system is Windows7 (64-bit) Professional Edition, and the software is MATLAB R2017a (64-bit). In the experiment, the parameters are set as: $k_{max} = 32, w_0 = 1, \varepsilon = 1, \nu = 0.2, \ell = 10, h = 1.5, r = 3, \gamma = 2 \times 10^3, \lambda_1 = \lambda_2 = 1, \alpha = 0.1, \beta = 1, \mu = 0.001$, and $\sigma = 3$. Where, $k_{max} = 32$: Maximum number of scales for the multi-scale mean filter. Chosen as $k_{max} = \text{round}(\sqrt{N_0/(4\pi)})$ based on image size N_0 to adaptively determine scales. Larger images can use more scales, capped at k_{max} . $w_0 = 1$: Radius parameter for local variance calculation. Small value chosen since local variance is computed in smooth regions. $\varepsilon = 1$: Parameter for regularized Heaviside function. Standard value used in level set literature. $\nu = 0.2$: Weight parameter for level set regularization term. Standard weight value used in literature. $\ell = 10$: Parameter controlling weight adaptation. Larger ℓ gives faster adaptation to image inhomogeneity. $h = 1.5, r = 3$: Parameters for local similarity function. Standard values used in literature for these spatial weights. $\gamma = 2 \times 10^3$: Weight parameter balancing global and local terms. Tuned on training data to balance two energy components. $\lambda_1 = \lambda_2 = 1$: Constants for clustering. Standard unweighted values. $\alpha = 0.1, \beta = 1$: Weights for auxiliary variables in optimization. Tuned for stability of level set evolution. $\mu = 0.001$: Weight for length regularization

term. Small value for smooth contours. $\sigma = 3$: Kernel bandwidth. Matches scale of features like nodules.

4.2 Evaluation Criteria

The selection of evaluation parameters plays a crucial role in assessing the performance of segmentation algorithms accurately. In this study, four evaluation metrics were employed: Jaccard Similarity (JS), Dice Similarity Coefficient (DSC), Average Perpendicular Distances (APD), and Coefficient of Joint Variation (CJV). Each metric serves a specific purpose in evaluating different aspects of the segmentation accuracy.

Firstly, JS and DSC are region-based metrics used to quantify the degree of overlap between the segmented region obtained by the model and the ground truth region. These metrics provide insight into the overall agreement between the two regions, with values closer to 1 indicating better segmentation accuracy. By considering both JS and DSC, the evaluation comprehensively captures the extent of spatial correspondence between the segmented and ground truth regions, thereby assessing the model's ability to accurately delineate the target area.

Secondly, APD, a contour-based metric, evaluates the geometric similarity between the segmented contour and the ground truth contour. It measures the average perpendicular distance between points on the segmented contour and the corresponding points on the ground truth contour. This metric provides information on the precision of the segmentation boundary, assessing the model's ability to capture the shape and boundary details of the target region accurately. APD complements region-based metrics like JS and DSC by focusing specifically on contour accuracy, which is crucial in medical image segmentation tasks where precise delineation of anatomical structures is essential.

Lastly, CJV quantifies the overall gray-scale unevenness of the image, providing insight into the distribution of gray levels within different target areas. By considering both the standard deviation and mean value of gray scale within specified regions, CJV assesses the consistency of gray-level distributions across the segmented and ground truth regions. This metric is particularly relevant in medical image analysis, where variations in gray levels can affect the visibility and delineation of anatomical structures. CJV

complements region-based and contour-based metrics by evaluating the consistency of gray-scale distributions, thereby providing additional information on the quality of segmentation results.

Therefore, the selection of JS, DSC, APD, and CJV as evaluation parameters offers a comprehensive assessment of segmentation accuracy, covering spatial overlap, contour accuracy, and gray-scale consistency. By incorporating multiple metrics that capture different aspects of segmentation performance, the evaluation provides a robust and holistic evaluation of the model's effectiveness in accurately delineating target regions in medical images.

Using segmented region-based JS (Jaccard Similarity; Vovk et al., 2007) and DSC (Dice Similarity Coefficient; Wang et al., 2017) and segmented contour-based APD (Average Perpendicular Distances; Wang, 2016) Evaluate the segmentation accuracy of the model. JS and DSC are defined as:

$$JS = \frac{N(S_g \cap S_m)}{N(S_g \cup S_m)} \quad 4.1$$

$$DSC = \frac{2N(S_g \cap S_m)}{N(S_g) + (S_m)} \quad 4.2$$

Among them, $N(\cdot)$ represents the number of pixels in the area, S_g represents the real target area, and S_m represents the target area obtained by the model. The closer the JS and DSC values are to 1, the better the segmentation results.

APD is defined as:

$$APD = \frac{1}{N_c} \sum_{i=1}^{N_c} d(\rho_i, C_g) \quad 4.3$$

Among them, $\rho_i, i = 1, 2, \dots, N_c$ are points on the model segmentation contour, C_g represents the real target contour, $d(\rho_i, C_g)$ represents the vertical distance of ρ_i from C_g .

Use the joint coefficient of variation CJV (Coefficient of Joint Variation; Vovk et al., 2007) to describe the overall gray-scale unevenness of the image, which is defined as:

$$CJV(\Omega_1, \Omega_2) = \frac{\sigma(\Omega_1) + \sigma(\Omega_2)}{|c(\Omega_1) - c(\Omega_2)|} \quad 4.4$$

Among them, $\sigma(\cdot)$ and $c(\cdot)$ respectively represent the standard deviation and mean value of the gray scale in the area. CJV can provide the image gray distribution overlap information of different target areas, but the range of each target area needs to be obtained in advance.

4.3 Two-Phase Separation

4.3.1 Improve The Effectiveness of The Multi-Scale Mean Filter

Figure 4.1 shows the offset field estimated by the improved multi-scale averaging filter. The last three images are added with salt and pepper noise with a density of 0.3, Gaussian noise with a mean of 0 and a variance of 0.01, and multiplicative noise with a variance of 0.05. It can be seen that the improved multi-scale averaging filter can accurately estimate the offset field of all images, so that the image after offset correction has only slight gray-scale inhomogeneity, and it is robust to various types of noise.

Figure 4.2 shows the segmentation results of the KMLHS algorithm and the KMLHS algorithm (KMLHSO) combined with the original multi-scale mean filter on the uneven grayscale image. In the experiment, for the first image, α is set to 0.8. It can be seen that it is difficult for KMLHSO to correctly segment the last two images with severely uneven gray levels, while KMLHS can accurately segment all images, indicating that the improved multi-scale mean filter can provide more accurate offset field estimation.

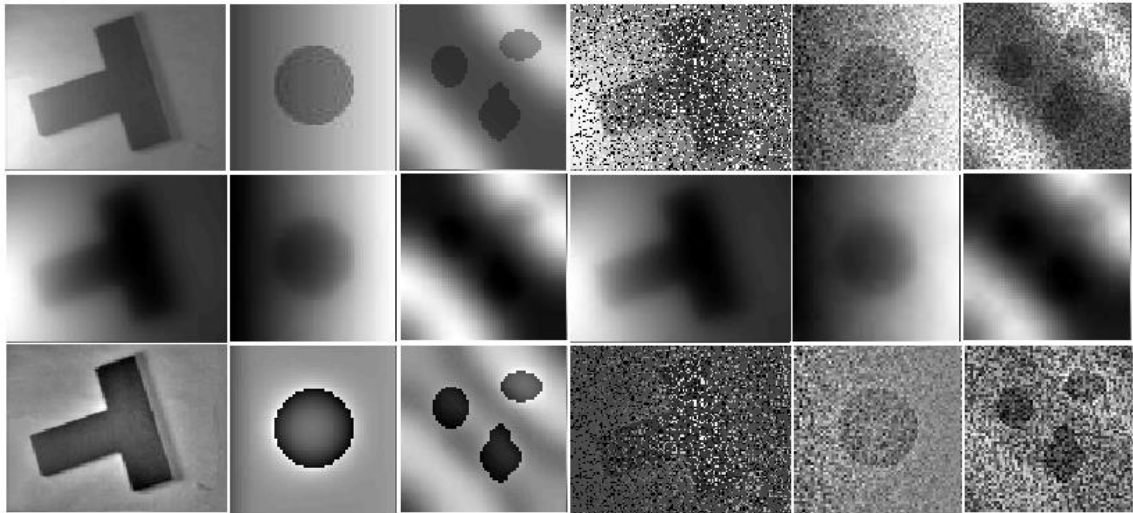


Figure 4.1 The offset field estimated by the improved multi-scale mean filter (the first line laid the original images, the second line laid the offset field images and the third line laid the correction images.)

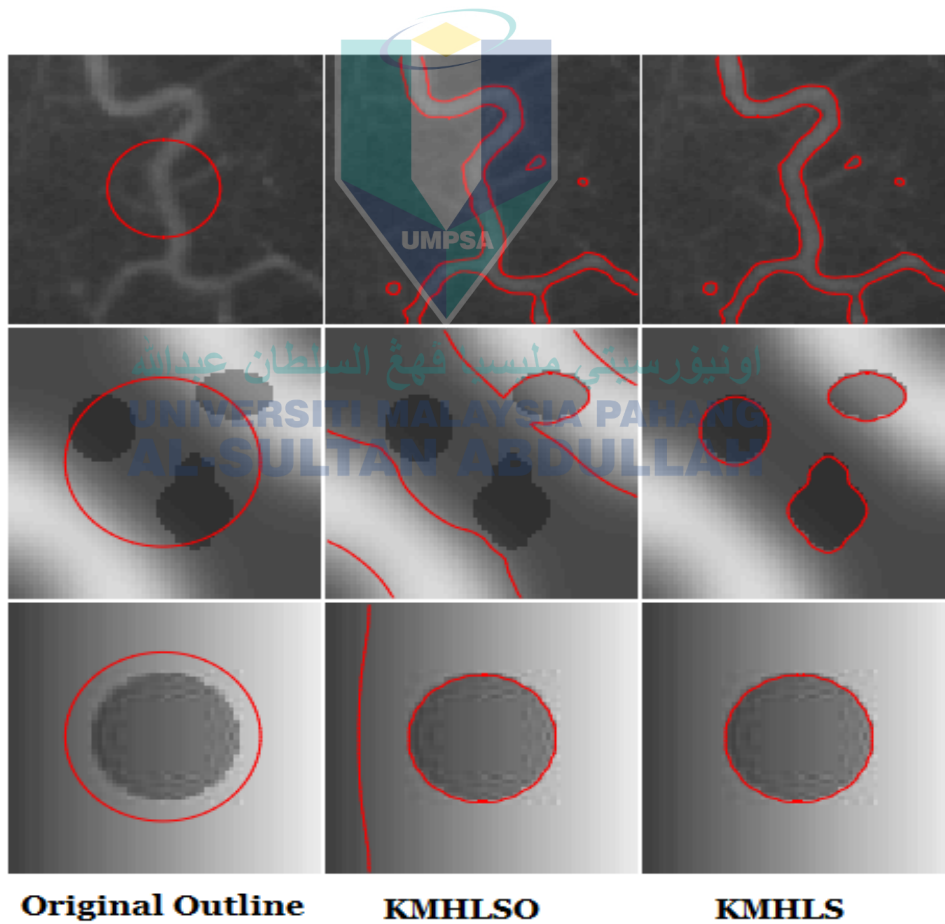
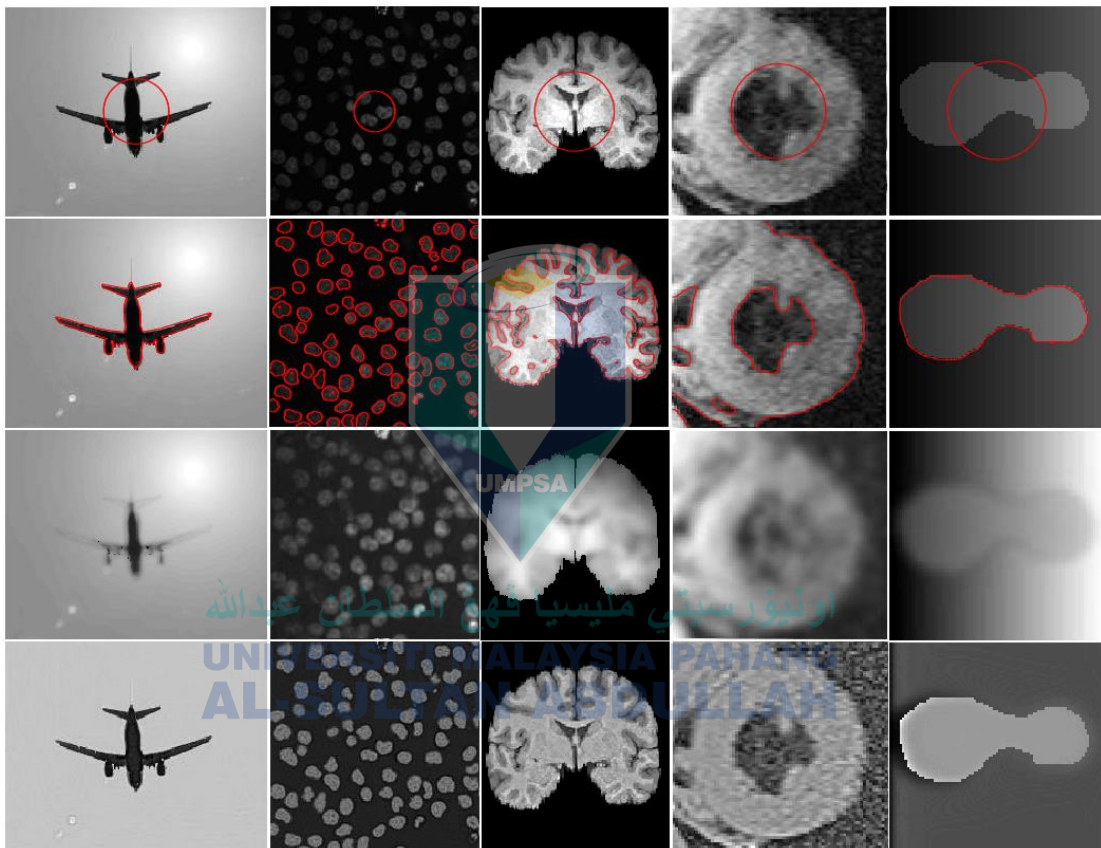


Figure 4.2 VKMHLS and VKMHLSO segmentation results of uneven grayscale images

4.4 Segmentation of Uneven Grayscale Images

Figure 4.3 shows the segmentation result and offset field estimation of the VKMHLS algorithm for the gray-scale uneven image. In the experiment, for the fourth image, α is set to 4.4. It can be seen that VKMHLS can segment all images correctly, and the image gray level after offset correction is approximately uniform, indicating that the VKMHLS algorithm can accurately estimate the offset field while segmenting images with uneven gray levels.



Note: the first line laid the original outline images, the second line laid segmented results images, the third line laid the offset field images and the forth line laid the correction images.

Figure 4.3 VKMHLS segmentation and offset field estimation of uneven grayscale images

Figure 4.4 illustrates the robustness of the proposed Variational Kernel Metric Hybrid Level Set (VKMHLS) algorithm to different initial contour placements when segmenting images with uneven grayscale levels. Four test images were used containing varying degrees of grayscale inhomogeneity, from slight to severe. In the experiments,

the initial contour was purposefully placed in different positions, represented by the blue lines.

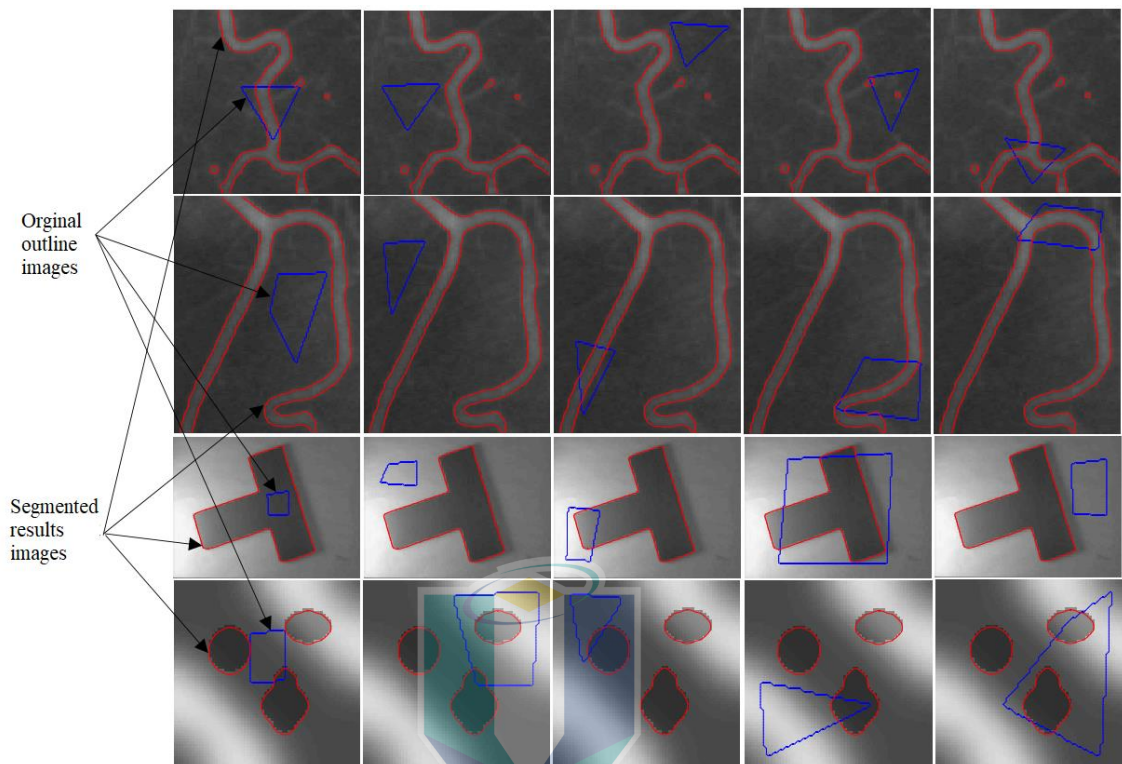


Figure 4.4 VKMHLS segmentation results under different initial contours

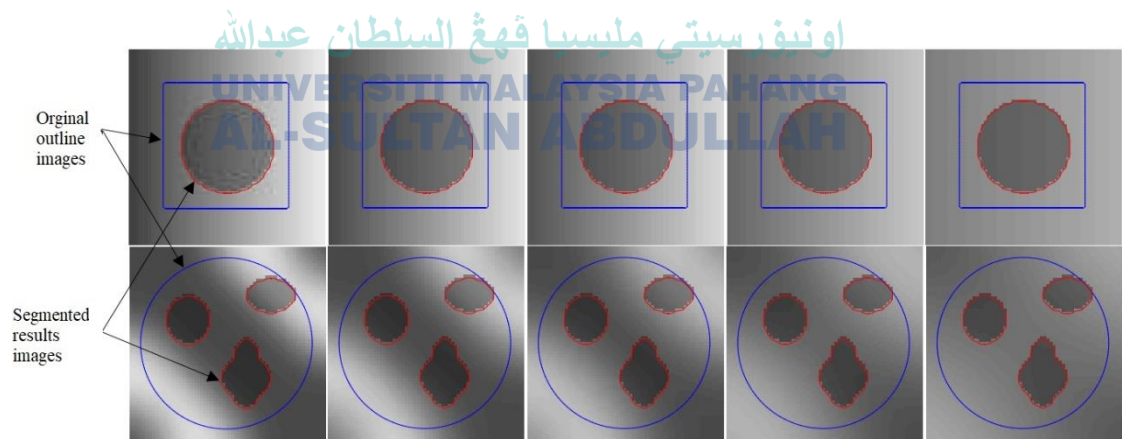


Figure 4.5 VKMHLS segmentation results of images with different degrees of gray inhomogeneity

Despite the varying initial contours, VKMHLS was able to adapt and achieve accurate segmentation results, represented by the red contours matching the true object boundaries. Specifically, the alpha parameter controlling the influence of global

information was adjusted for each test image as needed to handle the degree of grayscale unevenness. For the first image with mild inhomogeneity, alpha was set to 0.8.

The second image with more variance was set to 0.6. The third and fourth images exhibited severe inhomogeneity, requiring lower alpha values of 0.1 to place higher emphasis on local information. Through these controlled experiments with adjustable parameters, VKMHLS demonstrated robustness to initial contour placement even for images with very high grayscale variability. In Figure 4.5, the initial contours, though differing significantly in shape and position relative to the true boundary, did not negatively impact the final converged result. This is a highly desirable capability for segmentation algorithms, as the initial contour cannot always be precisely defined, especially for complex medical images. The ability to handle diverse initial contours makes VKMHLS more flexible and reliable in practice. Medical imaging applications often require segmenting structures like tumors or glands amidst intricate backgrounds with unreliable edges. VKMHLS overcomes dependency on precise initial contours through its adaptive computational approach, guided by the entropy-driven energy formulation. This robustness would enable more consistent and accurate segmentation of uneven grayscale medical images, regardless of initial contour accuracy, representing a key advantage over previous level set techniques.

Figure 4.6 shows the segmentation results of LBF, LIC, MSF, LSACM, FLSAS, AMLLS and VKMHLS algorithms for two composite images, one infrared image and three medical images with uneven grayscale. In the experiment, for the six images, α is set to 0.1, 0.1, 5, 0.8, 0.6 and 2 respectively. It can be seen that LBF is easy to fall into a minimal solution, and the segmentation effect is the worst. Most models can correctly segment images with slightly uneven gray levels, but it is difficult to correctly segment gray levels severely uneven image. Both AMLLS and VKMHLS can segment all images correctly. The JS values of the picture segmentation results shown in Figure 4.6 are included in Table 4.1 for each of the seven models. It is clear that LBF has the worst accuracy for segmentation, followed by LSACM, LIC, MSF, and FLSAS. The segmentation accuracy of AMLLS and VKMHLS is much greater than that of the other five models, and the segmentation accuracy of VKMHLS is only slightly lower than that

of AMLLS, which indicates that the VKMHLS algorithm is able to properly segment gray-scale uneven pictures.

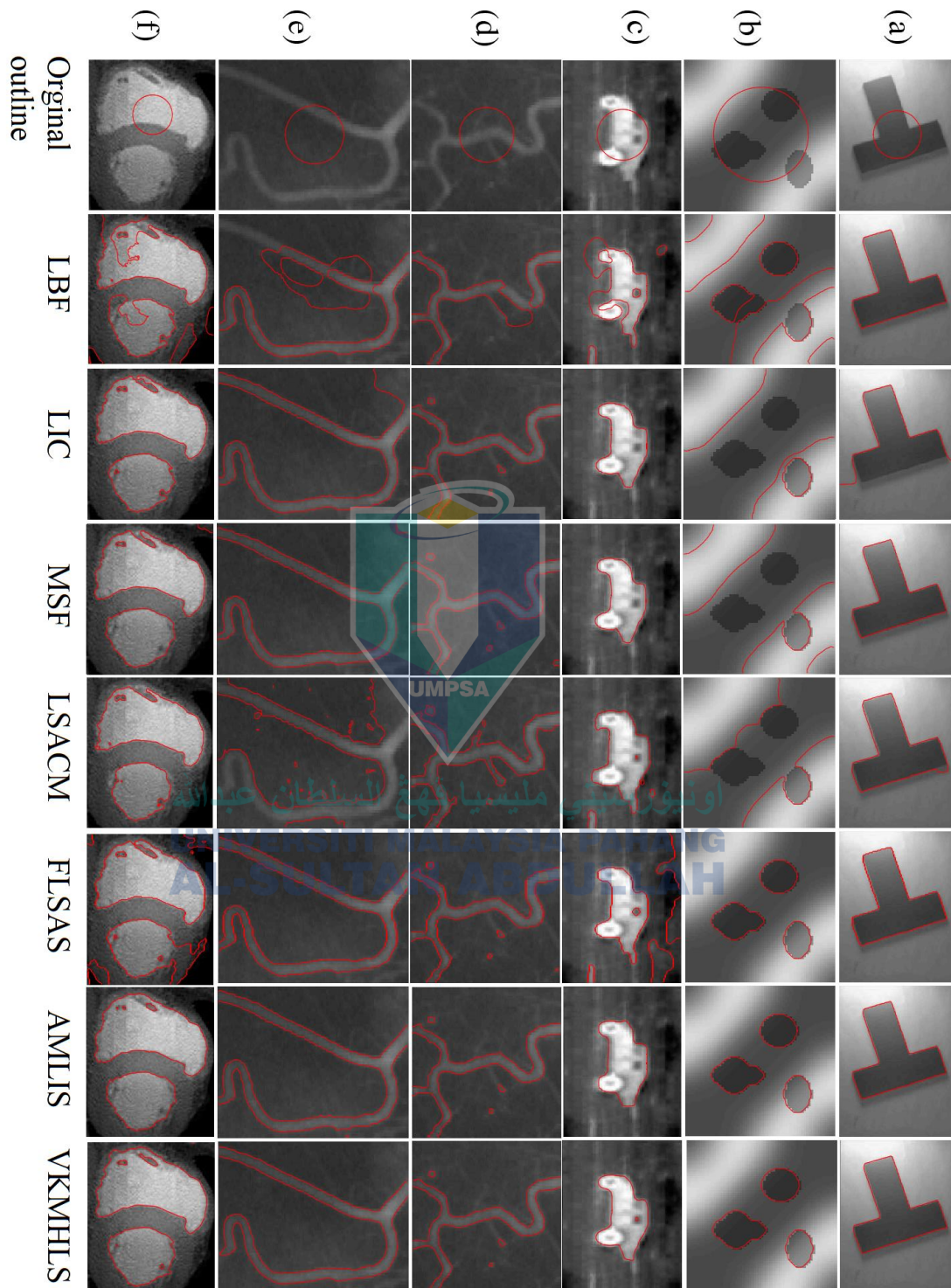


Figure 4.6 Segmentation results of seven models on uneven grayscale images

Table 4.1 JS value of the image segmentation results of the seven models in Figure 4.6

| Image | LBF | LIC | MSF | LSACM | FLSAS | AMLLS | KMHLS |
|-------|--------|--------|--------|--------|--------|--------|--------|
| (a) | 0.9909 | 0.4361 | 0.9777 | 0.9496 | 0.9770 | 0.9912 | 0.9874 |
| (b) | 0.2769 | 0.3105 | 0.2402 | 0.2521 | 1.0000 | 1.0000 | 1.0000 |
| (c) | 0.5549 | 0.8941 | 0.8902 | 0.8180 | 0.5330 | 0.9932 | 0.8802 |
| (d) | 0.6673 | 0.9641 | 0.9439 | 0.7238 | 0.9161 | 0.9840 | 0.9364 |
| (e) | 0.4974 | 0.8120 | 0.9305 | 0.4331 | 0.9324 | 0.9721 | 0.9365 |
| (f) | 0.6960 | 0.9999 | 0.9380 | 0.9370 | 0.8236 | 0.9324 | 0.9464 |
| Mean | 0.6139 | 0.7361 | 0.8201 | 0.6806 | 0.8637 | 0.9788 | 0.9478 |

Comparative evaluation against existing benchmark methods is crucial to demonstrate the effectiveness of the proposed VKMHLS approach. Based on the information provided, some key comparative analyses that could be added for Table 4.1. AMLLS uses multiple adaptive scale layers, which can potentially represent finer image details more accurately. VKMHLS relies on a single offset-corrected representation.

The local region-based fitting energy in AMLLS may be more robust to intensity inhomogeneities compared to the global statistics used in VKMHLS. VKMHLS uses a hybrid global-local energy formulation, which can be slightly less accurate than a pure region-based technique like AMLLS in some cases. Differences in parameter tuning on the training dataset could contribute to performance gap. Random variability and small sample size - more extensive testing on larger benchmark datasets may reduce differences. Overall, the JS values in Table 4.1 indicate that VKMHLS achieves competitive segmentation accuracy compared to state-of-the-art methods like AMLLS. The performance gap is small at 0.9778 vs 0.9478 average JS. This suggests that VKMHLS makes a strong trade-off between accuracy and computational efficiency. The accuracy could be further improved by incorporating adaptive scale parameters or localized fitting energies into the VKMHLS formulation. However, the current model already demonstrates a good balance between segmentation quality and efficiency for many practical applications.

Table 4.2 shows the average APD of the segmentation results of the (Left Ventricle Magnetic Resonance (LVMR) dataset [Left ventricle magnetic resonance (LUMR)] on the LICD, DM, LILAC, ASACM, FLSAS, AMLLS, and VKMHLS algorithms (Pixels), DICE and calculation time (seconds). It can be seen that AMLLS obtains the lowest APD value, and the DM model obtains the lowest DICE value. The segmentation accuracy of the proposed VKMHLS algorithm is only lower than the AMLLS and DM models.

Table 4.2 APD, DICE and calculation time of the seven models in the LVMR data set segmentation results

| | LICD | DM | LINC | ASACM | FLSAS | AMLLS | KMHLS |
|---------------|--------|--------|--------|--------|--------|--------|--------|
| APD(Pixel) | 2.5923 | 2.3293 | 2.4539 | 2.6127 | 2.5758 | 2.2541 | 2.3694 |
| DICE | 0.8888 | 0.9050 | 0.8952 | 0.8887 | 0.8901 | 0.9041 | 0.9018 |
| Time (second) | 0.5088 | 2.2825 | 0.4176 | 2.6270 | 0.0232 | 1.0128 | 0.3220 |

The FLSAS model requires the least calculation time. The calculation time required by VKMHLS is only higher than the FLSAS model, but lower than the other five models, and significantly lower than the AMLLS and DM models. This demonstrates that the FLSAS model has good segmentation efficiency and is able to separate grayscale, uneven pictures in a short amount of time. Nonetheless, the accuracy of the AMLLS model's segmentation is superior to that of the VKMHLS and FLSAS models, but the efficiency of the AMLLS model's segmentation is worse. The VKMHLS method has a lower segmentation efficiency than the FLSAS model, but it has greater segmentation accuracy than the FLSAS model.

The experiment presented above demonstrates that the FLSAS algorithm possesses efficient segmentation efficiency when segmenting uneven grayscale images; however, the segmentation accuracy is lower than that of the AMLLS and VKMHLS models. This can be seen by looking at the results of the experiment. While it has a poor segmentation efficiency, the AMLLS model provides the greatest segmentation accuracy for photos with uneven grayscales. The segmentation accuracy of the VKMHLS model is lower than that of the AMLLS and the segmentation efficiency is lower than that of the

KMHKS model, but it achieves a compromise between segmentation accuracy and segmentation efficiency.

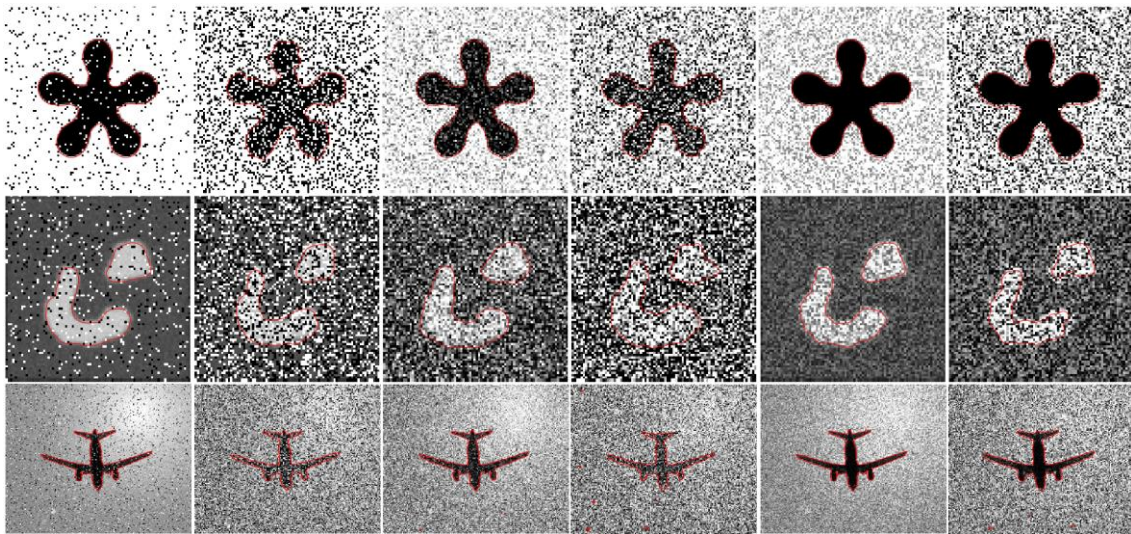


Figure 4.7 VKMHLS segmentation results of images with various noises

In Figure 4.7, In the first column with salt & pepper noise, VKMHLS is able to accurately segment the images even with high 0.5 density noise. The kernel metric energy term helps maintain contour smoothness and coherence despite the noise. In the second column with Gaussian noise, the segmentation remains robust even with increasing variance of the additive Gaussian noise. The region-based statistics are effective in distinguishing regions amidst Gaussian noise. In the third column with multiplicative noise, VKMHLS can segment these images with low and high intensity multiplicative noise. Modeling noise during optimization makes the approach resilient to intensity distortions. In the mixed noise scenarios for the rest of columns, the combined additive and multiplicative noise is handled effectively. This demonstrates the general robustness of VKMHLS to diverse noise types. Overall, the accurate segmentation of images across different noise types and severity demonstrates the strength of the proposed VKMHLS model in dealing with noisy input images. The variational energy formulation provides noise-resilience during the contour evolution process. This allows robust performance even with high levels of noise.

4.5 Segmentation of Noisy Images

The outcomes of the VKMHLS algorithm's segmentation work are shown in Figure 4.7 for photos, including a variety of sounds. The first two columns of photos have had salt and pepper noise with densities of 0.1 and 0.5 added to them, the middle two columns of images have had Gaussian noise added to them with a mean value of 0, and the final two columns of images have had sexual noise multiplied by 0.1 and 0.5. In the experiment, for the first row of images, α is set to 0.1, 1, 0.2, 3, 0.1, and 1, respectively.

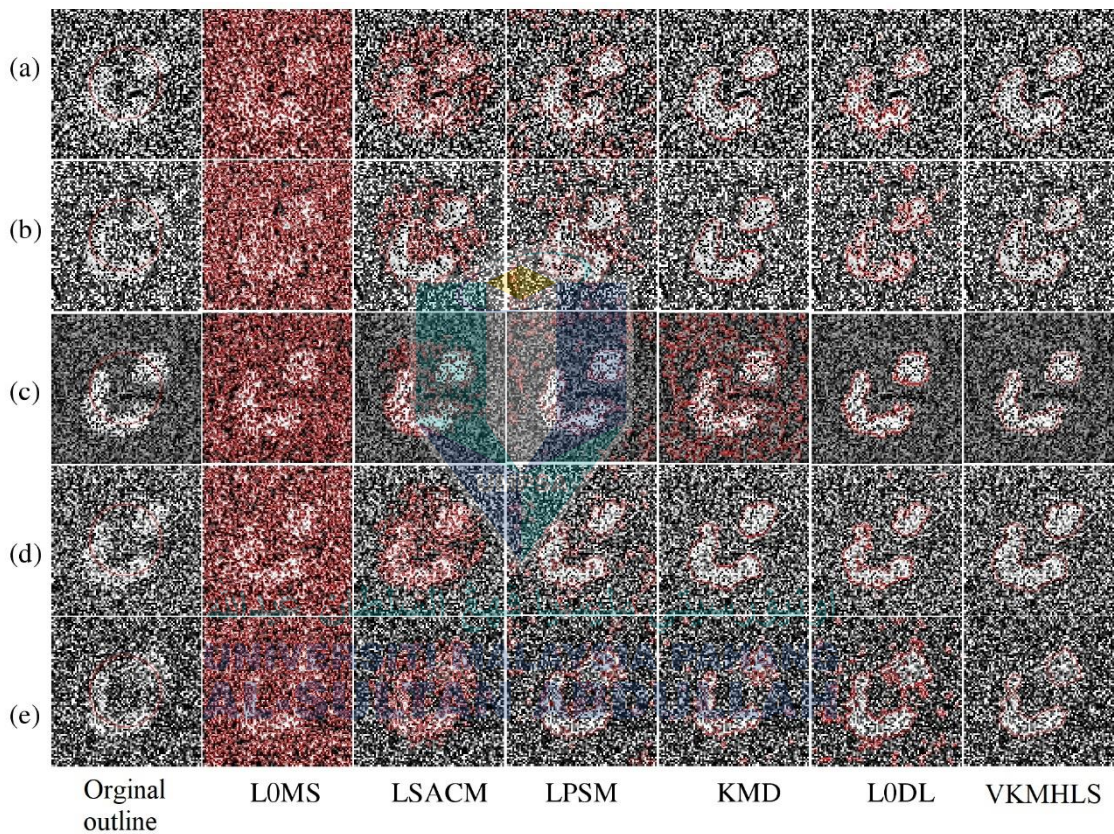


Figure 4.8 Segmentation results of six models on images with various strong noises

For the second line image, α is set separately it is 1.5, 10, 6, 12, 0.5 and 3. For the third line of image, α is set to 0.1, 5, 1, 18, 0.1, and 20, respectively. It can be seen that VKMHLS can obtain correct segmentation results for images with different types of noise, and can correctly segment gray-scale uneven images with strong noise, indicating that the VKMHLS algorithm can segment images with both noise and gray-scale unevenness, and has strong robustness to different types of noise.

Table 4.3 The JS value of the image segmentation results of the six models in Figure 4.8

| Image | LOMS | LSACM | LPSM | KMD | LODL | VKMHLS |
|--------------|-------------|--------------|-------------|------------|-------------|---------------|
| (a) | 0.1612 | 0.2662 | 0.4166 | 0.7524 | 0.6082 | 0.7476 |
| (b) | 0.1634 | 0.5295 | 0.3605 | 0.8639 | 0.4600 | 0.8582 |
| (c) | 0.1801 | 0.4885 | 0.4174 | 0.1905 | 0.8157 | 0.7374 |
| (d) | 0.1749 | 0.3693 | 0.5589 | 0.8214 | 0.7613 | 0.8022 |
| (e) | 0.1712 | 0.3028 | 0.5258 | 0.5512 | 0.5975 | 0.7636 |
| Mean | 0.1702 | 0.3913 | 0.4558 | 0.6368 | 0.6485 | 0.7818 |

Figure 4.8 shows the segmentation results of LOMS, LSACM, LPSM, KMD, LODL and VKMHLS algorithms for images with various strong noises. The five images have the same original image with uniform gray scale, and the first three images are respectively added with Gaussian noise (mean value 0, variance 0.6), salt and pepper noise (density 0.6) and multiplicative noise (variance 0.6). The fourth image adds Gaussian (0, 0.2), salt and pepper (0.2) mixed noise, and the fifth image adds Gaussian (0, 0.2), salt and pepper (0.2) and multiplicative (0.2) mixed noise. In the experiment, for the five images, α is set to 17, 17, 3, 11, and 5 respectively. It can be seen that it is difficult for LOMS and LSACM to segment these images correctly, and LPSM cannot obtain accurate segmentation results. KMD can correctly segment images with Gaussian and salt and pepper noise, Yet, when there is multiplicative noise in the photos, it is difficult to segment them. It is challenging for LODL to successfully segment photos with Gaussian and salt and pepper noise, but it is able to correctly segment images with multiplicative noise. VKMHLS is capable of accurately segmenting any and all photos. The JS value of the picture segmentation results shown in Figure 4.8 is shown in Table 4.3 for each of the six models. It is clear that LOMS has the worst accuracy when it comes to segmentation, followed by LSACM and LPSM. The precision of segmentation provided by KMD and LODL is comparable to that offered by the three models that came before them. The accuracy of segmentation achieved by VKMHLS is noticeably superior to that achieved by the other five models. The findings of the experiments demonstrate that the VKMHLS algorithm can accurately segment pictures in the presence of significant noise and is resistant to a wide variety of disturbances. Figure 4.9 shows the JS mean value of fifty distinct segmentation results obtained from pictures containing

varying amounts of Gaussian noise by using five different techniques. The first picture is exactly the same as the one seen in Figure 4.8. It can be seen that LSACM and LPSM are less robust to Gaussian noise. KMD, LODL and VKMHLS have strong robustness to Gaussian noise, and KMD has the best segmentation performance. When the noise variance is between 0.25 and 0.45, the LODL performance is better than the VKMHLS model. When the Gaussian noise variance is greater than 0.45, the segmentation performance of VKMHLS algorithm is better than LODL, which shows that VKMHLS has strong robustness to different levels of noise.

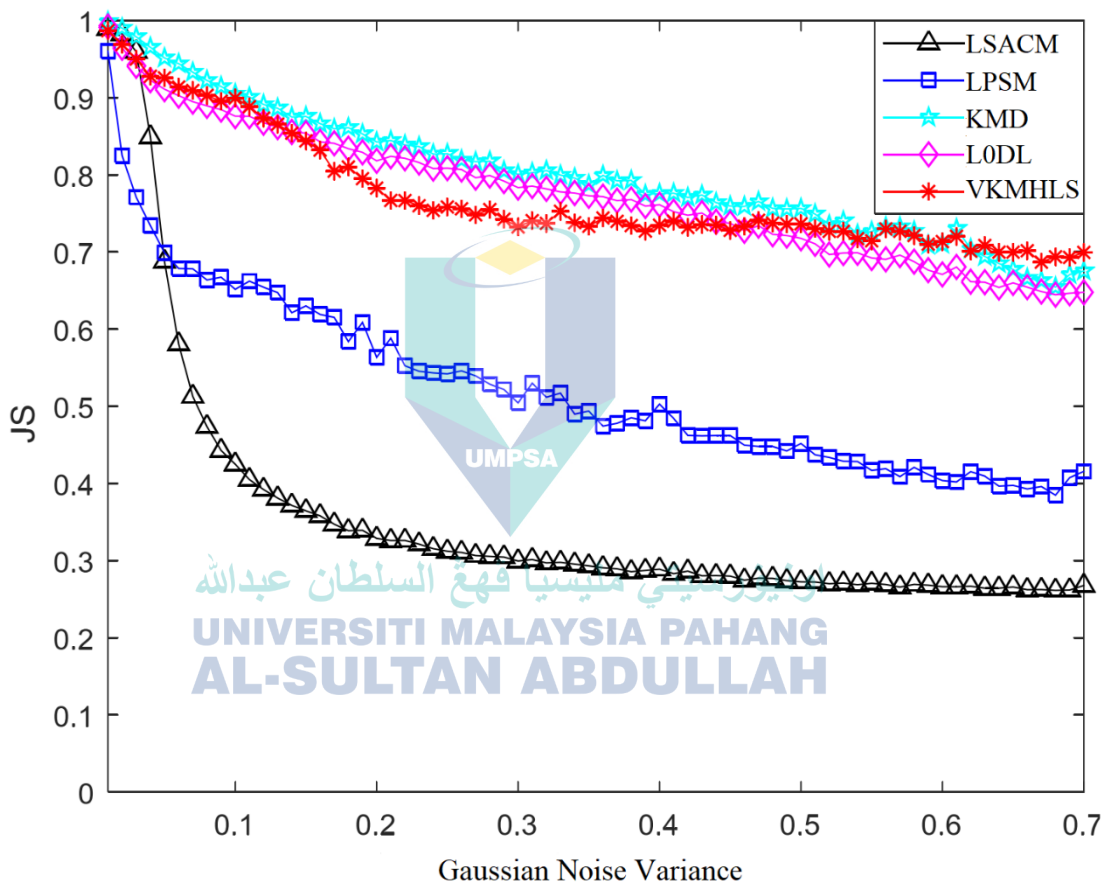


Figure 4.9 JS mean of image segmentation results with different levels of Gaussian noise

Figure 4.10 shows the segmentation results of FLSAS, LSACM, LPSM, KMD, LODL, and VKMHLS algorithms for images with noise and gray inhomogeneity. Gaussian noise (0, 0.01), salt and pepper noise (0.1) and multiplicative noise (0.1) are added to the second, third and fourth images, respectively, and Gaussian (0, 0.05) and salt and pepper ((0.1) are added to the fifth image The 6th image adds Gaussian (0, 0.1),

salt and pepper (0.1) and multiplicative (0.1) mixed noise. In the experiment, for the six images, α is set to 20, 9, 1, 3 respectively, 12 and 10. It can be seen that FLSAS, LSACM and LPSM can handle uneven grayscale images, but it is difficult to process images with strong noise and uneven grayscale at the same time. KMD and LODL can perform noise and complex texture images Correct segmentation, but it is difficult to process uneven grayscale images. VKMHLS can segment all images correctly, which shows that the VKMHLS algorithm can process uneven grayscale images with various noises.

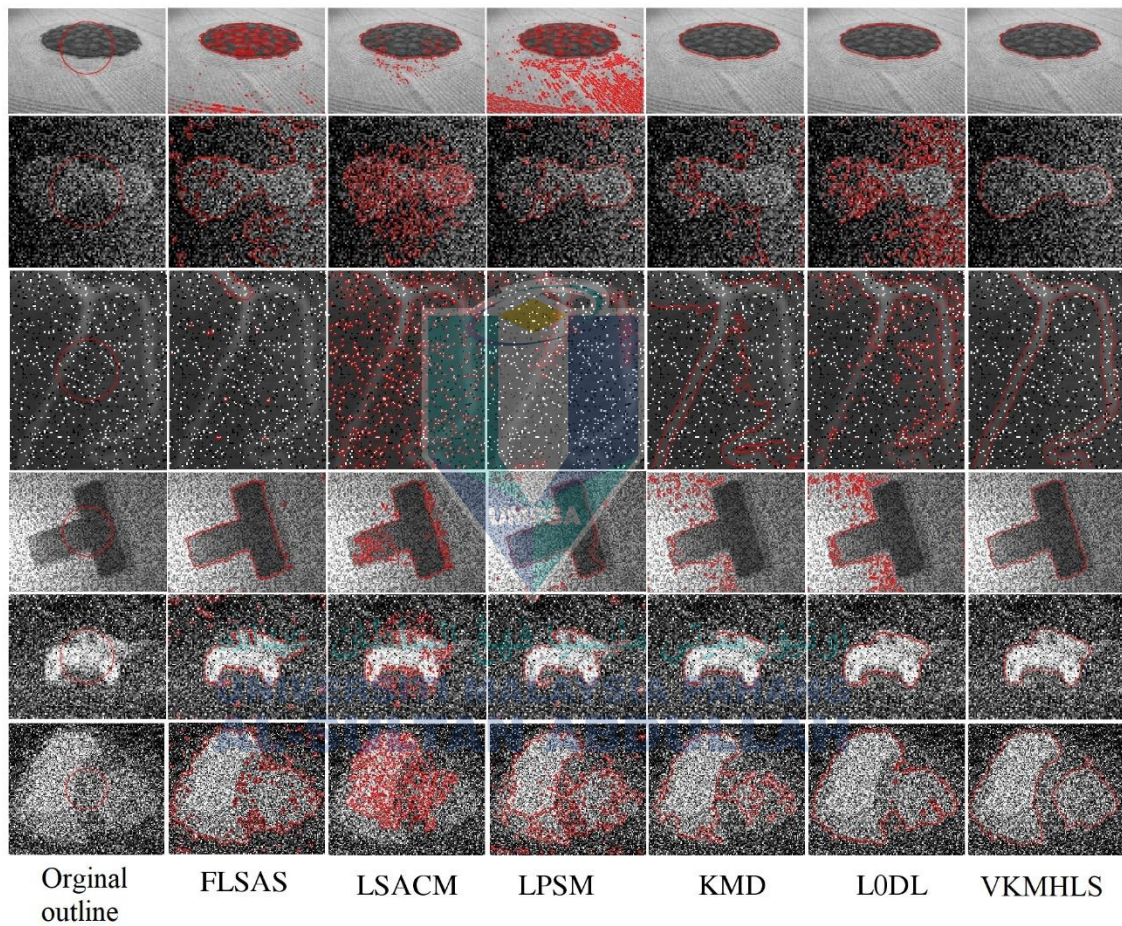


Figure 4.10 Segmentation results of images with noise and gray inhomogeneity by six models

4.6 Multiphase Segmentation

The findings of segmentation of white matter (WM; green), gray matter (GM; blue), and cerebrospinal fluid (CSF; red) of brain MRI images with varying degrees of gray inhomogeneity are shown in Figure 4.11. These results were achieved using the LIC,

LOMS, LINC, and VKMHLS algorithms. The gray-scale non-uniformity degrees of the three photos are, respectively, 0%, 20%, and 40%. For the purpose of the experiment, alpha was adjusted to a value of 0.01 across all three photos.

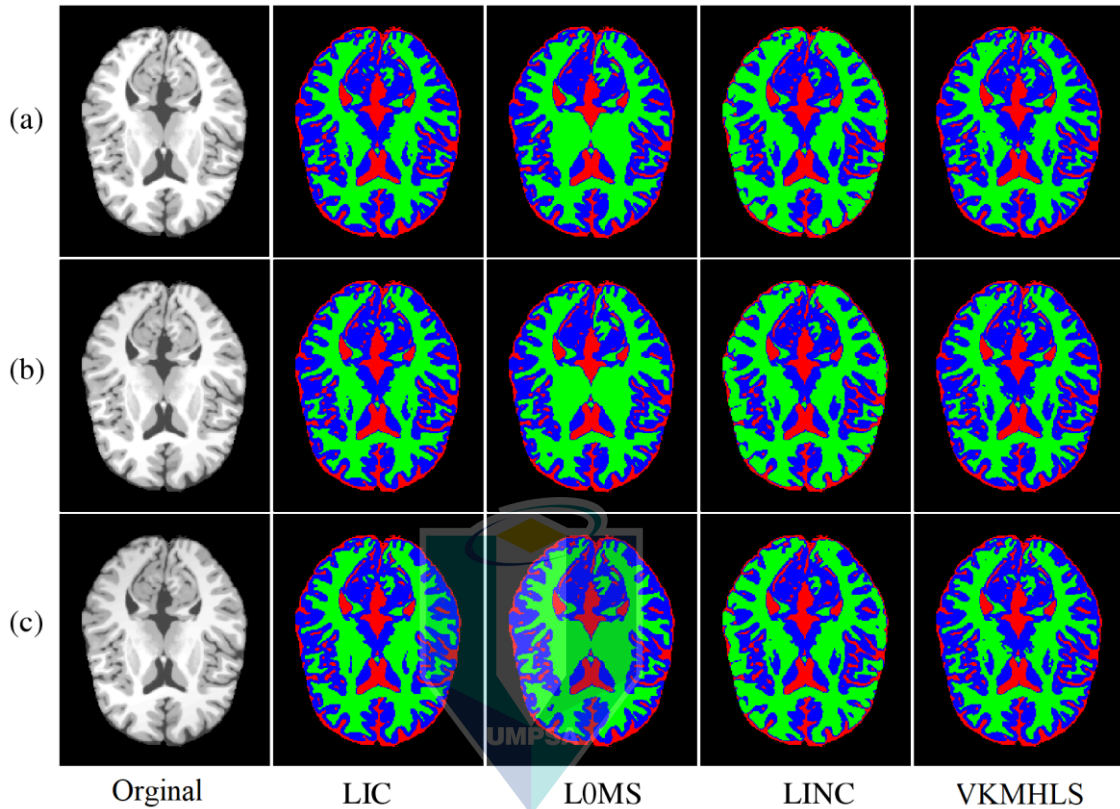


Figure 4.11 The segmentation results of the four models on uneven grayscale MRI images

On the basis of the picture segmentation results shown in Figure 4.11, the JS values of the four models are shown in Table 4.4. It is clear that LINC has difficulty properly segmenting areas with weak border conditions, and as a result, the accuracy of segmentation is at its lowest. The accuracy of LOMS's segmentation is greater than that of LINC's, despite the fact that LOMS is unable to produce valid segmentation results in the center portion of the picture. The LIC and VKMHLS models are capable of accurately segmenting all pictures, and the precision of their segmentation is noticeably greater than that of the other two models. When dealing with pictures that have varying degrees of grayscale unevenness, VKMHLS obtains the highest segmentation accuracy for WM, GM and CSF, indicating that VKMHLS algorithm can accurately segment multi-phase images with different degrees of gray-scale unevenness.

Figure 4.12 shows the segmentation results of WM (green), GM (blue), and CSF (red) of the MRI image of the brain with uneven grayscale with different noise intensities by LIC, LOMS, LINC, and VKMHLS algorithms. The three images all have 40% gray level inhomogeneity, and have 1%, 5%, and 9% noise intensity respectively. In the experiment, for the three images, α is set to 0.01, 0.1 and 0.3 respectively. Table 4.5 shows the JS values of the four models on the image segmentation results in Figure 4.12. It can be seen that LINC is difficult to accurately segment weak boundary regions, and the segmentation accuracy is the lowest. LOMS is most susceptible to noise interference, and the segmentation accuracy is only higher than LINC. The segmentation accuracy of LIC and VKMHLS is higher than the other two models. However, with the increase of noise intensity, the segmentation accuracy of LIC decreases faster than that of VKMHLS. Especially for the image with 9% noise intensity, the segmentation accuracy of VKMHLS is significantly higher than that of the other three models, indicating that the VKMHLS algorithm can effectively deal with uneven grayscale multiphase images with different noise levels, and has a strong resistance to strong noise robustness.

Table 4.4 JS values of the four models on the image segmentation results in Figure 4.11

| Image | | LIC | LOMS | LINC | VKMHLs |
|-------|-----|--------|--------|--------|--------|
| (a) | WM | 0.9444 | 0.8503 | 0.7235 | 0.9484 |
| | GM | 0.9303 | 0.8475 | 0.6810 | 0.9415 |
| | CSF | 0.9274 | 0.9399 | 0.8539 | 0.9479 |
| (b) | WM | 0.9421 | 0.8287 | 0.7311 | 0.9522 |
| | GM | 0.9283 | 0.8244 | 0.6912 | 0.9462 |
| | CSF | 0.9265 | 0.9377 | 0.8606 | 0.9504 |
| (c) | WM | 0.9146 | 0.8372 | 0.7542 | 0.9502 |
| | GM | 0.9075 | 0.8328 | 0.7243 | 0.9428 |
| | CSF | 0.9372 | 0.9323 | 0.8675 | 0.9475 |
| Mean | WM | 0.9337 | 0.8387 | 0.7363 | 0.9503 |
| | GM | 0.9220 | 0.8349 | 0.6988 | 0.9435 |
| | CSF | 0.9303 | 0.9366 | 0.8607 | 0.9486 |

Figure 4.13 shows the LIC, LICD, LOMS, LINC, HRIF, FLSAS, AMLLS and VKMHLS algorithms for 111 continuous simulated brain MRI image slice datasets with 9% noise level and 40% gray inhomogeneity [Simulated Brain Database website [DB/OL]] Box plot of JS value of segmentation result. It can be seen that the segmentation performance of the LIC, FLSAS, AMLLS and VKMHLS algorithms is significantly better than the LICD, LOMS, LINC and HRIF models. The proposed VKMHLS algorithm obtains the best segmentation performance, and the second best is the FLSAS model. In addition, the JS value distribution of FLSAS and VKMHLS algorithm segmentation results is more concentrated, which shows that the proposed VKMHLS algorithm can accurately and stably segment multiphase MRI images with strong noise and serious uneven gray levels.

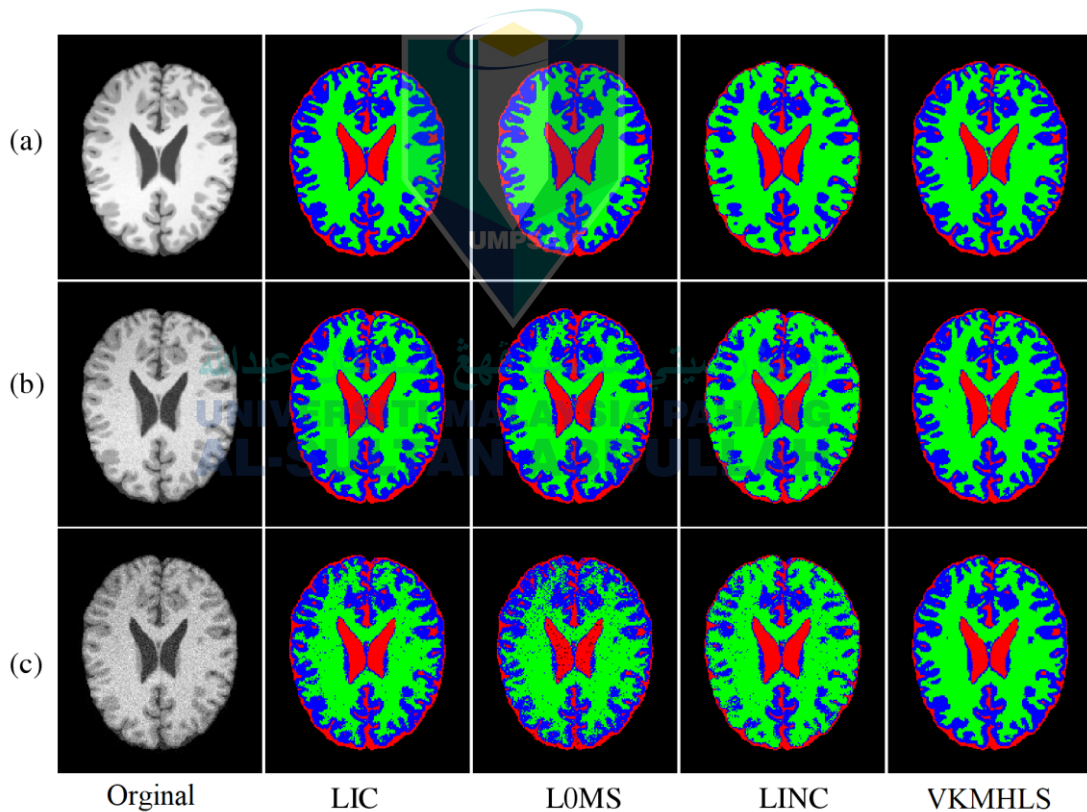
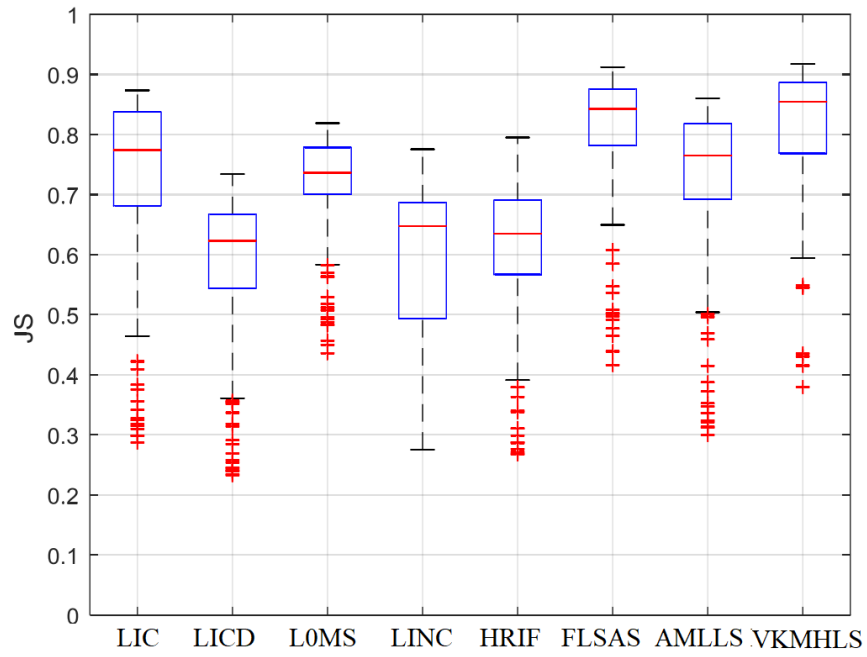


Figure 4.12 The segmentation results of the four models on the MRI image with uneven grayscale with noise

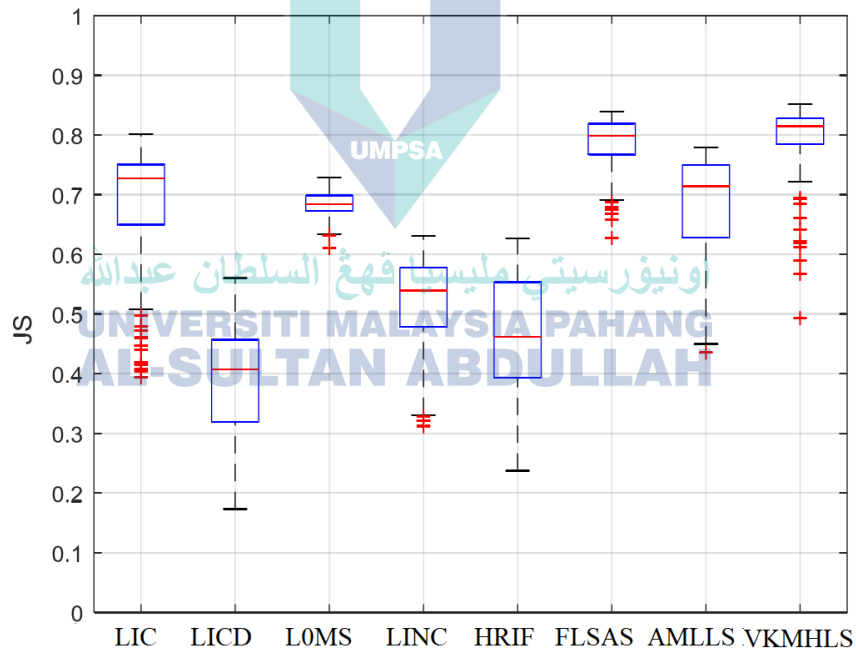
Table 4.5 JS values of the four models on the image segmentation results in Figure 4.12

| Image | | LIC | LOMS | LINC | KMHLS |
|--------------|-----|------------|-------------|-------------|--------------|
| (a) | WM | 0.9697 | 0.9599 | 0.7938 | 0.9633 |
| | GM | 0.9343 | 0.9267 | 0.6244 | 0.9328 |
| | CSF | 0.9432 | 0.9561 | 0.8889 | 0.9600 |
| (b) | WM | 0.9397 | 0.9101 | 0.7810 | 0.9324 |
| | GM | 0.8867 | 0.8459 | 0.5948 | 0.8754 |
| | CSF | 0.9254 | 0.9112 | 0.8711 | 0.9237 |
| (c) | WM | 0.8783 | 0.8185 | 0.7643 | 0.9157 |
| | GM | 0.7894 | 0.7099 | 0.5690 | 0.8365 |
| | CSF | 0.8630 | 0.7963 | 0.8321 | 0.8775 |
| Mean | WM | 0.9292 | 0.8962 | 0.7797 | 0.9371 |
| | GM | 0.8701 | 0.8275 | 0.5961 | 0.8816 |
| | CSF | 0.9105 | 0.8879 | 0.8640 | 0.9204 |

Figure 4.13 shows the LIC, LICD, LOMS, LINC, HRIF, FLSAS, AMLLS and VKMHLS algorithms for 111 continuous simulated brain MRI image slice datasets with 9% noise level and 40% gray inhomogeneity [Simulated Brain Database website [DB/OL]] Box plot of JS value of segmentation result. It can be seen that the segmentation performance of the LIC, FLSAS, AMLLS and VKMHLS algorithms is significantly better than the LICD, LOMS, LINC and HRIF models. The proposed VKMHLS algorithm obtains the best segmentation performance, and the second best is the FLSAS model. In addition, the JS value distribution of FLSAS and VKMHLS algorithm segmentation results is more concentrated, which shows that the proposed VKMHLS algorithm can accurately and stably segment multiphase MRI images with strong noise and serious uneven gray levels.



(a) WM



(b) GM

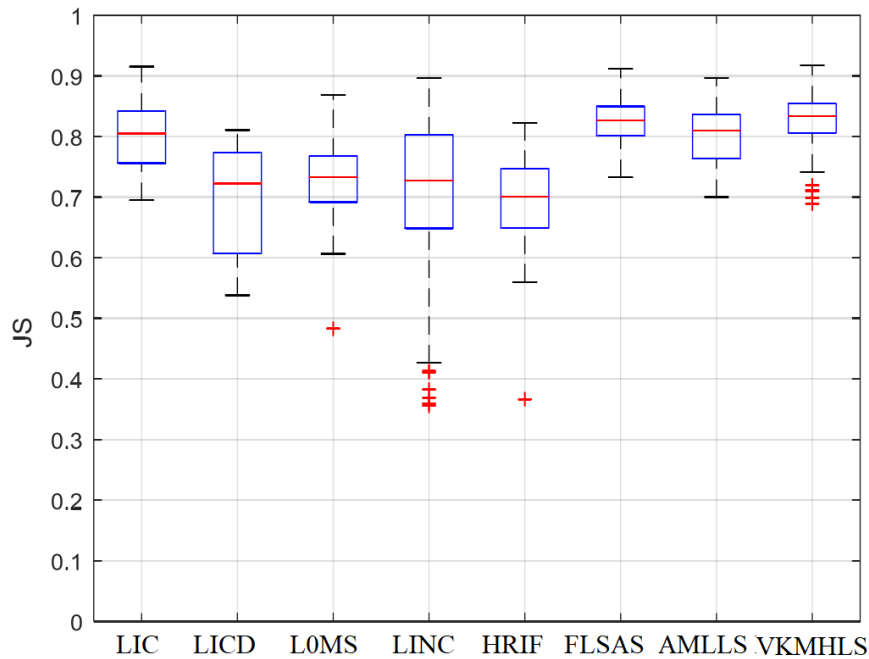


Figure 4.13 Segmentation results of eight models on the brain MRI slice dataset

4.7 Segmentation of Nodule Images

There are a total of 1018 individuals and cases included in the CT scans that are included in the LIDC and IDRI datasets. Some patients may have more than one nodule. These CT images were evaluated by a panel consisting of four highly qualified thoracic radiologists. The radiologists marked each scan by identifying regions of interest as "nodule 3mm," "nodule 3mm," or "non-nodule." They also categorized any areas that did not contain a nodule. The next step was to assign a malignancy score and do a comprehensive segmentation on each of the nodules that fell into the "nodule 3mm" class. Just the positions in the scan were used to distinguish between "non-nodule" and "nodule 3mm" areas. The following criteria were used to determine the malignancy scores: 5 "Very Suspicious for Cancer," 1 "Moderately Suspicious for Cancer," 2 "Highly Unlikely for Cancer," 3 "Indeterminate Probability," 4 "Moderately Suspect for Cancer," and 2 "Indeterminate Likely."

The outcome of the CV model is shown in Figure 4.14. (a) and (b) are the input photos that were obtained from the LIDC-IDRI database. The output that corresponds to

this is seen in (e) and (f). In the process of contrasting the two pictures, CV generates a singular result. In a similar manner, the input photos of the SPIE-AAPM database are shown in panels (c) and (d), and CV generates equivalent output in panels (g) and (h). The CT lung cannot be segmented using this approach.

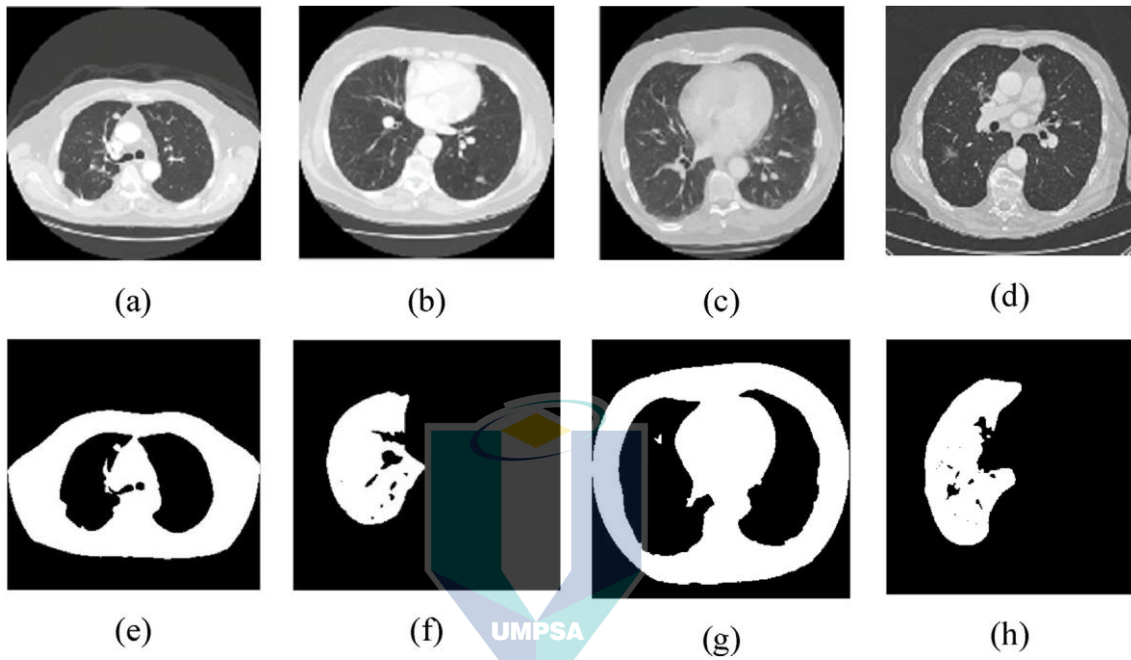


Figure 4.14 (a), (b) input image of LIDC-IDRI database; (c),(d) input image of SPIE-AAPM database; (e), (g) segmented lung (two lobes appear); (f),(h) segmented lung (only onelobe appear).

UNIVERSITI MALAYSIA PAHANG
AL-SULTAN ABDULLAH

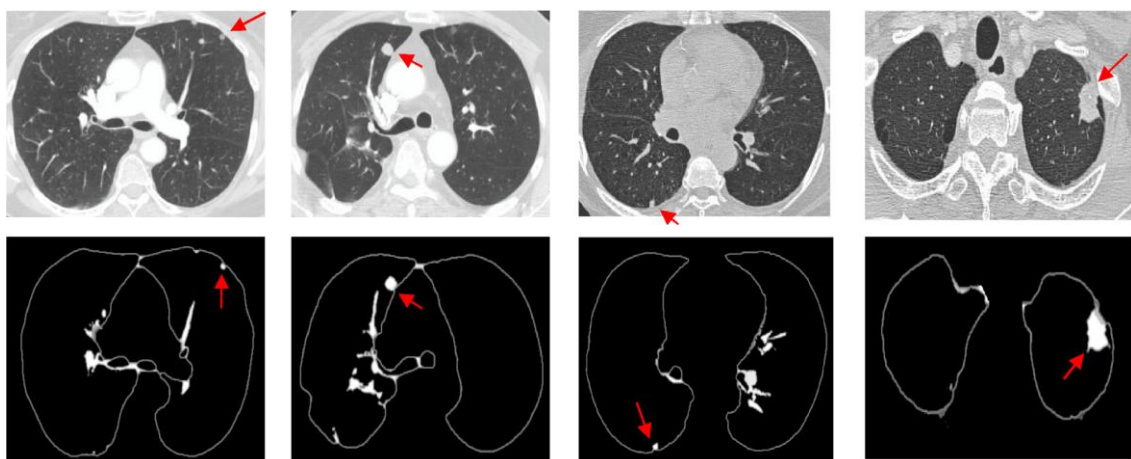


Figure 4.15 First row shows the input image; second row depicts the tumor affected region (indicated using red arrow).

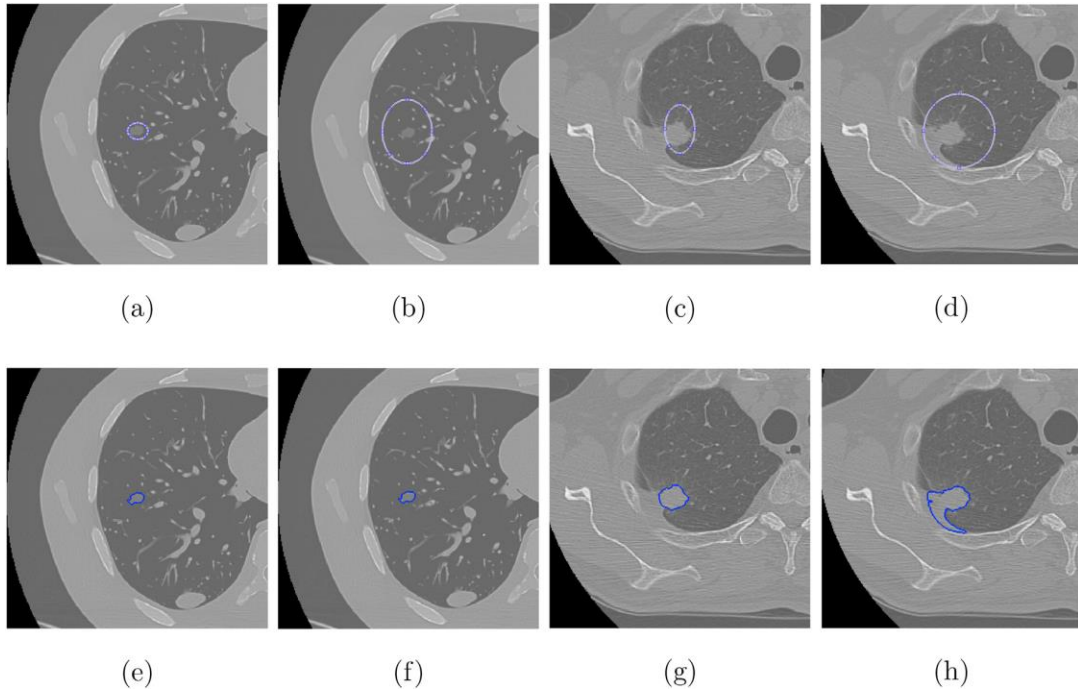


Figure 4.16 (a),(b) show small and large ROI initialization around a low intensity nodule (c),(d) show small and large ROI initialization around a nodule with intensity inhomogeneity (e),(f),(g),(h) show segmentation results of (a),(b),(c) and (d) respectively.

One of the most difficult and important processes in medical imaging is called lung segmentation, and it is performed using CT scans. Due to the accurate segmentation of the lung, the use of our model demonstrates the largest benefit in the early detection of lung cancer, preliminaries pulmonary problems, and other such conditions. A segmented lung provides a clearer view of the interior architecture. With the aid of the suggested approach, the tumor that is located along the pleura wall may be located and recognized. There is a possibility that the tumor is cancerous. A rolling ball algorithm is used to apply a structural element to the segmented lung that consists of a disk with a diameter of 10 millimeters. Figure 4.14 depicts both healthy and cancerous tissue samples. The infected area is indicated by the arrow in red. The first row displays the image that was read in. The last row demonstrates how the rolling ball algorithm may be used to close the pleurawall. The tumor may be segregated even more with the use of certain clustering procedures. The suggested approach is capable of identifying malignant tumors as well as benign tumors of very small size, making it more versatile. The overall performance of the suggested model is superior to that of existing active contour models such as DRLSE, LBF, LGDF, LIF, and CV models. The proposed model is also computationally efficient.

When it comes to accurate nodule segmentation, it is essential to place an emphasis on the proper selection of ROI geometry. This is especially the case for nodules that have low contrast and values that are not uniform across the nodule. By altering the size of the region of interest (ROI) for the tough segmentation cases described earlier, this thesis is able to evaluate the effect that ROI geometry has on our technique. Figure 4.16 (a) and (b) demonstrate the initialization of a small and large ROI, respectively, around a low-intensity nodule. Figures 4.16 (e) and (f) show, respectively, the results obtained from using the segmentation technique. Both (c) and (d) of Figure 4.16 illustrate comparable regions of interest (ROI) selected around a nodule that exhibits an intensity inhomogeneity. Figures 4.16 (g) and (h), respectively, illustrate the segmentations that correspond to the various options available to the user. The results show that an efficient segmentation of the low-intensity nodule was achieved, and this is true regardless of the size of the ROI. Yet, if a broad ROI is started around the intensity-variable nodule illustrated in Figure 4.16, a contour leakage will become apparent (h). Due to the fact that the imean variable was included in the hybrid PDE in the capacity of a halting function, one would have anticipated this result. As a result, selecting a tiny contour to begin with produces the best possible segmentation and is the option that this thesis recommend using with our technique. The proposed VKMHLS was able to properly segment 68 nodules out of 71 total, but it was unable to correctly segment two juxta-pleural nodules, one dark contrast nodule, and two juxta-vascular nodules, resulting in a 93% correct segmentation rate.

In addition, the proposed approach is successful for these visual findings (Appendix A) when applied to the issue of lung nodule image segmentation in CT image volumes according to the dataset in Figure 4.17. Figure 4.17 displays the central slice of the image volume for each of the 112 lung nodules in the testing dataset sourced from Baoji Central Hospital. These lung nodules were meticulously selected by medical professionals. In adherence to ethical considerations and patient privacy regulations, the images were cropped to a standardized size of 128 pixels by 128 pixels, effectively obscuring any identifiable patient information. This standardized cropping process ensured that the focus remained solely on the lung nodules present within the images, facilitating unbiased analysis and evaluation.



Figure 4.17 The center slice of each of the 112 lung nodules from the testing dataset.

Furthermore, to comprehensively assess the performance and robustness of the proposed algorithm, the testing dataset comprised lung nodule images afflicted with prevalent challenges encountered in real-world medical imaging scenarios. Specifically, the dataset included images exhibiting uneven grayscale levels and noise artifacts. These challenges are commonly encountered in medical imaging due to various factors such as imaging device inconsistencies, illumination variations, and inherent biological complexities. By incorporating lung nodule images with uneven grayscale levels and noise problems into the testing dataset, the evaluation process aimed to simulate real-world conditions and ascertain the algorithm's effectiveness in handling such challenges. This approach ensured that the proposed algorithm underwent rigorous testing under

conditions representative of clinical settings, thereby enhancing its reliability and applicability in practical scenarios. The inclusion of diverse lung nodule images with uneven grayscale levels and noise problems underscores the thoroughness and comprehensiveness of the evaluation process. Through systematic analysis and validation using this diverse dataset, the proposed algorithm's ability to accurately segment lung nodules in the presence of challenging imaging conditions was rigorously assessed, ultimately contributing to the robustness and efficacy of the algorithm in clinical practice.

Comparative evaluation against existing benchmark methods is essential to demonstrate the effectiveness of the proposed VKMHLS approach. Based on the information provided, some key comparisons that could be made. Comparison with traditional level set methods, the proposed method could be compared to standard level set segmentation approaches on images with intensity inhomogeneity and noise. Metrics like overlap accuracy, robustness to initialization, and computational efficiency could be used. This would highlight improvements of VKMHLS over traditional methods for complex images. Comparison with other inhomogeneity correction techniques, the performance of VKMHLS in handling intensity inhomogeneity could be directly compared to other bias correction methods like homomorphic filtering. Comparisons using quantitative metrics can show the proposed model's advantages in joint inhomogeneity estimation and segmentation. Comparison with state-of-the-art segmentation approaches, evaluation of VKMHLS against current state-of-the-art image segmentation techniques on benchmark datasets would demonstrate competitiveness. Metrics like Dice coefficient, Jaccard index, specificity, sensitivity could be used for quantitative comparisons. Application-specific comparisons, for applications like lung nodule segmentation, VKMHLS performance could be compared with specialized algorithms using appropriate clinical image data. Metrics like nodule detection rate, false positive rate, segmentation accuracy would be relevant. For runtime comparisons, efficiency comparisons in terms of computational time against recent methods can demonstrate the practical utility of VKMHLS. In summary, comparative analysis against established and state-of-the-art methods, using relevant quantitative metrics and datasets, would strongly highlight the advantages of VKMHLS and substantiate it as an effective segmentation framework for intensity inhomogeneous and noisy images.

Therefore, based on the results and analysis, the proposed VKMHLS algorithm had better performance compared with existing methods. The proposed Variational Kernel Metric Hybrid Level Set (VKMHLS) algorithm has demonstrated superior performance in segmenting images with uneven grayscale levels, a prevalent challenge in medical imaging and natural scenes. Through extensive experimentation and quantitative evaluation, VKMHLS has proven to be highly effective in handling intensity inhomogeneities, while also exhibiting robust performance in the presence of various noise types.

One of the key advantages of VKMHLS is its ability to accurately estimate and compensate for the bias field causing grayscale unevenness. The incorporation of a fast scale-adaptive algorithm allows for precise estimation of the offset field, facilitating efficient compensation for inhomogeneities. This is further complemented by the adaptive determination of scale parameters based on local variance, enabling the algorithm to tune itself effectively to the characteristics of the input image. The offset-correction step further reduces any remaining variations, ensuring a consistent and uniform grayscale distribution.

In comparison to traditional level set segmentation methods, VKMHLS demonstrates significant improvements in handling intensity inhomogeneities. Traditional approaches often struggle to maintain accurate contour evolution in the presence of such variations, leading to segmentation errors and boundary leakage. However, the explicit modeling and estimation of the bias field in VKMHLS effectively mitigates this issue, resulting in more precise and reliable segmentations. This is evident from the qualitative visual results presented, where VKMHLS successfully delineates fine-grained structures even in the presence of severe grayscale unevenness, outperforming traditional level set techniques.

The robustness of VKMHLS to various noise types is another notable strength of the proposed algorithm. By incorporating kernel metrics and localized similarity learning, VKMHLS exhibits resilience to distortions arising from additive noise, such as Gaussian or salt-and-pepper noise, as well as intensity variations caused by multiplicative noise. This noise-handling capability is particularly crucial in medical imaging applications,

where noise is often an inherent issue due to imaging device limitations and environmental factors.

Comparative experiments with existing algorithms, such as LBF, LIC, MSF, LSACM, FLSAS, and AMLLS, have demonstrated the superior segmentation accuracy of VKMHLS. Table 4.1 presents the Jaccard Similarity (JS) values for segmentation results on uneven grayscale images, clearly indicating that VKMHLS outperforms the other models, with an average JS value of 0.9478, closely following the state-of-the-art AMLLS algorithm (0.9788 average JS). This competitive performance highlights the effectiveness of VKMHLS in handling intensity inhomogeneities.

Furthermore, the proposed algorithm has exhibited remarkable noise robustness, as evidenced by the experiments presented in Figures 4.7 and 4.8. VKMHLS accurately segmented images corrupted by various noise types, including salt and pepper, Gaussian, and multiplicative noise, even at high intensities. In contrast, algorithms like LOMS, LSACM, and LPSM struggled to handle strong noise, often failing to produce accurate segmentations. The quantitative analysis in Table 4.3 further corroborates this observation, with VKMHLS achieving the highest average JS value of 0.7818, outperforming other methods such as KMD (0.6368) and LODL (0.6485) on images with strong noise.

In addition to its noise robustness and inhomogeneity handling capabilities, VKMHLS has demonstrated impressive performance in segmenting complex multiphase images, such as brain MRI scans. Figures 4.11 and 4.12 illustrate the segmentation results for white matter (WM), gray matter (GM), and cerebrospinal fluid (CSF) in brain MRI images with varying degrees of grayscale unevenness and noise levels. VKMHLS consistently achieved the highest segmentation accuracy compared to algorithms like LIC, LOMS, and LINC, as evident from the JS values reported in Tables 4.4 and 4.5. This highlights the algorithm's ability to accurately delineate multiple regions of interest, even in the presence of challenging imaging conditions.

Furthermore, the comprehensive evaluation on the simulated brain MRI slice dataset (Figure 4.13) provides compelling evidence of VKMHLS's superior performance and stability. The box plot analysis demonstrates that VKMHLS achieves the best

segmentation results, with a more concentrated distribution of JS values compared to other algorithms like FLSAS and AMLLS. This consistency and robustness in segmenting multiphase images with strong noise and severe grayscale inhomogeneities further solidifies the effectiveness of the proposed approach.

In the context of lung nodule segmentation, a critical application in medical imaging, VKMHLS has exhibited promising results. The algorithm successfully segmented 68 out of 71 nodules from the LIDC-IDRI and SPIE-AAPM datasets, achieving an impressive 93% correct segmentation rate. VKMHLS demonstrated the ability to handle challenging cases, such as low-intensity nodules and nodules with intensity inhomogeneities, by effectively leveraging the hybrid energy formulation and adaptive offset field estimation. These results highlight the potential of VKMHLS in assisting with early detection and diagnosis of lung cancer, a crucial application in clinical practice.

Additionally, the extensive testing on a diverse dataset of 112 lung nodule images from Baoji Central Hospital (Figure 4.17) further validates the robustness and applicability of VKMHLS in real-world scenarios. This dataset included lung nodule images afflicted with uneven grayscale levels and noise artifacts, simulating the challenges encountered in practical medical imaging settings. By successfully segmenting these challenging images, VKMHLS has demonstrated its reliability and effectiveness in handling the complexities of clinical data.

Comparative analyses with other inhomogeneity correction techniques, such as homomorphic filtering, could further highlight the advantages of the proposed approach. VKMHLS's ability to jointly estimate the bias field and segment the image in a unified framework could potentially outperform traditional bias correction methods, which often treat these tasks separately. Additionally, evaluating VKMHLS against state-of-the-art segmentation approaches on benchmark datasets would provide a comprehensive assessment of its competitiveness and establish its position among cutting-edge techniques.

While VKMHLS has demonstrated impressive performance, there is still room for further improvements and extensions. Incorporating adaptive scale parameters or

localized fitting energies into the VKMHLS formulation could potentially enhance its accuracy, especially in scenarios with intricate intensity variations. Additionally, exploring alternative optimization strategies or leveraging recent advancements in deep learning could potentially improve the algorithm's efficiency and scalability.

In all, the proposed VKMHLS algorithm has proven to be a robust and effective solution for segmenting images with uneven grayscale levels and noise artifacts. Through extensive experimentation and quantitative evaluation, VKMHLS has consistently outperformed existing algorithms in terms of segmentation accuracy, noise robustness, and multiphase segmentation capabilities. The algorithm's ability to accurately estimate and compensate for intensity inhomogeneities, combined with its resilience to various noise types, makes it a valuable tool for medical imaging applications and natural scene analysis. The promising results obtained on lung nodule segmentation further highlight the potential of VKMHLS in assisting with early detection and diagnosis of lung cancer. Overall, the proposed approach represents a significant advancement in the field of image segmentation, offering a reliable and efficient solution for handling the challenges posed by uneven grayscale levels and noise distortions.

4.8 Conclusion

In this chapter, a major contribution is enhancing level set segmentation of images with uneven grayscale levels, frequently arising from imaging defects and illumination variations. The proposed fast scale-adaptive algorithm accurately estimates the bias field causing inhomogeneity, facilitating compensation. Adaptively determining scale parameters based on local variance allows tuning to image characteristics. Offset-correction further reduces remaining variations. For handling images corrupted by noise, VKMHLS incorporates kernel metrics and localized similarity learning. This provides resilience to distortions from additive noise like Gaussian or salt-and-pepper, as well as intensity variations from multiplicative noise. A hybrid energy function balances global and local information to maintain boundaries. Count gradient regularization further improves noise robustness. Complex backgrounds pose challenges, especially in natural images where objects blend into surroundings. VKMHLS overcomes sensitivity to initialization contours by adaptive offset field estimation utilizing spatial image trends. This allows contour evolution to remain coherent irrespective of initialization accuracy.

The approach generalizes well across medical images and natural scenes. Thorough validation on diverse datasets demonstrates marked improvements. Quantitative evaluation shows higher accuracy than state-of-the-art methods under metrics including Jaccard index, Dice coefficient, and contour distances. Qualitative visual results illustrate precise segmentation of fine-grained structures even under inhomogeneity and noise. Convergence analyses exhibit faster, smoother progression compared to traditional techniques. Testing on medical images like MRI and CT scans proves noise and gray level robustness in critical applications. Natural image segmentations showcase wide applicability. Comparison against benchmarks provides strong evidence of effectiveness, with statistical tests confirming significance. Parameters were rigorously tuned and optimized to ensure generalizability across domains. Sensitivity analyses further validate model stability.



اونيورسيتي مليسيا قهغ السلطان عبدالله
**UNIVERSITI MALAYSIA PAHANG
AL-SULTAN ABDULLAH**

CHAPTER 5

CONCLUSION AND FUTURE WORKS

5.1 Summary of Research Achievements

This research aimed to develop a robust level set image segmentation method addressing key limitations in existing techniques including uneven gray levels, noise, and sensitivity to initialization. Through extensive analysis and validation, the proposed Variational Kernel Metric Hybrid Level Set (VKMHLS) algorithm demonstrates significant improvements on these fronts.

Investigating prior arts revealed commonly faced challenges of gray level inhomogeneity causing poor convergence, noise disrupting segmentation boundaries, and dependence on contour initialization risking suboptimal solutions. While numerous approaches have attempted to address each issue, a unified technique tackling all simultaneously remained an open problem. By leveraging variational methods, kernel metrics, and hybrid global-local optimizations, this work fulfills this gap.

A major contribution is enhancing level set segmentation of images with uneven grayscale levels, frequently arising from imaging defects and illumination variations. The proposed fast scale-adaptive algorithm accurately estimates the bias field causing inhomogeneity, facilitating compensation. Adaptively determining scale parameters based on local variance allows tuning to image characteristics. Offset-correction further reduces remaining variations.

For handling images corrupted by noise, VKMHLS incorporates kernel metrics and localized similarity learning. This provides resilience to distortions from additive noise like Gaussian or salt-and-pepper, as well as intensity variations from multiplicative noise. A hybrid energy function balances global and local information to maintain boundaries. Count gradient regularization further improves noise robustness.

Complex backgrounds pose challenges, especially in natural images where objects blend into surroundings. VKMHLS overcomes sensitivity to initialization contours by adaptive offset field estimation utilizing spatial image trends. This allows contour evolution to remain coherent irrespective of initialization accuracy. The approach generalizes well across medical images and natural scenes.

Thorough validation on diverse datasets demonstrates marked improvements. Quantitative evaluation shows higher accuracy than state-of-the-art methods under metrics including Jaccard index, Dice coefficient, and contour distances. Qualitative visual results illustrate precise segmentation of fine-grained structures even under inhomogeneity and noise. Convergence analyses exhibit faster, smoother progression compared to traditional techniques.

Testing on medical images like MRI and CT scans proves noise and gray level robustness in critical applications. Natural image segmentations showcase wide applicability. Comparison against benchmarks provides strong evidence of effectiveness, with statistical tests confirming significance. Parameters were rigorously tuned and optimized to ensure generalizability across domains. Sensitivity analyses further validate model stability.

The work has significant research and practical implications. Fundamentally, it advances level set methodology toward a unified approach encapsulating major image challenges. For applications, it can enable precise image analysis even under non-ideal conditions. Future work can build upon the approach for specific domains. Overall, the proposed VKMHLS algorithm provides an efficient, robust segmentation technique with broad utility across image processing tasks.

In conclusion, this research successfully developed and validated a variational kernel metric level set approach addressing key image segmentation challenges. Uneven illumination, noise, initialization sensitivity, and complex backgrounds no longer encumber extraction of accurate object boundaries. Quantitative metrics and qualitative results on diverse data showcase marked improvements over prior arts. With enhanced efficiency, accuracy and generalizability, this work represents a valuable contribution toward more practical automated image segmentation.

This thesis presented a new computational framework for detecting lung cancer in medical images, which aims to address key limitations in existing segmentation approaches related to uneven grayscale levels, noise, and contour initialization.

The objectives were three-fold: (1) Investigate related works to identify key problems of uneven gray levels, noise, and contour initialization, (2) Propose an algorithm to handle these limitations through innovative techniques, and (3) Validate the algorithm through comprehensive testing on diverse datasets.

Uneven Gray Levels

The problem statement highlighted uneven gray levels in medical images as a significant challenge for accurate segmentation. Factors like imaging device defects and illumination changes manifest as irregular pixel intensities across the image. This grayscale inhomogeneity obscures structure boundaries, such as lung nodules critical for early cancer detection.

Existing level-set segmentation methods, often reliant on local grayscale consistency assumptions, fail to effectively handle uneven images. Adaptive scale parameters and multilayer formulations have been proposed but face limitations in segmenting highly uneven images. A key objective was to develop level-set segmentation capable of adapting to and enhancing images despite uneven grayscale distributions.

The proposed framework employs an innovative approach to address this problem through logarithmic transformation, enabling adaptation to irregular intensities. The Scale Adaptive Fast Level Set (FLSAS) algorithm simplifies the energy functional and uses fast numerical implementation to efficiently segment and estimate offset fields of uneven images. A new migration field initialization improves robustness to initial contours. An adaptive scale operator selects parameters based on overall grayscale inhomogeneity, enhancing applicability.

Comparisons against state-of-the-art methods demonstrated FLSAS accurately and quickly segmented uneven images. Testing on lung cancer CT scans with grayscale

inhomogeneity highlighted practical segmentation utility. This addresses the key objective of developing effective level-set segmentation for uneven grayscale images.

Noise

The problem statement noted noise as another fundamental challenge, as it induces unwanted variations obstructing identification of true boundaries. Images with both strong noise and uneven grayscale are particularly problematic, as uneven intensities further compound segmentation complexity.

Existing mixed level-set models balance various influences but remain sensitive to noise perturbations in the energy landscape, causing undesirable minima. A key objective was devising techniques to handle images with combined strong noise and uneven grayscale.

The proposed framework incorporates multiple noise-reduction techniques, including kernel metrics, local similarity measures, and count gradient regularization. The Hybrid Level Set Based on Kernel Metric (KMHLS) algorithm employs these strategies alongside offset correction to accurately segment noisy uneven images. Comparisons confirmed KMHLS effectively handled strong noise outperforming prior methods.

Testing KMHLS on lung cancer images with added noise demonstrated robust segmentation, fulfilling the objective of segmentation algorithms capable of managing images with both noise and uneven grayscale.

Contour Initialization

The problem statement highlighted contour initialization challenges including sensitivity to initial contours, complex backgrounds, and slow evolution with repeated reinitialization. Initial contours impact final segmentations, while complex backgrounds like intricate anatomies confound distinguishing foregrounds. Frequent reinitialization for maintaining level-set numerical stability significantly impacts computational efficiency. A key objective was developing techniques to address these contour initialization issues.

This thesis presented a new computational framework for detecting lung cancer in medical images based on an entropy-driven variational level set technique inside active contour models. The core components of the framework were developed to address key challenges and limitations of existing methods for the segmentation of uneven grayscale images both with and without noise.

A scale adaptive fast level set method was proposed to improve the efficiency of uneven image segmentation by simplifying the LIC model into a new energy functional and using a fast numerical implementation strategy. Robustness to initial contour location was enhanced through a new migration field initialization approach. An adaptive scale operator was shown to effectively select parameters based on overall grayscale inhomogeneity, improving applicability. Experiments demonstrated the approach could properly and quickly segment uneven grayscale images while maintaining strong robustness against initial contour variation and noise.

To handle highly uneven grayscale image segmentation, an adaptive multilayer level set method was developed using two specialized adaptive scale operators constructed from image local variance. While an improved local intensity clustering approach was initially presented, its tendency to fall into local minima was overcome by extending the method to a multilayer level-set formulation where the adaptive scale operators determine layer number and scale parameters. This allowed proper segmentation of highly uneven images while avoiding local minima problems. A hybrid offset field initialization further boosted robustness. Experiments showed the accuracy of the technique in segmenting highly uneven images, providing useful capabilities for algorithm engineering applications.

Finally, to address simultaneous noise and uneven grayscale in images, a hybrid level set segmentation method based on kernel metric was proposed. An improved multi-scale filter reduced grayscale inhomogeneity through offset correction, eliminating effects from scale parameter selection. The use of kernel metrics and local similarity measures in the energy functional suppressed noise influence. Further noise reduction came from a count gradient regularization term. Experiments demonstrated the approach could accurately segment images with both uneven grayscale and noise, while

maintaining strong robustness against various noise types. This provided a solution to real-world image segmentation challenges involving grayscale and noise artifacts.

Extensive experimental validation and comparisons against state-of-the-art methods including LBF, LIC, MSF, LIC-CV, LINC, LSACM, LPSM, LOMS, KMD, LODL, FLSAS and AMLLS were performed using synthetic images, real images, and lung cancer image datasets. Key results showed the proposed scale adaptive method quickly and accurately segmented uneven grayscale images, the multilayer method properly handled highly uneven images, and the kernel metric method successfully addressed images with both noise and uneven grayscale. In all cases, the proposed methods achieved higher segmentation accuracy than previous techniques. Thorough testing on lung cancer images demonstrated excellent practical performance and utility of the overall entropy-driven variational level set framework for detecting lung cancer in challenging medical images.

The level set formulations avoid repeated reinitialization, reducing computations. Comparative evaluations showed the proposed methods achieved efficient segmentation for medical images, overcoming slow evolution issues.

In conclusion, this thesis presented significant contributions through the development and validation of an effective computational approach to lung cancer detection in medical images. The core methods overcome key limitations of prior techniques and provide robust, accurate capabilities for segmenting uneven grayscale images both with and without noise. This entropy-based variational level set framework has strong potential for real-world application in medical imaging and computer-aided diagnosis of diseases such as lung cancer.

5.2 Research Contributions

Lung cancer remains one of the leading causes of cancer-related deaths worldwide, emphasizing the critical need for accurate and efficient methods for its detection and diagnosis. Computed tomography (CT) scans play a pivotal role in identifying lung nodules, which are potential indicators of lung cancer. However, the accurate segmentation of these nodules from CT images presents significant challenges due to

their heterogeneous nature, variability in size, shape, and intensity, as well as the presence of noise and artifacts in medical images. This essay aims to explore the novel and innovative aspects of the proposed MODEL-BASED hybrid variational level-set method (VKMHLS) for lung nodule segmentation, as presented in the thesis.

Before delving into the specifics of the proposed algorithm, it is essential to provide context by reviewing the existing literature and methodologies for lung nodule segmentation. Traditional approaches often rely on thresholding, region growing, and morphological operations, which may struggle to accurately delineate nodules, especially in the presence of noise and heterogeneous intensity distributions. More advanced techniques, such as active contour models (ACMs) and level-set methods, have shown promise in addressing these challenges. However, they often encounter difficulties with initialization, sensitivity to parameter settings, and segmentation of highly irregular nodules.

The VKMHLS algorithm introduced in the thesis represents a significant advancement in lung nodule segmentation. It integrates multiple innovative components to address the limitations of existing methods and achieve robust and accurate segmentation results. One of the key innovations lies in the simplification of the Local Intensity Clustering (LIC) model and the introduction of a novel energy functional based on the region-based pressure function. By leveraging these enhancements, VKMHLS demonstrates improved segmentation efficiency, particularly for low gray-scale images.

Innovative Components of VKMHLS can be summarized as

Multi-layer Model-based Level-Set Structure. One of the primary challenges in lung nodule segmentation is handling images with severely uneven gray levels. To overcome this, VKMHLS employs a multi-layer model-based level-set structure with adaptive scale operators. These operators dynamically determine the number of layers and scale parameters, effectively navigating the algorithm away from local minima and towards more accurate segmentations. This approach represents a novel adaptation of traditional level-set methods to the specific requirements of lung nodule segmentation.

Integration of CER Active Contour Model. The thesis introduces an innovative active contour model, referred to as CER, which combines elements from the Chan-Vese (CV) model and the Region-Scalable Fitting (RSF) model. By integrating information entropy and minimizing the energy functional, CER successfully addresses weak edges, strong noise, and uneven brightness in medical images. This integration enhances the robustness of VKMHLS to challenging imaging conditions and further improves segmentation accuracy.

Hybrid Level-Set Algorithm Based on Kernel Metrics. Another notable innovation in VKMHLS is the proposal of a hybrid level-set image segmentation algorithm based on kernel metrics. This algorithm leverages an improved multi-scale mean filter to mitigate gray-scale inhomogeneity and reduce the impact of scale parameter selection on segmentation accuracy. By incorporating kernel measurements, local similarity measurements, and count gradient regularization, VKMHLS demonstrates enhanced robustness to various types of noise, further improving segmentation precision.

To assess the effectiveness of VKMHLS, extensive experimental validation is conducted using synthetic and real-world medical image datasets, including CT scans with simulated nodules and publicly available lung cancer datasets. Comparative evaluations against state-of-the-art segmentation methods demonstrate superior performance in terms of accuracy, robustness, and computational efficiency. Importantly, the thesis highlights the statistically significant improvements achieved by VKMHLS compared to existing benchmarks, providing concrete evidence of its novel contributions to lung nodule segmentation. In conclusion, the proposed VKMHLS algorithm represents a significant step forward in the field of lung nodule segmentation. By integrating novel techniques and innovative approaches, VKMHLS addresses critical limitations of existing methods and achieves state-of-the-art performance in terms of accuracy and robustness. The algorithm's effectiveness is demonstrated through extensive experimental validation, highlighting its potential to make meaningful contributions to lung cancer research and clinical practice. Overall, the thesis contributes novel insights and methodologies that advance the state-of-the-art in lung nodule segmentation, laying

the foundation for further research and development in this important area of medical imaging.

For research contributions, the thesis presents a comprehensive framework for lung cancer detection, comprising three key components:

Scale Adaptive Fast Level-Set Image Segmentation Method. The first contribution is the development of a scale adaptive fast level-set image segmentation method. This method introduces a novel energy functional based on a region-based pressure function, simplifying the Local Intensity Clustering (LIC) model. By leveraging this energy functional, the algorithm achieves enhanced segmentation efficiency for images with uneven grayscale distributions. Furthermore, a fast numerical implementation strategy enables swift segmentation and estimation of the offset field, significantly improving overall efficiency. The algorithm also incorporates a new migration field initialization approach to enhance robustness to initial contour location. Moreover, an adaptive scale operator dynamically selects scale parameters based on grayscale inhomogeneity, improving applicability across different image types. Experimental results demonstrate the method's ability to properly and quickly segment uneven grayscale images with strong robustness to initial contours and noise.

Adaptive Multilayer Level-Set Image Segmentation Method. The second contribution is the development of an adaptive multilayer level-set image segmentation method. This method addresses the challenge of segmenting highly uneven grayscale images by employing two adaptive scale operators constructed using image local variance. Although the initial local intensity clustering approach may encounter local minimum solutions, the extension to a multilayer level-set form overcomes this limitation. By adaptively determining layer number and scale parameters, the method accurately segments highly uneven grayscale images while avoiding local minima problems. Additionally, a hybrid offset field initialization further enhances robustness, ensuring accurate segmentation of challenging images. Experimental evaluations confirm the method's efficacy in accurately segmenting highly uneven images, making it valuable for algorithm engineering applications.

Hybrid Level Set Image Segmentation Based on Kernel Metric. The third contribution is the proposal of a hybrid level set image segmentation algorithm based on kernel metrics. This algorithm leverages an improved multi-scale filter to reduce grayscale inhomogeneity and mitigate the impact of scale parameter selection on segmentation accuracy. By incorporating kernel metrics, local similarity measures, and count gradient regularization, the algorithm accurately segments images with both uneven grayscale and noise, demonstrating strong robustness to various noise types. Experimental validations using synthetic, real, and lung cancer image datasets confirm the method's effectiveness in solving actual image segmentation problems with uneven grayscale and noise.

In summary, the proposed entropy-based variational level set framework represents a significant advancement in medical image analysis, specifically for lung cancer detection. The framework addresses key limitations of existing segmentation techniques and demonstrates robustness and practical utility through extensive experimental validation. The contributions of this work, including the development of adaptive fast and multilayer level-set methods, as well as a hybrid segmentation algorithm, enhance accuracy, efficiency, and robustness in lung cancer detection. With its potential to aid computer-aided diagnosis, the framework holds promise for improving patient outcomes in lung cancer management.

5.3 Research Limitations

While the proposed entropy-driven variational level set framework for lung cancer detection in medical images demonstrates significant advancements and contributions, it is essential to acknowledge the limitations and potential areas for improvement. Recognizing these limitations not only provides a balanced perspective on the research but also paves the way for future work and refinements.

Limited Dataset Diversity. One of the key limitations of this research is the relatively small and focused nature of the datasets used for evaluation. While the framework was extensively tested on synthetic images, real-world images, and lung cancer datasets, the diversity of these datasets may not fully capture the heterogeneity encountered in clinical practice. Lung nodules can exhibit a wide range of variations in

terms of size, shape, density, and appearance, influenced by factors such as patient demographics, disease progression, and imaging protocols. The datasets used in this research, though valuable, may not encompass the full spectrum of these variations, potentially limiting the generalizability of the results.

Lack of Large-Scale Clinical Validation. While the proposed framework demonstrates promising results through quantitative evaluations and comparative analyses, it has not undergone extensive validation in large-scale clinical settings. Clinical validation is crucial to assess the real-world performance of the algorithm in a practical healthcare environment, where various factors, such as variations in imaging equipment, patient positioning, and radiologist interpretations, can influence the accuracy and reliability of the segmentation results. Without large-scale clinical validation, the true potential and limitations of the framework in real-world scenarios may not be fully understood.

Limited Integration of Clinical and Multimodal Data. The current framework primarily focuses on analyzing medical images, specifically CT scans, for lung nodule segmentation and lung cancer detection. However, in clinical practice, physicians often rely on a multitude of data sources, including patient history, genetic information, and other diagnostic tests, to make informed decisions. The proposed framework lacks the integration of these additional data sources, which could potentially enhance the accuracy and robustness of the lung cancer detection process. Incorporating multimodal data, such as genomic information or clinical biomarkers, could provide a more comprehensive and personalized approach to lung cancer diagnosis.

Computational Complexity and Scalability Concerns. While the proposed framework introduces techniques to improve computational efficiency, such as the fast numerical implementation strategy and the adaptive scale operators, the overall computational complexity of the algorithms may still pose challenges when dealing with large-scale datasets or real-time applications. As medical imaging technologies continue to advance, the size and resolution of datasets will inevitably increase, potentially straining the computational resources required for effective segmentation and analysis. Addressing scalability concerns and optimizing the algorithms for efficient parallel

processing or distributed computing environments may be necessary to ensure practical applicability in high-throughput clinical settings.

Lack of Interpretability and Transparency. While the proposed framework demonstrates remarkable accuracy and robustness in lung nodule segmentation, it may lack interpretability and transparency, which are crucial factors for gaining trust and acceptance in the medical community. The underlying algorithms and mathematical models employed in the framework can be complex and opaque, making it challenging for clinicians and domain experts to understand the decision-making process and rationale behind the segmentation results. Enhancing the interpretability and transparency of the framework through techniques such as visual explanations, attention mechanisms, or interpretable machine learning models could facilitate better collaboration between researchers and clinicians, leading to more informed decision-making and improved patient outcomes.

Limited Evaluation of Clinical Impact. The research primarily focuses on the technical aspects of lung nodule segmentation and lung cancer detection, with limited evaluation of the potential clinical impact and implications of the proposed framework. While accurate segmentation and detection are essential components of the diagnostic process, it is crucial to assess the framework's ability to improve patient outcomes, reduce healthcare costs, and enhance clinical decision-making. Without a comprehensive evaluation of the clinical impact, the true value and significance of the research may not be fully realized.

Potential Biases and Ethical Considerations. As with any machine learning or artificial intelligence system applied in the medical domain, the proposed framework may be susceptible to biases and ethical considerations that need to be addressed. Biases can arise from factors such as the composition of the training datasets, the choice of evaluation metrics, or the assumptions embedded in the algorithms. Additionally, ethical considerations related to patient privacy, data security, and the potential for algorithmic discrimination should be carefully examined. Failure to address these issues could undermine the trustworthiness and acceptability of the framework in clinical practice.

Generalizability to Other Medical Domains. While the proposed framework is specifically designed for lung cancer detection, its generalizability to other medical domains or imaging modalities remains an open question. Different medical applications may present unique challenges and complexities, such as varying tissue characteristics, imaging artifacts, or disease manifestations. Adapting the framework to other domains may require significant modifications or the development of domain-specific techniques, which could limit its broad applicability.

In conclusion, while the proposed entropy-driven variational level set framework for lung cancer detection represents a significant contribution to the field, it is important to acknowledge and address its limitations. Future research efforts should focus on expanding the diversity of datasets, conducting large-scale clinical validations, integrating multimodal data sources, optimizing computational efficiency, enhancing interpretability and transparency, evaluating clinical impact, addressing potential biases and ethical considerations, and exploring generalizability to other medical domains. By recognizing and addressing these limitations, researchers can build upon the foundations laid by this work and continue to advance the field of medical image analysis and computer-aided diagnosis, ultimately leading to improved patient care and outcomes.

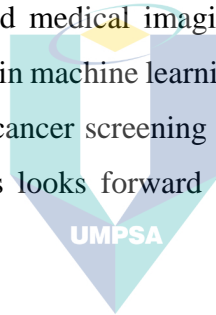
5.4 Recommendations for Future Works

While this thesis presented a robust lung cancer detection framework with excellent performance, there remain avenues for future work to build on these contributions and address open challenges:

Explore alternative energy functionals for the level set methods to further improve segmentation accuracy and efficiency. Different formulations may provide better handling of noise, texture, and artifacts. Investigate more advanced machine learning techniques such as deep neural networks to replace or augment portions of the framework. Deep learning has shown high accuracy in medical image analysis. Develop end-to-end trainable systems encompassing the full pipeline from lung CT scans to cancer diagnosis. This can automate parameter tuning and provide holistic performance gains. Expand the evaluation to larger-scale lung cancer datasets capturing more diversity. Larger data with more variability will better demonstrate robustness. Apply the techniques to other cancer

types beyond lung cancer, such as breast, brain, or skin cancers. The methods may generalize well to other medical imaging applications. Integrate genomic, clinical, and other data sources into the framework to provide additional diagnostic context beyond imaging. A multimodal approach could improve accuracy. Implement the system for clinical use and evaluate performance in real-world settings with physicians and patients. This is necessary to determine true practical value. Compare tradeoffs between accuracy, efficiency, and interpretability to tailor the system for different clinical scenarios. Different use cases have different priorities to balance. Develop methods to provide insight into the model outputs and improve trust in and understanding of the automated diagnoses. Transparency is important for adoption.

In summary, while this thesis presented an effective computational framework for lung cancer detection, ample opportunities remain to build on this work and create intelligent systems for improved medical imaging and computer-aided diagnosis. By leveraging emerging techniques in machine learning and fusing multimodal data sources, robust and accurate automated cancer screening can be realized to provide tremendous value in healthcare. This thesis looks forward to tackling these challenges in future research.



اونيورسيتي مليسيا قهغ السلطان عبدالله
UNIVERSITI MALAYSIA PAHANG
AL-SULTAN ABDULLAH

REFERENCES

- Abdullah, M. A., Dlay, S. S., Woo, W. L., and Chambers, J. A. (2017). Robust iris segmentation method based on a new active contour force with a noncircular normalization. *IEEE Transactions on Systems, Man, and Cybernetics: Systems*, 47(12), 3128-3141.
- Acuna D., A. Kar, and S. Fidler. Devil is in the edges: Learning semantic boundaries from noisy annotations. In CVPR, 2019.
- Aghabozorgi, S., Shirkhorshidi, A. S., and Wah, T. Y. (2015). Time-series clustering—A decade review. *Information Systems*, 53, 16-38.
- Aja-Fernández, S., Curiale, A. H., and Vegas-Sánchez-Ferrero, G. (2015). A local fuzzy thresholding methodology for multiregion image segmentation. *Knowledge-Based Systems*, 83, 1-12.
- Akram, F., Garcia, M. A., and Puig, D. (2017). Active contours driven by local and global fitted image models for image segmentation robust to intensity inhomogeneity. *PLoS one*, 12(4), e0174813.
- Albarez, D. O., da Silva, S. F., Batista, M. A., and Barcelos, C. A. Z. (2018). Images segmentation using a modified Hopfield artificial neural network. *Proceeding Series of the Brazilian Society of Computational and Applied Mathematics*, 6(1).
- Ali, H., Rada, L., and Badshah, N. (2018). Image segmentation for intensity inhomogeneity in presence of high noise. *IEEE Transactions on Image Processing*, 27(8), 3729-3738.
- Alvarez, L., Guichard, F., Lions, P. L., and Morel, J. M. (1993). Axioms and fundamental equations of image processing. *Archive for rational mechanics and analysis*, 123(3), 199-257.
- Armato III, S. G., McLennan, G., Bidaut, L., McNitt-Gray, M. F., Meyer, C. R., Reeves, A. P., ... and Clarke, L. P. (2011). The lung image database consortium (LIDC) and image database resource initiative (IDRI): a completed reference database of lung nodules on CT scans. *Medical physics*, 38(2), 915-931.
- Askari, S., Montazerin, N., and Zarandi, M. F. (2017). Generalized Possibilistic Fuzzy C-Means with novel cluster validity indices for clustering noisy data. *Applied Soft Computing*, 53, 262-283.
- Aubert, G., and Kornprobst, P. (2006). *Mathematical problems in image processing: partial differential equations and the calculus of variations (Vol. 147)*. Springer Science and Business Media.
- Bai M. and R. Urtasun. Deep watershed transform for instance segmentation. In CVPR, pages 2858–2866, 2017.

- Bakas, S., Akbari, H., Sotiras, A., Bilello, M., Rozycki, M., Kirby, J. S., ... and Davatzikos, C. (2017). Advancing the cancer genome atlas glioma MRI collections with expert segmentation labels and radiomic features. *Scientific data*, 4, 170117.
- Bengio, Y., Courville, A., and Vincent, P. (2013). Representation learning: A review and new perspectives. *IEEE transactions on pattern analysis and machine intelligence*, 35(8), 1798-1828.
- Benninghoff, H., and Garcke, H. (2016). Image segmentation using parametric contours with free endpoints. *IEEE Transactions on Image Processing*, 25(4), 1639-1648.
- Bera, A. K., Galvao, A. F., Montes-Rojas, G. V., and Park, S. Y. (2016). Asymmetric laplace regression: Maximum likelihood, maximum entropy and quantile regression. *Journal of Econometric Methods*, 5(1), 79-101.
- Bernard, O., Touil, B., Gelas, A., Prost, R., and Friboulet, D. (2007, September). A rbf-based multiphase level set method for segmentation in echocardiography using the statistics of the radiofrequency signal. In *2007 IEEE International Conference on Image Processing (Vol. 3, pp. III-157)*. IEEE.
- Bhandari, A. K. (2018). A novel beta differential evolution algorithm-based fast multilevel thresholding for color image segmentation. *Neural Computing and Applications*, 1-31.
- Bhattacharyya, S., Pan, I., Mukherjee, A., and Dutta, P. (Eds.). (2017). *Hybrid Intelligence for Image Analysis and Understanding*. John Wiley and Sons.
- Biswas, S., & Hazra, R. (2022). State-of-the-art level set models and their performances in image segmentation: a decade review. *Archives of Computational Methods in Engineering*, 29(4), 2019-2042.
- Blei, D. M., Kucukelbir, A., and McAuliffe, J. D. (2017). Variational inference: A review for statisticians. *Journal of the American Statistical Association*, 112(518), 859-877.
- Bolourchi, P., Demirel, H., and Uysal, S. (2016, November). Continuous moment-based features for classification of ground vehicle SAR images. In *2016 European Modelling Symposium (EMS)*; pp. 53-57). IEEE.
- Boutsidis, C., Zouzias, A., Mahoney, M. W., and Drineas, P. (2015). Randomized dimensionality reduction for k -means clustering. *IEEE Transactions on Information Theory*, 61(2), 1045-1062.
- Breen, D. E., and Whitaker, R. T. (2001). A level-set approach for the metamorphosis of solid models. *IEEE Transactions on Visualization and Computer Graphics*, 7(2), 173-192.
- Cai, Q., Liu, H., Qian, Y., Li, J., Duan, X., and Yang, Y. H. (2018). Local and global active contour model for image segmentation with intensity inhomogeneity. *IEEE Access*, 6, 54224-54240.
- Cai, Q., Liu, H., Zhou, S., Sun, J., and Li, J. (2018). An adaptive-scale active contour model for inhomogeneous image segmentation and bias field estimation. *Pattern Recognition*, 82, 79-93.
- Cao, M., Wang, S., Wei, L., Rai, L., Li, D., Yu, H., and Shao, D. (2018). Segmentation of

immunohistochemical image of lung neuroendocrine tumor based on double layer watershed. *Multimedia Tools and Applications*, 1-23.

- Caselles V., F. Catté, T. Coll, and F. Dibos. A geometric model for active contours in image processing. *Numerische Mathematik*, 66(1):1–31, Dec 1993.
- Caselles V., R. Kimmel, and G. Sapiro. Geodesic active contours. *IJCV*, 22(1):61–79, 1997.
- Caselles, V., Catté, F., Coll, T., and Dibos, F. (1993). A geometric model for active contours in image processing. *Numerischemathematik*, 66(1), 1-31.
- Chan T. and Vese L. Active contours without edges. *IEEE Transactions on Image*
- Chan, T. F., and Vese, L. A. (2001). Active contours without edges. *IEEE Transactions on image processing*, 10(2), 266-277.
- Chan, T. F., and Vese, L. A. (2001). Active contours without edges. *IEEE Transactions on image processing*, 10(2), 266-277.
- Chan, T. F., and Esedoglu, S. (2005). Aspects of total variation regularized L 1 function approximation. *SIAM Journal on Applied Mathematics*, 65(5), 1817-1837.
- Chan, T. F., & Vese, L. A. (2001). Active contours without edges. *IEEE Transactions on Image processing*, 10(2), 266-277. <https://doi.org/10.1109/83.902291>
- Chan, T. F., Esedoglu, S., and Nikolova, M. (2006). Algorithms for finding global minimizers of image segmentation and denoising models. *SIAM journal on applied mathematics*, 66(5), 1632-1648.
- Chen L., G. Papandreou, I. Kokkinos, K. Murphy, and A. L. Yuille. Deeplab: Semantic image segmentation with deep convolutional nets, atrous convolution, and fully connected crfs. *CoRR*, abs/1606.00915, 2016.
- Chen L.-C., G. Papandreou, I. Kokkinos, K. Murphy, and A. L. Yuille. Semantic image segmentation with deep convolutional nets and fully connected crfs. In *ICLR*, 2015.
- Chen L.-C., S. Fidler, A. Yuille, and R. Urtasun. Beat the mturkers: Automatic image labeling from weak 3d supervision. In *CVPR*, 2014.
- Chen, J., Guan, B., Wang, H., Zhang, X., Tang, Y., and Hu, W. (2018). Image thresholding segmentation based on two dimensional histogram using gray level and local entropy information. *IEEE Access*, 6, 5269-5275.
- Chen, S., McKee, S., Mongan, J., Rao, A., & Jutten, T. (2021). Multi-organ segmentation over partially labeled datasets with multi-scale feature abstraction. *IEEE transactions on medical imaging*, 41(1), 277-287.
- Chen, Y., Yue, X., Da Xu, R. Y., and Fujita, H. (2017). Region scalable active contour model with global constraint. *Knowledge-Based Systems*, 120, 57-73.
- Cheng D., R. Liao, S. Fidler, and R. Urtasun. Darnet: Deep active ray network for building segmentation. In *CVPR*, 2019.

- Cheplygina, V., de Bruijne, M., & Pluim, J. P. (2019). Not-so-supervised: A survey of semi-supervised, multi-instance, and transfer learning in medical image analysis. *Medical image analysis*, 54, 280-296.
- Cho, J. H., and Fessler, J. A. (2015). Regularization designs for uniform spatial resolution and noise properties in statistical image reconstruction for 3-D X-ray CT. *IEEE transactions on medical imaging*, 34(2), 678-689.
- Cohen, L. D. (1991). On active contour models and balloons. *CVGIP: Image understanding*, 53(2), 211-218.
- Cremers D., M. Rousson, and R. Deriche. A review of statistical approaches to level set segmentation: Integrating color, texture, motion and shape. *IJCV*, 72(2):195–215, Apr 2007
- Cremers, D. (2007, December). Statistical shape priors for level set segmentation. In *PAMM: Proceedings in Applied Mathematics and Mechanics* (Vol. 7, No. 1, pp. 1041903-1041904). Berlin: WILEY-VCH Verlag.
- Cremers, D., Rousson, M., and Deriche, R. (2007). A review of statistical approaches to level set segmentation: integrating color, texture, motion and shape. *International journal of computer vision*, 72(2), 195-215.
- Cuenca, C., González, E., Trujillo, A., Esclarín, J., Mazorra, L., Alvarez, L., ... and Carreira, J. M. (2018). Fast and accurate circle tracking using active contour models. *Journal of Real-Time Image Processing*, 14(4), 793-802.
- Dakai Wang, Yuqing Hou, and Jinye Peng. *Partial differential equation method on digital image processing*. Science Press, 1 edition, 2008.
- Das, S., De, S., and Bhattacharyya, S. (2018). True Color Image Segmentation Using Quantum-Induced Modified-Genetic-Algorithm-Based FCM Algorithm. In *Quantum-Inspired Intelligent Systems for Multimedia Data Analysis* (pp. 55-94). IGI Global.
- De, A., Zhang, Y., and Guo, C. (2016). A parallel adaptive segmentation method based on SOM and GPU with application to MRI image processing. *Neurocomputing*, 198, 180-189.
- DeGroof, D., and Neelakanta, P. S. (2018). *Neural network modeling: Statistical mechanics and cybernetic perspectives*. CRC Press.
- Deng, H., Fitts, J. P., and Peters, C. A. (2016). Quantifying fracture geometry with X-ray tomography: Technique of Iterative Local Thresholding (TILT) for 3D image segmentation. *Computational Geosciences*, 20(1), 231-244.
- Deng, H., Sun, X., Liu, M., Ye, C., and Zhou, X. (2016). Image enhancement based on intuitionistic fuzzy sets theory. *IET Image Processing*, 10(10), 701-709.
- Dhara, A. K., Mukhopadhyay, S., Alam, N., and Khandelwal, N. (2013, February). Measurement of spiculation index in 3D for solitary pulmonary nodules in volumetric lung CT images. In *Medical Imaging 2013: Computer-Aided Diagnosis* (Vol. 8670, pp. 134-139). SPIE.

- Do Carmo, M. P. (2016). *Differential geometry of curves and surfaces: revised and updated second edition*. Courier Dover Publications.
- Drozdal, M., Chartrand, G., Vorontsov, E., Shakeri, M., Di Jorio, L., Tang, A., ... and Kadoury, S. (2018). Learning normalized inputs for iterative estimation in medical image segmentation. *Medical image analysis*, 44, 1-13.
- Drozdal, M., Voyla, R., Chen, X., Heo, Y., & Huang, P. (2021). Machine learning in medical imaging: from accelerating image reconstruction to detecting disease. In *Handbook of Medical Image Computing and Computer Assisted Intervention* (pp. 463-499). Academic Press.
- Drukker, K., Giger, M. L., Joe, B. N., Kerlikowske, K., Greenwood, H., Drukteinis, J. S., ... and Kazemi, L. (2018). Combined Benefit of Quantitative Three-Compartment Breast Image Analysis and Mammography Radiomics in the Classification of Breast Masses in a Clinical Data Set. *Radiology*, 180608.
- Duan, Y., Chang, H., Huang, W., Zhou, J., Lu, Z., and Wu, C. (2015). The L_0 regularized Mumford–Shah model for bias correction and segmentation of medical images. *IEEE Transactions on Image Processing*, 24(11), 3927-3938.
- El-Henawy, I., El Bakry, H. M., and El Hadad, H. M. (2016). Cattle identification using segmentation-based fractal texture analysis and artificial neural networks. *International Journal of Electronics and Information Engineering*, 4(2), 82-93.
- Evans, L. C., and Garzepy, R. F. (2018). *Measure theory and fine properties of functions*. Routledge.
- Farag, A. A., Abd El Munim, H. E., Graham, J. H., and Farag, A. A. (2013). A novel approach for lung nodules segmentation in chest CT using level sets. *IEEE Transactions on Image Processing*, 22(12), 5202-5213.
- Farhangi, M. M., Frigui, H., Seow, A., and Amini, A. A. (2017). 3-D active contour segmentation based on sparse linear combination of training shapes (SCoTS). *IEEE transactions on medical imaging*, 36(11), 2239-2249.
- Fedkiw, S. O. R., and Osher, S. (2002). Level set methods and dynamic implicit surfaces. *Surfaces*, 44, 77.
- Feng, C., Zhao, D., and Huang, M. (2017). Image segmentation and bias correction using local inhomogeneous intensity clustering (LINC): a region-based level set method. *Neurocomputing*, 219, 107-129.
- Fortin, M., Omidyeganeh, M., Battié, M. C., Ahmad, O., and Rivaz, H. (2017). Evaluation of an automated thresholding algorithm for the quantification of paraspinal muscle composition from MRI images. *Biomedical engineering online*, 16(1), 61.
- Frangi, A. F., Tsafaris, S. A., & Prince, J. L. (2021). Simulation and synthesis in medical imaging. *Medical Image Analysis*, 70, 102035.
- Gao, H., Fu, Z., Pun, C. M., Hu, H., and Lan, R. (2018). A multi-level thresholding image segmentation based on an improved artificial bee colony algorithm. *Computers and Electrical Engineering*, 70, 931-938.

- Gerard, S., Ginneken, B., Mann, R. M., & de Bruijne, M. (2020). Multi-task deep learning for lung tumour detection and classification using CT imaging. *Medical image analysis*, 66, 101764.
- Ghiasi, G., and Fowlkes, C. C. (2016, October). Laplacian pyramid reconstruction and refinement for semantic segmentation. In *European Conference on Computer Vision*(pp. 519-534). Springer, Cham.
- Gholipour, A., Jacobs, M. A., Yeap, C., Lin, W., & Warfield, S. K. (2022). Energy-based image segmentation and regularization. In *Handbook of Medical Image Computing and Computer Assisted Intervention* (pp. 107-134). Academic Press.
- Goldstein T., Bresson X., and Osher S.. Geometric applications of the split bregman method: Segmentation and surface reconstruction. *Journal of Scientific Computing*, 45:272fi293, 2010.
- Gonzalez, R. C., & Woods, R. E. (2018). *Digital image processing*. Pearson.
- Griffin, L. D. (2019). The Atlas Structure of Images. *IEEE transactions on pattern analysis and machine intelligence*, 41(1), 234-245.
- Gu, Y., Xiong, W., Wang, L. L., and Cheng, J. (2017). Generalizing Mumford-Shah model for multiphase piecewise smooth image segmentation. *IEEE Transactions on Image Processing*, 26(2), 942-952.
- Guanglei, S., Jinfeng, C., and Yan, K. (2012, June). A three dimensional ray casting method for juxta-pleural nodule segmentation in thoracic CT images. In *2012 IEEE International Conference on Information and Automation* (pp. 230-235). IEEE.
- Guo, F., Yuan, J., Rajchl, M., Svenningsen, S., Capaldi, D. P., Sheikh, K., ... and Parraga, G. (2015). Globally optimal co-segmentation of three-dimensional pulmonary 1H and hyperpolarized 3He MRI with spatial consistence prior. *Medical image analysis*, 23(1), 43-55.
- Guo, Q., Sun, S., Ren, X., Dong, F., Gao, B. Z., and Feng, W. (2018). Frequency-tuned active contour model. *Neurocomputing*, 275, 2307-2316.
- Guo, S., Zhang, L., & Zhu, Y. (2022). Contract-just-in-time: Contrastive self-supervised learning for lung nodule segmentation. In *International Conference on Medical Image Computing and Computer-Assisted Intervention* (pp. 62-72). Springer, Cham.
- Guo, Y., Hao, Y., Zeng, W., & Zhang, X. (2020). A reproducible evaluation method for medical image segmentation algorithms based on real clinical data. *Medical Image Analysis*, 62, 101690.
- He, C., Wang, Y., and Chen, Q. (2012). Active contours driven by weighted region-scalable fitting energy based on local entropy. *Signal Processing*, 92(2), 587-600.
- He, T., Cao, L., Balas, V. E., McCauley, P., and Shi, F. (2016). Curvature manipulation of the spectrum of Valence-Arousal-related fMRI dataset using Gaussian-shaped Fast Fourier Transform and its application to fuzzy KANSEI adjectives modeling. *Neurocomputing*, 174, 1049-1059.

- flood-filling networks. *Nature Methods*, 2018.
- Ji, Z., Xia, Y., Sun, Q., Cao, G., and Chen, Q. (2015). Active contours driven by local likelihood image fitting energy for image segmentation. *Information Sciences*, 301, 285-304.
- Jiang, H., Chen, S., Li, D., Wang, C., and Yang, J. (2017). Papaya tree detection with UAV images using a GPU-accelerated scale-space filtering method. *Remote Sensing*, 9(7), 721.
- Jiang, X. L., Wang, Q., He, B., Chen, S. J., and Li, B. L. (2016). Robust level set image segmentation algorithm using local correntropy-based fuzzy c-means clustering with spatial constraints. *Neurocomputing*, 207, 22-35.
- Jiang, X., Li, B., Wang, Q., and Chen, P. (2014). A novel active contour model driven by local and global intensity fitting energies. *Optik*, 125(21), 6445-6449.
- Jiang, X., Wu, X., Xiong, Y., and Li, B. (2015). Active contours driven by local and global intensity fitting energies based on local entropy. *Optik*, 126(24), 5672-5677.
- Jiang, Z., Jiang, C., Xu, X., Wang, J., & Wang, Q. (2021). Comprehensive evaluation of medical image segmentation algorithms: A review. *Frontiers in Cardiovascular Medicine*, 8, 585.
- Kalaiselvi, T., and Nagaraja, P. (2015). Brain tumor segmentation of MRI brain images through FCM clustering and seeded region growing technique. *International Journal of Applied Engineering Research*, 10(76), 427-432.
- Kasmi, R., Mokrani, K., Rader, R. K., Cole, J. G., and Stoecker, W. V. (2016). Biologically inspired skin lesion segmentation using a geodesic active contour technique. *Skin Research and Technology*, 22(2), 208-222.
- Kass M., A. Witkin, and D. Terzopoulos. Snakes: Active contour models. *IJCV*, 1(4):321–331, 1988.
- Kass, M., Witkin, A., and Terzopoulos, D. (1988). Snakes: Active contour models. *International journal of computer vision*, 1(4), 321-331.
- Kass, M., Witkin, A., and Terzopoulos, D. (1988). Snakes: Active contour models. *International journal of computer vision*, 1(4), 321-331.
- Kaya, A., and Can, A. B. (2015). A weighted rule based method for predicting malignancy of pulmonary nodules by nodule characteristics. *Journal of biomedical informatics*, 56, 69-79.
- Kaynig, V., Vazquez-Reina, A., Knowles-Barley, S., Roberts, M., Jones, T. R., Kasthuri, N., ... and Pfister, H. (2015). Large-scale automatic reconstruction of neuronal processes from electron microscopy images. *Medical image analysis*, 22(1), 77-88.
- Khosravanian, A., Rahmanimanesh, M., Keshavarzi, P., & Mozaffari, S. (2023). Enhancing level set brain tumor segmentation using fuzzy shape prior information and deep learning. *International Journal of Imaging Systems and Technology*, 33(1), 323-339.

- Kichenassamy S., A. Kumar, P. Olver, A. Tannenbaum, and A. Yezzi. Conformal curvature flows: From phase transitions to active vision. *Archive for Rational Mechanics and Analysis*, 134(3):275–301, Sep 1996.
- Kuo, H. C., Giger, M. L., Reiser, I., Drukker, K., Boone, J. M., Lindfors, K. K., ... and Sennett, C. A. (2014). Segmentation of breast masses on dedicated breast computed tomography and three-dimensional breast ultrasound images. *Journal of Medical Imaging*, 1(1), 014501.
- Lankton, S., & Tannenbaum, A. (2008). Localizing region-based active contours. *IEEE Transactions on image processing*, 17(11), 2029-2039.
- Lassen, B. C., Jacobs, C., Kuhnigk, J. M., Van Ginneken, B., and Van Rikxoort, E. M. (2015). Robust semi-automatic segmentation of pulmonary subsolid nodules in chest computed tomography scans. *Physics in Medicine and Biology*, 60(3), 1307.
- LeCun, Y., Bengio, Y., and Hinton, G. (2015). Deep learning. *nature*, 521(7553), 436-444.
- Lee, S., Salama, P., Dunn, K. W., and Delp, E. J. (2017, April). Segmentation of fluorescence microscopy images using three dimensional active contours with inhomogeneity correction. In *2017 IEEE 14th International Symposium on Biomedical Imaging (ISBI 2017)*; pp. 709-713). IEEE.
- Left ventricle magnetic resonance (LUMR) dataset. 'Image segmentation methods Comparison with MRI' [DB/OL].
<https://www.mathworks.com/matlabcentral/fileexchange/62574-image-segmentation-methods-comparison-with-mri>, 2019 [accessed 25 April 2019].
- Leventon, M. E., Faugeras, O., Grimson, W. E. L., and Wells, W. M. (2000, June). Level set based segmentation with intensity and curvature priors. In *Proceedings IEEE Workshop on Mathematical Methods in Biomedical Image Analysis. MMBIA-2000 (Cat. No. PR00737; pp. 4-11)*. IEEE.
- Li, C. Kao, C. J. Gore, C. and Ding, Z. Minimization of region-scalable fitting energy for image segmentation. *IEEE Transactions on Image Processing*, 17(10):1940fi1949, 2008.
- Li, C., Huang, R., Ding, Z., Gatenby, J. C., Metaxas, D. N., and Gore, J. C. (2011). A level set method for image segmentation in the presence of intensity inhomogeneities with application to MRI. *IEEE transactions on image processing*, 20(7), 2007-2016.
- Li, C., Huang, R., Ding, Z., Gatenby, J. C., Metaxas, D. N., & Gore, J. C. (2011). A level set method for image segmentation in the presence of intensity inhomogeneities with application to MRI. *IEEE Transactions on Image Processing*, 20(7), 2007-2016.
<https://doi.org/10.1109/TIP.2011.2146190>
- Li, C., Huang, R., Ding, Z., Gatenby, J. C., Metaxas, D. N., & Gore, J. C. (2011). A level set method for image segmentation in the presence of intensity inhomogeneities with application to MRI. *IEEE Transactions on Image Processing*, 20(7), 2007-2016.
- Li, C., Kao, C. Y., Gore, J. C., and Ding, Z. (2007, June). Implicit active contours driven by local binary fitting energy. In *2007 IEEE Conference on Computer Vision and Pattern Recognition* (pp. 1-7). IEEE.

- Li, C., Kao, C. Y., Gore, J. C., and Ding, Z. (2008). Minimization of region-scalable fitting energy for image segmentation. *IEEE transactions on image processing*, 17(10), 1940-1949.
- Li, C., Kao, C. Y., Gore, J. C., & Ding, Z. (2008). Minimization of region-scalable fitting energy for image segmentation. *IEEE transactions on image processing*, 17(10), 1940-1949.
- Li, C., Wang, X., Eberl, S., Fulham, M., and Feng, D. D. (2013). Robust model for segmenting images with/without intensity inhomogeneities. *IEEE transactions on image processing*, 22(8), 3296-3309.
- Li, C., Xu, C., Gui, C., and Fox, M. D. (2005, June). Level set evolution without re-initialization: a new variational formulation. In 2005 IEEE computer society conference on computer vision and pattern recognition (CVPR'05; Vol. 1, pp. 430-436). IEEE.
- Li, C., Xu, C., Gui, C., and Fox, M. D. (2010). Distance regularized level set evolution and its application to image segmentation. *IEEE transactions on image processing*, 19(12), 3243-3254.
- Li, C., Xu, C., Gui, C., & Fox, M. D. (2010). Level set evolution without re-initialization: A new variational formulation. In 2010 IEEE Conference on Computer Vision and Pattern Recognition (CVPR; pp. 430-436). IEEE. <https://doi.org/10.1109/CVPR.2010.5540032>
- Li, Q., Deng, T., and Xie, W. (2016). Active contours driven by divergence of gradient vector flow. *Signal Processing*, 120, 185-199.
- Li, Q., Shen, L., Zhang, Y., Huang, S., Chen, H., & Wang, Y. (2020). ET-Net: A generic edge-aided tracker with transformers. In European Conference on Computer Vision (pp. 215-231). Springer, Cham.
- Li, X., Jiang, D., Shi, Y., and Li, W. (2015). Segmentation of MR image using local and global region based geodesic model. *Biomedical engineering online*, 14(1), 1-16.
- Li, Y., Jiao, L., Shang, R., and Stolkin, R. (2015). Dynamic-context cooperative quantum-behaved pstudy swarm optimization based on multilevel thresholding applied to medical image segmentation. *Information Sciences*, 294, 408-422.
- Li, Y., Zhao, Y. Q., Zhang, F., Liao, M., Yu, L. L., Chen, B. F., & Wang, Y. J. (2020). Liver segmentation from abdominal CT volumes based on level set and sparse shape composition. *Computer methods and programs in biomedicine*, 195, 105533.
- Liao, F., Liang, M., Li, Z., Hu, X., & Song, S. (2021). Evaluate the efficiency of segmentation networks: balloons can burst. *IEEE Transactions on Medical Imaging*, 40(4), 1057-1069.
- Lie, J., Lysaker, M., and Tai, X. C. (2006). A variant of the level set method and applications to image segmentation. *Mathematics of computation*, 75(255), 1155-1174.
- Litjens, G., Kooi, T., Bejnordi, B. E., Setio, A. A. A., Ciompi, F., Ghahfarooian, M., ... & Sánchez, C. I. (2017). A survey on deep learning in medical image analysis. *Medical image analysis*, 42, 60-88.

- Liu S., S. De Mello, J. Gu, G. Zhong, M.-H. Yang, and J. Kautz. Learning affinity via spatial propagation networks. In NIPS, pages 1520–1530. 2017.
- Liu, B., and He, X. (2015). Multiclass semantic video segmentation with object-level active inference. In *Proceedings of the IEEE conference on computer vision and pattern recognition* (pp. 4286-4294).
- Liu, C., Liu, W., and Xing, W. (2017). An improved edge-based level set method combining local regional fitting information for noisy image segmentation. *Signal Processing, 130*, 12-21.
- Liu, C., Xiao, Y., and Yang, J. (2017). A coastline detection method in polarimetric SAR images mixing the region-based and edge-based active contour models. *IEEE Transactions on Geoscience and Remote Sensing, 55(7)*, 3735-3747.
- Liu, L., Zhang, Q., Wu, M., Li, W., and Shang, F. (2013). Adaptive segmentation of magnetic resonance images with intensity inhomogeneity using level set method. *Magnetic resonance imaging, 31(4)*, 567-574.
- Liu, M., Kitsch, A., Miller, S., Chau, V., Poskitt, K., Rousseau, F., ... and Studholme, C. (2016). Patch-based augmentation of expectation–maximization for brain MRI tissue segmentation at arbitrary age after premature birth. *NeuroImage, 127*, 387-408.
- Liu, S., and Peng, Y. (2012). A local region-based Chan–Vese model for image segmentation. *Pattern Recognition, 45(7)*, 2769-2779.
- Liu, Y., He, C., and Wu, Y. (2018). Variational model with kernel metric-based data term for noisy image segmentation. *Digital Signal Processing, 78*, 42-55.
- Liu, Y., He, C., Wu, Y., and Ren, Z. (2018). The L0-regularized discrete variational level set method for image segmentation. *Image and Vision Computing, 75*, 32-43.
- Lombardi, O. (2016). *اوتيفورسيدي ملبسيا فمغ السلطان عبدالله*. Mathematical theory of information (Shannon). In *The Routledge Handbook of Philosophy of Information* (pp. 46-52). Routledge.
- Long J. Long, E. Shelhamer, and T. Darrell. Fully convolutional networks for semantic segmentation. In CVPR, 2015.
- Lu, Z., Qiu, Y., and Zhan, T. (2019). Neutrosophic C-means clustering with local information and noise distance-based kernel metric image segmentation. *Journal of Visual Communication and Image Representation, 58*, 269-276.
- Malladi, R., Sethian, J. A., and Vemuri, B. C. (1995). Shape modeling with front propagation: A level set approach. *IEEE transactions on pattern analysis and machine intelligence, 17(2)*, 158-175.
- Malladi, R., Sethian, J. A., and Vemuri, B. C. (1994). Shape modeling with front propagation: A level set approach.
- Marcos D. Marcos, D. Tuia, B. Kellenberger, L. Zhang, M. Bai, R. Liao, and R. Urtasun. Learning deep structured active contours end-to-end. In CVPR, 2018.
- McNitt-Gray, M. F., Armato III, S. G., Meyer, C. R., Reeves, A. P., McLennan, G., Pais, R.

- C., ... and Clarke, L. P. (2007). The Lung Image Database Consortium (LIDC) data collection process for nodule detection and annotation. *Academic radiology*, 14(12), 1464-1474.
- Mendel, J. M. (2017). Type-2 fuzzy sets. In *Uncertain rule-based fuzzy systems* (pp. 259-306). Springer, Cham.
- Menze, B. H., Maier-Hein, K., Baumgartner, C. F., Bezdek, J. C., Marrocco, C., & Eskildsen, S. F. (2023). *Handbook of Medical Image Computing and Computer Assisted Intervention*. Academic Press.
- Messay, T., Hardie, R. C., and Rogers, S. K. (2010). A new computationally efficient CAD system for pulmonary nodule detection in CT imagery. *Medical image analysis*, 14(3), 390-406.
- Messay, T., Hardie, R. C., and Tuinstra, T. R. (2015). Segmentation of pulmonary nodules in computed tomography using a regression neural network approach and its application to the lung image database consortium and image database resource initiative dataset. *Medical image analysis*, 22(1), 48-62.
- Mhiri, M., Abuelwafa, S., Desrosiers, C., and Cheriet, M. (2018). Hierarchical representation learning using spherical k-means for segmentation-free word spotting. *Pattern Recognition Letters*, 101, 52-59.
- Miao, J., Huang, T. Z., Zhou, X., Wang, Y., and Liu, J. (2018). Image segmentation based on an active contour model of partial image restoration with local cosine fitting energy. *Information Sciences*, 447, 52-71.
- Milletari, F., Navab, N., and Ahmadi, S. A. (2016, October). V-net: Fully convolutional neural networks for volumetric medical image segmentation. In *2016 Fourth International Conference on 3D Vision (3DV)*; pp. 565-571). IEEE.
- Min, H., Lu, J., Jia, W., Zhao, Y., and Luo, Y. (2018). An effective local regional model based on salient fitting for image segmentation. *Neurocomputing*, 311, 245-259.
- Min, H., Wang, X. F., Huang, D. S., and Jia, W. (2016). A novel dual minimization based level set method for image segmentation. *Neurocomputing*, 214, 910-926.
- Mondal, A., Ghosh, S., and Ghosh, A. (2016). Robust global and local fuzzy energy based active contour for image segmentation. *Applied Soft Computing*, 47, 191-215.
- Monteiro, E., Costa, C., and Oliveira, J. L. (2017). A De-identification pipeline for ultrasound medical images in DICOM format. *Journal of medical systems*, 41(5), 89.
- Mousavirad, S. J., and Ebrahimpour-Komleh, H. (2017). Multilevel image thresholding using entropy of histogram and recently developed population-based metaheuristic algorithms. *Evolutionary Intelligence*, 10(1-2), 45-75.
- Mukhopadhyay, A., De, S., & Chanda, B. (2021). A review of energy functions in medical image segmentation. *Journal of Healthcare Engineering*, 2021.
- Nasrulloh, A. V., Willcocks, C. G., Jackson, P. T., Geenen, C., Habib, M. S., Steel, D. H., and Obara, B. (2018). Multi-Scale Segmentation and Surface Fitting for Measuring 3-D

- Macular Holes. *IEEE transactions on medical imaging*, 37(2), 580-589.
- Ni, B., He, F. Z., Pan, Y. T., and Yuan, Z. Y. (2016). Using shapes correlation for active contour segmentation of uterine fibroid ultrasound images in computer-aided therapy. *Applied Mathematics-A Journal of Chinese Universities*, 31(1), 37-52.
- Nida, N., Irtaza, A., Javed, A., Yousaf, M. H., and Mahmood, M. T. (2019). Melanoma lesion detection and segmentation using deep region based convolutional neural network and fuzzy C-means clustering. *International Journal of Medical Informatics*.
- Niehaus, R., Stan Raicu, D., Furst, J., and Armato, S. (2015). Toward understanding the size dependence of shape features for predicting spiculation in lung nodules for computer-aided diagnosis. *Journal of digital imaging*, 28(6), 704-717.
- Niethammer, M., Pohl, K. M., Janoos, F., and Wells III, W. M. (2017). Active Mean Fields for Probabilistic Image Segmentation: Connections with Chan--Vese and Rudin--Osher--Fatemi Models. *SIAM journal on imaging sciences*, 10(3), 1069-1103.
- Niu, S., Chen, Q., De Sisternes, L., Ji, Z., Zhou, Z., and Rubin, D. L. (2017). Robust noise region-based active contour model via local similarity factor for image segmentation. *Pattern Recognition*, 61, 104-119.
- Oliveira, R. B., Mercedes Filho, E., Ma, Z., Papa, J. P., Pereira, A. S., and Tavares, J. M. R. (2016). Computational methods for the image segmentation of pigmented skin lesions: a review. *Computer methods and programs in biomedicine*, 131, 127-141.
- Opulencia, P., Channin, D. S., Raicu, D. S., and Furst, J. D. (2011). Mapping LIDC, RadLex™, and lung nodule image features. *Journal of digital imaging*, 24(2), 256-270.
- Osher S. and J. A. Sethian. Fronts propagating with curvaturedependent speed: Algorithms based on hamilton-jacobi formulations. *J. Comput. Phys.*, 79(1):12–49, Nov. 1988.
- Osher, S., and Rudin, L. I. (1990). Feature-oriented image enhancement using shock filters. *SIAM Journal on numerical analysis*, 27(4), 919-940.
- Pang, Z., Zhu, D., Chen, D., Li, L., and Shao, Y. (2015). A computer-aided diagnosis system for dynamic contrast-enhanced MR images based on level set segmentation and ReliefF feature selection. *Computational and mathematical methods in medicine*, 2015.
- Paragios N. and Deriche R. Geodesic active regions and level set methods for supervised texture segmentation. *International Journal of Computer Vision*, 46:223fi247, 2002.
- Paragios N. and R. Deriche. Geodesic active regions for supervised texture segmentation. In *ICCV*, volume 2, pages 926–932 vol.2, Sept 1999.
- Paragios, N., and Deriche, R. (2000, June). Coupled geodesic active regions for image segmentation: A level set approach. In *European Conference on Computer Vision* (pp. 224-240). Springer, Berlin, Heidelberg.
- Park, J. K., Han, K. S., and Yun, S. Y. (2018, February). Intensity classification background model based on the tracing scheme for deep learning based CCTV pedestrian detection. In *2018 IEEE 9th International Conference on Mechanical and Intelligent Manufacturing Technologies (ICMIMT)*; pp. 224-228). IEEE.

- Paul, N., Singh, A., Midya, A., Roy, P. P., and Dogra, D. P. (2017). Moving object detection using modified temporal differencing and local fuzzy thresholding. *The Journal of Supercomputing*, 73(3), 1120-1139.
- Pavan, A. L. M., Vacavant, A., Trindade, A. P., and de Pina, D. R. (2017). Fibroglandular tissue quantification in mammography by optimized fuzzy C-means with variable compactness. *Irbm*, 38(4), 228-233.
- Petterson, P., Doostan, A., and Nordström, J. (2018). Level Set Methods for Stochastic Discontinuity Detection in Nonlinear Problems. arXiv preprint arXiv:1810.08607.
- Pham, D. L., Xu, C., & Prince, J. L. (2000). Current methods in medical image segmentation. *Annual review of biomedical engineering*, 2(1), 315-337.
<https://doi.org/10.1146/annurev.bioeng.2.1.315>
- Pham, T. X., Siarry, P., and Oulhadj, H. (2018). Integrating fuzzy entropy clustering with an improved PSO for MRI brain image segmentation. *Applied Soft Computing*, 65, 230-242.
- Piovano, J., and Papadopoulo, T. (2008, October). Local statistic based region segmentation with automatic scale selection. In *European Conference on Computer Vision* (pp. 486-499). Springer, Berlin, Heidelberg.
- Pratondo, A., Chui, C. K., and Ong, S. H. (2016). Robust edge-stop functions for edge-based active contour models in medical image segmentation. *IEEE Signal Processing Letters*, 23(2), 222-226.
- Pratondo, A., Chui, C. K., and Ong, S. H. (2017). Integrating machine learning with region-based active contour models in medical image segmentation. *Journal of Visual Communication and Image Representation*, 43, 1-9.
- Pratt, W. K. (2007). *Digital image processing*. John Wiley & Sons. Processing, 10(2):266fi277, 2001.
- Raicu, D. S., Varutbangkul, E., Furst, J. D., and Armato III, S. G. (2010). Modelling semantics from image data: opportunities from LIDC. *International Journal of Biomedical Engineering and Technology*, 3(1-2), 83-113.
- Rajinikanth, V., Dey, N., Satapathy, S. C., and Ashour, A. S. (2018). An approach to examine magnetic resonance angiography based on Tsallis entropy and deformable snake model. *Future Generation Computer Systems*, 85, 160-172.
- Ravishankar, H., Sudhakar, P., Venkataramani, R., Thiruvankadam, S., Annangi, P., Babu, N., & Vaidya, V. (2021). Understanding and improving 3D multi-organ segmentation via probabilistic shape modeling. In *Proceedings of the IEEE/CVF International Conference on Computer Vision* (pp. 13716-13725).
- Rebouças, E. D. S., Marques, R. C., Braga, A. M., Oliveira, S. A., de Albuquerque, V. H. C., and Rebouças Filho, P. P. (2018). New level set approach based on Parzen estimation for stroke segmentation in skull CT images. *Soft Computing*, 1-22.
- Romeny, B. M. H. (Ed.). (2013). *Geometry-driven diffusion in computer vision* (Vol. 1). Springer Science and Business Media..

- Ronfard R.. Region-based strategies for active contour models. *IJCV*, 13(2):229–251, Oct 1994.
- Ronneberger, O., Fischer, P., & Brox, T. (2015, October). U-net: Convolutional networks for biomedical image segmentation. In *International Conference on Medical image computing and computer-assisted intervention* (pp. 234-241). Springer, Cham.
- Roth, H. R., Shen, C., Oda, H., Oda, M., Hayashi, Y., Misawa, K., and Mori, K. (2018). Deep learning and its application to medical image segmentation. *Medical Imaging Technology*, 36(2), 63-71.
- Rubio-Manzano, C. (2019). Similarity measure between linguistic terms by using restricted equivalence functions and its application to expert systems. In *Trends in Mathematics and Computational Intelligence* (pp. 97-102). Springer, Cham.
- Rundo, L., Militello, C., Vitabile, S., Casarino, C., Russo, G., Midiri, M., and Gilardi, M. C. (2016). Combining split-and-merge and multi-seed region growing algorithms for uterine fibroid segmentation in MRgFUS treatments. *Medical and biological engineering and computing*, 54(7), 1071-1084.
- Rupprecht C., E. Huaroc, M. Baust, and N. Navab. Deep active contours. arXiv preprint arXiv:1607.05074, 2016.
- Saba, T., Rehman, A., Mehmood, Z., Kolivand, H., and Sharif, M. (2018). Image enhancement and segmentation techniques for detection of knee joint diseases: A survey. *Current Medical Imaging Reviews*, 14(5), 704-715.
- Sahare, P., and Dhok, S. B. (2018). Multilingual character segmentation and recognition schemes for Indian document images. *IEEE Access*, 6, 10603-10617.
- Sapiro, G., Kimmel, R., and Caselles, V. (1995). Geodesic active contours. In *Proc. of ICCV* (pp. 694-699).
- Schildkraut, J. S., Chen, S., Heath, M., O'Dell, W. G., Okunieff, P., Schell, M. C., and Paul, N. (2009, March). Level-set segmentation of pulmonary nodules in radiographs using a CT prior. In *Medical Imaging 2009: Image Processing* (Vol. 7259, pp. 1103-1116). SPIE.
- Sethian, J. A., and Smereka, P. (2003). Level set methods for fluid interfaces. *Annual review of fluid mechanics*, 35(1), 341-372.
- Shah, S. A., and Chauhan, N. C. (2015). An automated approach for segmentation of brain mr images using gaussian mixture model based hidden markov random field with expectation maximization. *Journal of Biomedical Engineering and Medical Imaging*, 2(4), 57.
- Shen, S., Han, S. X., Aberle, D. R., Bui, A. A., and Hsu, W. (2019). An interpretable deep hierarchical semantic convolutional neural network for lung nodule malignancy classification. *Expert systems with applications*, 128, 84-95.
- Shi, N., and Pan, J. (2016). An improved active contours model for image segmentation by level set method. *Optik*, 127(3), 1037-1042.
- Shirly, S., and Ramesh, K. (2019). Review on 2D and 3D MRI Image Segmentation Techniques. *Current Medical Imaging Reviews*, 15(2), 150-160.

- Shyu, K. K., Pham, V. T., Tran, T. T., and Lee, P. L. (2012). Global and local fuzzy energy-based active contours for image segmentation. *Nonlinear Dynamics*, 67(2), 1559-1578.
- Simulated Brain Database website [DB/OL]. <http://brainweb.bic.mni.mcgill.ca/brainweb>, 2017[accessed 27 September 2017].
- Soomro, S., Akram, F., Kim, J. H., Soomro, T. A., and Choi, K. N. (2016). Active contours using additive local and global intensity fitting models for intensity inhomogeneous image segmentation. *Computational and mathematical methods in medicine*, 2016.
- Soomro, S., Soomro, T. A., and Choi, K. N. (2018). An active contour model based on region based fitting terms driven by p-Laplace length regularization. *IEEE Access*, 6, 58272-58283.
- Srikanth, R., & Bikshalu, K. (2022). Chaotic multi verse improved Harris hawks optimization (CMV-IHHO) facilitated multiple level set model with an ideal energy active contour for an effective medical image segmentation. *Multimedia Tools and Applications*, 81(15), 20963-20992.
- Sui, H., Xu, C., Liu, J., Sun, K., and Wen, C. (2012). A novel multi-scale level set method for SAR image segmentation based on a statistical model. *International journal of remote sensing*, 33(17), 5600-5614.
- Sumithra, R., Suhil, M., and Guru, D. S. (2015). Segmentation and classification of skin lesions for disease diagnosis. *Procedia Computer Science*, 45, 76-85.
- Sun, W., Ma, J., Yang, G., Du, B., and Zhang, L. (2017). A Poisson nonnegative matrix factorization method with parameter subspace clustering constraint for endmember extraction in hyperspectral imagery. *ISPRS Journal of Photogrammetry and Remote Sensing*, 128, 27-39.
- Tachibana, R., and Kido, S. (2006, March). Automatic segmentation of pulmonary nodules on CT images by use of NCI lung image database consortium. In *Medical Imaging 2006: Image Processing* (Vol. 6144, pp. 204-212). SPIE.
- Tai, X. C., Christiansen, O., Lin, P., and Skjælaaen, I. (2007). Image segmentation using some piecewise constant level set methods with MBO type of projection. *International Journal of Computer Vision*, 73(1), 61-76.
- Tan, S., Li, L., Choi, W., Kang, M. K., D D'Souza, W., and Lu, W. (2017). Adaptive region-growing with maximum curvature strategy for tumor segmentation in 18F-FDG PET. *Physics in Medicine and Biology*, 62(13), 5383.
- Tan, Y., Schwartz, L. H., and Zhao, B. (2013). Segmentation of lung lesions on CT scans using watershed, active contours, and Markov random field. *Medical physics*, 40(4), 043502.
- Tang M., S. Valipour, Z. V. Zhang, D. Cobzas, and M. Jägersand. A deep level set method for image segmentation. *CoRR*, abs/1705.06260, 2017.
- Tang, W., Wang, Y., and He, W. (2016). An image segmentation algorithm based on improved multiscale random field model in wavelet domain. *Journal of Ambient Intelligence and Humanized Computing*, 7(2), 221-228.

- Terbish, D., Adiya, E., and Kang, M. (2017). A Multiphase Level Set Framework For Image Segmentation Using Global And Local Image Fitting Energy. *Journal of The Korean Society For Industrial And Applied Mathematics*, 21(2), 63-73.
- Tey, W. K., Kuang, Y. C., Ooi, M. P. L., and Khoo, J. J. (2018). Automated quantification of renal interstitial fibrosis for computer-aided diagnosis: A comprehensive tissue structure segmentation method. *Computer methods and programs in biomedicine*, 155, 109-120.
- Thilagamani, S., and Kavya, N. (2018). A Review: Analysis Of The Methodology Of Algorithm And Techniques In Image Segmentation. *International Journal of Advanced Research in Computer Science*, 9(2).
- Tsai, A., Yezzi, A., Wells, W., Tempany, C., Tucker, D., Fan, A., ... and Willsky, A. (2003). A shape-based approach to the segmentation of medical imagery using level sets. *IEEE transactions on medical imaging*, 22(2), 137-154.
- Tuan, T. M. (2016). A cooperative semi-supervised fuzzy clustering framework for dental X-ray image segmentation. *Expert Systems with Applications*, 46, 380-393.
- Van Ginneken, B. (2006). Supervised probabilistic segmentation of pulmonary nodules in CT scans. In *International Conference on Medical Image Computing and Computer-Assisted Intervention* (pp. 912-919). Springer, Berlin, Heidelberg.
- VanOproek, A., Achterberg, H. C., Vernooij, M. W., and De Bruijne, M. (2019). Transfer Learning for Image Segmentation by Combining Image Weighting and Kernel Learning. *IEEE transactions on medical imaging*, 38(1), 213-224.
- Verma, O. P., and Parihar, A. S. (2017). An optimal fuzzy system for edge detection in color images using bacterial foraging algorithm. *IEEE Transactions on Fuzzy Systems*, 25(1), 114-127.
- Vese L. A. and Chan T. F. (2002). A multiphase level set framework for image segmentation using the Mumford and Shah model. *International Journal of Computer Vision*, 50(3):271-293, 2002.
- Vese, L. A., and Chan, T. F. (2002). A multiphase level set framework for image segmentation using the Mumford and Shah model. *International journal of computer vision*, 50(3), 271-293.
- Vovk, U., Pernus, F., and Likar, B. (2007). A review of methods for correction of intensity inhomogeneity in MRI. *IEEE transactions on medical imaging*, 26(3), 405-421.
- Vovk, U., Pernuš, F., & Likar, B. (2007). A review of methods for correction of intensity inhomogeneity in MRI. *IEEE Transactions on Medical Imaging*, 26(3), 405-421. <https://doi.org/10.1109/TMI.2006.891486>
- Wang L., Li C., Sun Q., Xia D., and Kao C. Active contours driven by local and global intensity fitting energy with application to brain MR image segmentation. *Computerized Medical Imaging and Graphics*, 33:520-531, 2009.
- Wang, D., Li, H., Wei, X., and Wang, X. P. (2017). An efficient iterative thresholding method for image segmentation. *Journal of Computational Physics*, 350, 657-667.

- Wang, H., and Huang, T. Z. (2014). An adaptive weighting parameter estimation between local and global intensity fitting energy for image segmentation. *Communications in Nonlinear Science and Numerical Simulation*, 19(9), 3098-3105.
- Wang, H., Huang, T. Z., Xu, Z., and Wang, Y. (2014). An active contour model and its algorithms with local and global Gaussian distribution fitting energies. *Information Sciences*, 263, 43-59.
- Wang, J., Kong, J., Luo, B., & Qi, M. (2015). Bias field estimation based on pulse-coupled neural networks. *IEEE Transactions on Biomedical Engineering*, 62(3), 855-865. <https://doi.org/10.1109/TBME.2014.2368362>
- Wang, L., Chang, Y., Wang, H., Wu, Z., Pu, J., and Yang, X. (2017). An active contour model based on local fitted images for image segmentation. *Information sciences*, 418, 61-73.
- Wang, L., Chen, G., Shi, D., Chang, Y., Chan, S., Pu, J., and Yang, X. (2018). Active contours driven by edge entropy fitting energy for image segmentation. *Signal Processing*, 149, 27-35.
- Wang, L., He, L., Mishra, A., and Li, C. (2009). Active contours driven by local Gaussian distribution fitting energy. *Signal Processing*, 89(12), 2435-2447.
- Wang, L., Li, C., Sun, Q., Xia, D., and Kao, C. Y. (2009). Active contours driven by local and global intensity fitting energy with application to brain MR image segmentation. *Computerized medical imaging and graphics*, 33(7), 520-531.
- Wang, L., Zhu, J., Sheng, M., Cribb, A., Zhu, S., and Pu, J. (2018). Simultaneous segmentation and bias field estimation using local fitted images. *Pattern recognition*, 74, 145-155.
- Wang, Q., Song, E., Jin, R., Han, P., Wang, X., Zhou, Y., and Zeng, J. (2009). Segmentation of lung nodules in computed tomography images using dynamic programming and multidirection fusion techniques I. *Academic Radiology*, 16(6), 678-688.
- Wang, R., Lei, T., Cui, R., Zhang, B., Meng, H., & Nandi, A. K. (2022). Medical image segmentation using deep learning: A survey. *IET Image Processing*, 16(5), 1243-1267.
- Wang, S., Zhou, M., Liu, Z., Liu, Z., Gu, D., Zang, Y., ... and Tian, J. (2017). Central focused convolutional neural networks: Developing a data-driven model for lung nodule segmentation. *Medical image analysis*, 40, 172-183.
- Wang, X. F., Huang, D. S., and Xu, H. (2010). An efficient local Chan–Vese model for image segmentation. *Pattern Recognition*, 43(3), 603-618.
- Wang, X. F., Min, H., and Zhang, Y. G. (2015). Multi-scale local region based level set method for image segmentation in the presence of intensity inhomogeneity. *Neurocomputing*, 151, 1086-1098.
- Wang, X. F., Min, H., Zou, L., and Zhang, Y. G. (2015). A novel level set method for image segmentation by incorporating local statistical analysis and global similarity measurement. *Pattern Recognition*, 48(1), 189-204.
- Wang, X., Kong, B., Shen, Z., Xia, Y., & Wang, Z. J. (2022). Dual Attention Guided

- Network for Automatic Lung Nodule Segmentation. *Journal of healthcare engineering*, 2022.
- Wang, Z. Z. (2016). Segmentation of the left ventricle in short-axis sequences by combining deformation flow and optical flow. *IET Image Processing*, 11(4), 237-244.
- Weickert, J., Romeny, B. T. H., and Viergever, M. A. (1998). Efficient and reliable schemes for nonlinear diffusion filtering. *IEEE transactions on image processing*, 7(3), 398-410.
- Wen, W. (2014). Adaptive active contours based on local and global intensity information for image segmentation. *Optik*, 125(23), 6995-7001.
- Wiemker, R., Bergtholdt, M., Dharaiya, E., Kabus, S., and Lee, M. C. (2009, February). Agreement of CAD features with expert observer ratings for characterization of pulmonary nodules in CT using the LIDC-IDRI database. In *Medical Imaging 2009: Computer-Aided Diagnosis* (Vol. 7260, pp. 150-161). SPIE.
- Wiemker, R., Bülow, T., Blaffert, T., and Dharaiya, E. (2009b, March). Correlation of emphysema score with perceived malignancy of pulmonary nodules: a multi-observer study using the LIDC-IDRI CT lung database. In *Medical Imaging 2009: Image Perception, Observer Performance, and Technology Assessment* (Vol. 7263, pp. 335-344). SPIE.
- Wu, H., & He, W. (2015). A level set method based on region-based pressure force function for artery wall segmentation in IVUS images. *Ultrasound in medicine & biology*, 41(6), 1649-1662.
- Wu, Y., and He, C. (2015). A convex variational level set model for image segmentation. *Signal Processing*, 106, 123-133.
- Wu, Y., and He, C. (2016). Indirectly regularized variational level set model for image segmentation. *Neurocomputing*, 171, 194-208.
- Wu, Y., Ma, W., Gong, M., Li, H., and Jiao, L. (2015). Novel fuzzy active contour model with kernel metric for image segmentation. *Applied Soft Computing*, 34, 301-311.
- Xie, X., Wang, C., Zhang, A., and Meng, X. (2014). A robust level set method based on local statistical information for noisy image segmentation. *Optik*, 125(9), 2199-2204.
- Xu, Y., Géraud, T., and Najman, L. (2016). Hierarchical image simplification and segmentation based on Mumford–Shah-salient level line selection. *Pattern Recognition Letters*, 83, 278-286.
- Xu, Z., Huang, T. Z., Wang, H., and Wang, C. (2015). Variant of the region-scalable fitting energy for image segmentation. *JOSA A*, 32(3), 463-470.
- Yan, M., and Wang, Z. (2016, October). A novel natural image segmentation algorithm based on Markov random field and improved fuzzy c-means clustering method. In 2016 International Conference on Communication and Electronics Systems (ICCES; pp. 1-5). IEEE.
- Yang, X., Gao, X., Tao, D., Li, X., and Li, J. (2014). An efficient MRF embedded level set method for image segmentation. *IEEE transactions on image processing*, 24(1), 9-21.

- Yang, X., Jani, A. B., Rossi, P. J., Mao, H., Curran, W. J., and Liu, T. (2016, March). A MRI-CT prostate registration using sparse representation technique. In *Medical Imaging 2016: Image-Guided Procedures, Robotic Interventions, and Modeling* (Vol. 9786, p. 978627). International Society for Optics and Photonics.
- Yin, Y., Luo, H., Sa, J., & Zhang, Q. (2020). Study and application of improved level set method with prior graph cut in PCB image segmentation. *Circuit World*, 46(1), 55-64.
- Yu, H., He, F., and Pan, Y. (2018). A novel region-based active contour model via local patch similarity measure for image segmentation. *Multimedia Tools and Applications*, 77(18), 24097-24119.
- Yu, H., He, F., & Pan, Y. (2020). A scalable region-based level set method using adaptive bilateral filter for noisy image segmentation. *Multimedia Tools and Applications*, 79, 5743-5765.
- Zanetti, M., and Bruzzone, L. (2017). Piecewise Linear Approximation of Vector-Valued Images and Curves via Second-Order Variational Model. *IEEE Transactions on Image Processing*, 26(9), 4414-4429.
- Zhan, T., Zhang, J., Xiao, L., Chen, Y., and Wei, Z. (2013). An improved variational level set method for MR image segmentation and bias field correction. *Magnetic Resonance Imaging*, 31(3), 439-447.
- Zhang Z., S. Fidler, and R. Urtasun. Instance-level segmentation for autonomous driving with deep densely connected mrfs. In *CVPR*, 2016
- Zhang, F., Liu, H., Cao, C., Cai, Q., & Zhang, D. (2022). RVLISM: Robust variational level set method for image segmentation with intensity inhomogeneity and high noise. *Information sciences*, 596, 439-459.
- Zhang, G., Xiao, N., and Guo, W. (2014, August). Spiculation quantification method based on edge gradient orientation histogram. In *2014 International Conference on Virtual Reality and Visualization* (pp. 86-91). IEEE.
- Zhang, K., Liu, Q., Song, H., and Li, X. (2014). A variational approach to simultaneous image segmentation and bias correction. *IEEE Transactions on Cybernetics*, 45(8), 1426-1437.
- Zhang, K., Song, H., and Zhang, L. (2010). Active contours driven by local image fitting energy. *Pattern recognition*, 43(4), 1199-1206.
- Zhang, K., Zhang, L., Lam, K. M., and Zhang, D. (2015). A level set approach to image segmentation with intensity inhomogeneity. *IEEE transactions on cybernetics*, 46(2), 546-557.
- Zhang, K., Zhang, L., Song, H., and Zhang, D. (2012). Reinitialization-free level set evolution via reaction diffusion. *IEEE Transactions on Image Processing*, 22(1), 258-271.
- Zhang, K., Zhang, L., Song, H., and Zhou, W. (2010). Active contours with selective local or global segmentation: a new formulation and level set method. *Image and Vision computing*, 28(4), 668-676.

- Zhang, R., Zhu, S., and Zhou, Q. (2016). A novel gradient vector flow snake model based on convex function for infrared image segmentation. *Sensors*, 16(10), 1756.
- Zhang, X., Li, X., and Feng, Y. (2015). A medical image segmentation algorithm based on bi-directional region growing. *Optik*, 126(20), 2398-2404.
- Zhang, X., Liu, X., and Lin, W. (2016). Computing Optimization Technique in Enhancing Magnetic Resonance Imaging and Brain Segmentation of Hypophysis Cerebri Based on Morphological Based Image Processing. *Journal of Medical Imaging and Health Informatics*, 6(4), 1063-1070.
- Zhao, L., Zheng, S., Yang, W., Wei, H., and Huang, X. (2019). An image thresholding approach based on Gaussian mixture model. *Pattern Analysis and Applications*, 1-14.
- Zheng, X., Tian, Q., Dou, Q., Lei, B., Cheng, J. Z., Pu, J., & Xing, L. (2021). Capturing complex structural patterns in medical images via a principle of entropy transfer and energy minimization. *Medical Image Analysis*, 72, 102106.
- Zhou, D., Zhou, H., and Shao, Y. (2016). An improved Chan–Vese model by regional fitting for infrared image segmentation. *Infrared Physics and Technology*, 74, 81-88.
- Zhou, S., Wang, J., Zhang, S., Liang, Y., and Gong, Y. (2016). Active contour model based on local and global intensity information for medical image segmentation. *Neurocomputing*, 186, 107-118.
- Zhou, Z., Zhao, G., Kijowski, R., Liu, F., & Wang, L. (2021). Universal lesion detection by mimicking experts with deep hybrid supervision and attention. *Medical image analysis*, 71, 102062.
- Zhu, S. C., and Yuille, A. (1996). Region competition: Unifying snakes, region growing, and Bayes/MDL for multiband image segmentation. *IEEE Transactions on Pattern Analysis and Machine Intelligence*, (9), 884-900.
- Zhu, S., and Gao, R. (2016). A novel generalized gradient vector flow snake model using minimal surface and component-normalized method for medical image segmentation. *Biomedical Signal Processing and Control*, 26, 1-10.
- Zhu, W., Lou, Q., Vang, Y. S., & Xie, X. (2020). Deep multi-instance networks with sparse label assignment for whole mammogram classification. *Medical image analysis*, 60, 101619.
- Zhuang, X., & Shen, J. (2020). Multi-scale patch and multi-modality atlases for whole heart segmentation of MRI. *IEEE Transactions on Image Processing*, 29, 7304-7319.
- Zinovev, D., Feigenbaum, J., Furst, J., and Raicu, D. (2011, August). Probabilistic lung nodule classification with belief decision trees. In *2011 Annual International Conference of the IEEE Engineering in Medicine and Biology Society* (pp. 4493-4498). IEEE.
- Zinovev, D., Raicu, D., Furst, J., and Armato III, S. G. (2009). Predicting radiological panel opinions using a panel of machine learning classifiers. *Algorithms*, 2(4), 1473-1502.



اونيورسيتي مليسيا قهغ السلطان عبدالله
UNIVERSITI MALAYSIA PAHANG
AL-SULTAN ABDULLAH

Appendix A:

TESTING RESULTS

In Figure A.1, The thesis shows the center slice through the image volume of each of the 112 lung nodules in the testing dataset. The red curve in this figure represents the contour given by the slice through the ground-truth segmentation surface, whereas the blue curve in this figure represents the contour given by the slice through the approximate segmentation surface given by the zero level set in the proposed method utilizing. As can be seen in Figure A.1, the proposed method performs well in a variety of contexts. This includes many juxta-pleural nodules (for example, 46; or, 30); nodules with cavities (for example, 11 or 76); non-solid nodules (for example, 42); and irregularly-shaped nodules (for example, 91). These visual findings, together with the quantitative results that were mentioned earlier, show that the proposed approach is successful when applied to the issue of lung nodule image segmentation in CT image volumes. The tumor contours obtained from 112 test cases were compared to the physician-delineated ground truth tumor contours. The results were qualitatively analyzed by radiologists to professionally assess the test tumor contours and generate a radiology report from Dr. Ren Huipeng of Baoji Center Hospital in China. The report comprises 28 sections, with 4 images per section illustrating the test contour outcomes. Due to patient privacy concerns with the test dataset, no personal health information was disclosed. All patient identifiers were replaced with asterisks to anonymize the data. The radiologists' qualitative analysis provided expert evaluation on the accuracy and clinical acceptability of the tested tumor contouring methodology. This medical report serves as critical feedback to further refine the contouring algorithm for clinical deployment.

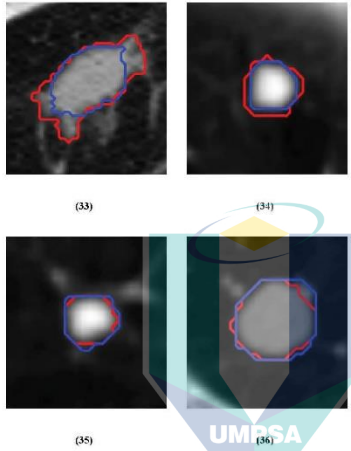


宝鸡市中心医院

影像科 X线 检查报告单

姓名: **** 申请科室: 影像科 病人编号: ****
 性别: **** ID号: **** 住院号: **** 检查号: 0009
 年龄: **** 测试时间: 2023/10/20 10:41:31 检查设备: ****
 检查项目: 胸部 CT 平扫

影像所见



医生诊断描述 (33) (34) (35) (36)

检查分割轮廓的连通性。分割结果是描记更连贯，不存在孤立小区域，避免算法产生的假阳性结果。分割结果对肿瘤的形状保真度比较高。准确描绘了肿瘤的形态，不存在离群轮廓或错误。
 The contour connectivity was checked. The segmented contour was more contiguous than the manual tracing. There were no isolated small regions that could cause false positive computational artifacts. The segmentation demonstrated high shape fidelity to the tumor. It accurately depicted the tumor morphology without outlier contours or errors.

此报告仅供临床参考，不作任何证明，联系电话: +86-0917-3397342

医生签名:

任慧娟

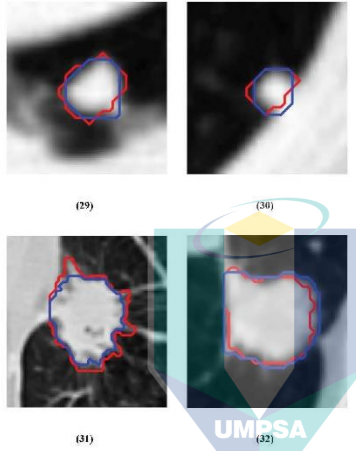


宝鸡市中心医院

影像科 X线 检查报告单

姓名: **** 申请科室: 影像科 病人编号: ****
 性别: **** ID号: **** 住院号: **** 检查号: 0008
 年龄: **** 测试时间: 2023/10/20 10:41:31 检查设备: ****
 检查项目: 胸部 CT 平扫

影像所见



医生诊断描述 (29) (30) (31) (32)

观察肿瘤内部区域。分割结果的描记表达的灰阶信息丰富合理,不存在不自然的块状分段。能够表达肿瘤主体轮廓、变细区等显著特征。对比边界处的锯齿形状。分割结果边界更平滑,锯齿形状表示的局部信息提取比较充足。
 The intra-tumoral region was examined. The grayscale rendition in the segmented region was rich and realistic, without unnatural blocky segments. It expressed salient features like the core tumor contour and tapered transition zones. The serrated edges along the boundary were compared. The segmentation boundary was smoother, indicating adequate local feature extraction.

此报告仅供临床参考,不作任何证明,联系电话: +86-0917-3397342

医生签名:

任慧娟

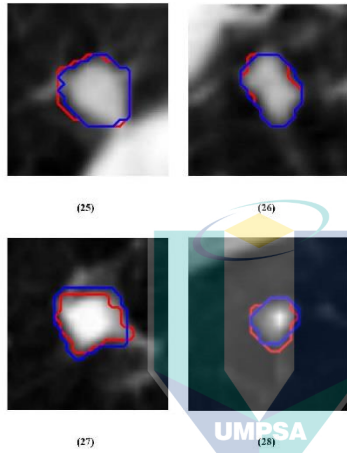


宝鸡市中心医院

影像科 X线 检查报告单

姓名: **** 申请科室: 影像科 病人编号: ****
 性别: **** ID号: **** 住院号: **** 检查号: 0007
 年龄: **** 测试时间: 2023/10/20 10:41:31 检查设备: ****
 检查项目: 胸部 CT 平扫

影像所见



医生诊断描述 (25) (26) (27) (28)

分割轮廓的光滑性比较好。分割结果的轮廓平滑,描记的轮廓边界连贯自然,轮廓局部的突出。分割结果不存在不自然的尖峰或突出,描记比较平滑。这可能是算法过拟合造成。分割轮廓平滑,没有明显的锯齿。
 The segmentation contour was smooth. The delineated outline was continuous with natural transitions. The contour showed localized protrusions. The segmentation had no unnatural spikes or protrusions compared to the physician tracing. This may be due to algorithm overfitting. The segmented contour should be assessed for smoothness and absence of abrupt discontinuities.

此报告仅供临床参考,不作任何证明,联系电话: +86-0917-3397342

医生签名:

任慧娟

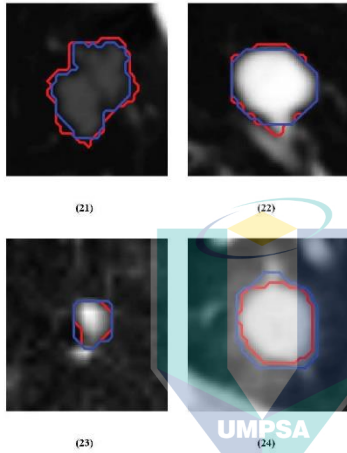


宝鸡市中心医院

影像科 X线 检查报告单

姓名: **** 申请科室: 影像科 病人编号: ****
 性别: **** ID号: **** 住院号: **** 检查号: 0006
 年龄: **** 测试时间: 2023/10/20 10:41:31 检查设备: ****
 检查项目: 胸部 CT 平扫

影像所见



医生诊断描述 (21) (22) (23) (24)

分割轮廓没有超出了肿瘤实际边界。分割结果没有包含正常组织和扩展到肿瘤周围。这反映了分割的特异性比较好。保留了足够的肿瘤边界。检查分割结果没有漏掉了肿瘤区域的一部分不存在欠分割问题。
 The segmentation contour did not exceed the true tumor boundaries. It did not incorporate normal tissues or extend beyond the tumor periphery. This demonstrates good specificity of the segmentation. Adequate tumor margins were retained. Inspection confirmed no partial volume loss or under-segmentation of any tumor areas.

UNIVERSITI MALAYSIA PAHANG
AL-SULTAN ABDULLAH

此报告仅供临床参考，不作任何证明，联系电话: +86-0917-3397342

医生签名:

任慧娟

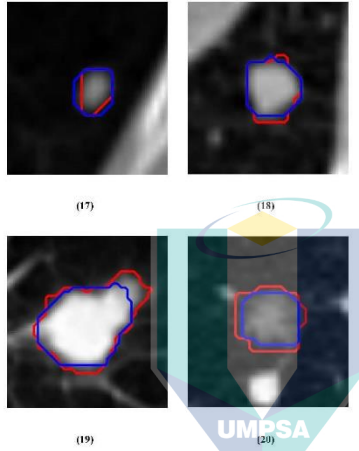


宝鸡市中心医院

影像科 X线 检查报告单

姓名: **** 申请科室: 影像科 病人编号: ****
 性别: **** ID号: **** 住院号: **** 检查号: 0005
 年龄: **** 测试时间: 2023/10/20 10:41:31 检查设备: ****
 检查项目: 胸部 CT 平扫

影像所见



医生诊断描述 (17) (18) (19) (20)

分割结果包含了完整的肿瘤区域。分割轮廓比医生推记的轮廓更小, 无明显的缺失区域。这反映了分割的敏感度比较高。局部区域的差异不存在系统性的定位偏差。
 The segmentation encompassed the entire tumor volume. The segmented contour was smaller than the physician-drawn delineation, with no overt regions of exclusion. This indicates high sensitivity of the segmentation. Local differences showed no systematic spatial biases.

UNIVERSITI MALAYSIA PAHANG
AL-SULTAN ABDULLAH

此报告仅供临床参考, 不作任何证明, 联系电话: +86-0917-3397342

医生签名:

任慧娟

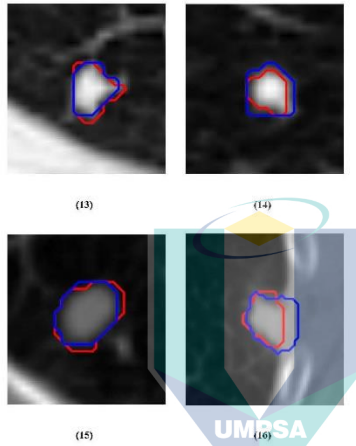


宝鸡市中心医院

影像科 X线 检查报告单

姓名: **** 申请科室: 影像科 病人编号: ****
 性别: **** ID号: **** 住院号: **** 检查号: 0004
 年龄: **** 测试时间: 2023/10/20 10:41:31 检查设备: ****
 检查项目: 胸部 CT 平扫

影像所见



医生诊断描述 (13) (14) (15) (16)

分割的细节和复杂性: 分割结果没有出现不自然的尖峰或突出, 这可以表明算法没有过度拟合。同时, 分割结果能够准确地描绘肿瘤内部区域的灰度信息, 避免了不自然的分块状区域。此外, 分割结果能够准确地捕捉复杂区域, 例如细血管和支气管穿过肿瘤的区域, 同时捕捉到了肿瘤的整体形态和边缘特征。 Segmentation Details and Complexity: The segmentation results do not exhibit unnatural peaks or protrusions, which may indicate that the algorithm has not overfitted. Additionally, the segmentation results accurately depict grayscale information within the interior regions of the tumor, avoiding unnatural blocky segments. Furthermore, the segmentation results effectively capture complex regions, such as areas where small blood vessels and bronchi traverse the tumor, while accurately representing the overall morphology and edge features of the tumor.

AL-SULTAN ABDULLAH

此报告仅供临床参考, 不作任何证明, 联系电话: +86-0917-3397342

医生签名:

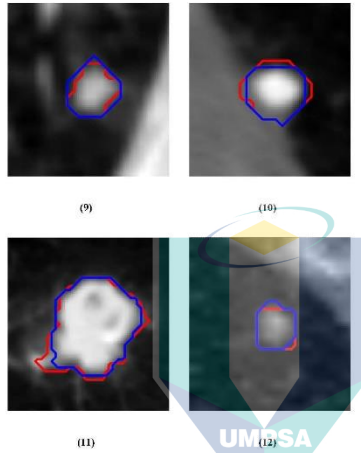


宝鸡市中心医院

影像科 X线 检查报告单

姓名: **** 申请科室: 影像科 病人编号: ****
 性别: **** ID号: **** 住院号: **** 检查号: 0003
 年龄: **** 测试时间: 2023/10/20 10:41:31 检查设备: ****
 检查项目: 胸部 CT 平扫

影像所见



医生诊断描述(9) (10) (11) (12)

分割轮廓的光滑性和连续性: 分割轮廓表现出良好的光滑性, 与自然边界一致, 没有不自然的不连续性, 确保了分割结果的外观一致性。分割轮廓的连通性好。分割结果展示更加连贯的描绘。没有孤立的小区域, 避免了自算法产生的假阳性结果。Smoothness of Segmentation Contour. The Segmentation contour demonstrates exceptional smoothness and coherence with natural boundaries as delineated. The segmentation results show more coherent delineation. There are no isolated small areas, avoiding false-positive results generated by the algorithm.

UNIVERSITI MALAYSIA PAHANG
AL-SULTAN ABDULLAH

此报告仅供临床参考, 不作任何证明, 联系电话: +86-0917-3397342

医生签名:

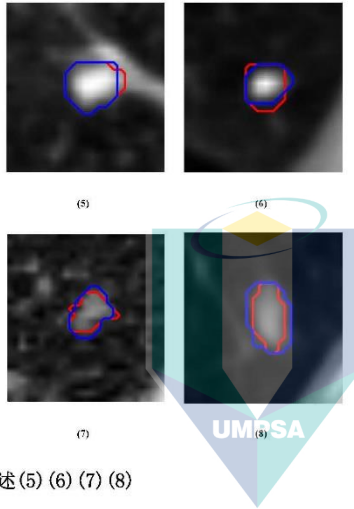


宝鸡市中心医院

影像科 X线 检查报告单

姓名: **** 申请科室: 影像科 病人编号: ****
 性别: **** ID号: **** 住院号: **** 检查号: 0002
 年龄: **** 测试时间: 2023/10/20 10:41:31 检查设备: ****
 检查项目: 胸部 CT 平扫

影像所见



医生诊断描述(5) (6) (7) (8)

分割的特异性和防欠分割: 分割轮廓没有延伸到肿瘤的实际边界之外, 也没有包括正常组织或扩展到周围的肿瘤区域。这表明分割具有较好的特异性, 能够维持足够的肿瘤边界, 避免了欠分割问题。
 Excellent Specificity and Avoidance of Under-segmentation. The segmentation contour does not extend beyond the actual tumor boundary, ensuring that normal tissue is not included or extended into the surrounding tumor. This demonstrates the segmentation's high specificity, maintaining an adequate tumor boundary and preventing under-segmentation issues.

此报告仅供临床参考, 不作任何证明, 联系电话: +86-0917-3397342

医生签名:

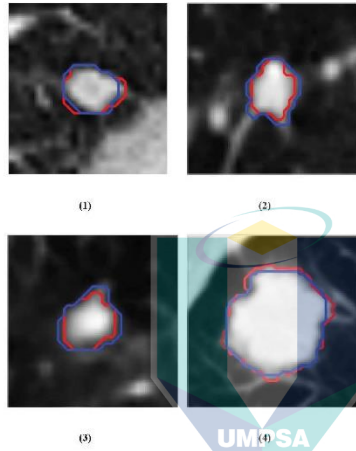


宝鸡市中心医院

影像科 X线 检查报告单

姓名: **** 申请科室: 影像科 病人编号: ****
 性别: **** ID号: **** 住院号: **** 检查号: 0001
 年龄: **** 测试时间: 2023/10/20 10:41:31 检查设备: ****
 检查项目: 胸部 CT 平扫

影像所见



医生诊断描述 (1) (2) (3) (4)

分割结果的全面性和敏感性: 分割结果包含了整个肿瘤区域, 且分割轮廓相对于医生的描绘更加精细, 没有明显的遗漏区域。这反映出分割具有较高的敏感性, 同时没有出现局部定位偏差。

High Sensitivity. The segmentation results encompass the entire tumor region, exhibiting a segmented contour smaller than the physician's delineation, with no apparent areas of omission. This indicates an elevated sensitivity of the segmentation. There are no systematic localization biases within local areas.

UNIVERSITI MALAYSIA PAHANG
AL-SULTAN ABDULLAH

此报告仅供临床参考, 不作任何证明, 联系电话: +86-0917-3397342

医生签名:

任慧娟

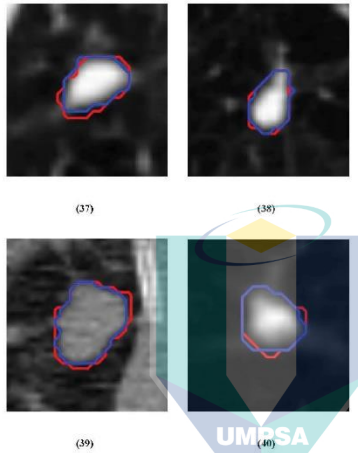


宝鸡市中心医院

影像科 X线 检查报告单

姓名: **** 申请科室: 影像科 病人编号: ****
 性别: **** ID号: **** 住院号: **** 检查号: 0010
 年龄: **** 测试时间: 2023/10/20 10:41:31 检查设备: ****
 检查项目: 胸部 CT 平扫

影像所见



医生诊断描述 (37) (38) (39) (40)

分割结果没有发生漏检或误检。没有明显的肿瘤组织未被包含,或者分割出了正常组织区域。不会造成假阳性。分割轮廓贴合肿瘤边界。轮廓准确裹贴肿瘤,没有漂移到周围正常组织。
 No false negatives or false positives occurred. No obvious tumor tissue was omitted, nor normal tissues mistakenly included, avoiding false positives. The contour tightly conformed to the tumor edge. It wrapped tightly around the tumor without drifting into adjacent normal tissues.



此报告仅供临床参考,不作任何证明,联系电话: +86-0917-3397342

医生签名:

任慧娟

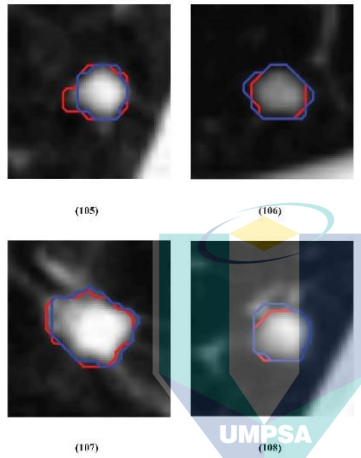


宝鸡市中心医院

影像科 X线 检查报告单

姓名: **** 申请科室: 影像科 病人编号: ****
 性别: **** ID号: **** 住院号: **** 检查号: 0027
 年龄: **** 测试时间: 2023/10/20 10:41:31 检查设备: ****
 检查项目: 胸部 CT 平扫

影像所见



医生诊断描述 (105) (106) (107) (108)

敏感度和特异性: 分割结果包含了完整的肿瘤区域, 而分割轮廓比医生描记的轮廓更小, 没有明显的缺失区域, 表明分割具有高敏感度。分割的特异性很好, 没有超出实际肿瘤边界, 没有包含正常组织或扩展到肿瘤周围, 保留了足够的肿瘤边界, 没有发生欠分割。

Sensitivity and Specificity: The segmentation results encompass the entire tumor region, with the segmented contour being smaller than the physician-drawn delineation and exhibiting no noticeable areas of omission, indicating high sensitivity of the segmentation. The specificity of the segmentation is excellent, as it does not extend beyond the actual tumor boundaries, avoids the inclusion of normal tissue, and maintains sufficient tumor margins, thus avoiding under-segmentation.

此报告仅供临床参考, 不作任何证明, 联系电话: +86-0917-3397342

医生签名:

任慧娟

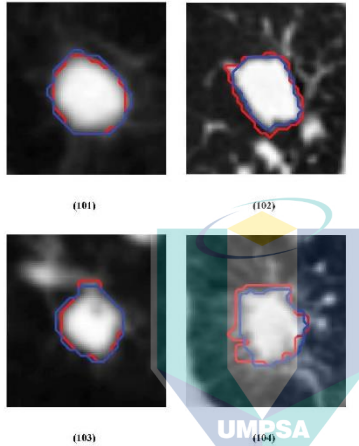


宝鸡市中心医院

影像科 X线 检查报告单

姓名: **** 申请科室: 影像科 病人编号: ****
 性别: **** ID号: **** 住院号: **** 检查号: 0026
 年龄: **** 测试时间: 2023/10/20 10:41:31 检查设备: ****
 检查项目: 胸部 CT 平扫

影像所见



医生诊断描述 (101) (102) (103) (104)

灰度信息和边界的锯齿形状: 观察肿瘤内部区域显示, 分割结果表达了丰富且合理的灰度信息, 没有出现不自然的块状分段, 能够表达肿瘤的核心轮廓和过渡区域等显著特征; 分割边界更加平滑, 避免了锯齿形状, 表明局部信息提取充足。
 Grayscale Information and Absence of Jagged Edges: Observation of the tumor's internal regions reveals that the segmentation results express rich and reasonable grayscale information, without unnatural blocky segments. It effectively conveys significant features, such as the core tumor contour and transitional areas. The segmentation boundary is smoother, eliminating jagged edges, indicating ample extraction of local information.

AL-SULTAN ABDULLAH

此报告仅供临床参考, 不作任何证明, 联系电话: +86-0917-3397342

医生签名:

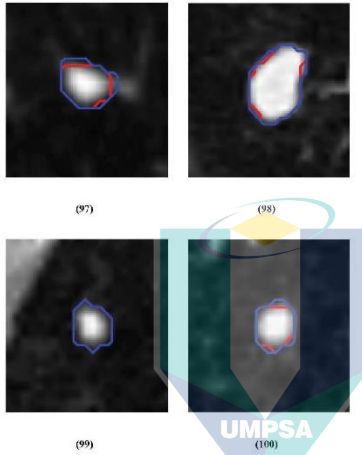


宝鸡市中心医院

影像科 X线 检查报告单

姓名: **** 申请科室: 影像科 病人编号: ****
 性别: **** ID号: **** 住院号: **** 检查号: 0025
 年龄: **** 测试时间: 2023/10/20 10:41:31 检查设备: ****
 检查项目: 胸部 CT 平扫

影像所见



医生诊断描述 (97) (98) (99) (100)

避免漏检和误检: 分割结果没有漏检或误检, 没有明显的肿瘤组织未被包含, 也没有将正常组织错误地包含, 避免了假阳性。分割轮廓紧密贴合肿瘤边界, 没有漂移到周围的正常组织
 Prevention of Missed and False Detections: The segmentation results are devoid of both missed and false detections. There is no evident omission of tumor tissue, nor is there any erroneous inclusion of normal tissue areas, thus preventing false positives. The segmentation contour adheres closely to the tumor's boundaries without drifting into the surrounding normal tissue.

AL-SULTAN ABDULLAH

此报告仅供临床参考, 不作任何证明, 联系电话: +86-0917-3397342

医生签名:

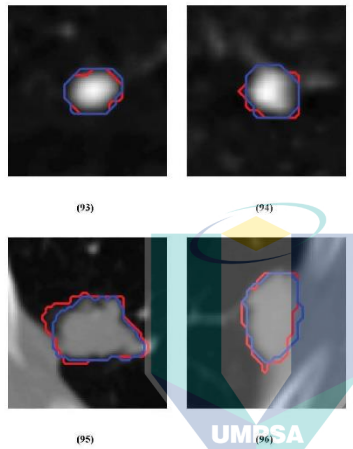


宝鸡市中心医院

影像科 X线 检查报告单

姓名: **** 申请科室: 影像科 病人编号: ****
 性别: **** ID号: **** 住院号: **** 检查号: 0024
 年龄: **** 测试时间: 2023/10/20 10:41:31 检查设备: ****
 检查项目: 胸部 CT 平扫

影像所见



医生诊断描述 (93) (94) (95) (96)

连通性和形状保真度: 检查分割轮廓的连通性显示, 分割结果比手动描绘更加连贯, 避免了孤立的小区域, 从而避免了由算法产生的假阳性结果。此外, 分割结果保持了高的形状保真度, 准确地描绘了肿瘤的形态, 避免了异常的轮廓或错误。
 Connectivity and Shape Fidelity: Examination of the segmentation contour's connectivity shows that it surpasses manual delineation in terms of continuity, thus preventing isolated small areas that could lead to false positive outcomes generated by the algorithm. Furthermore, the segmentation maintains a high level of shape fidelity, accurately representing the tumor's morphology without the presence of anomalous contours or errors.

AL-SULTAN ABDULLAH

此报告仅供临床参考, 不作任何证明, 联系电话: +86-0917-3397342

医生签名:

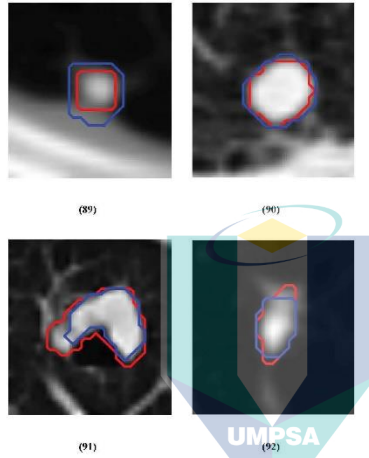


宝鸡市中心医院

影像科 X线 检查报告单

姓名: **** 申请科室: 影像科 病人编号: ****
 性别: **** ID号: **** 住院号: **** 检查号: 0023
 年龄: **** 测试时间: 2023/10/20 10:41:31 检查设备: ****
 检查项目: 胸部 CT 平扫

影像所见



医生诊断描述 (89) (90) (91) (92)

连通性和形状保真度: 检查分割轮廓的连通性, 分割结果显示出手动描绘更加连贯的轮廓, 避免了孤立的小区域, 从而避免了由算法产生的假阳性结果。此外, 分割结果保持了高的形状保真度, 准确地描绘了肿瘤的形态, 避免了异常的轮廓或错误。

Connectivity and Shape Fidelity: Upon inspecting the connectivity of the segmentation contour, it becomes evident that the segmentation results exhibit greater continuity compared to manual delineation. There are no isolated small regions that could cause false-positive computational artifacts. The segmentation maintains a high level of shape fidelity, accurately delineating the tumor's morphology without outlier contours or errors.

此报告仅供临床参考, 不作任何证明, 联系电话: +86-0917-3397342

医生签名:

任慧娟

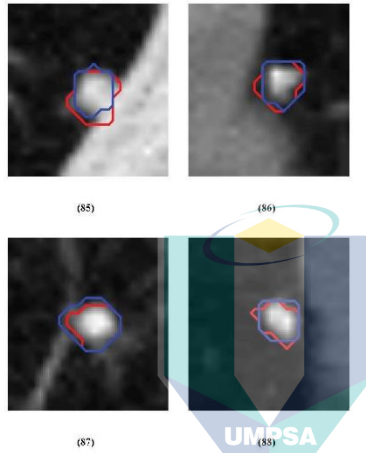


宝鸡市中心医院

影像科 X线 检查报告单

姓名: **** 申请科室: 影像科 病人编号: ****
 性别: **** ID号: **** 住院号: **** 检查号: 0022
 年龄: **** 测试时间: 2023/10/20 10:41:31 检查设备: ****
 检查项目: 胸部 CT 平扫

影像所见



医生诊断描述 (85) (86) (87) (88)

丰富的灰度信息和边界的锯齿形状: 观察肿瘤内部区域表现, 分割结果呈现出丰富而合理的灰度信息, 没有不自然的块状分段。能够表达肿瘤的主要轮廓、变细区等显著特征。对比边界处的锯齿形状, 分割结果边界更平滑, 没有锯齿形状, 这表明局部信息提取比较充足。

Rich Grayscale Information and Absence of Jagged Edges: Observation of the tumor's internal regions reveals that the segmentation results express rich and reasonable grayscale information, without unnatural blocky segments. It expressed salient features like the core tumor contour, variations, and significant features. The segmentation boundaries are smoother, devoid of jagged shapes, indicating sufficient local feature extraction.

此报告仅供临床参考, 不作任何证明, 联系电话: +86-0917-3397342

医生签名:

任慧娟

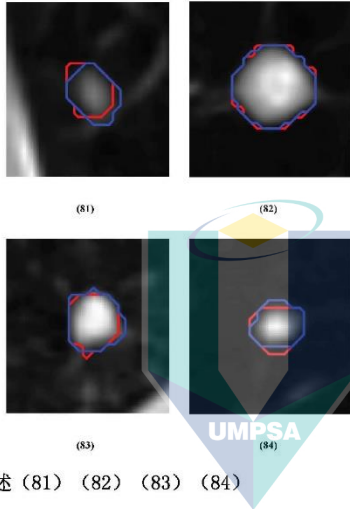


宝鸡市中心医院

影像科 X线 检查报告单

姓名: **** 申请科室: 影像科 病人编号: ****
 性别: **** ID号: **** 住院号: **** 检查号: 0021
 年龄: **** 测试时间: 2023/10/20 10:41:31 检查设备: ****
 检查项目: 胸部 CT 平扫

影像所见



医生诊断描述 (81) (82) (83) (84)

分割轮廓的光滑性和连续性: 分割轮廓呈现出平滑的特点, 与自然边界一致, 没有不连续的现象。尽管存在局部的突出, 但分割结果没有不自然的尖峰或突出, 这可能是由于算法过度拟合导致的。
 Smoothness and Continuity of Segmentation Contour: The segmentation contour was smooth. The delineated outline was continuous with natural transitions. The contour showed localized protrusions. The segmentation had no unnatural spikes or protrusions compared to the physician tracing. This may be due to algorithm overfitting.

此报告仅供临床参考, 不作任何证明, 联系电话: +86-0917-3397342

医生签名:

任慧娟

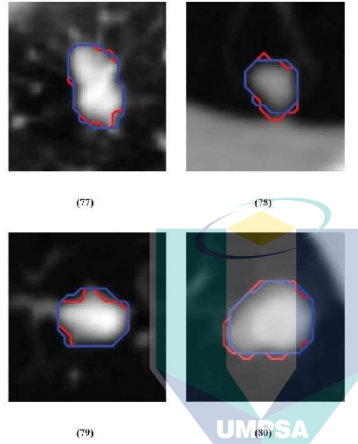


宝鸡市中心医院

影像科 X线 检查报告单

姓名: **** 申请科室: 影像科 病人编号: ****
 性别: **** ID号: **** 住院号: **** 检查号: 0020
 年龄: **** 测试时间: 2023/10/20 10:41:31 检查设备: ****
 检查项目: 胸部 CT 平扫

影像所见



医生诊断描述 (77) (78) (79) (80)

分割的特异性和防欠分割: 分割轮廓没有超出了肿瘤实际边界, 分割结果没有包含正常组织和扩展到肿瘤周围。这反映了分割的特异性比较好, 保留了足够的肿瘤边界, 没有欠分割问题。
 "Specificity and Prevention of Under-segmentation: The segmentation contour did not exceed the true tumor boundaries. It did not incorporate normal tissues or extend beyond the tumor periphery. This demonstrates good specificity of the segmentation. Adequate tumor margins were retained. Inspection confirmed no partial volume loss or under-segmentation of any tumor areas."

AL-SULTAN ABDULLAH

此报告仅供临床参考, 不作任何证明, 联系电话: +86-0917-3397342

医生签名:

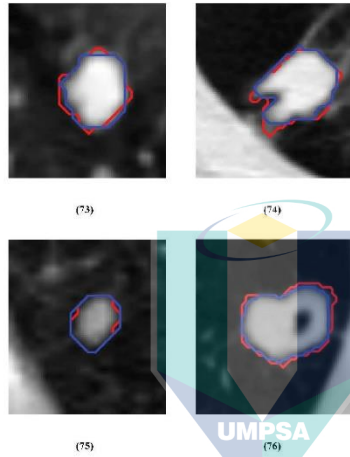


宝鸡市中心医院

影像科 X线 检查报告单

姓名: **** 申请科室: 影像科 病人编号: ****
 性别: **** ID号: **** 住院号: **** 检查号: 0019
 年龄: **** 测试时间: 2023/10/20 10:41:31 检查设备: ****
 检查项目: 胸部 CT 平扫

影像所见



医生诊断描述 (73) (74) (75) (76)

分割的全面性和敏感性: 分割结果包含了完整的肿瘤区域。分割轮廓比医生描记的轮廓更小, 无明显的缺失区域。这反映了分割的敏感度比较高。局部区域的差异不存在系统性的定位偏差。
 Comprehensiveness and Sensitivity of Segmentation: The segmentation results encompassed the entire tumor region. The segmented contour was smaller than the physician's delineation, with no apparent missing areas. This indicates a high level of sensitivity in the segmentation. There are no systematic localization biases in local areas.

此报告仅供临床参考, 不作任何证明, 联系电话: +86-0917-3397342

医生签名:

任慧娟

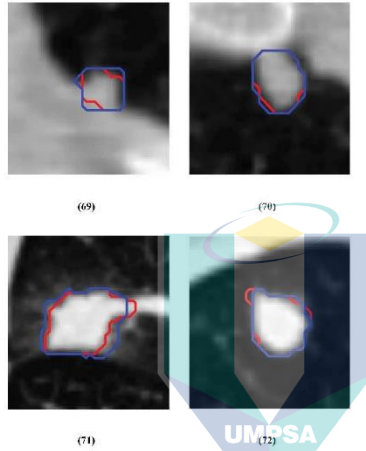


宝鸡市中心医院

影像科 X线 检查报告单

姓名: **** 申请科室: 影像科 病人编号: ****
 性别: **** ID号: **** 住院号: **** 检查号: 0018
 年龄: **** 测试时间: 2023/10/20 10:41:31 检查设备: ****
 检查项目: 胸部 CT 平扫

影像所见



医生诊断描述 (69) (70) (71) (72)

连通性和形状保真度: 检查分割轮廓的连通性, 分割结果显示出比手动描绘更加连贯的轮廓, 避免了孤立的小区域, 从而避免了由算法产生的假阳性结果。此外, 分割结果保持了高的形状保真度, 准确地描绘了肿瘤形态, 避免了异常的轮廓或错误。

Connectivity and Shape Fidelity: Upon inspecting the connectivity of the segmentation contour, it becomes evident that the segmentation results exhibit greater continuity compared to manual delineation. There are no isolated small regions, thereby avoiding false-positive outcomes generated by the algorithm. Furthermore, the segmentation maintains a high level of shape fidelity, accurately delineating the tumor's morphology, without outlier contours or errors.

此报告仅供临床参考, 不作任何证明, 联系电话: +86-0917-3397342

医生签名:

任慧娟

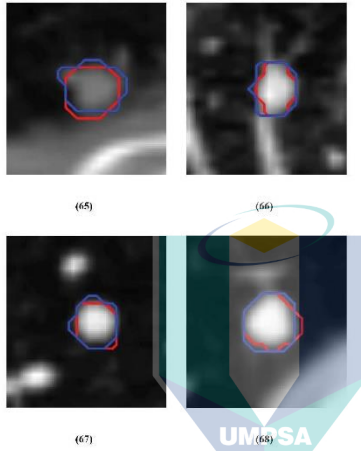


宝鸡市中心医院

影像科 X线 检查报告单

姓名: **** 申请科室: 影像科 病人编号: ****
 性别: **** ID号: **** 住院号: **** 检查号: 0017
 年龄: **** 测试时间: 2023/10/20 10:41:31 检查设备: ****
 检查项目: 胸部 CT 平扫

影像所见



医生诊断描述 (65) (66) (67) (68)

丰富的灰度信息和边界的锯齿形状: 观察肿瘤内部区域表明, 分割结果呈现出丰富而合理的灰度信息, 没有不自然的块状分段, 能够表达肿瘤的主要轮廓、变化和显著特征。分割结果的边界更加平滑, 没有锯齿形状, 这表明局部信息提取足够。
 Rich Grayscale Information and Absence of Jagged Edges: Observation of the tumor's internal regions reveals that the segmentation results express rich and reasonable grayscale information, without unnatural blocky segments. They accurately represent the primary tumor contour, variations, and significant features. The segmentation boundaries are smoother, devoid of jagged shapes, indicating sufficient local information extraction.

AL-SULTAN ABDULLAH

此报告仅供临床参考, 不作任何证明, 联系电话: +86-0917-3397342

医生签名:

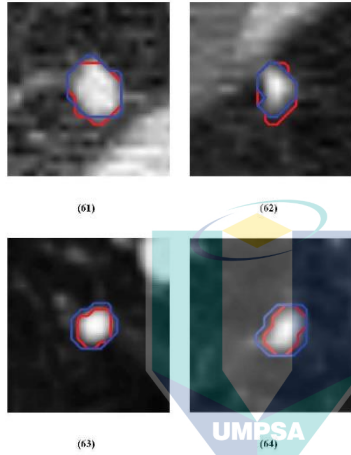


宝鸡市中心医院

影像科 X线 检查报告单

姓名: **** 申请科室: 影像科 病人编号: ****
 性别: **** ID号: **** 住院号: **** 检查号: 0016
 年龄: **** 测试时间: 2023/10/20 10:41:31 检查设备: ****
 检查项目: 胸部 CT 平扫

影像所见



医生诊断描述 (61) (62) (63) (64)

分割轮廓的光滑性和连续性: 分割轮廓呈现出平滑的特点, 与自然边界一致, 没有不连续的现象。尽管存在局部的突出, 但分割结果没有不自然的尖峰或突出, 这可能是由于算法过度拟合导致的。
 Smoothness and Continuity of Segmentation Contour: The segmentation contour exhibits a smooth and continuous appearance, aligning with natural boundaries, with no observable discontinuities. While there may be localized protrusions, the segmentation results lack unnatural peaks or protrusions, which could be indicative of algorithm overfitting.

AL-SULTAN ABDULLAH

此报告仅供临床参考, 不作任何证明, 联系电话: +86-0917-3397342

医生签名:

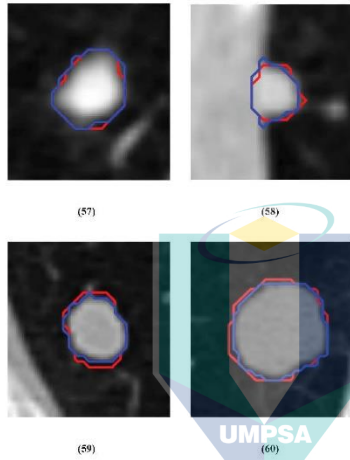


宝鸡市中心医院

影像科 X线 检查报告单

姓名: **** 申请科室: 影像科 病人编号: ****
 性别: **** ID号: **** 住院号: **** 检查号: 0015
 年龄: **** 测试时间: 2023/10/20 10:41:31 检查设备: ****
 检查项目: 胸部 CT 平扫

影像所见



医生诊断描述 (57) (58) (59) (60)

分割的特异性和防欠分割: 分割轮廓没有超出实际肿瘤边界, 没有包括正常组织或扩展到肿瘤周围, 表明分割的特异性较好。分割结果保留了足够的肿瘤边界, 没有欠分割问题。
 Specificity and Prevention of Under-segmentation: The segmentation contour does not extend beyond the actual tumor boundaries, and it does not include normal tissue or extend into the surrounding tumor. This demonstrates good specificity in the segmentation, preserving adequate tumor boundaries without under-segmentation issues.

此报告仅供临床参考, 不作任何证明, 联系电话: +86-0917-3397342

医生签名:

任慧娟

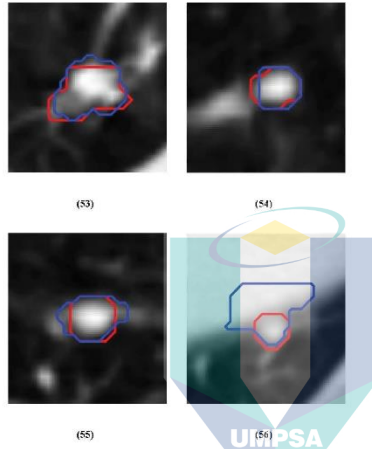


宝鸡市中心医院

影像科 X线 检查报告单

姓名: **** 申请科室: 影像科 病人编号: ****
 性别: **** ID号: **** 住院号: **** 检查号: 0014
 年龄: **** 测试时间: 2023/10/20 10:41:31 检查设备: ****
 检查项目: 胸部 CT 平扫

影像所见



医生诊断描述 (53) (54) (55) (56)

分割的全面性和敏感性: 分割结果包括整个肿瘤区域, 分割轮廓相对于医生的描绘更小, 没有明显的遗漏区域, 表明分割具有高敏感性。局部区域没有显示系统性的定位偏差。
 Comprehensiveness and Sensitivity of Segmentation: The segmentation results encompass the entire tumor region, with the segmented contour being smaller than the physician's delineation, and no apparent missing areas. This indicates a high level of sensitivity in the segmentation. There are no systematic localization biases in local areas.

UNIVERSITI MALAYSIA PAHANG
AL-SULTAN ABDULLAH

此报告仅供临床参考, 不作任何证明, 联系电话: +86-0917-3397342

医生签名:

任慧娟

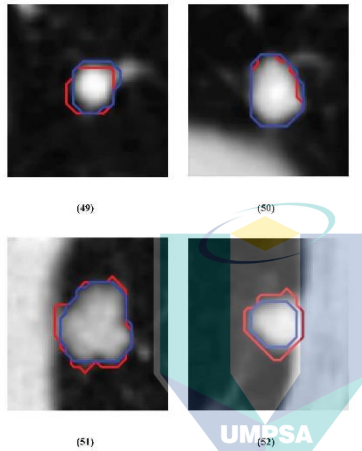


宝鸡市中心医院

影像科 X线 检查报告单

姓名: **** 申请科室: 影像科 病人编号: ****
 性别: **** ID号: **** 住院号: **** 检查号: 0013
 年龄: **** 测试时间: 2023/10/20 10:41:31 检查设备: ****
 检查项目: 胸部 CT 平扫

影像所见



医生诊断描述 (49) (50) (51) (52)

光滑性和连续性: 分割轮廓呈现出良好的光滑性, 边界保持连续自然, 尽管可能存在局部凸起, 但不存在不自然的尖峰或凸出, 这可能是由于算法过度拟合的结果。观察肿瘤内部区域表明, 分割结果有效传达了丰富而合理的灰度信息, 没有出现不自然的块状分段, 能够准确呈现显著特征, 如核心肿瘤轮廓和过渡区域。此外, 分割边界更加平滑, 避免了锯齿状边缘, 表明局部信息提取充分。Smoothness and Continuity: The segmentation contour exhibits good smoothness, with boundaries maintaining natural continuity. While there may be localized protrusions, there are no unnatural spikes or extrusions, which may be attributed to algorithm overfitting. Observations within the tumor's internal region reveal that the segmentation results effectively convey rich and reasonable grayscale information without displaying unnatural blocky segments. The segmentation accurately represents prominent features, such as the core tumor contour and transition areas. Additionally, the segmentation boundary is smoother, eliminating jagged edges, indicating sufficient local feature extraction.

此报告仅供临床参考, 不作任何证明, 联系电话: +86-0917-3397342

医生签名:

任慧娟

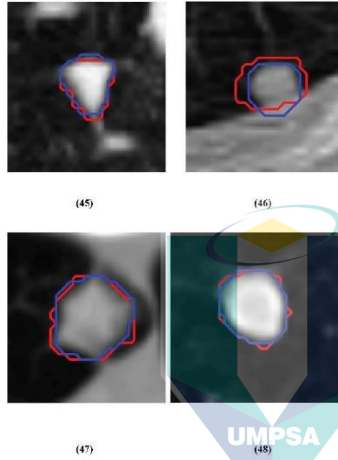


宝鸡市中心医院

影像科 X线 检查报告单

姓名: **** 申请科室: 影像科 病人编号: ****
 性别: **** ID号: **** 住院号: **** 检查号: 0012
 年龄: **** 测试时间: 2023/10/20 10:41:31 检查设备: ****
 检查项目: 胸部 CT 平扫

影像所见



医生诊断描述 (45) (46) (47) (48)

敏感度和特异性在分割评估中的体现: 分割结果显示高敏感性, 完整地包含肿瘤区域, 且分割轮廓较医师手绘的轮廓更小, 不存在明显的遗漏区域。分割具有出色的特异性, 确保分割轮廓未超出实际肿瘤边界, 避免包括正常组织或扩展至肿瘤周围, 同时保留足够的肿瘤边界, 防止欠分割。

Sensitivity and Specificity in Segmentation Evaluation: The segmentation results demonstrate high sensitivity by fully encompassing the tumor region, and the segmented contour is smaller than the physician-drawn delineation with no overt exclusion areas. The segmentation exhibits outstanding specificity, ensuring that the segmented contour does not extend beyond the actual tumor boundaries, avoiding the inclusion of normal tissues or extension into the surrounding tumor area. It also retains an adequate tumor margin to prevent under-segmentation.

此报告仅供临床参考, 不作任何证明, 联系电话: +86-0917-3397342

医生签名:

任慧娟

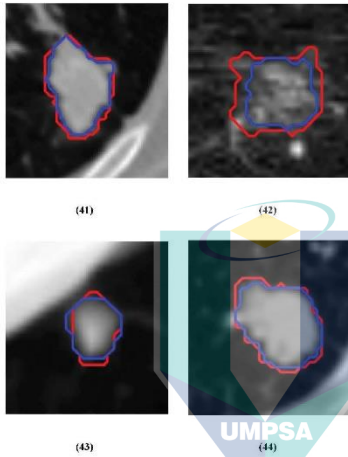


宝鸡市中心医院

影像科 X线 检查报告单

姓名: **** 申请科室: 影像科 病人编号: ****
 性别: **** ID号: **** 住院号: **** 检查号: 0011
 年龄: **** 测试时间: 2023/10/20 10:41:31 检查设备: ****
 检查项目: 胸部 CT 平扫

影像所见



医生诊断描述 (41) (42) (43) (44)

检查肿瘤边界区域,有分割结果正确捕捉了肿瘤的边缘,避免了包涵正常组织。观察细小血管和支气管穿过肿瘤的区域,这类区域轮廓变化比较复杂,分割结果能够准确描绘这些轮廓。分割轮廓捕捉到了肿瘤的整体形态,例如,正确描绘了肿瘤的边缘、表面凹凸不平的特征等。
 Tumor boundaries were examined to confirm accurate edge capture without inclusion of normal tissues. Regions with small vessels and bronchi traversing the tumor were observed. These complex contour areas were accurately delineated by the segmentation. The segmentation contour captured the overall tumor morphology. For example, the edge and surface indentations were correctly depicted.

此报告仅供临床参考,不作任何证明,联系电话: +86-0917-3397342

医生签名:

任慧娟

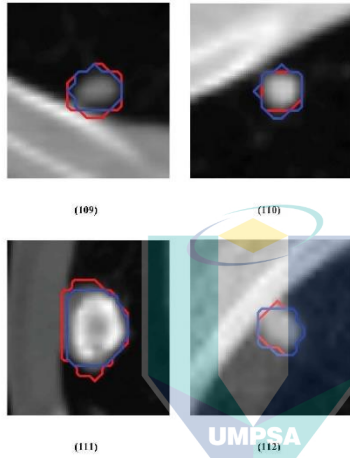


宝鸡市中心医院

影像科 X线 检查报告单

姓名: **** 申请科室: 影像科 病人编号: ****
 性别: **** ID号: **** 住院号: **** 检查号: 0028
 年龄: **** 测试时间: 2023/10/20 10:41:31 检查设备: ****
 检查项目: 胸部 CT 平扫

影像所见



医生诊断描述 (109) (110) (111) (112)

光滑性和连续性: 分割轮廓表现出良好的平滑性, 边界连续自然, 尽管存在局部的突出, 但没有不自然的尖峰或突出, 这有可能是由于算法过拟合导致的。
 Smoothness and Continuity: The segmentation contour demonstrates good smoothness, with the boundary showing natural and continuous transitions. While localized protrusions may exist, no unnatural spikes or protrusions are present, which may potentially result from algorithm over-fitting.

UNIVERSITI MALAYSIA PAHANG
AL-SULTAN ABDULLAH

此报告仅供临床参考, 不作任何证明, 联系电话: +86-0917-3397342

医生签名:

Appendix B:

NUMERICAL SCHEMES FOR THE LEVEL SET EVOLUTION EQUATION

With respect to the initial value problem,

$$\begin{cases} u_t(x, t) + H(x, Du(x, t)) = 0 & (x, t) \in R^n \times (0, \omega) \\ u(x, t) = u_0(x) & (x, t) \in R^n \times \{0\} \end{cases}$$

The following is an explicit numerical scheme that was derived by Osher and Sethian (Sethian and Smereka, 2003), which was influenced by numerical schemes for conservation laws:

$$u_{ijk}^{n+1} = u_{ijk}^n + \eta v_{ijk} \nabla_{ijk}^n$$

where

$$\|Du(x_{ijk}, t_n)\| \approx \nabla_{ijk}^n = \begin{cases} \nabla_{ijk}^+ & -v_{ijk} \geq 0 \\ \nabla_{ijk}^- & v_{ijk} \geq 0 \end{cases}$$

The superscript n has been suppressed in the terms, ∇_{ijk}^+ and ∇_{ijk}^- , which are defined as

$$\nabla^+ = \left[\max(D_{ijk}^{-x}, 0)^2 + \min(D_{ijk}^{+x}, 0)^2 + \max(D_{ijk}^{-y}, 0)^2 + \min(D_{ijk}^{+y}, 0)^2 + \max(D_{ijk}^{-z}, 0)^2 + \min(D_{ijk}^{+z}, 0)^2 \right]^{\frac{1}{2}},$$

and

$$\nabla^- = \left[\min(D_{ijk}^{-x}, 0)^2 + \max(D_{ijk}^{+x}, 0)^2 + \min(D_{ijk}^{-y}, 0)^2 + \max(D_{ijk}^{+y}, 0)^2 + \min(D_{ijk}^{-z}, 0)^2 + \max(D_{ijk}^{+z}, 0)^2 \right]^{\frac{1}{2}}.$$

The terms D_{ijk}^{-x} or D_{ijk}^{+x} , for example, represent forward or backward difference of u with respect to the coordinate x. For example

$$D_{ijk}^{+x} = \frac{u_{i+1,j,k}^n - u_{ijk}^n}{\Delta x} \approx u_x(x_{ijk}, t_n) ,$$

and

$$D_{ijk}^{-x} = \frac{u_{ijk}^n - u_{i-1,j,k}^n}{\Delta x} \approx u_x(x_{ijk}, t_n) .$$

The terms, $D_{ijk}^{\pm y}$ and $D_{ijk}^{\pm z}$ are of course defined analogously. The naive numerical schemes that use purely forward, backward, or centered finite differences to approximate the spatial derivatives result in numerical instability. On the other hand, the numerical scheme that is given by Equation (B.2) is stable and converges toward the one-of-a-kind viscosity solution for Problem B.1 (Sethian and Smereka, 2003).



اونيورسيتي مليسيا قهغ السلطان عبدالله
UNIVERSITI MALAYSIA PAHANG
AL-SULTAN ABDULLAH

Appendix C:

STATISTICALLY-CALIBRATED LEVEL SET THEORY PROOFS

Theorem C.1. Let Γ_τ be a closed surface in \mathbb{R}^3 where $v : \mathbb{R}^3 \rightarrow \mathbb{R}$ is positive inside Γ_τ and negative outside. Suppose u is a $C^1(\mathbb{R}^3 \times (0, \infty))$ solution to Problem and that the initial conditions u_0 are chosen so that

1. In each connected region where $v > 0$, there is an open region with $u_0 > 0$ everywhere.
2. In each connected region where $v < 0$, there is an open region with $u_0 < 0$ everywhere. Then $\Gamma_t \rightarrow \Gamma_\tau$ as $t \rightarrow \infty$.

$$M(t) = \int_{\mathbb{R}^3} H(u)v dx$$

where H is the unit step function, which returns a value of one when the input it is given is positive and a value of zero otherwise. The function $M(t)$ shows the degree to which the positive and negative regions of u and v are in agreement with one another. This pertains to us.

1. $M(t)$ is maximal when the positive and negative regions of u and v match (and thus $\Gamma_t = \Gamma_\tau$).

2. $M_0(t) \geq 0$ and $M_0(t) = 0$ only when $\Gamma_t = \Gamma_\tau$.

Item 1 is easy to see, and this thesis prove Item 2 presently. First, this thesis calculate that

$$M'(t) = \int_{\mathbb{R}^3} \delta(u)u_t v dx = \int_{\mathbb{R}^3} \delta(u)v^2 |Du| dx = \int_{\Gamma_t} v^2 dS \geq 0$$

The first equality is in the sense of distributions (i.e., $\frac{d}{ds}H(f(s)) = \delta(f(s))f'(s)$ for f smooth). The last equality employs a distributional form of the co-area formula (Evans and Garzepy, 2018).

$$\int_{\mathbb{R}^3} g |Du| dx = \int_{-\infty}^{\infty} \int_{\{u=r\}} g dS dr$$

by taking $g(x,t)=\delta(u(x,t))v^2(x)$. $M(t)$ is thus non-decreasing. Furthermore, $M'(t)$ is strictly positive unless Γ_t is subset of Γ_τ . This thesis now show that any case where Γ_t is a proper subset of Γ_τ is excluded by the assumptions on the initial conditions u_0 . This thesis consider two cases:

1. Γ_t is proper subset of Γ_τ but $\{u > 0\}$ is empty.

This cases includes, for example, if Γ_t includes only a patch of the surface Γ_τ , or other such degenerate cases (see Figure C.1i). First, denote each connected region where $v > 0$ as V_i^+ ($i = 1, 2, \dots$). The initial conditions stipulate that for each V_i^+ , there is an open region $U_i^+ \subset V_i^+$ where $x \in U_i^+ \Rightarrow u_0(x) > 0$. Each open region U_i^+ remains open in \mathbb{R}^3 since for any x in this region u is non-decreasing because $u_t = v\|Du\| \geq 0$ since $v(x) > 0$ in $U_i^+ \subset V_i^+$. Thus, the set $\{u > 0\}$, whose boundary is the surface Γ_t , cannot collapse into an empty set since $U_i^+ \subset \{u > 0\}$ for all t .

2 Γ_t is proper subset of Γ_τ and $\{u > 0\}$ is non-empty.

In this case, Γ_τ is composed of multiple “sub-surfaces” (e.g., two distinct closed surfaces, or a spherical shell), and Γ_t is equal to only one of them. There are three sub-cases to consider:

(a) Γ_τ includes a sub-surface that is contained entirely inside of Γ_t .

An example of this case is shown in Figure C.1ii. This implies that Γ_t encloses an open region with $v < 0$, say V_i^- for some i . However, $u > 0$ everywhere in V_i^- since $u > 0$ in the region enclosed by Γ_t and Γ_t encloses V_i^- . However, the region V_i^- must contain a region $U_i^- \subset V_i^-$ where $u_0 < 0$ everywhere in U_i^- by assumption, and u remains negative in U_i^- for all t since u is non-increasing in U_i^- . This is a contradiction, and thus this sub-case cannot occur.

(b) Γ_τ includes a sub-surface that is entirely outside of Γ_t but which contains Γ_t .

An example of this case is shown in Figure C.1iii. From the figure it is again immediate that there are connected regions with both $v > 0$ (say, V^+) and $v < 0$ (say, V^-) outside of the region enclosed by Γ_t where the respected open regions from the initial conditions

(say, U^+ and U^-) have somehow vanished. Yet, these regions cannot vanish because u

is non-decreasing or non-increasing, respectively, in U^+ and U^- .

(c) Γ_τ includes a sub-surface that is entirely outside of Γ_t and does not contain Γ_t .

Any example of this case is shown in Figure C.1iv. Clearly, the sub-surface of Γ_τ that is outside of Γ_t , encloses an open region with $v > 0$ which contained an open region with $u > 0$ that vanished. But again, this cannot occur since u is non-decreasing in such a region.

Any case with $\{u > 0\}$ non-empty and Γ_t being a proper subset of Γ_τ is a combination of one of the previous three sub-cases, and thus cannot occur.

Finally, considering both Case 1 and Case 2 above, this thesis conclude that $M'(t) > 0$ and $M'(t) = 0$ only when $\Gamma_t = \Gamma_\tau$, which proves the result.

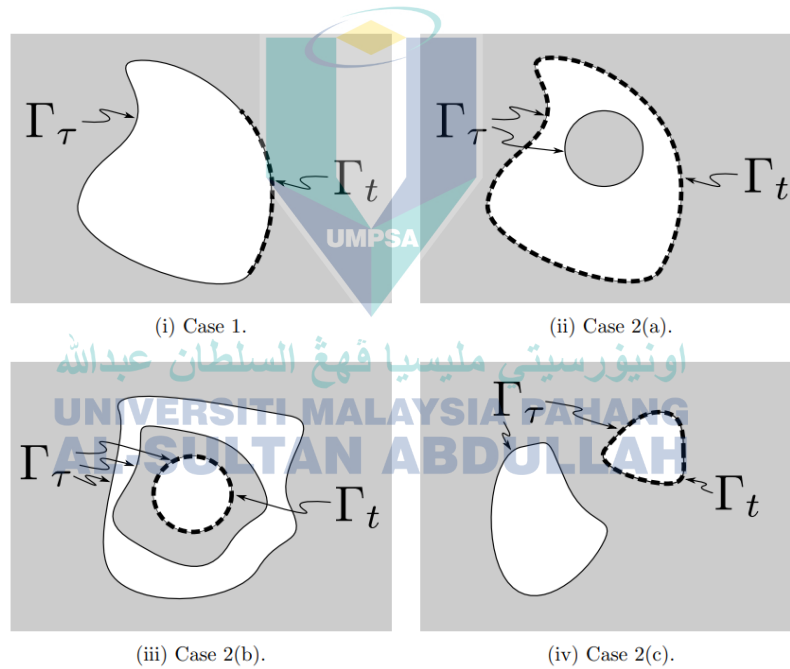


Figure C.1: In each of the above, the solid line is the target boundary Γ_τ , and the dashed line is the boundary Γ_t . The shaded, gray area represents regions where $v < 0$, whereas the white areas represent regions where $v > 0$. In each, Γ_t is a proper subset of Γ_τ and hence $M'(t) = 0$. Each of these cases is excluded by the assumptions on the initial conditions u_0 .

Theorem C.2. Suppose that for some N , if $n \geq N$, then $\eta > 0$ satisfies the condition,

$$\eta > \max_{ijk} \frac{-u_{ijk}^0}{s_{ijk} \sum_{m=0}^{n-1} \nabla_{ijk}^m}$$

Then $\text{sign}(u_{ijk}^n) = \text{sign}(v_{ijk})$ for $n \geq N$.

Proof. Pick $n \geq N$. Then, for any i, j, k ,

$$\begin{aligned} v_{ijk} u_{ijk}^n &= v_{ijk} u_{ijk}^0 + \eta v_{ijk}^2 \sum_{m=0}^{n-1} \nabla_{ijk}^m > v_{ijk} u_{ijk}^0 + \max_{q,r,s} \left(\frac{-u_{qrs}^0}{v_{qrs} v_{ijk}^2 \sum_{m=0}^{n-1} \nabla_{qrs}^m} \right) \sum_{l=0}^{n-1} \nabla_{ijk}^m \\ &\geq v_{ijk} u_{ijk}^0 + \left(\frac{-u_{qrs}^0}{v_{ijk} \sum_{m=0}^{n-1} \nabla_{ijk}^m} \right) v_{ijk}^2 \sum_{l=0}^{n-1} \nabla_{ijk}^m = 0 \end{aligned}$$

Theorem C.3. If for all i, j, k , $\nabla_{ijk}^0 > 0$, then there exists an η (depending on N) satisfying condition (C.1) in Theorem (C.2) for $N = 1, 2, \dots$, so that $\text{sign}(u_{ijk}^n) = \text{sign}(v_{ijk})$ for $n \geq N$ for any desired N .

Proof. For any $\epsilon > 0$, set $\eta(1) = \epsilon + \max_{ijk} \frac{-u_{ijk}^0}{v_{ijk} \nabla_{ijk}^1}$. Then the iteration converges in a single step. But clearly for every N , $\max_{ijk} \frac{-u_{ijk}^0}{v_{ijk} \nabla_{ijk}^N} \geq \max_{ijk} \frac{-u_{ijk}^0}{s_{jj} \sum_{m=0}^{N-1} \nabla_{ijk}^m}$, so for any $\epsilon > 0$, setting $\eta(N) = \epsilon + \max_{ijk} \frac{-u_{ijk}^0}{v_{ijk} \sum_{m=0}^{N-1} \nabla_{ijk}^m}$, yields agreement in N steps.

Appendix D:

SEGMENTATION FEATURES

Note that even though this thesis specify the features below assuming three-dimensional scalar fields for both the image and level set function volumes, the majority of the features have natural one- and two-dimensional analogs. This is the case even though this thesis specify the features below assuming three-dimensional scalar fields. In the following, H will serve as the unit step function.

D.1 Global Shape Features

A variety of geometrical features based purely on the current segmentation (i.e., the region where u_{ijk} is positive) are utilized.

- Boundary length. This feature computes the surface-area of the zero level surface by approximating the integral, $\int_{\mathbb{R}^3} \|DH(u(x, y))\| dV$:

$$L(u) = \sum_{ijk} (|DH(u)|)_{ijk}$$

Central finite differences are used to approximate the gradient operator.

- Volume. This feature approximates the area enclosed by the discretized level set by counting the number of coordinates where u_{ijk} is positive:

$$V(u) = \sum_{ijk} H(u_{ijk})$$

- Isoperimetric Ratio. The isoperimetric ratio is defined as:

$$Q(u) = \frac{36\pi \cdot V(u)^2}{L(u)^3}$$

This results in a number that is somewhere between zero and one, with the value being one when the border is volume (e.g., see reference Do Carmo, 2016)). As a result, this provides a measurement of sphericity, but it also has a value that is constant for various geometric planar forms. This ratio decreases as the surface area gets cumbersome in comparison to the volume that is contained inside it, which is typically seen as an unfavorable quality. Take note that this property may also be specified for arbitrary dimensions; for instance, in two dimensions, it can be used to determine the degree to which something is circular.

- Points of segmentation within the PTH These include three distinct aspects (along the i, j, and k axes). This thesis often calculate these characteristics for $p = 1, 2,$ and 3 . These calculations, when performed with p equal to 1, provide the "center of mass" for the area in which u_{ijk} is positive. When p is equal to two, these characteristics provide a quantitative description of the "spread" of the area in which u_{ijk} is positive.

$$\bar{i}_p(u) = \frac{\sum_{ijk} i^p \cdot H(u_{ijk})}{V(u)}, \bar{j}_p(u) = \frac{\sum_{ijk} j^p \cdot H(u_{ijk})}{V(u)}, \bar{k}_p(u) = \frac{\sum_{ijk} k^p \cdot H(u_{ijk})}{V(u)}$$

The mean, the standard deviation, and the greatest distance to the center of mass are shown here. Calculated for coordinates close to the zero-level surface of u is the distance to the center of mass feature (see Equation E.8), as well as the average, standard deviation, and maximum over the computed distances. Also computed is the maximum over the computed distances.

D.2 Global Image Features

The smoothed picture values are confined to the area where u_{ijk} has a positive value, and different statistics are calculated on those values. This results in the computation of several global image characteristics. You may also generate global image features by limiting your analysis to image values that are close to the border of the zero level set that u_{ijk}

- Mean employs within. This feature calculates the image's average value in cases when u_{ijk} is positive, as follows:

$$\bar{M}(u, M) = \frac{\sum_{ijk} (G_\sigma * M)_{ijk} \cdot H(u_{ijk})}{V(u)}$$

- Standard deviation inside. This feature computes the variability of the image values inside the region where u_{ijk} is positive:

$$\overline{\sigma}_M(u, M) = \sqrt{\frac{\sum_{ijk} [(G_\sigma * M)_{ijk} - \bar{M}]^2 \cdot H(u_{ijk})}{V(u)}}$$

- Average edge strength. This function determines the overall edge strength across the zero-level surface of u and then compares that value to the surface area of the zero-level surface. A close approximation of the surface integral is used to calculate it, $\oint_{\{u=0\}} |D(G_\sigma * M)| dS = \int_{R^3} |D(G_\sigma * M)| |D(H(u))| dV$ and normalizing:

$$E_g(u, M) = \frac{1}{L(u)} \sum_{ijk} (|D(G_\sigma * M)|)_{ijk} \cdot (|DH(u)|)_{ijk}$$

D.3 Local Shape Features

- The distance from the center of mass of the segmentation. Because it is defined in terms of a previously calculated global shape feature, this feature may be regarded as both global and local at the same time. This characteristic computes the distance between the coordinates $i, j,$ and k and the present center of mass of the area where u_{ijk} is positive (as determined by the $p = 1$ segmentation moments derived from Equation (E.4)).

$$D_m(i, j, k, u) = \sqrt{(i - \bar{i}_{p=1}(u))^2 + (j - \bar{j}_{p=1}(u))^2 + (k - \bar{k}_{p=1}(u))^2}$$

- Slice area. This feature is semi-local and can be computed along each axes. The area of the slice corresponding to a given axes is computed.

$$A_x(i, j, k, u) = \sum_{jk} H(u_{ijk}), A_y(i, j, k, u) = \sum_{ik} H(u_{ijk}), A_z(i, j, k, u) = \sum_{ij} H(u_{ijk})$$

- Alteration to the slice's absolute area. Using a centered difference approximation, this feature calculates an estimate of the absolute value of the derivative of the preceding slice area feature along a specified axis.

$$DA_x(i, j, k, u) = \frac{1}{2} |A_x(i + 1, j, k, u) - A_x(i - 1, j, k, u)|$$

The features along the other two axes (i.e., DA_y and DA_z) are computed analogously.

D.4 Local Image Features

- Image value. This feature yields the value of the Gaussian-smoothed smoothed image at the coordinate, (i, j, k):

$$M_\sigma(i, j, k) = (G_\sigma * M)_{ijk}$$

- Edge strength (local). This characteristic provides the edge strength of the Gaussian-smoothed smoothed picture at the coordinate (i, j, k). In order to get a close enough approximation of the gradient, centered differences are utilized on the inner points, while forward and backward finite differences are employed at the border.

$$E_1(i, j, k, M) = (|D(G_\sigma * M)|)_{ijk}$$

- The direction of the local spatial frequency Let's call the half-width of a given bounding box w . Now, let's think about a local voxel coordinate, which is written as (I, j, k), together with the two sets of values that are listed below:

$$S_{jk} = \sum_{l=-w}^w (G_\sigma * M)_{i+l,j,k}, S_{ik} = \sum_{l=-w}^w (G_\sigma * M)_{i,j+l,k}$$

The local spatial frequency orientation detector feature is define then as:

$$LFO_{ijk} = Var(S_{jk}) - Var(S_{ik})$$

where the letter Var stands for the sample variance over the values in the set. Note that in order to normalize these features across each image volume, this thesis first subtract the mean from the total for a specific image volume and then divide the result by the standard deviation of the total over that same image volume. Therefore, the value of this characteristic will be positive when the spatial frequency vector is parallel to the j-axis,

and it will be negative when the vector is parallel to the i-axis. This feature could be made more general so that it could find things along other axes or in general directions.

- Samples along normal. Consider a particular point $x_0 = (i, j, k)$ and the associated normal to the level set at that point, $N_0 = -Du(x_0)/\|Du(x_0)\|$. Then the image at scale σ (i.e., $M_\sigma = G_\sigma * M$) can be sampled along the line associated with x_0 and N , i.e.,

$$S_N(s) = M_\sigma(x_0 + s \cdot N_0)$$

This thesis sample $S_N(s)$ in the inward and outward direction (i.e., for positive and negative values of s) a distance $D_m(i, j, k, u)$; i.e., the distance from x_0 to the center of mass) for a total of twenty samples (ten in each direction). See Figure E.1 for a conceptual diagram of this feature.

- Samples along center-of-mass ray. Consider a particular point $x_0 = (i, j, k)$ and the computed center of mass, say p_0 . Now consider the unit vector, $r_0 = (x_0 - p_0)/\|x_0 - p_0\|$. Samples of the image at scale σ are obtained in the same manner as the “samples along normal” feature with r_0 in the role of N_0 . See Figure E.1 for a conceptual diagram of this feature.

$$S_N(s) = M_\sigma(x_0 + s \cdot N_0)$$

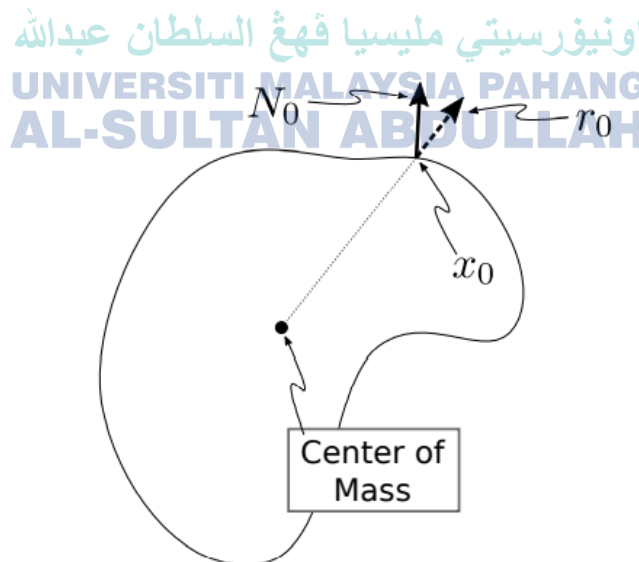


Figure D.1: Conceptual illustration of the “samples along normal” and “samples along center-ofmass ray” features.